

DYNAMICS AND CONTROL OF DRIFTING IN AUTOMOBILES

A DISSERTATION
SUBMITTED TO THE DEPARTMENT OF MECHANICAL
ENGINEERING
AND THE COMMITTEE ON GRADUATE STUDIES
OF STANFORD UNIVERSITY
IN PARTIAL FULFILLMENT OF THE REQUIREMENTS
FOR THE DEGREE OF
DOCTOR OF PHILOSOPHY

Rami Yusef Hindiyeh

March 2013

© 2013 by Rami Yusef Hindiyeh. All Rights Reserved.
Re-distributed by Stanford University under license with the author.



This work is licensed under a Creative Commons Attribution-
Noncommercial 3.0 United States License.
<http://creativecommons.org/licenses/by-nc/3.0/us/>

This dissertation is online at: <http://purl.stanford.edu/vz162hz7668>

I certify that I have read this dissertation and that, in my opinion, it is fully adequate in scope and quality as a dissertation for the degree of Doctor of Philosophy.

J Christian Gerdes, Primary Adviser

I certify that I have read this dissertation and that, in my opinion, it is fully adequate in scope and quality as a dissertation for the degree of Doctor of Philosophy.

Oussama Khatib

I certify that I have read this dissertation and that, in my opinion, it is fully adequate in scope and quality as a dissertation for the degree of Doctor of Philosophy.

Stephen Rock

Approved for the Stanford University Committee on Graduate Studies.

Patricia J. Gumpert, Vice Provost Graduate Education

This signature page was generated electronically upon submission of this dissertation in electronic format. An original signed hard copy of the signature page is on file in University Archives.

This dissertation is dedicated to my parents.

Abstract

In rally racing, it is quite common for drivers to deliberately corner with the rear tires of their racecar operating at their friction limits. Under such circumstances, the rear tires are said to be *saturated*. This practice is intriguing because it directly opposes the principles on which current vehicle safety systems are based; these systems react to rear tire saturation by restoring the vehicle to an operating regime in which the tires are not saturated. By deliberately saturating the rear tires when cornering, some of the world's best drivers are clearly utilizing control possibilities that have not yet been harnessed in automotive control design. Through a more thorough understanding of these drivers' cornering techniques, it may be possible to take advantage of these control possibilities in future safety systems, especially in the design of collision mitigation and avoidance systems for agile autonomous vehicles.

This dissertation focuses upon *drifting*, a cornering technique that involves steady-state operation with rear tire saturation. Drifts are typically characterized by countersteer, large sideslip angles, and significant rear wheelspin as a result of large rear drive torques. A drift corresponds to operation at an open-loop unstable equilibrium condition of a vehicle at which the rear tires are saturated. This dissertation examines the characteristics of "drift equilibria" using simple vehicle models and establishes three key characteristics of these equilibria.

The first characteristic is that yaw rate variations have a significant influence upon the sideslip dynamics around drift equilibria; in fact, the direct effect of a steering input upon the sideslip dynamics around a drift equilibrium is ultimately outweighed by the effect of that input acting through the yaw dynamics. The second characteristic is near-saturation of the front lateral force at drift equilibria, meaning that lateral

control authority through front steering is nearly unidirectional in character. The third and final characteristic is that the rear drive force input has significant lateral control authority around drift equilibria; this is as a result of the coupling between the rear tire lateral and longitudinal forces that arises from rear tire saturation.

These characteristics shape the design of a control algorithm that drifts a vehicle by stabilizing a desired drift equilibrium. The drift controller developed in this dissertation utilizes a successive loop structure in which yaw rate variations are used to control the sideslip dynamics in an outer loop and tire forces are used to control the yaw dynamics in an inner loop. The controller coordinates front lateral force (via steering) and rear drive force such that the front lateral force is used for lateral control whenever additional cornering force is available at the front tire, but the rear drive force is used for lateral control whenever the front tire is friction limited.

When implemented on a steer- and drive-by wire test vehicle, the drift controller achieves sustained, robust drifts while operating on a surface where friction varies considerably. Furthermore, stability analyses such as phase portraits and a numerically-validated Lyapunov function demonstrate the controller's ability to stabilize a desired drift equilibrium and create a sizable region of convergence around that equilibrium.

Nevertheless, the dual role of rear drive force as a longitudinal and lateral control input when drifting presents challenges from a stability analysis standpoint. A fundamental incompatibility between lateral and longitudinal control objectives arises when using the rear drive force for lateral control that makes it difficult to provide analytical stability guarantees for the drift controller. This same incompatibility also makes it difficult to develop a drift controller with a sufficiently large region of feasibility that explicitly prescribes stable lateral and longitudinal dynamics.

One way of addressing this issue is through the use of a third input for lateral control. Towards this end, this dissertation presents a drift controller design that incorporates differential control of drive and brake torques at the rear wheels as an additional means to generate a yaw moment. This drift controller has a fairly large region of feasibility while also enabling a straightforward, analytical demonstration of stability.

Acknowledgements

The years that I have spent in graduate school working towards this dissertation have been amongst the best years of my life thus far. My time at Stanford has provided me with many opportunities for intellectual, emotional, and artistic growth. I would not have had many of these opportunities were it not for the people who accompanied me on my journey to a doctorate, and I owe them all a debt of gratitude.

My advisor, Chris Gerdes, has given me so much in my time as his student. He laid the foundations for an incredibly unique thesis project (How many people can say they that their Ph.D. was about drifting?), and made sure that I never lacked the resources I needed to do the very best work I could. Chris' invaluable guidance not only helped me develop as an engineer, but also as a problem-solver, writer, and presenter. He has taught me to ask big questions, seek out simple, elegant answers, and enthusiastically share those answers with the world.

The members of my defense committee have helped make my final months at Stanford very fruitful from an intellectual standpoint. I am grateful to Professors Per Enge, Oussama Khatib, Paul Mitiguy, and Steve Rock for fostering lively, insightful discussions during my defense, especially during the closed session. The diversity of their perspectives has helped me view my work from a broader lens and develop a better sense for its future implications. I owe special thanks to Professors Khatib and Rock for serving on my reading committee; the feedback they provided has proven integral to the refinement and completion of this dissertation.

The students of the Dynamic Design Lab have proven to be a constant source of support and camaraderie. Senior students in the DDL during my early years in the lab — Chris Gadda, Judy Hsu, Shad Laws, Matt Roelle, Nikhil Ravi, Josh Switkes,

and Kirstin Talvala — always impressed me with their know-how and willingness to help a younger student navigate through technical and non-technical issues alike. My contemporaries in the lab — Craig Beal, Carrie Bobier, Adam Jungkunz, Krisada Kritayakirana, and Hsien Hsin Liao — are part of many fond memories from my time as a DDLer. From enduring the trials and tribulations of vehicle testing in remote locales to countless hours spent working on problem sets to the DDL “Family Vacation” in Munich, they are not only highly capable colleagues that I respect, but friends that I value greatly. As for the younger members of the lab — Avinash Balachandran, Holly Butterfield, Steve Erlien, Joe Funke, Nitin Kapania, John Kegelman, Jackie Liao, Hyungchai Park, and Paul Theodosis — thank you for helping to create such an exciting (and entertaining) atmosphere in the lab, both socially and intellectually. I will miss you all not only as colleagues, but as bocce ball opponents and fellow food truck connoisseurs.

The DDL administrators, Denise Curti and Jennifer Rahn, have been instrumental in the day-to-day business of getting research done. I am indebted to them for their assistance with a dizzying array of tasks, from ordering parts to arranging meetings and making travel plans. They definitely helped make the daunting process of completing a Ph.D. more manageable through their constant efforts.

I do not think I can fully express my gratitude to the Frank H. and Eva B. Buck Foundation for the support they have provided me throughout my higher education. Their unbelievable generosity provided me with amazing opportunities to explore my interests as both an engineer and musician. I would especially like to acknowledge Robert Walker, Gloria Brown, and Teresa Willis at the Buck Foundation for their devotion to the foundation and its objectives. They always ensured that I had access to the foundation’s resources and have worked tirelessly to create a tight-knit community of Buck Scholars; I am honored to be a part of this incredibly diverse and gifted group of people.

It is difficult to imagine the past six years without the support and companionship of my friends. From my oldest childhood friends to friends that I made in my final months at Stanford, I am blessed to have such loving, generous, and loyal people in my life. They are an integral part of many happy memories from my time at Stanford,

from birthday parties and weddings to my defense, which many of them went out of their way to attend. As an only child, I often miss having siblings, and I view my friends as the next best thing; I know that I can count on them to help me through lows, but also to celebrate highs in grand fashion.

Music and trombone performance have been a huge part of my life at Stanford University. Many fulfilling evenings and weekends of my graduate career have been spent in lessons, rehearsals, and performances. I offer my hearty thanks to Giancarlo Aquilanti, Jindong Cai, Martin Fraile, and McDowell Kenley from the Stanford Music Department for helping me to pursue trombone performance seriously during my time at Stanford; their efforts provided me with a much-needed counterbalance to the trials and tribulations of doctoral research. I would also like to thank my friends who are fellow musicians; through a shared passion for performance and classical music, I have forged strong, enduring bonds with these people that were a defining part of my graduate experience. I hope that they will join me in celebrating the completion of my dissertation by singing (or at least humming) a tune that we all know and love:



Finally, I would like to offer my most heartfelt thanks to my parents, Yusef and Randa Hindiyeh. It is only through their unconditional and unrelenting support that I find myself where I am today. From early on, they have nurtured the engineer within me, providing me with whatever I needed to pursue my dreams. As a child, they patiently allowed me to take over the family room coffee table with an airport that I built from LEGOs over the course of many months. As a graduate student, they were always there for me and helping me in any way they could, from an encouraging phone call to an amazing home-cooked meal. They have been astonishingly generous with their time and love in all stages of my development and education, and I know that will continue to be true as I enter into the next phase of my life.

Contents

	iv
Abstract	v
Acknowledgements	vii
1 Introduction	1
1.1 Vehicle motion during typical cornering versus drifting	4
1.2 Background	9
1.2.1 Modeling of drifting	9
1.2.2 Control strategies for drifting	11
1.3 Dissertation Contributions	12
1.3.1 Modeling for drift controller design	13
1.3.2 Physically-motivated design of a drift controller	13
1.3.3 Experimental validation of the drift controller	14
1.3.4 Analysis of closed-loop dynamics	15
1.3.5 Conceptual study of alternate controller designs	16
1.4 Dissertation Outline	16
2 Vehicle Modeling and Testbeds	20
2.1 Tire Modeling	21
2.1.1 The Brush Tire Model	21
2.1.2 Longitudinal Force Modeling	28
2.2 Chassis Modeling	36

2.2.1	The Bicycle Model	36
2.3	P1, the By-wire Testbed	40
2.3.1	Overview	40
2.3.2	Vehicle Parameters	41
3	Vehicle Equilibrium Analysis	46
3.1	Equilibria of the two-state model	48
3.1.1	Calculating equilibrium locations	48
3.1.2	Phase portrait analysis	55
3.1.3	Linearized dynamics around the drift equilibria	58
3.2	Equilibria of the three-state model	64
3.2.1	Calculating equilibrium locations	65
3.2.2	Phase portraits around equilibria	72
3.3	Implications for control design	77
4	Control Design for Drifting	79
4.1	The effects of vehicle inputs around equilibria	80
4.1.1	Straight-ahead driving	84
4.1.2	Typical cornering	85
4.1.3	Drift equilibria	88
4.2	Understanding the role of steering and rear drive force inputs in drifting	91
4.2.1	A steering-based controller for drifting	93
4.2.2	Regulation using rear drive force	97
4.2.3	A roadmap for coordinating steering and rear drive force inputs	105
4.3	A controller for sustained drifting	107
4.3.1	Overview of structure	107
4.3.2	Outer loop design	109
4.3.3	Inner loop design	110
4.3.4	Input coordination scheme	111
4.4	Experimental implementation	113

5 Stability Analysis	119
5.1 Sliding surface interpretation	121
5.2 Demonstration of closed-loop stability	124
5.2.1 Closed-loop dynamics	124
5.2.2 Local stability	126
5.2.3 Computation of an invariant set	128
5.3 Phase portrait analysis	131
5.3.1 Region of convergence	131
5.3.2 Graphical interpretation of sliding surface behavior	135
5.3.3 Analysis of the longitudinal dynamics	138
5.4 An alternate drift controller design	140
5.4.1 Closed-loop dynamics and local stability	142
5.4.2 Phase portrait and feasibility analysis	143
5.5 The dilemma of rear drive force control	152
6 Additional Actuation	153
6.1 Rear wheel steering	154
6.1.1 Modeling	154
6.1.2 Pseudodrift equilibria	156
6.1.3 Rear wheel steering around a true drift equilibrium	159
6.2 Differential torque control at the rear axle	162
6.2.1 Modeling	162
6.2.2 Stable decoupled dynamics using differential torque control .	165
6.2.3 Sliding surface control using differential torques	172
7 Conclusions	192
7.1 Future Work	195
7.1.1 Refinement of drifting using differential torque control	195
7.1.2 Extension to agile autonomous vehicle research	197
7.2 Outlook	198
Bibliography	199

List of Tables

2.1	Summary of bicycle models	39
2.2	Parameters for the P1 by-wire testbed on test surface used for experiments	42
4.1	Target equilibrium and gains for implementation of the steering-based drift controller.	94
4.2	Target equilibrium and gains for implementation of the drive force-based regulator	97
4.3	Target equilibrium and gains for implementation of the drift controller.	114
5.1	Equilibrium data and controller gains used in stability analysis	127
6.1	Pseudodrift equilibrium data	158
6.2	Parameters used for implementation of the control equation in Equation 6.15.	166
6.3	Parameters used for solution of the optimization problem in Equation 6.27	180

List of Figures

1.1	Nobuhiro “Monster” Tajima racing in the 2010 Pikes Peak International Hillclimb [28].	3
1.2	Body-fixed coordinate system for defining vehicle motion [3].	5
1.3	Visualization of vehicle motion during cornering when using a non-holonomic vehicle model.	6
1.4	Visualization of vehicle motion during typical cornering (left) and a drift (right) when using a holonomic vehicle model.	8
1.5	Example phase portrait depicting three equilibria, denoted by red dots. Two are unstable high-sideslip equilibria and one is a stable equilibrium corresponding to conventional cornering.	10
2.1	Components of the brush tire model and assumptions associated with the brush tire model in this dissertation.	22
2.2	Graphical representation of tire slip angle and the resulting contact patch deflection.	23
2.3	Graphical representation of lateral force demand along the contact patch.	23
2.4	Graphical representation of normal load per unit length along the contact patch.	24
2.5	Evolution of lateral force per unit length $q_y(x)$ (shown in red) with increasing slip angle.	25
2.6	Tire lateral force as a function of slip angle magnitude.	26
2.7	Longitudinal deflection of brush elements in the contact patch due to a positive wheel slip ($\kappa > 0$) induced by drive torque.	29

2.8	Coupling of lateral and longitudinal forces at fixed values of wheel slip κ (top) and fixed values of slip angle α (bottom)	31
2.9	Graphical depiction of the friction circle constraint in the (F_x, F_y) plane.	33
2.10	Variation in tire lateral force curve with longitudinal force input.	34
2.11	Diagram of the bicycle model for a RWD vehicle.	36
2.12	P1, the student-built steer- and drive-by-wire test vehicle.	41
2.13	Empirical tire curve for the front lumped tire fitted with the lateral tire model (in red).	44
2.14	Empirical tire curve for the rear lumped tire fitted with the lateral tire model (in red).	45
3.1	Equilibrium sideslip versus steer angle with $U_x^{eq} = 8$ m/s for the two-state bicycle model.	50
3.2	Equilibrium yaw rate versus steer angle with $U_x^{eq} = 8$ m/s for the two-state bicycle model.	51
3.3	Equilibrium front lateral force versus steer angle with $U_x^{eq} = 8$ m/s for the two-state bicycle model.	52
3.4	Equilibrium rear lateral force versus steer angle with $U_x^{eq} = 8$ m/s for the two-state bicycle model.	53
3.5	Phase portrait of state trajectories for the two-state bicycle model with $U_x^{eq} = 8$ m/s and $\delta^{eq} = 0^\circ$	56
3.6	Phase portrait of state trajectories for the two-state bicycle model with $U_x^{eq} = 8$ m/s and $\delta^{eq} = -5^\circ$	56
3.7	Phase portrait of state trajectories for the two-state bicycle model with $U_x^{eq} = 8$ m/s and $\delta^{eq} = -15^\circ$	57
3.8	Graphical representation of the effective front cornering stiffness \tilde{C}_{α_F} at an equilibrium operating point on the front tire curve.	61
3.9	Step response of the linearized sideslip dynamics for the two-state model with $\tilde{C}_{\alpha_F} = 13,239$ N/rad and $\delta\delta = 0.5$ deg.	63
3.10	Equilibrium sideslip versus steer angle with $U_x^{eq} = 8$ m/s for the three-state bicycle model.	66

3.11	Equilibrium yaw rate versus steer angle with $U_x^{eq} = 8$ m/s for the three-state bicycle model.	67
3.12	Equilibrium front lateral force versus steer angle with $U_x^{eq} = 8$ m/s for the three-state bicycle model.	68
3.13	Equilibrium rear drive force versus steer angle with $U_x^{eq} = 8$ m/s for the three-state bicycle model.	69
3.14	Rear tire force magnitude versus steer angle with $U_x^{eq} = 8$ m/s for the three-state bicycle model.	70
3.15	Phase portrait of state trajectories of the three-state bicycle model with $\delta^{eq} = -12^\circ$ and $F_{xR}^{eq} = 2293$ N.	73
3.16	Two-dimensional section of the phase portrait for the three-state bicycle model: Vector field of sideslip and yaw rate derivatives when $U_x^{eq} = 8$ m/s with $\delta^{eq} = -12^\circ$ and $F_{xR}^{eq} = 2293$ N.	74
3.17	Step response of sideslip perturbation dynamics computed from the three-state model with $\delta\delta = 0.5$ deg	76
4.1	b_{12} (top), b_{22} (center), and b_{31} (bottom) versus $a_y^{eq}/(\mu g)$ for typical cornering at $U_x^{eq} = 8$ m/s, as computed using typical cornering equilibria from Chapter 3. The points marked by diamonds (\diamond) and squares (\square) denote the values of b_{12} , b_{22} , and b_{31} at 40% and 96% of the steady-state lateral acceleration limit, respectively.	86
4.2	Sideslip angle (top), yaw rate (middle), and longitudinal velocity (bottom) for an experimental run with the steering-based drift controller.	94
4.3	Steer angle (top) and front lateral force (bottom) for an experimental run of the steering-based drift controller.	95
4.4	Phase portrait of state trajectories from initial conditions where $\delta\beta_0 > 0$, $\delta r_0 < 0$, and $\delta U_{x0} = 0$ for the drive force-based regulator.	98
4.5	δU_x and δF_{xR} versus time for initial conditions where $\delta\beta_0 > 0$, $\delta r_0 < 0$, and $\delta U_{x0} = 0$ when using the drive force-based regulator.	99
4.6	$\delta\beta$ and δr versus time for initial conditions where $\delta\beta_0 > 0$, $\delta r_0 < 0$, and $\delta U_{x0} = 0$ when using the drive force-based regulator.	100

4.7	Phase portrait of state trajectories from initial conditions where $\delta\beta_0 < 0$, $\delta r_0 > 0$, and $\delta U_{x0} = 0$ for the drive force-based regulator.	102
4.8	δU_x and δF_{xR} versus time for initial conditions where $\delta\beta_0 < 0$, $\delta r_0 > 0$, and $\delta U_{x0} = 0$ when using the drive force-based regulator.	103
4.9	$\delta\beta$ and δr versus time for initial conditions where $\delta\beta_0 < 0$, $\delta r_0 > 0$, and $\delta U_{x0} = 0$ when using the drive force-based regulator.	104
4.10	Nested loop structure of the drift controller. Blue signal paths denote the inner loop of the controller.	107
4.11	Sideslip compared to β^{eq} (top) and yaw rate compared to r_{des} (bottom) during an experimental run.	114
4.12	Front lateral force command (top) and steering command (bottom) during an experimental run.	115
4.13	Longitudinal velocity (top) and rear drive force command (bottom) during an experimental run.	116
5.1	Level curves of the sliding surface variable s plotted in the (e_β, e'_r) plane.	123
5.2	2D sections of invariant set, $U_x = 8.848$ m/s. For reference, the $s = 0$ line is shown in red.	130
5.3	Phase portrait of closed-loop state trajectories, perspective view. The red dot denotes the desired drift equilibrium location.	132
5.4	Phase portrait of closed-loop state trajectories, viewed from the $(e_\beta e'_r)$ plane. The red line denotes the $s = 0$ plane.	133
5.5	Phase portrait of closed-loop state trajectories, viewed from $e'_r - e_{U_x}$ plane. Red dot denotes desired drift equilibrium location.	134
5.6	Sliding phase dynamics shown in the (e_β, e'_r, e_{U_x}) space. The red dot denotes desired the drift equilibrium location.	136
5.7	Two-dimensional view of the sliding phase dynamics (on the $s = 0$ plane). The red dot denotes desired drift equilibrium location.	137
5.8	Phase portrait for the alternate drift controller, perspective view. The red dot denotes the desired drift equilibrium location.	144

5.9	Phase portrait for the alternate drift controller, viewed from the (e_β, e'_r) plane. The red line denotes the $s = 0$ plane.	145
5.10	Phase portrait for the alternate drift controller, viewed from (e'_r, e_{U_x}) plane. The red dot denotes the desired drift equilibrium location.	146
5.11	Steering solutions for the alternate drift controller when $\delta_{max} = 23^\circ$. Black lines denote the range in the (e_β, e'_r) plane over which the phase portrait for the original drift controller was plotted. The black asterisk denotes the desired drift equilibrium location.	147
5.12	Front lateral force solutions for the alternate drift controller. Black lines denote the range in the (e_β, e'_r) plane over which the phase portrait for the original drift controller was plotted. The black asterisk denotes the desired drift equilibrium location.	148
5.13	Rear drive force force solutions for the alternate drift controller. Black lines denote the range in the (e_β, e'_r) plane over which the phase portrait for the original drift controller was plotted. The black asterisk denotes the desired drift equilibrium location.	149
6.1	Bicycle model of a RWD vehicle with rear wheel steering capability. .	155
6.2	Graphical representation of a pseudodrift equilibrium.	157
6.3	Phase portrait of open-loop state trajectories around a pseudodrift equilibrium, perspective view. The red dot denotes the pseudodrift equilibrium location.	158
6.4	Left: Bicycle model with the rear lumped tire expanded to show independent longitudinal force inputs at left rear and right rear tires. Right: Bicycle model with an equivalent rear axle yaw moment and net longitudinal force.	162
6.5	Front lateral force solutions for the three-objective drift controller. An asterisk denotes the desired drift equilibrium location.	167
6.6	Right rear longitudinal force solutions for the three-objective drift controller. An asterisk denotes the desired drift equilibrium location. . .	168

6.16 Approximate region of convergence calculated using the Lyapunov function defined by Equation 6.34 as compared to the infeasible region when $e_{U_x} = 0$ for the three-input sliding surface controller. 190

Chapter 1

Introduction

The four palm-sized contact patches between a car’s tires and the road are at the heart of that car’s ability to accelerate, decelerate, and corner. Deflection of the tire tread elements in these contact patches generates the forces that largely dictate a car’s motion. One of the primary challenges of vehicle control, whether by a human being or control algorithm, is that this force generation mechanism is ultimately limited by the available friction between the tread elements and the road.

A vehicle is said to operate at the limits of handling when its tires are *saturated*, meaning that they are generating the maximum force available from friction. If a vehicle’s front tires saturate before the rear when cornering, it exhibits a tendency to plow out of a turn, known as limit understeer. Conversely, if a vehicle’s rear tires saturate before the front when cornering, it exhibits a tendency to “fish tail” and spin out known as limit oversteer. In either case, the average driver typically lacks the skills to respond to tire saturation and properly control the vehicle.

In recognition of the danger that tire saturation poses to the average driver, significant effort has been invested into the development of electronic stability control (ESC) algorithms that are now standard on vehicles in the United States starting in model year 2012 [1]. ESC algorithms are designed to brake the wheels of a vehicle differentially in response to excursions into operating regimes where either the front or rear tires of the vehicle saturate [37]. According to the National Highway Transportation Safety Administration (NHTSA), these systems have had a significant

effect on vehicle safety, producing a 36% reduction in single vehicle car crashes, 70% reduction in fatal rollover crashes, and 19% reduction in fatal multi-vehicle crashes as of 2007 [10].

While the efficacy of ESC cannot be disputed, the functionality of ESC is built upon a conservative model of driver intent and capabilities. ESC systems respond to deviations between the vehicle’s behavior and a driver model that reflects an average driver’s understanding of vehicle dynamics [37]. Consequently, ESC control interventions are designed to guide a vehicle’s motion back to an operating regime in which an average driver can maintain control of the vehicle. These systems do not necessarily reflect or emulate the vehicle control techniques that would be used by a skilled driver to contend with rear tire saturation.

In fact, some of the best drivers utilize vehicle control techniques that are antithetical to the principles on which ESC is based. A technique known as *drifting* is a prime example, as it is defined by deliberate, steady-state cornering with saturated rear tires. To an observer, a drift can typically be identified by three distinctive characteristics. The first (and most prominent) of these is a large sideslip angle β , which reflects a large mismatch between the direction the vehicle is pointed and the direction that its center of gravity (CG) is moving; this corresponds to the vehicle cornering while moving noticeably sideways. The second is countersteer, where the vehicle is steered opposite the direction that it is turning. The final characteristic is large drive torques at the rear wheels, which manifests itself as significant rear wheelspin; these torques act to induce and maintain the rear tire saturation inherent to a drift.

Drifting is ubiquitous in rally racing, which frequently involves surfaces where friction is uncertain and varying, such as dirt, gravel, and snow/ice. Figure 1.1 depicts Nobuhiro “Monster” Tajima using a drift to negotiate a corner during a dirt stretch of a grueling rally race known as the Pikes Peak International Hillclimb that he has won multiple times.

It goes without saying that the drivers participating in rally races are extremely skilled. Therefore, they must have a rationale for controlling the vehicle in a fashion that requires deliberate rear tire saturation, in a way that an ESC system would



Figure 1.1: Nobuhiro “Monster” Tajima racing in the 2010 Pikes Peak International Hillclimb [28].

never permit. This intriguing mismatch between the basis for current safety systems and drifting suggests that conventional wisdom for vehicle control algorithms ignores control possibilities that can be opened up by understanding and emulating control techniques that use rear tire saturation rather than avoiding it. Such an investigation lends itself to a broader perspective on future systems for vehicle safety and performance enhancement, especially within the context of autonomous (self-driving) car development.

In fact, researchers are already investigating control algorithms for agile autonomous and semi-autonomous vehicles that utilize maneuvers involving rear tire saturation for the purposes of collision mitigation and avoidance. Chakraborty et al. [9] have proposed an algorithm that mitigates the severity of an impending “T-bone” collision between vehicles traveling in perpendicular directions by rapidly re-orienting one of the vehicles prior to collision using control inputs that deliberately saturate the rear tires. Along similar lines, an obstacle avoidance algorithm developed by Gray et al. in [19] explicitly incorporates drifting as an allowable operating condition for a vehicle in order to solve obstacle avoidance problems that would otherwise prove infeasible.

In both cases, the authors present intriguing practical applications for cornering with rear tire saturation. Furthermore, their work highlights the significant safety benefits that could arise from imbuing autonomous cars with the control skills of the world’s best drivers.

1.1 Vehicle motion during typical cornering versus drifting

The agile autonomous vehicle research described above leverages the fact that cornering with rear tire saturation allows for a less constrained form of vehicle motion when compared to typical cornering. In particular, cornering with rear tire saturation effectively decouples the vehicle’s heading (e.g., the direction it is pointed) from the direction its CG is moving, whereas these two quantities are tightly coupled during typical cornering.

In order to understand why this is true, it is necessary to compare the motion of the vehicle during typical cornering and drifting in vehicle dynamics terms. From the body-fixed coordinate system in Figure 1.2, the motion of the vehicle in the (x, y) plane is described in terms of the velocity vector \vec{V} at the CG, the sideslip angle β between \vec{V} and the x -axis of the vehicle, and the angular velocity (yaw rate) r of the vehicle about the z -axis of the vehicle.

The velocity vectors at the locations of the tire contact patches with the ground are also important in understanding the vehicle’s motion because they play a central role in how the dynamics of the vehicle are modeled. Assuming rigid motions of the vehicle, the velocity vector at the CG and the velocity vectors at the contact patches are related via kinematic equations. This means that the velocity vector at the CG and the vehicle yaw rate can be used to determine the velocity vectors at the contact patches, and vice versa; this turns out to have interesting implications for the motion of the vehicle.

Rudimentary models for vehicle motion often assume that the velocity vector at each tire contact patch is aligned with the longitudinal axis of the corresponding tire,

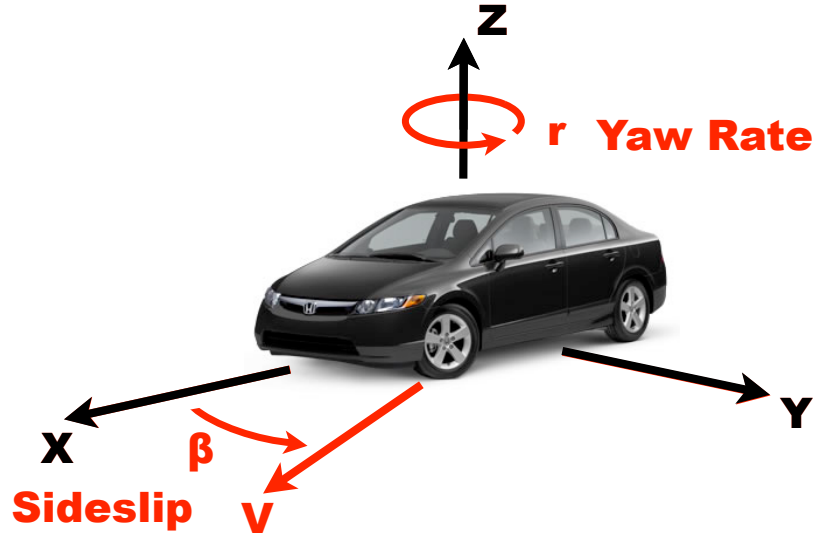


Figure 1.2: Body-fixed coordinate system for defining vehicle motion [3].

as depicted in Figure 1.3. This assumption amounts to a set of kinematic constraints on the velocity variables for the vehicle, meaning that such models treat the vehicle as a non-holonomic system. With these constraints, the velocity vectors at the front contact patches are rotated from the x -axis of the vehicle by the front steer angle δ , and the velocity vectors of the rear contact patches are aligned with the x -axis. As a result, the direction of the velocity vector at the CG, and therefore the sideslip angle β , is dictated purely by the front steer angle δ .

When maneuvering at parking lot speeds, where δ can be quite large, this means that β can be quite large. But in the case of higher speeds and lateral (y -direction) accelerations, friction limitations dictate that δ cannot be larger than a few degrees, meaning that the β cannot be larger than a few degrees as well. Consequently, non-holonomic models dictate that a vehicle's heading and motion at the CG *must* be tightly coupled at higher velocities and lateral accelerations. Obviously, this constraint makes non-holonomic models inappropriate for modeling vehicle motion during drifting.

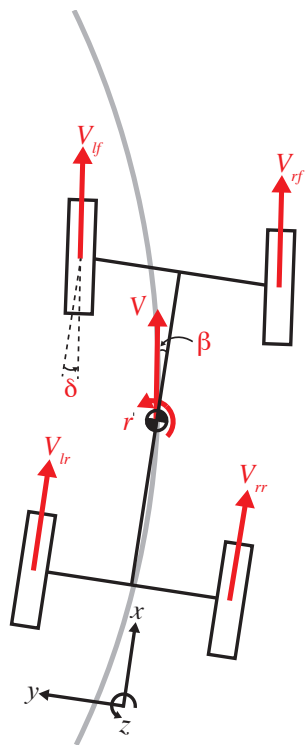


Figure 1.3: Visualization of vehicle motion during cornering when using a non-holonomic vehicle model.

In reality, non-holonomic models for vehicle motion are only accurate for describing low speed maneuvering of the vehicle. More dynamic behavior of the vehicle is better captured by models based on force constraints, rather than kinematic constraints. These models are based on the principle that a tire generates lateral force (directed along the y -direction of the tire) through tread deflection in the contact patch that results from a non-zero *slip angle* α at the tire. Along the same lines as the vehicle sideslip angle, tire slip angles describe the mismatch between the direction that the tire is pointed and the direction of the velocity vector at the contact patch. At the front tires, the slip angles (and therefore lateral forces) can be adjusted through steering; at the rear tires, the slip angles evolve with vehicle motion.

Models that incorporate tire slip angles as a mechanism for tire force generation treat the vehicle as a holonomic system subject to force constraints that arise from the friction limitations of the vehicle's tires. Tire force magnitude increases with slip angle magnitude until some threshold slip angle at which the friction available between the road and contact patch can no longer support further tread deflection in the contact patch and the tire saturates.

Even though holonomic models for vehicle motion are based on force constraints rather than kinematic ones, the tire slip angles in holonomic models are small for typical cornering. Tire force saturation typically occurs at slip angles of about 4° , meaning that the entire spectrum of typical cornering, from low acceleration turns in everyday driving to turns utilizing the full force capability of the tires in racing, is encompassed by a small slip angle range. Because the tire slip angles are so small during typical cornering, the vehicle sideslip angle β remains small as well, as shown in the left panel of Figure 1.4. For this reason, the vehicle heading and velocity vector at the CG are still tightly coupled when modeling typical cornering with holonomic models, even though these models are based on completely different assumptions than non-holonomic models.

Since rear tire saturation is an inherent aspect of drifting, the rear tire slip angles are no longer restricted to small values as they are in typical cornering. Whereas the rear slip angles do not exceed a few degrees during typical cornering, they can reach tens of degrees in a drift. Through the kinematic relationships discussed earlier, this

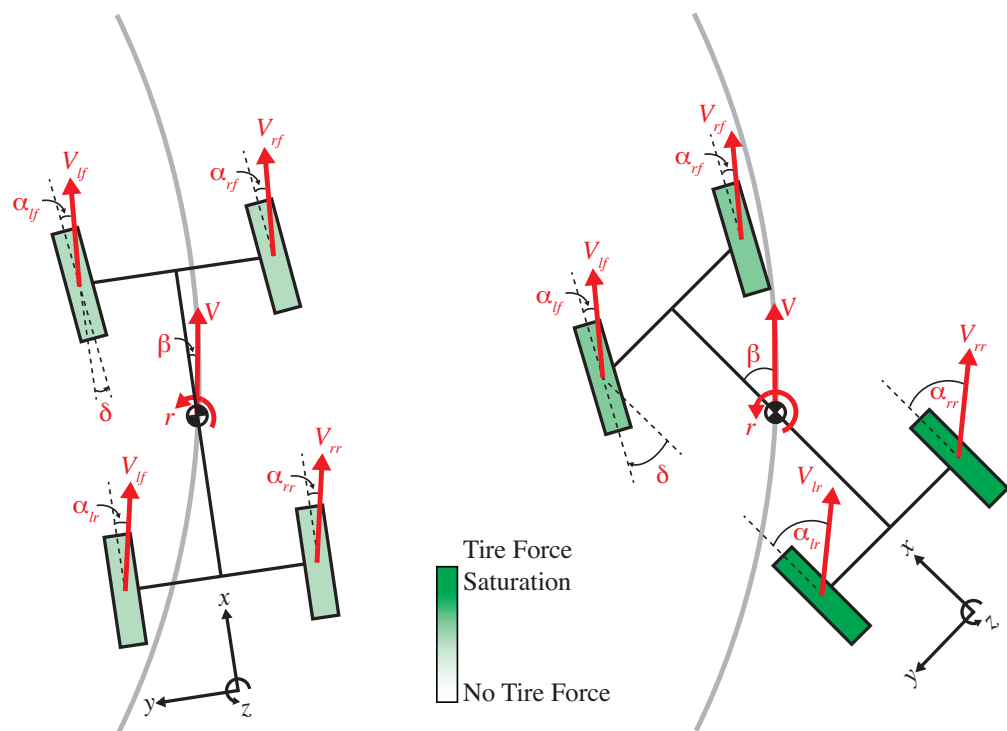


Figure 1.4: Visualization of vehicle motion during typical cornering (left) and a drift (right) when using a holonomic vehicle model.

translates to the large vehicle sideslip β that is characteristic of drifting, as shown in the right panel of Figure 1.4. More importantly, the fact that the rear slip angles are no longer constrained means that the vehicle sideslip angle is no longer constrained, effectively decoupling the direction the CG is moving from the heading of the vehicle.

In rally racing, this decoupling provides valuable flexibility to alter vehicle’s trajectory on surfaces with uncertain friction. But the work of Chakraborty et al. [9] and Gray et al. [19] suggests that this decoupling may have powerful applications in a vehicle safety context as well. With this in mind, this dissertation seeks to develop a fundamental understanding of the dynamics of drifting and the vehicle control possibilities enabled by sustained operation at conditions where the rear tire is saturated.

1.2 Background

Broadly speaking, there are two components to an investigation of drifting: how to model drifting, and the proper approach for controlling a drift. General investigations of vehicle dynamics in the literature have provided considerable insight into the modeling component, while recent interest in agile autonomous vehicles has led to research focused specifically on drifting that addresses both the modeling and control components.

1.2.1 Modeling of drifting

Since drifting is defined by steady-state operation with rear tire saturation, intuition would suggest that it should be modeled as an *equilibrium* of a vehicle at which the rear tires are saturated. This is indeed the case, as the existence of “drift equilibria” has been demonstrated repeatedly in the literature across a broad range of model fidelities.

Using simple, two-state models for the lateral dynamics of a vehicle, Inagaki et al. [24], Ono et al. [29], Hoffman et al. [23], Klomp [25], Bobier et al. [6], and Beal et al. [4] all demonstrated the existence of open-loop unstable drift equilibria.

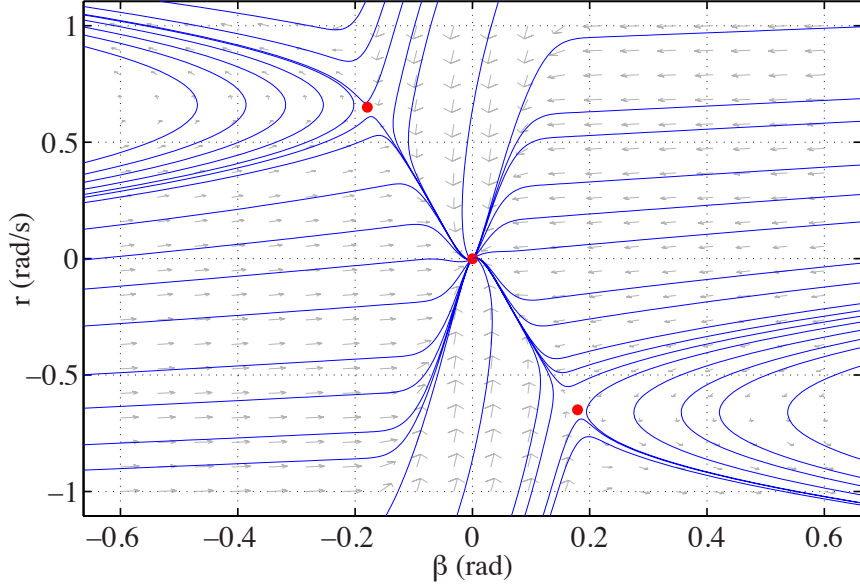


Figure 1.5: Example phase portrait depicting three equilibria, denoted by red dots. Two are unstable high-sideslip equilibria and one is a stable equilibrium corresponding to conventional cornering.

These researchers all employed a technique known as phase portrait analysis, which visualizes trajectories of the vehicle in the sideslip-yaw rate plane for a fixed steer angle and speed. This yields plots similar to the one shown in Figure 1.5, which depicts the existence of three equilibrium conditions: a stable equilibrium corresponding to straight-ahead driving in between two high-sideslip, unstable drift equilibria.

However, analysis using models of lateral dynamics alone provides only a partial characterization of drift equilibria. In research focused specifically on drifting, Edelmann et al. [12] and Velenis et al. [38, 39] established that drift equilibria are associated with large rear drive torques, and that these drive torques play a critical role in a drift. The tire models used by both authors reflect the fact that a tire saturates when the combined lateral and longitudinal force demand on the tire exceeds the force available from friction. Therefore, the large rear drive torques at drift equilibria are essential to creating rear tire saturation at drift equilibria. These torques translate to large longitudinal forces, which induce rear tire saturation by railing the combined force demand at the rear tires up against the friction limits of the tires.

In order to incorporate rear drive torque inputs into the analysis, it was necessary for Edelmann et al. and Velenis et al. to use models that include longitudinal dynamics. Compared to the two-state model mentioned earlier, both authors used considerably more elaborate models for this purpose that feature five states, load transfer effects, and complex tire models that include longitudinal wheel slip. The relative complexity of these models precluded simple analysis techniques like phase portraits. Nevertheless, Edelmann et al. established that drift equilibria are unstable in [12] through a root locus analysis of drift equilibrium stability with variations in longitudinal velocity.

Regardless of the model fidelity used for analysis, prior work indicates that drift equilibria are unstable. This of course means that drifting in practice requires closed-loop stabilization of these equilibria by a skilled driver; understanding and attempting to reproduce this control task embodies the second component of research efforts to understand drifting.

1.2.2 Control strategies for drifting

Researchers have explored control strategies for high-sideslip cornering through a combination of experimental data analysis and control design to drift a vehicle. This prior work suggests that coordination of steering and rear drive torque inputs plays a critical role in drifting.

Velenis et al. [39] and Abdulrahim et al. [2] collected measurements of both steering and longitudinal inputs during drifts executed by a skilled driver in a rear wheel drive (RWD) vehicle. Consistent with the equilibrium analyses described above, successful drifts are associated with large rear drive forces, indicated in the data by near-maximum or maximum throttle pedal inputs. Furthermore, the measurements obtained by these researchers indicate that coordination of this large rear drive force with front steering is essential to maintaining a drift.

Both Edelmann et al. [14] and Velenis et al. [39] developed controllers for a RWD vehicle that reflect this insight by coordinating front steering and rear drive torques in order to drift a vehicle. In both cases, the controller is designed by linearizing a

vehicle model at one of its drift equilibria and using full state feedback to compute steering and rear drive torque inputs that stabilize the linearized model in closed-loop. Gain selection is accomplished using multiple-input multiple-output (MIMO) design techniques, specifically pole placement in [14] and linear quadratic regulator (LQR) techniques in [39]. When implemented on nonlinear models in simulation, both controllers successfully stabilize a neighborhood around the desired equilibrium, though Edelmann et al. acknowledge that their design can only tolerate moderate disturbances.

Velenis et al. [38] have also proposed a control design for drifting using a more elaborate actuation strategy. Along the same lines as their work in [39], they present the design of a full-state feedback controller for drifting designed using LQR and linearization of the vehicle model around one of its drift equilibria. In this case, however, only longitudinal inputs are used for control, with the front and rear wheel torques (both braking and drive) treated as separate inputs. Formally speaking, this represents capabilities beyond the “standard” actuation available to a driver, though the driver does have some capability to create front/rear torque differentials through a technique known as “left foot braking,” where the brake and throttle pedals are operated simultaneously. Nevertheless, the success of the control design in [38] in simulation reflects a unique scenario in which a controller based purely on longitudinal actuation controls the lateral *and* longitudinal dynamics of the vehicle when operating in the neighborhood of a drift equilibrium.

1.3 Dissertation Contributions

This dissertation presents an examination of the dynamics and control of drifting through the development of a controller that coordinates steering and rear drive torque inputs to drift a car in a sustained, robust fashion. The process of developing this controller comprises five scientific contributions. The first two of these contributions establish the physical intuition that is used to design a drift controller, while the third contribution is a successful experimental implementation of this controller. The

final two contributions consist of an examination of the controller's stability characteristics and a conceptual study of alternate controller designs, including controllers utilizing additional actuation.

1.3.1 Modeling for drift controller design

The models used for the analysis of drift equilibria in prior work lie on opposite ends of the spectrum of model fidelity. On one end are simple models that are physically intuitive and enable the use of powerful analysis techniques like phase portrait analysis, but do not include all the dynamics and inputs relevant in drifting. On the other end are high fidelity models with several degrees of freedom that include the necessary dynamics and inputs, but at the expense of considerable complexity and a loss of physical intuition.

This dissertation presents a modeling approach that achieves a balance between sufficient model fidelity to capture the key physics associated with drifting and intuitive simplicity for the purposes of control design. This is accomplished by augmenting a two-state, lateral dynamics model with an additional longitudinal velocity state, rear drive force as a direct input, and a simple model for coupling of lateral and longitudinal forces at the rear tires. The drift equilibria of this three-state model are unstable saddle points that are similar to the drift equilibria of two-state models while also reflecting the need for large rear drive forces predicted by higher fidelity models.

1.3.2 Physically-motivated design of a drift controller

An examination of the dynamics around drift equilibria in this dissertation reveals three key physical characteristics of these equilibria. These characteristics dictate the proper technique for controlling a drift and shape the design of the drift controller presented in this dissertation.

Phase portraits and transfer functions derived from linearized dynamics reveal the first characteristic, which is that variations in yaw rate significantly influence the sideslip dynamics of the vehicle around a drift equilibrium. In fact, transfer function

analysis demonstrates that yaw rate has a more significant influence on the sideslip dynamics than direct control through steering when in a drift. With this in mind, the drift controller developed here has a successive loop structure in which yaw rate is treated a synthetic input to the sideslip dynamics in an outer loop and tire forces are used to control yaw rate by modulating the yaw moment acting on the vehicle

Examining a state space representation of the linearized dynamics around drift equilibria reveals the second key characteristic: when in a drift, rear drive force (which is nominally a longitudinal input) has significant control authority over the lateral dynamics of the vehicle. This results from the fact that rear tire saturation during a drift couples the lateral and longitudinal forces at the rear tires, making it possible to control the lateral forces at the rear tires through modulation of the rear drive force. This capability is incorporated into the drift controller design, which coordinates front lateral force (controlled through steering) and rear lateral force (controlled through rear drive force) commands to influence the yaw moment acting on the vehicle.

In spite of this added control capability when drifting, controller performance issues arise if one uses standard MIMO techniques to coordinate steering and rear drive force inputs. This is because of the third key characteristic of drift equilibria: near saturation of the front lateral force. Because the front tire operates so close to its friction limits when drifting, control authority through front steering is essentially unidirectional in character; front steering offers ample ability to decrease the yaw moment acting on the vehicle, but a significantly restricted ability to increase the yaw moment. This limitation is at the heart of the input coordination scheme developed for the drift controller, which uses steering for lateral control (and the rear drive force for longitudinal control) when controller commands can be realized within the friction limits of the front tire, but switches to the rear drive force for lateral control when the front tire is saturated.

1.3.3 Experimental validation of the drift controller

When implemented on a steer- and drive-by-wire test vehicle, the drift controller co-ordinates steering and rear drive force inputs to achieve sustained and robust drifts in

the presence of significant friction variability. This dissertation presents experimental data of a controlled drift that demonstrates the controller's ability to provide stabilization to a desired drift equilibrium over a broad region of the state space. To the author's knowledge, this is the first controller capable of achieving long, sustained drifts, and its performance matches or betters data of drifts performed by human drivers in the literature [39].

The experimental results obtained with the controller have broader implications as well. They support the assertion that a relatively simple three-state bicycle model is quite valid for analyzing the physics of a drift and developing a drift controller. Furthermore, the results also suggest that drifting is an effective cornering technique for contending with friction uncertainty.

1.3.4 Analysis of closed-loop dynamics

Even though the drift controller has been designed largely based on physical intuition, it has an alternate, control theoretic interpretation as a sliding surface controller that drives a linear combination of sideslip and yaw rate errors to zero. Within the context of this interpretation, a three dimensional extension of phase portrait analysis indicates that the controller stabilizes the desired drift equilibrium and creates a broad region of convergence around it, consistent with the experimental performance of the controller. These observations are corroborated by a numerical demonstration of local stability of the equilibrium.

Phase portrait analysis is also used to establish that the closed-loop longitudinal dynamics of the vehicle vary considerably depending upon whether the rear drive force is acting as a longitudinal or lateral control input. This behavior arises as a result of a conflict between longitudinal and lateral control objectives when the drive force is used for lateral control. While the controller creates a large region of convergence around a desired drift equilibrium in spite of this conflict, the significant variation in longitudinal dynamics between modes of operation makes it difficult to provide analytical stability guarantees for the controller.

1.3.5 Conceptual study of alternate controller designs

In the interest of developing a control design that facilitates analytical stability guarantees, a variant of the original drift controller design is proposed that prescribes stable longitudinal dynamics while blending steering and rear drive force inputs for lateral control instead of using a switching coordination scheme. The controller turns out to have an impractically small region of feasibility in the state space as a result of the same conflict between lateral and longitudinal control objectives observed for the original design. This result shows that this conflict of objectives is simply a physical constraint of using rear drive force for the dual purposes of lateral and longitudinal control.

This dissertation demonstrates that additional actuation can be used to develop drift controllers that avoid this constraint. Differential control of the drive and brake torques at the rear tires makes it possible to satisfy a longitudinal control command while also generating a yaw moment on the vehicle for lateral control. Incorporating this capability into the control design described in the preceding paragraph enables an analytical guarantee of stability and significantly enlarges the region of feasibility around the desired drift equilibrium, though the region of feasibility for this controller is still somewhat smaller than that for the original drift controller.

1.4 Dissertation Outline

The subsequent chapters of the dissertation are organized as follows:

Chapter 2: Vehicle Modeling and Testbeds

Chapter 2 presents the tire and vehicle models used throughout this dissertation. It introduces multiple approaches to tire force modeling, including a simplified model for lateral-longitudinal force coupling at the rear tire that figures prominently in this work. It then presents two versions of the “bicycle” model for a vehicle’s dynamics: a two-state model of the lateral dynamics, and a three-state model that incorporates longitudinal dynamics and a rear drive force input. The chapter closes by introducing

P1, the by-wire test vehicle used for experiments in this dissertation.

Chapter 3: Vehicle Equilibrium Analysis

Chapter 3 presents an in-depth investigation of the equilibrium conditions of the vehicle models introduced in the preceding chapter, with a particular focus upon drift equilibria. It begins by studying the equilibria of the two-state vehicle model, comparing and contrasting the equilibria corresponding to typical cornering and drifting. The chapter then examines the dynamics around drift equilibria of this model through phase portraits and analytical linearization. These analyses demonstrate that the drift equilibria of the two-state model are unstable saddle points, and that the linearized sideslip dynamics around drift equilibria have a RHP zero arising from the significant influence of yaw rate variations upon the sideslip dynamics.

The second half of the chapter conducts an analogous investigation for equilibria of the three-state model. The drift equilibria of this model have similar characteristics to those of the two-state model but also reflect the large rear drive forces associated with drifting.

Chapter 4: Control Design for Drifting

Chapter 4 develops physical intuition for the role of steering and rear drive force inputs when drifting in order to design a controller that coordinates these inputs to successfully drift a vehicle. The chapter begins by analytically linearizing the three-state vehicle model around equilibrium conditions corresponding to straight-ahead driving, typical cornering, and cornering with a saturated rear tire. These linearizations provide insight into the relative influence of front lateral force (steering) and rear drive force upon the vehicle's dynamics at these different operating conditions. From this analysis, it becomes clear that rear drive force has a significant direct influence upon the lateral dynamics around drift equilibria.

Two drift controller case studies, one steering-based and the other drive force-based, are used to highlight the capabilities and limitations of these inputs and develop a simple scheme for coordinating steering and rear drive force inputs in a drift.

Insights from this chapter and Chapter 3 are then synthesized to design a physically-motivated drift controller that uses this coordination scheme. Finally, the controller is validated experimentally by showing that it achieves sustained, robust drifts when implemented on the P1 test vehicle.

Chapter 5: Stability Analysis

Chapter 5 investigates the stability characteristics of the drift controller developed in the preceding chapter. It begins by deriving a sliding surface interpretation of the controller and then uses this interpretation to study the closed-loop dynamics around a desired drift equilibrium through a combination of phase portrait analysis, numerical linearization, and numerical computation of an invariant set using Lyapunov-based techniques. This analysis establishes local stability of the desired equilibrium and a broad region of convergence, but it also suggests that modifications to the design may allow for analytical stability guarantees. The remainder of the chapter examines a drift controller that incorporates these modifications; this modified design turns out to have an impractically small region of feasibility around the desired drift equilibrium because of a conflict between lateral and longitudinal control objectives when using the rear drive force input.

Chapter 6: Additional Actuation

Chapter 6 examines the drift control design problem when additional actuation is available to generate a yaw moment on the vehicle. The chapter first considers rear wheel steering capability, but quickly establishes that this actuator does not provide a distinct input from rear drive force when the rear tire is saturated, as is the case at drift equilibria.

The focus then shifts to differential torque control at the rear axle. Two controllers using differential torque capability are examined; the first design enforces decoupled, stable dynamics for all three vehicle states, and the second design employs the same sliding surface structure as the original controller while also prescribing stable longitudinal dynamics. While the first design is effectively infeasible, phase portrait

analysis indicates that the sliding surface controller has a fairly large region of convergence. Furthermore, semidefinite programming techniques are used to demonstrate local exponential stability of the desired drift equilibrium when using this controller. Nevertheless, the sliding surface controller's region of feasibility is somewhat smaller than that of the original drift controller because of the considerable control effort required to enforce the desired closed-loop longitudinal dynamics.

Chapter 7: Conclusions

The final chapter summarizes the key characteristics of drift equilibria revealed in this dissertation and how these characteristics inform the design of a drift controller. This chapter also highlights the control possibilities that are opened up by letting a vehicle drift which are otherwise not available when cornering in a typical fashion. The dissertation concludes by presenting future research directions, including extensions of drift controllers to agile autonomous vehicle applications like collision mitigation and avoidance.

Chapter 2

Vehicle Modeling and Testbeds

A major aspect of the analysis and control design presented in this dissertation is the selection of a vehicle model that achieves a proper balance between model fidelity and intuitive simplicity for the purposes of control design. Obviously, a high fidelity model with many degrees of freedom can capture drift equilibria and the dynamics around them, but at the expense of considerable complexity and a loss of physical intuition. Conversely, an excessively simplistic model may fail to adequately capture the all the characteristics of drift equilibria, which inherently involve such nonlinear effects as tire force saturation.

This chapter presents the spectrum of model fidelities used for the work in this dissertation. Section 2.1 focuses upon tire force modeling, especially for the purposes of incorporating longitudinal tire forces and coupling of lateral and longitudinal tire forces due to friction limitations. Section 2.2 introduces the vehicle dynamics models used in this dissertation, namely two- and three-state variations of the lumped tire “bicycle” model.

Finally, Section 2.3 introduces P1, the drive-by-wire test vehicle used for experiments in this dissertation. The test conditions for experiments are also discussed, as well as techniques for obtaining tire model parameters used in these experiments.

2.1 Tire Modeling

For the dynamics under consideration in this dissertation, this vehicle is moving at relatively low speeds, so forces acting on the vehicle due to aerodynamic drag are negligible. Consequently, the four contact patches between the vehicle’s tires and the ground represent the vehicle’s primary interaction with the environment and the sole means by which forces are applied to the vehicle. With this in mind, an adequate tire model is an essential component of the modeling for the purposes of this work.

The pneumatic tire can represent a considerable modeling challenge, owing to a wide array of factors. Tires are heterogenous in nature, with components constructed from steel, rubber, and synthetic fibers like kevlar. Furthermore, different tires can vary considerably in their construction, especially when it comes to such characteristics as the type of rubber compound used and the tread pattern. Finally, tires are routinely subjected to several factors affecting their behavior, including tread wear, variations in temperature, and variations in inflation pressure.

There are modeling approaches that endeavor to capture the more complex aspects of tire behavior, including techniques based upon finite element analysis [21, 26, 35, 36, 17] and data-driven empirical models like Pacejka’s “Magic Tire Formula” [31, 30]. For the purposes of this dissertation, however, these techniques are either prohibitively complex or lacking in physical intuition. Instead, variants of a relatively simple brush tire model are used in an effort to capture the most important aspects of tire behavior. These models employ lumped parameters with a clear physical interpretation that can be used to implicitly account (at least in part) for the influence of unmodeled effects and dynamics.

2.1.1 The Brush Tire Model

As shown in Figure 2.1, a brush tire model divides the tire into three substructures: the ring, carcass, and flexible ”brushes” representing tread elements that come into contact with the road. There are multiple variants of brush tire models in the literature which share this fundamental structure but vary in their specific approach to modeling the substructures and the interaction between the brushes and the road

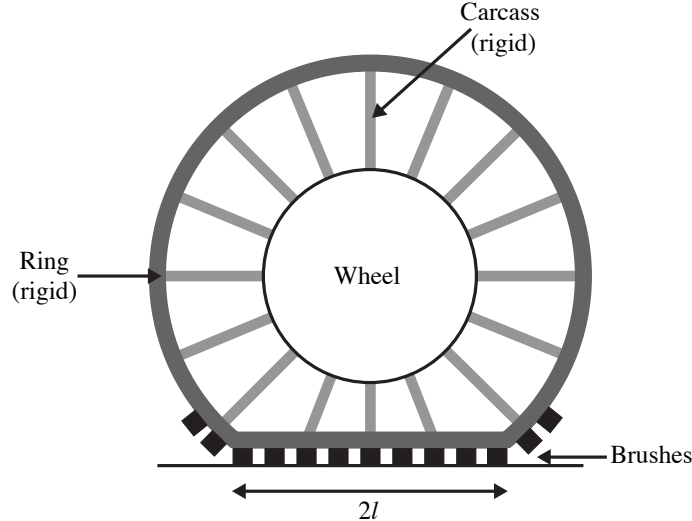


Figure 2.1: Components of the brush tire model and assumptions associated with the brush tire model in this dissertation.

[11, 16, 5, 20]. This work uses the variant proposed by Fromm in [20] to model the generation of tire lateral forces. As indicated in Figure 2.1, this model assumes a rigid tire ring, rigid carcass, and a rectangular contact patch of length $2l$ between the brushes and road.

In this model, the net lateral force generated by the tire is dictated by a combination of two factors: the force demanded from the tire when cornering and the total force available from friction. The force demanded when cornering is the result of the tire slip angle α , which gives the angle of the tire's velocity vector at center of the contact patch with respect to the longitudinal axis of the tire, as depicted in Figure 2.2. This slip angle translates to a demanded lateral deflection in the contact patch that increases linearly from zero at the beginning of the contact patch (where the brushes first come into contact with the road) to its maximum value at the back of the contact patch (where the brushes leave the road). When multiplied by the lateral stiffness c_{py} of the brush elements (specified in units of force/area), this demanded deflection translates to a demanded lateral force per unit length $q_y^{dem}(x)$ as given in

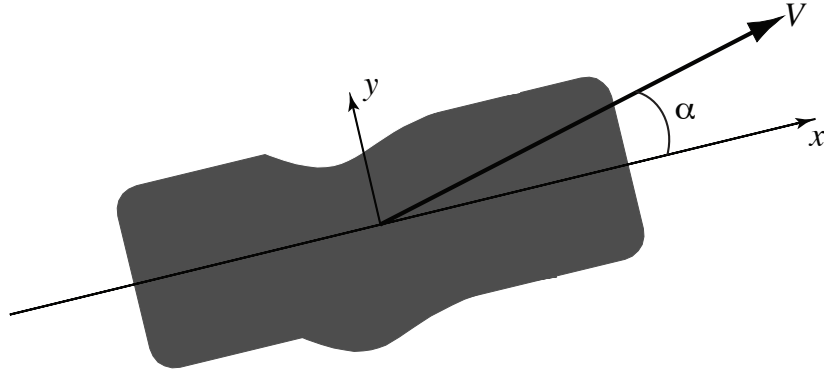


Figure 2.2: Graphical representation of tire slip angle and the resulting contact patch deflection.

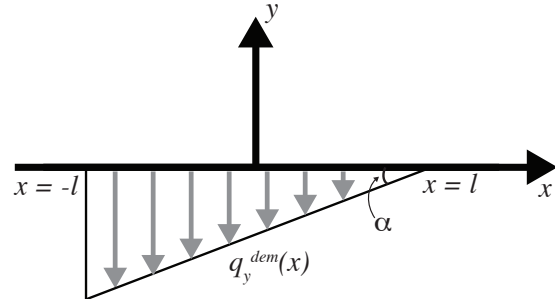


Figure 2.3: Graphical representation of lateral force demand along the contact patch.

Equation 2.1 and depicted graphically in Figure 2.3:

$$q_y^{dem}(x) = -c_{py}(a - x) \tan \alpha, \quad (2.1)$$

where x is measured from the center of the contact patch.

The lateral force demanded per unit length along the contact patch can only be generated where there is sufficient force available from friction to meet the demand. The force available from friction is usually dictated by three factors: the normal load acting on the tire in the z -direction, the peak friction coefficient μ_p between the contact patch and the ground, and the sliding friction coefficient $\mu_s < \mu_p$ between

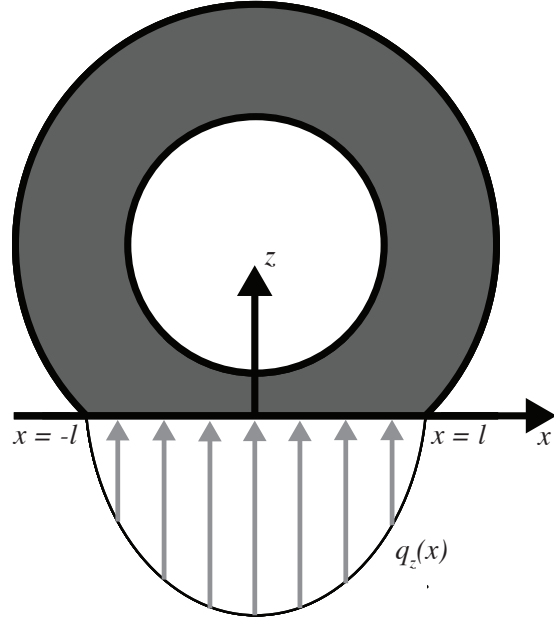


Figure 2.4: Graphical representation of normal load per unit length along the contact patch.

the contact patch and ground. For the gravel surface considered in this dissertation, however, μ_s and μ_p are similar enough that any discernible difference between them is obscured by variability in empirically measured tire curve data. In recognition of this, a single friction coefficient μ is used for modeling instead.

Assuming a uniform normal load in the y -direction for a given x , the normal load acting on the contact patch can be modeled as a normal force per unit length $q_z(x)$ that is a quadratic function of position x from the center of the contact patch as shown in Equation 2.2 and depicted graphically in Figure 2.4:

$$q_z(x) = \frac{3F_z}{4l} \left(\frac{l^2 - x^2}{l^2} \right), \quad (2.2)$$

where F_z is the net normal force acting on the tire as obtained when $q_z(x)$ is integrated across the length of the contact patch.

The total force per unit length available from friction is given by $\mu q_z(x)$, the

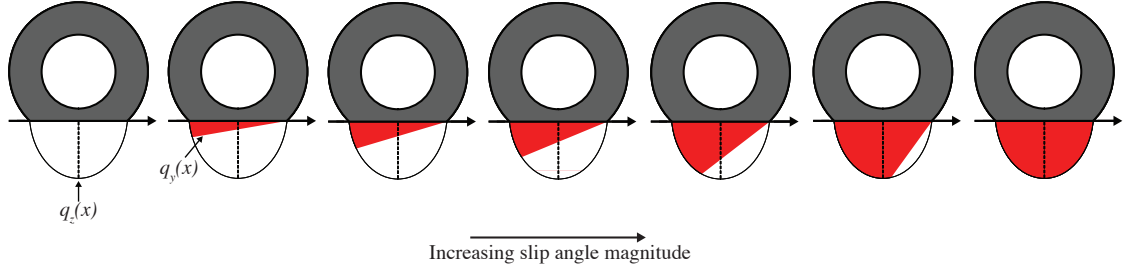


Figure 2.5: Evolution of lateral force per unit length $q_y(x)$ (shown in red) with increasing slip angle.

product of $q_z(x)$ with the friction coefficient μ . This expression dictates the amount of force available per unit length to deflect the brushes at any point along the contact patch. Thus, the *actual* lateral force per unit length $q_y(x)$ along the contact patch is constrained by friction in the following fashion:

$$|q_y(x)| \leq \mu q_z(x) \quad (2.3)$$

Figure 2.5 shows the evolution of $q_y(x)$ subject to this friction constraint as slip angle is increased. At small slip angles, $q_y(x)$ is approximately equivalent to the demanded force distribution, since $q_y^{dem}(x)$ lies almost entirely within the limits of the parabola $\mu q_z(x)$, as depicted in the second panel of Figure 2.5. At these small angles, the total force generated by the tire (obtained by integrating the lateral force distribution) is essentially a linear function of the tire slip angle. This should be evident from Figure 2.6, which gives the net tire lateral force F_y as a function of slip angle magnitude $|\alpha|$.

As slip angle is increased, $q_y^{dem}(x)$ starts to intersect the parabola towards the rear of the contact patch, as depicted in the middle panels of Figure 2.5. On the portion of the contact path ahead of this intersection point, $q_y(x) = q_y^{dem}(x)$. Beyond this point, however, the deflection of the brush elements is friction-limited, meaning that $q_y = \mu q_z$. This results in a roll off of the tire curve from its initial, roughly linear behavior with increasing $|\alpha|$, as shown in Figure 2.6. As the slip angle increases

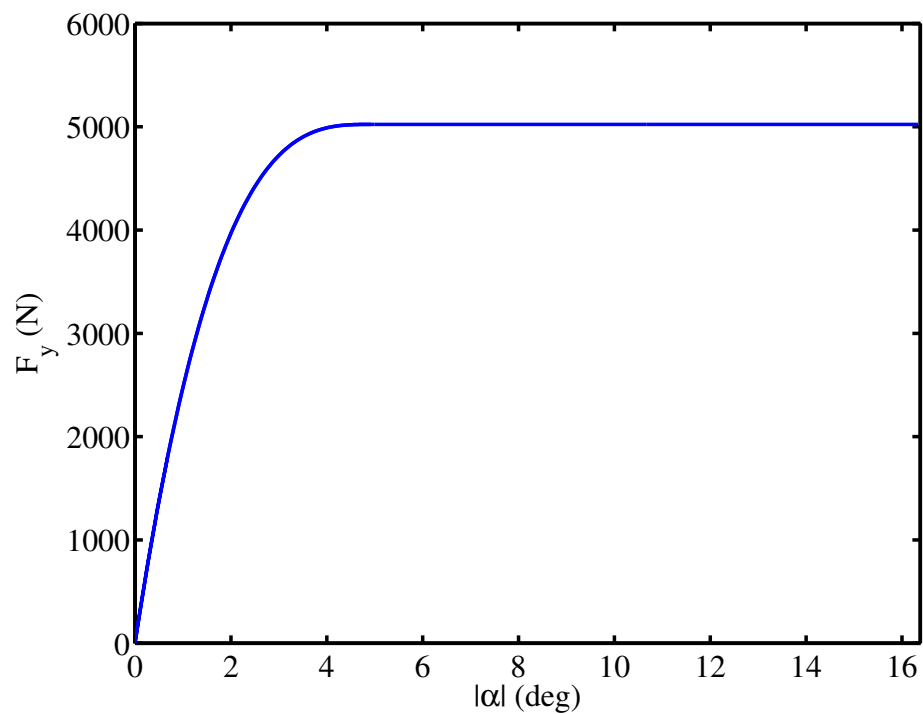


Figure 2.6: Tire lateral force as a function of slip angle magnitude.

further, deflection in an increasingly larger portion of the contact patch is friction limited, and the tire curve rolls off even further.

Eventually, for a large enough slip angle, the deflection of the brushes is friction-limited within the entirety of the contact patch. In this case, $q_y(x) = \mu q_z(x)$ across the entire length of the contact patch, as shown in the final panel of Figure 2.5. This results in complete saturation of the tire lateral force, where any further increases in $|\alpha|$ do not increase the tire lateral force at all, as shown in Figure 2.6.

By integrating $q_y(x)$ at a given slip angle across the length of the contact patch, it is possible to obtain the following expression for the tire lateral force F_y as a function of tire slip angle α :

$$F_y = \begin{cases} -C_\alpha \tan \alpha + \frac{C_\alpha^2}{3\mu F_z} |\tan \alpha| \tan \alpha - \frac{C_\alpha^3}{27\mu^2 F_z^2} \tan^3 \alpha & |\alpha| \leq \alpha_{sl} \\ -\mu F_z \operatorname{sgn} \alpha & |\alpha| > \alpha_{sl} \end{cases}, \quad (2.4)$$

where $C_\alpha = 2c_{py}l^2$ is the tire “cornering stiffness” and μF_z is the maximum achievable tire lateral force that gives the saturation level of the tire curve. α_{sl} is the smallest magnitude slip angle at which the entire contact patch is at the friction limit (as in the final panel of Figure 2.5) and can be derived analytically:

$$\alpha_{sl} = \arctan \frac{3\mu F_z}{C_\alpha}. \quad (2.5)$$

With this model, it is possible to capture two major characteristics of tire behavior: linear dependence of tire force upon slip angle at small slip angles and saturation due to friction limitation at large slip angles. However, note that Equation 2.4 only models lateral force generation, not combined lateral and *longitudinal* force generation. Considering that evidence in prior work [13, 12, 2] shows that large drive forces at the rear tires are characteristic of a drift, a tire model that includes longitudinal tire forces is essential to an investigation of drifting.

2.1.2 Longitudinal Force Modeling

There are multiple approaches of varying complexity for incorporating longitudinal force into the tire model derived above. All of these approaches reflect the fact that the lateral and longitudinal forces of a tire are coupled when operating at or near the friction limits of the tire. This section first introduces a more rigorous approach in order to shed light upon the physical underpinnings of this force coupling, followed by two simpler techniques that have been used for the work in this dissertation.

Combined slip brush tire model

The combined slip brush tire model is a direct extension of the brush tire model introduced in the preceding subsection. Whereas the prior model only allowed lateral deflection of the tire brush elements, this model permits both lateral and longitudinal brush deflection, thus capturing both lateral and longitudinal force generation.

As before, lateral deflection of the brush elements is a result of a tire slip angle α developed during cornering. Similarly, longitudinal deflection of the brush elements is the result of a longitudinal wheel slip κ that develops when a drive or brake torque is applied to the wheel. κ is defined in terms of the rotational velocity ω of the wheel (wheel speed), the longitudinal velocity V_w of the wheel center over the ground, and the rolling radius R_w of the wheel:

$$\kappa = \frac{\omega R_w - V_w}{V_w}. \quad (2.6)$$

Physically, κ reflects the mismatch between the free rolling velocity $R_w\omega$ of the wheel and the longitudinal velocity V_w of the wheel center over the ground when torques are applied to the wheel.

A given wheel slip κ translates to a demanded longitudinal deflection of the brush elements that increases linearly from zero deflection at the front of the contact patch to maximum demanded deflection at the rear of the contact patch, as shown for a positive wheel slip ($\kappa > 0$) due to drive torque in Figure 2.7. Scaling the demanded longitudinal deflection by the longitudinal stiffness c_{px} of the brush elements gives the corresponding longitudinal force demand per unit length $q_x^{dem}(x)$ along the contact

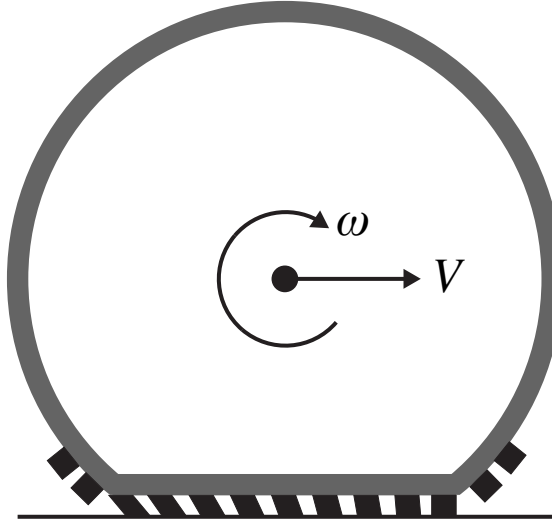


Figure 2.7: Longitudinal deflection of brush elements in the contact patch due to a positive wheel slip ($\kappa > 0$) induced by drive torque.

patch:

$$q_x^{dem}(x) = c_{px}(a - x) \left(\frac{\kappa}{1 + \kappa} \right) \quad (2.7)$$

As is the case with the lateral force per unit length q_y , the *actual* longitudinal force per unit length q_x is not necessarily equal to $q_x^{dem}(x)$ because of friction constraints. For straight-ahead driving (no lateral force demand), the friction constraint on $q_x(x)$ is analogous to Equation 2.3:

$$|q_x(x)| \leq \mu q_z(x), \quad (2.8)$$

where μ is the friction coefficient between the brush elements in the contact patch and the road and q_z is the normal load per unit length in the contact patch from Equation 2.2.

In the more general case, however, the tire lateral and longitudinal forces are coupled in this model because the *total* force per unit length along the contact patch must obey the friction constraint:

$$\sqrt{q_x^2 + q_y^2} \leq \mu q_z. \quad (2.9)$$

By integrating the expression $\sqrt{q_x^2 + q_y^2}$ across the length of the contact patch, it is possible to derive the following expression for the total tire force F , longitudinal component F_x , and lateral component F_y :

$$\gamma = \sqrt{C_x^2 \left(\frac{\kappa}{1 + \kappa} \right)^2 + C_\alpha^2 \left(\frac{\tan \alpha}{1 + \kappa} \right)^2} \quad (2.10a)$$

$$F = \begin{cases} \gamma - \frac{1}{3\mu F_z} \gamma^2 + \frac{1}{27\mu^2 F_z^2} \gamma^3 & \gamma \leq 3\mu F_z \\ \mu_s F_z & \gamma > 3\mu F_z \end{cases} \quad (2.10b)$$

$$F_x = \frac{C_x}{\gamma} \left(\frac{\kappa}{1 + \kappa} \right) F \quad (2.10c)$$

$$F_y = \frac{-C_\alpha}{\gamma} \left(\frac{\tan \alpha}{1 + \kappa} \right) F, \quad (2.10d)$$

where C_x is the longitudinal stiffness of the tire. Note that for a free-rolling tire ($\kappa = 0$), the model in Equation 2.10 reduces to the brush tire model for lateral force in Equation 2.4.

While this is the most rigorous approach for incorporating longitudinal force into the brush tire model used in this work, it adds considerable complexity. This should be evident from the expressions in Equation 2.10 as compared to the lateral force model in Equation 2.4. More importantly, the combined slip brush tire model necessitates the addition of wheel speed dynamics to the overall vehicle model, since κ is a function of wheel speed ω . This adds up to four additional states to the vehicle model (one for each wheel), and longitudinal control inputs (drive and brake torques) must act through these dynamics to influence longitudinal tire forces.

It is important to note that the wheel speed dynamics are considerably faster than the overall chassis dynamics. Thus, for the purposes of chassis control, they can add unnecessary complexity to the model. With this in mind, it is preferable to incorporate longitudinal force and the effects of lateral-longitudinal force coupling due to friction limitations in a fashion that does not necessitate the inclusion of wheelspeed dynamics.

In order to do this, it is first necessary to understand the nature of the coupling between lateral and longitudinal forces at the friction limits of a tire. Consider Figure

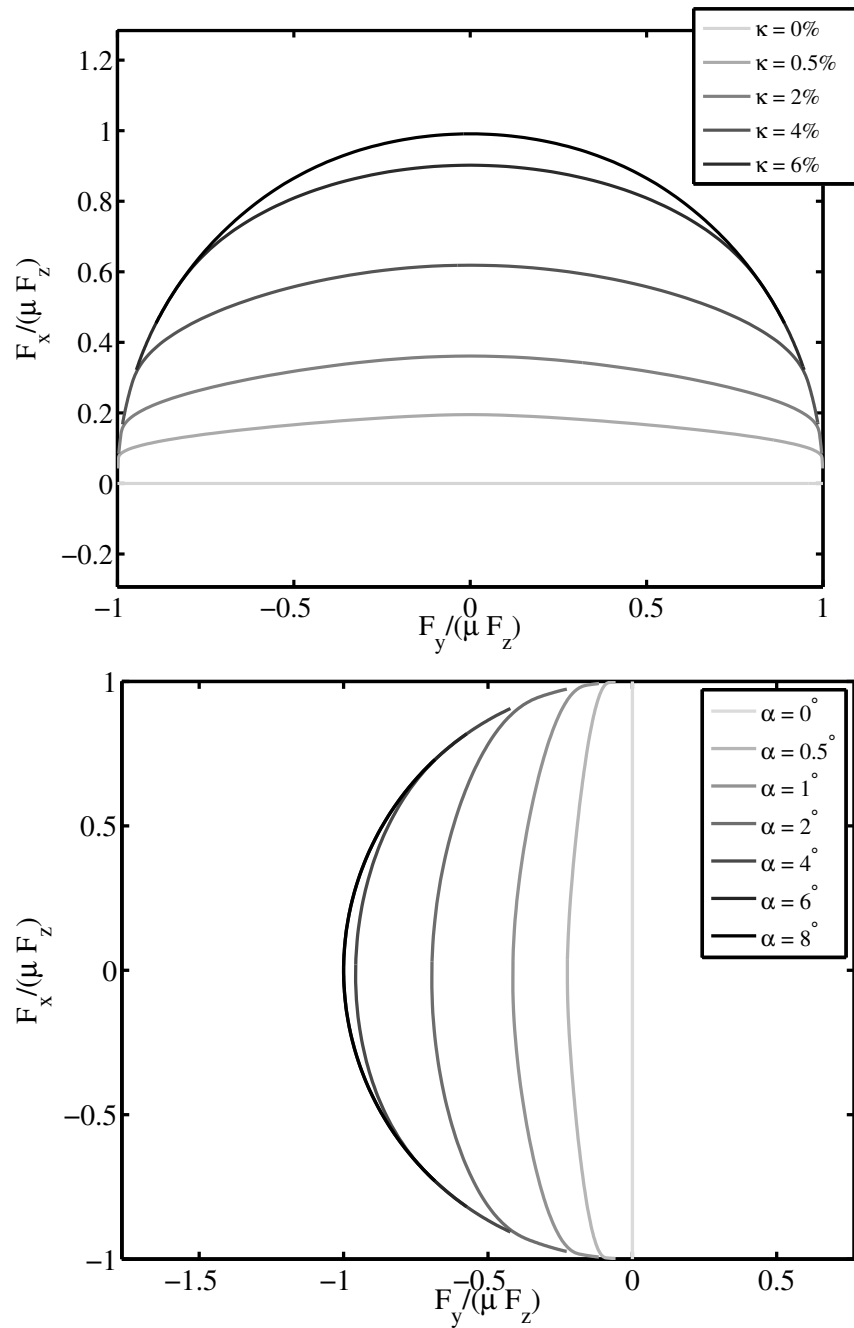


Figure 2.8: Coupling of lateral and longitudinal forces at fixed values of wheel slip κ (top) and fixed values of slip angle α (bottom).

2.8, which visualizes the relationship between lateral and longitudinal forces at a tire as computed using Equation 2.10 and normalized by the friction capability μF_z of the tire. The top plot in the figure shows the relationship between the tire forces at several different values of longitudinal wheel slip κ , while the bottom plot shows the relationship between the tire forces at several different values of slip angle α . In both plots, the lateral-longitudinal force curves are contained within a circular boundary where the combined force demand on the tire is constrained by the friction limits of the tire.

In the top plot of Figure 2.8, the portion of the force curve falling on the circular boundary increases with the magnitude of longitudinal wheel slip. At $\kappa = 6\%$, the longitudinal force demand is large enough that the tire operates at its friction limit even at zero lateral force. Consequently, the friction constraint is active at any amount of lateral force when $\kappa = 6\%$, and the entire lateral-longitudinal force curve for $\kappa = 6\%$ falls on the circular boundary.

Similarly, the portion of the lateral-longitudinal force curve falling on the boundary in the bottom plot of Figure 2.8 increases with slip angle. At $\alpha = 8^\circ$, the lateral force demand is large enough that the tire operates at its friction limit even at zero longitudinal force. This means that the total force demand is constrained by friction at any amount of longitudinal force when $\alpha = 8^\circ$, and the entirety of the curve for $\alpha = 8^\circ$ lies on the circular boundary.

Appropriately enough, the circular boundary evident in Figure 2.8 is known as the “friction circle” for a tire. It dictates that the total force at a tire cannot exceed the force available from friction:

$$\sqrt{F_x^2 + F_y^2} \leq \mu F_z. \quad (2.11)$$

When plotted in the (F_x, F_y) plane, the relationship in above results in a circular boundary of radius μF_z , as shown in Figure 2.9. By applying the friction circle constraint directly, it is possible to incorporate longitudinal force and lateral-longitudinal coupling into a tire model in a simplified fashion, as described below.

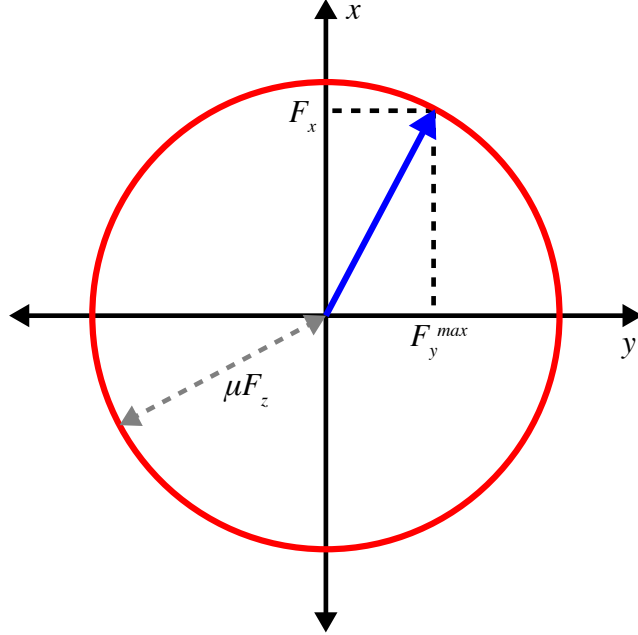


Figure 2.9: Graphical depiction of the friction circle constraint in the (F_x, F_y) plane.

Modeling lateral-longitudinal coupling with the friction circle

Suppose that longitudinal force is treated as a direct input to the vehicle. In this case, the friction circle relationship can be used to dictate the maximum achievable lateral force F_y^{max} for a given input F_x :

$$F_y^{max} = \sqrt{(\mu F_z)^2 - F_x^2}. \quad (2.12)$$

This lateral force limit can also be written in terms of a derating factor ξ that describes F_y^{max} as fraction of the total force available from friction, where $0 \leq \xi \leq 1$:

$$F_y^{max} = \xi \mu F_z \quad (2.13a)$$

$$\xi = \frac{\sqrt{(\mu F_z)^2 - F_x^2}}{\mu F_z} \quad (2.13b)$$

Using this derating factor, it is straightforward to modify the lateral force model in Equation 2.4 to include the effect of lateral-longitudinal force coupling at the friction

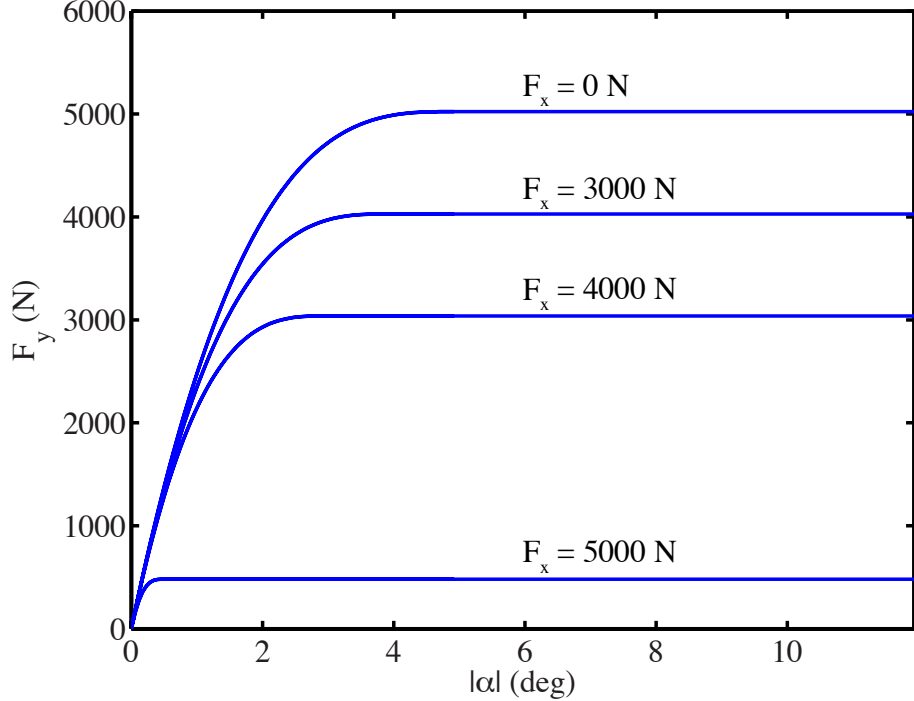


Figure 2.10: Variation in tire lateral force curve with longitudinal force input.

limits:

$$F_y = \begin{cases} -C_\alpha \tan \alpha + \frac{C_\alpha^2}{3\xi\mu F_z} |\tan \alpha| \tan \alpha - \frac{C_\alpha^3}{27\xi^2\mu^2 F_z^2} \tan^3 \alpha & |\alpha| \leq \alpha_{sl} \\ -\xi\mu F_z \text{sgn } \alpha & |\alpha| > \alpha_{sl} \end{cases} \quad (2.14a)$$

$$\alpha_{sl} = \arctan \frac{3\xi\mu F_z}{C_\alpha}. \quad (2.14b)$$

This modification adjusts the saturation level of the lateral force curve as a function of the longitudinal force applied to the tire, as shown in Figure 2.10 for a range of longitudinal force inputs. Note that the maximum achievable lateral force decreases as the longitudinal force increases.

Like the combined slip brush tire model, this approach allows for both lateral and longitudinal force at the tire and accounts for coupling of the forces at the friction limit. Unlike the combined slip model, however, this technique does not capture

generation of longitudinal force through tread deflection. Instead, it treats F_x as a direct input, eliminating the need for wheel speed dynamics.

Empirically derated friction coefficient

The simplest technique used in this dissertation to account for lateral-longitudinal force coupling in the tire model does not explicitly include longitudinal force. This approach instead uses a derated friction coefficient for the lateral force model in Equation 2.4 at tires where drive or brake torques are applied. In terms of the friction circle technique introduced above, this corresponds to fixing the amount of longitudinal force applied at a tire and using the corresponding (fixed) derating factor ξ . The appropriate derating factor can be chosen based upon the longitudinal force associated with a drift equilibrium of interest or by fitting vehicle simulation predictions to experimental data of the vehicle operating in the desired region of the state space; the latter approach is taken here.

Since this dissertation is focused upon drifting with rear wheel drive (RWD) vehicles, it is necessary to derate the friction coefficient μ_r for the rear tires relative to the friction coefficient μ_f for the front tires, meaning that $\mu_r < \mu_f$. An appropriate value for μ_r can be determined by fitting experimental data of drifts to a vehicle model.

This approach is a special case of the friction circle coupling technique that makes it possible to account (at least in part) for the effect of lateral-longitudinal force coupling in a simple model that does not have longitudinal dynamics. While such a model cannot be used for control design with the rear drive force, it does enable insightful analysis that is applicable to a model incorporating longitudinal dynamics, as shown in Chapter 3.

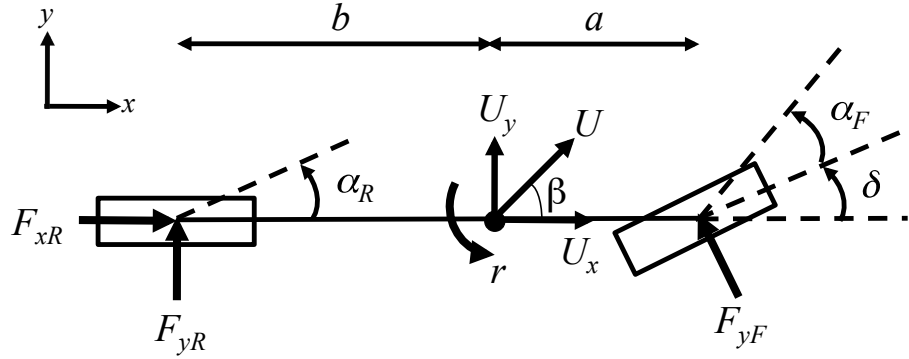


Figure 2.11: Diagram of the bicycle model for a RWD vehicle.

2.2 Chassis Modeling

2.2.1 The Bicycle Model

The analysis and control design in this dissertation relies on variants of a relatively simple planar vehicle model known as the “bicycle model,” depicted in Figure 2.11. The model gets its name from the fact that it uses a single “lumped” tire at each axle with twice the cornering stiffness and force capability of the individual tires at the axle.

Since the bicycle model assumes planar motion of the vehicle, it does not incorporate rolling and pitching motion of the chassis. However, this dissertation is focused primarily upon small deviations around steady-state cornering of the vehicle. As a result, the effects of steady-state lateral load transfer induced by roll can be captured through empirically determined model parameters for each lumped tire, as discussed in a subsequent section.

Two- and three-state versions of the bicycle model are used in this dissertation. In both cases, the model states are defined in terms of the vehicle’s lateral velocity U_y at the center of gravity (CG), longitudinal velocity U_x at the CG, and yaw rate r , which describes the rotational velocity of the vehicle normal to the plane of motion. All three quantities are defined with respect to a body-fixed frame, as shown in Figure 2.11. The two-state variant of the model focuses only on the lateral dynamics of the

vehicle, while the three-state variant incorporates longitudinal dynamics as well.

The equations of motion for the lateral dynamics of the model can be derived by starting with a force balance in the y -direction and a moment balance in the z -direction:

$$ma_y = F_{yF} \cos \delta + F_{yR} \quad (2.15a)$$

$$I_z \dot{r} = aF_{yF} \cos \delta - bF_{yR} \quad (2.15b)$$

where a_y is the lateral acceleration of the vehicle, \dot{r} is the yaw acceleration of the vehicle, F_{yF} is the front (lumped) tire lateral force, F_{yR} is the rear (lumped) tire lateral force, δ is the front tire steer angle, m is the vehicle mass, and I_z is the vehicle's yaw inertia (moment of inertia about the z-axis). As depicted in Figure 2.11, a is the distance from the vehicle CG to the front axle, and b is the distance from the vehicle CG to the rear axle. Since the vehicle states are defined using a body-fixed frame, a_y relative to the inertial reference frame is given by:

$$a_y = \dot{U}_y + rU_x. \quad (2.16)$$

Substituting Equation 2.16 into Equation 2.15a and making the small angle approximation $\cos \delta \approx 1$, the dynamics become:

$$\dot{U}_y = \frac{F_{yF} + F_{yR}}{m} - rU_x \quad (2.17a)$$

$$\dot{r} = \frac{aF_{yF} - bF_{yR}}{I_z}. \quad (2.17b)$$

Since drifting is often characterized in terms of sideslip angle β , it makes sense to express the dynamics in terms of this quantity. As shown in Figure 2.11, β describes the angle between the velocity vector U at the CG and the longitudinal axis of the vehicle, and can be calculated in terms of U_y and U_x as follows:

$$\beta = \arctan \frac{U_y}{U_x} \approx \frac{U_y}{U_x} \quad (2.18)$$

With the approximations $\beta \approx U_y/U_x$ and $\dot{\beta} \approx \dot{U}_y/U_x$, the lateral velocity dynamics in Equation 2.17a can be written in terms of β , yielding the lateral dynamics of the vehicle in terms of sideslip angle and yaw rate:

$$\dot{\beta} = \frac{F_{yF} + F_{yR}}{mU_x} - r \quad (2.19a)$$

$$\dot{r} = \frac{aF_{yF} - bF_{yR}}{I_z}. \quad (2.19b)$$

The lumped tire slip angles α_F and α_R needed to compute the lateral force generated at each axle are given by the expressions below, which give the angle of the velocity vector at the center of the contact patch of each tire with respect to the longitudinal axis of the tire:

$$\alpha_F = \arctan \frac{U_y + ar}{U_x} - \delta \approx \arctan \left(\beta + \frac{a}{U_x} r \right) - \delta \quad (2.20a)$$

$$\alpha_R = \arctan \frac{U_y - br}{U_x} \approx \arctan \left(\beta - \frac{b}{U_x} r \right). \quad (2.20b)$$

Equation 2.19 defines the dynamics of the two-state bicycle model with front steering δ as its sole input, where δ is used to alter the front lateral force F_{yF} via the front slip angle α_F as defined in Equation 2.20a. Longitudinal velocity U_x is treated as a model parameter, and tire lateral forces are calculated using the lateral force model in Equation 2.4 with a derated rear tire friction coefficient μ_r , as is necessary to model drifting of a RWD vehicle.

It is important to note that the small-angle approximations made on steer angle δ and sideslip β to derive these dynamics are reasonable within the context of the work in this dissertation. For the sideslip magnitudes considered here ($|\beta| \approx 20$ deg), the small angle approximation on β introduces approximately 4.3% of error relative to the actual value. Similarly, the small angle approximation on $\cos \delta$ introduces 8.6% of error or less relative to the actual value within the steering range of the test vehicle ($|\delta| \leq 23$ deg); when operating near the drift equilibria considered in this work, where $\delta \approx 12^\circ$, the error is far smaller, at 2.2%. These errors are on the same order of magnitude (if not smaller) than the modeling errors caused by friction uncertainty

Model	States	Tire Modeling	Inputs
Two-state (Eq. 2.19)	β, r	Lateral Brush (Eq. 2.4), $\mu_r < \mu_f$	δ
Three-state (Eq. 2.23)	β, r, U_x	Friction Circle Coupling (Eq. 2.14)	δ, F_{xR}

Table 2.1: Summary of bicycle models

when operating on the dirt and gravel surfaces under consideration in this work.

The longitudinal dynamics of the vehicle are derived in the same fashion as the lateral velocity dynamics. The force balance in the x -direction is given by:

$$ma_x = \frac{F_{xR} - F_{yF} \sin \delta}{m}, \quad (2.21)$$

where a_x is the longitudinal acceleration of the vehicle and F_{xR} is the rear tire longitudinal force. The longitudinal acceleration relative to the inertial reference frame can be written in terms of the vehicle states as follows:

$$a_x = \dot{U}_x - rU_y \approx \dot{U}_x - rU_x\beta. \quad (2.22)$$

Substituting Equation 2.22 in to Equation 2.21 gives the dynamics of the longitudinal velocity U_x of the vehicle. Combining this result with the lateral dynamics already derived in Equation 2.19 gives the dynamics of the three-state bicycle model:

$$\dot{\beta} = \frac{F_{yF} + F_{yR}}{mU_x} - r \quad (2.23a)$$

$$\dot{r} = \frac{aF_{yF} - bF_{yR}}{I_z} \quad (2.23b)$$

$$\dot{U}_x = \frac{F_{xR} - F_{yF} \sin \delta}{m} + rU_x\beta. \quad (2.23c)$$

The three-state model has two inputs: the front steer angle δ and the rear longitudinal force F_{xR} . The tire lateral forces are calculated with the axle slip angle definitions in Equation 2.20 and the tire model in Equation 2.14 that uses the friction circle for lateral-longitudinal force coupling.

Table 2.1 summarizes the two- and three-state vehicle models. The table gives

the states for each model, the inputs for each model, and the associated tire modeling technique.

2.3 P1, the By-wire Testbed

2.3.1 Overview

The experimental investigations in this dissertation have all been conducted using P1, a drive-by-wire testbed built entirely by students at Stanford University and shown in Figure 2.12. P1 is an all-electric vehicle with extensive sensing and actuation capabilities, as detailed below.

P1 is equipped with an inertial navigation system (INS) as well as two separate global positioning system (GPS) receivers. The INS consists of automotive-grade accelerometers in all three translational degrees of freedom and gyroscopes that measure angular velocity in all three rotational degrees of freedom. A single-antenna GPS system with a 10 Hz update rate permits measurement of velocities with an accuracy of 2 cm/s. A second, two-antenna GPS system with a 5 Hz update rate allows measurement of heading and roll angle with an accuracy of 0.1 degrees. By fusing GPS and INS measurements with an extended Kalman filter as described in [34], it is possible to obtain high-accuracy estimates of vehicle sideslip angle, longitudinal velocity, and yaw rate at an update rate of 500 Hz. This state estimation technique has been validated for vehicle control purposes in [33].

P1's actuation capabilities include steer-by-wire and drive-by-wire systems. The steer-by-wire system enables independent, high-bandwidth steering control of the front left and front right tires, as detailed in [27]. The drive-by-wire system features independent left and right AC induction motors that generate drive torque at the rear wheels. The motors are controlled using an open-loop torque map. The torque commands to the drive motors are determined by neglecting drivetrain and wheel-speed dynamics and using Equation 2.24 to compute the rear torque command τ_r^{des}



Figure 2.12: P1, the student-built steer- and drive-by-wire test vehicle.

corresponding to a rear drive force command F_{xR}^{des} :

$$\tau_r^{des} = \frac{F_{xR}^{des} r_w}{k_{gr}}, \quad (2.24)$$

where R_w is the effective rear wheel radius and k_{gr} is the transmission gear ratio. The drive motors can also provide regenerative braking at the rear tires, used within the context of this work to induce rear tire saturation prior to activation of a drift controller.

2.3.2 Vehicle Parameters

The parameter set used for a bicycle model of P1 is given in Table 2.2. With the exception of the yaw inertia I_z , the parameters are similar to those for a typical sport sedan. Relative to its mass and wheelbase, P1's yaw inertia is rather small. As a consequence, the vehicle's yaw dynamics can be challenging to control, as the vehicle's yaw rate can build up and result in a spinout rather quickly.

Several of the vehicle parameters in Table 2.2, namely a , b , and m , are easily measured using wheel scales. The yaw inertia I_z can be approximated by fitting

Parameter	Description	Value
m	Mass	1724 kg
I_z	Yaw inertia	$1300 \text{ kg} - \text{m}^2$
a	Distance from CG to front axle	1.35 m
b	Distance from CG to rear axle	1.15 m
C_{α_F}	Front cornering stiffness	120,000 N/rad
C_{α_R}	Rear cornering stiffness	175,000 N/rad
μ	Tire friction coefficient	0.55

Table 2.2: Parameters for the P1 by-wire testbed on test surface used for experiments

the measured yaw rate of the vehicle to the yaw dynamics of the desired model given knowledge of all other vehicle parameters. Determination of the tire parameters requires fitting tire curves to experimental data obtained from specific vehicle maneuvers, as detailed below.

Determination of tire parameters

The data used to compute estimates of the tire parameters is obtained from a maneuver known as a ramp steer. During this maneuver, the vehicle corners at constant velocity with a linearly increasing steer angle.

If steer angle is increased slowly, it is valid to assume steady state cornering of the vehicle. Furthermore, since the amount of longitudinal force required to maintain the vehicle's speed is relatively small, the effect of lateral-longitudinal force coupling at the tire may be neglected. Utilizing these two assumptions, the following expressions for front lateral force F_{yF} and rear lateral force F_{yR} during the ramp steer can be derived by setting $\dot{\beta} = \dot{r} = 0$ in the two-state bicycle model from Equation 2.19:

$$F_{yF} = \frac{b}{L} m a_y^{SS} \quad (2.25a)$$

$$F_{yR} = \frac{a}{L} m a_y^{SS}, \quad (2.25b)$$

where a_y^{SS} is the lateral acceleration of the vehicle when operating in steady-state:

$$a_y^{SS} = rU_x. \quad (2.26)$$

Using the state estimation capabilities available on P1, it is possible to compute the force estimates from Equation 2.25 and tire slip angle estimates from Equation 2.20 that can then be used to generate empirical tire force curves. The scatter plots in Figures 2.13 and 2.14 give empirical tire curves obtained from ramp steers on a surface consisting of a layer of gravel with asphalt underneath. This surface was chosen because the tire friction coefficient ($\mu \approx 0.55$ as indicated in Table 2.2) is relatively low, enabling operation at the friction limits at modest vehicle speeds. Note the lack of discernible peaks before saturation in either of the empirical tire force curves; this is indicative of similar peak and sliding friction coefficients on this surface, which is why a single friction coefficient is used for tire modeling in this dissertation.

The empirical tire curves in Figures 2.13 and 2.14 can in turn be fitted to the lateral force model in Equation 2.4, adjusting the cornering stiffness and friction coefficient for each tire until satisfactory agreement is achieved between the model and the empirical tire curve. Note that while the vehicle models considered in this dissertation are planar in nature, determining tire parameters in this fashion makes it possible to account for steady-state load transfer between the inside and outside tires due to vehicle roll when cornering. This is because the lumped tire force estimates reflect the total lateral force being generated at an axle, including any effect of load transfer upon the force capability of the axle. Thus, while the tire parameters have a clear physical interpretation, they also act as lumped parameters that reflect the influence of this higher order effect.

Note from Figures 2.13 and 2.14 that force estimate data is scattered rather widely in the saturation regions of the empirical tire curves. This is because friction on the test surface is highly variable, especially as gravel is swept away and asphalt is exposed as a result of repeated operation in a particular area. For this reason, this surface represents quite a challenge from a controller robustness standpoint.

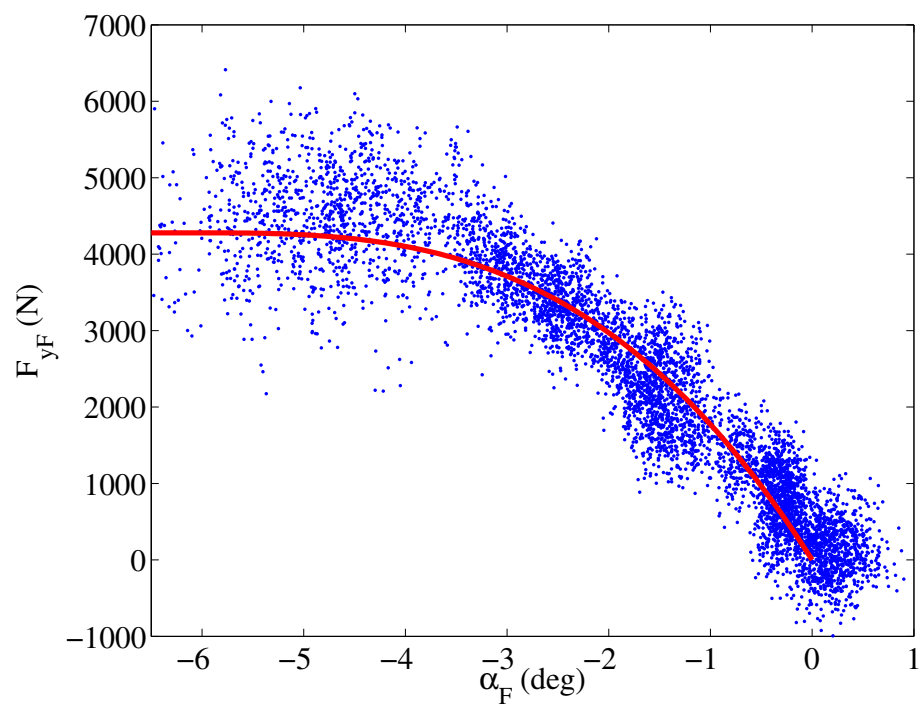


Figure 2.13: Empirical tire curve for the front lumped tire fitted with the lateral tire model (in red).

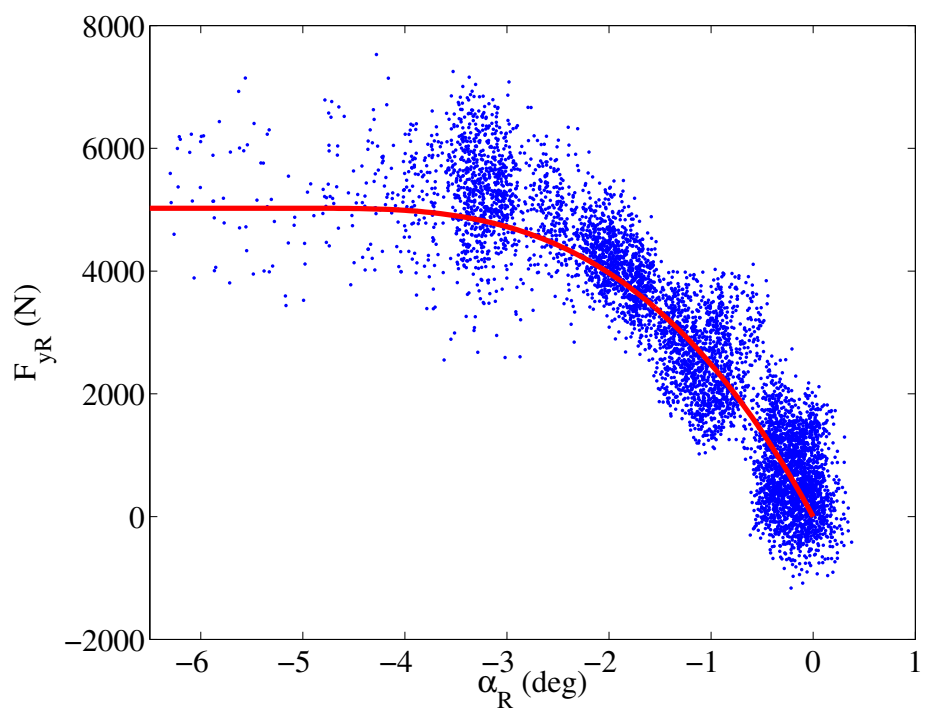


Figure 2.14: Empirical tire curve for the rear lumped tire fitted with the lateral tire model (in red).

Chapter 3

Vehicle Equilibrium Analysis

As the focus of this dissertation is steady-state cornering with rear tire saturation, a natural starting point for investigating this phenomenon is an exploration of the steady-state cornering conditions of the vehicle models introduced in the preceding chapter. These steady-state cornering conditions correspond to *equilibria* of these models.

For some nonlinear system $\dot{\mathbf{x}} = f(\mathbf{x}, \mathbf{u})$, where \mathbf{x} is the vector of states and \mathbf{u} is the vector of inputs, the equilibria of the system occur at state locations \mathbf{x}^{eq} and corresponding input values \mathbf{u}^{eq} where the state derivatives of the system are all zero:

$$f(\mathbf{x}^{eq}, \mathbf{u}^{eq}) = \mathbf{0} \quad (3.1)$$

Thus, the equilibrium locations and corresponding input values are defined by an algebraic system of equations derived from the system's dynamics.

If the number of inputs to the system is greater than or equal to the number of states, it is possible to make an arbitrary location in the state space an equilibrium of the system. In more concrete terms, it is possible to arbitrarily define \mathbf{x}^{eq} and then solve Equation 3.1 to determine the required inputs \mathbf{u}^{eq} .

If the system is underactuated, meaning that it has fewer inputs than states, this is no longer the case. At some arbitrary location in the state space, it is only possible to use the inputs to make the state derivatives zero for a subset of the states, but

not all of them. As a result, the system only has equilibria at certain locations in the state space and for certain input combinations, as the system of equations in 3.1 can only be solved by constraining a subset of the inputs and/or states.

Vehicles with standard actuation, namely steering and a longitudinal input (drive and braking), are underactuated systems. This is reflected in the models introduced in the preceding chapter, since the two-state bicycle model only has one input (steering) and the three-state bicycle model has two inputs (steering and rear drive force). Thus, according to these models, steady-state cornering will only be possible at certain locations in the state space. If these models are to adequately capture the dynamics of drifting, some of the achievable equilibrium conditions must be drift equilibria, where the rear tire is saturated in steady-state.

Section 3.1 establishes that the two-state bicycle model used in this dissertation does indeed have drift equilibria that are saddle points, much like similar two-state models in prior work. An in-depth study of these equilibria reveals characteristics that have clear implications for control design. These characteristics include near-saturation of the front lateral force at drift equilibria and a RHP zero in the linearized sideslip dynamics around a drift equilibrium. The RHP zero is especially intriguing because it indicates that the direct effect of the steering input upon the sideslip dynamics is ultimately outweighed by the effect of the steering input acting through the yaw rate term in the sideslip dynamics. This result suggests that changes in yaw rate have a significant influence upon the sideslip dynamics.

Section 3.2 demonstrates that the three-state bicycle model also has saddle points that are drift equilibria. By virtue of including longitudinal dynamics and the rear drive force input, this model reflects characteristics of drift equilibria not captured by the two-state model. It corroborates the higher fidelity models used in prior work by showing that drift equilibria are associated with large rear drive forces that induce rear tire saturation, and that this rear tire saturation directly couples the rear lateral and longitudinal forces via the friction circle.

At the same time, however, the drift equilibria of the three-state model share certain key characteristics with the drift equilibria of the two-state model. The front lateral force is also nearly saturated at the three-state model's drift equilibria, and

there is still a RHP zero in the transfer function from steering perturbations to sideslip perturbation that reflects the significant influence of changes in yaw rate upon the sideslip dynamics. Therefore, much of the intuition developed from an analytical examination of the two-state model also applies for the three-state model and has implications for control design using the three-state model.

3.1 Equilibria of the two-state model

3.1.1 Calculating equilibrium locations

In the preceding chapter, the following equations of motion were derived for the two-state bicycle model:

$$\dot{\beta} = \frac{F_{yF} + F_{yR}}{mU_x} - r \quad (3.2a)$$

$$\dot{r} = \frac{aF_{yF} - bF_{yR}}{I_z}, \quad (3.2b)$$

where the vehicle states are sideslip angle β and yaw rate r , and the sole input to the system is the front steer angle δ . Note that the vehicle longitudinal velocity U_x is *not* a vehicle state, but rather a model parameter in the case of the two-state model.

Thus, the equilibria of this model occur where $\dot{\beta} = \dot{r} = 0$, yielding the following algebraic system of equations:

$$\frac{F_{yF}^{eq} + F_{yR}^{eq}}{mU_x^{eq}} - r^{eq} = 0 \quad (3.3a)$$

$$\frac{aF_{yF}^{eq} - bF_{yR}^{eq}}{I_z} = 0, \quad (3.3b)$$

where F_{yF}^{eq} , F_{yR}^{eq} , δ^{eq} , β^{eq} , r^{eq} , and U_x^{eq} are the equilibrium values of the front lateral force, rear lateral force, steer angle, sideslip angle, yaw rate, and longitudinal velocity, respectively. Since F_{yF}^{eq} and F_{yR}^{eq} are a function of the four remaining quantities, Equation 3.3 is a system of two equations in four unknown quantities: δ^{eq} , β^{eq} , r^{eq} , and U_x^{eq} . Obviously, in order to solve the system of equations, two of the four unknown

quantities must be constrained. In this analysis, δ^{eq} and U_x^{eq} are specified, and the system of equations are solved for β^{eq} and r^{eq} .

The equations in 3.3 have been solved numerically in MATLAB for a specified U_x^{eq} and a range of values for δ^{eq} , using the vehicle parameters provided in the preceding chapter and a derated rear friction coefficient $\mu_r < \mu_f$. As discussed in Chapter 2, this de-rated rear friction coefficient is a simplified way to account for the effect of longitudinal force upon the lateral force capacity of the rear tire. From another perspective, it is also necessary to ensure that the model has drift equilibria, where the rear tire is saturated but the front tire is not.

This can be explained in terms of the relationship between the equilibrium lateral forces that arises from the yaw moment balance in Equation 3.3b:

$$aF_{yF}^{eq} = bF_{yR}^{eq} \quad (3.4)$$

When the yaw moments acting on the car are balanced, a linear relationship exists between F_{yF}^{eq} and F_{yR}^{eq} . As one of the lateral forces increases in equilibrium, the other must increase as well until one (or both) of the tires saturate. The de-rated rear friction coefficient ensures that the rear tire saturates before the front tire does, as is characteristic of drift equilibria. For the results presented here, $\mu_r = 0.53$ and $\mu_f = 0.55$; these values have been determined empirically using methods described in [40].

Figures 3.1 through 3.3 give the equilibrium sideslip, yaw rate, front lateral force, and rear lateral force as a function of the equilibrium steer angle δ^{eq} . Note that for several of the δ^{eq} considered, the system has multiple equilibrium conditions. This is because the model under consideration is nonlinear, meaning that the algebraic system in Equation 3.3 is also nonlinear and multiple solutions are possible.

Close study of these plots reveals that the model has two classes of equilibria, indicated in the plots by asterisks (*) and triangles (Δ). At the equilibria denoted by asterisks, the equilibrium sideslip angle (Figure 3.1) is on the order of only a few degrees. The vehicle is turning in the same direction as it is steered, as r^{eq} (Figure 3.2) for these equilibria has the same sign as the corresponding δ^{eq} . Furthermore,

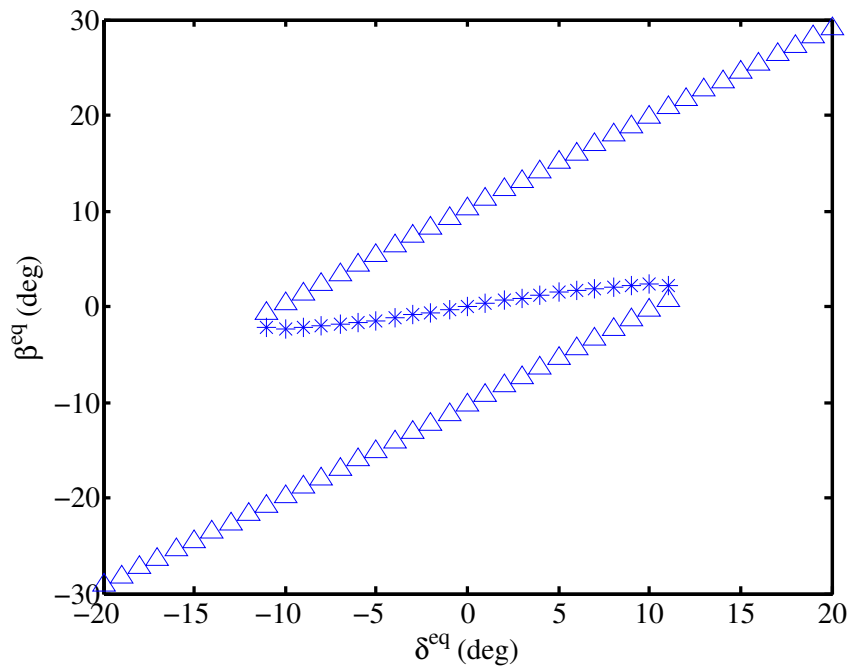


Figure 3.1: Equilibrium sideslip versus steer angle with $U_x^{eq} = 8$ m/s for the two-state bicycle model.

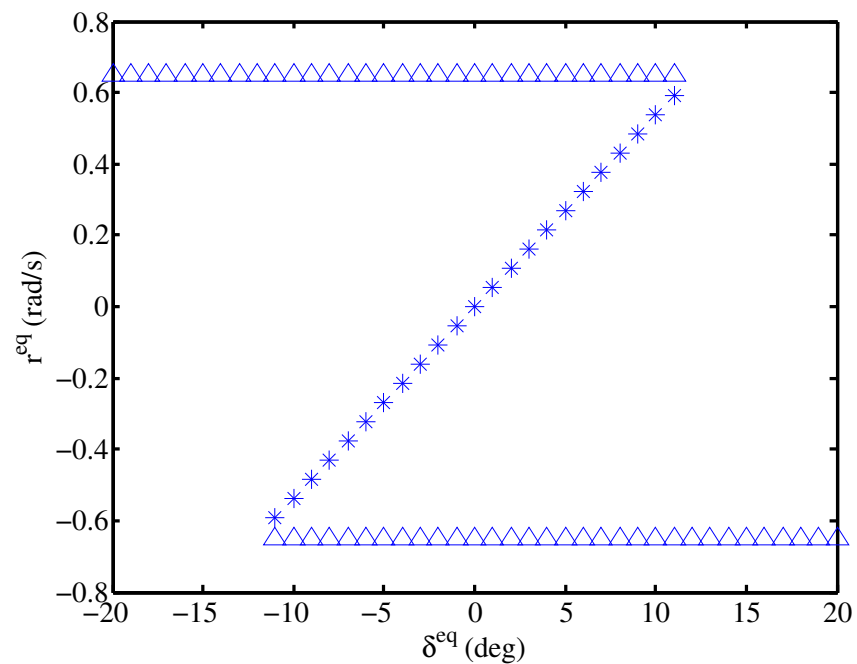


Figure 3.2: Equilibrium yaw rate versus steer angle with $U_x^{eq} = 8$ m/s for the two-state bicycle model.

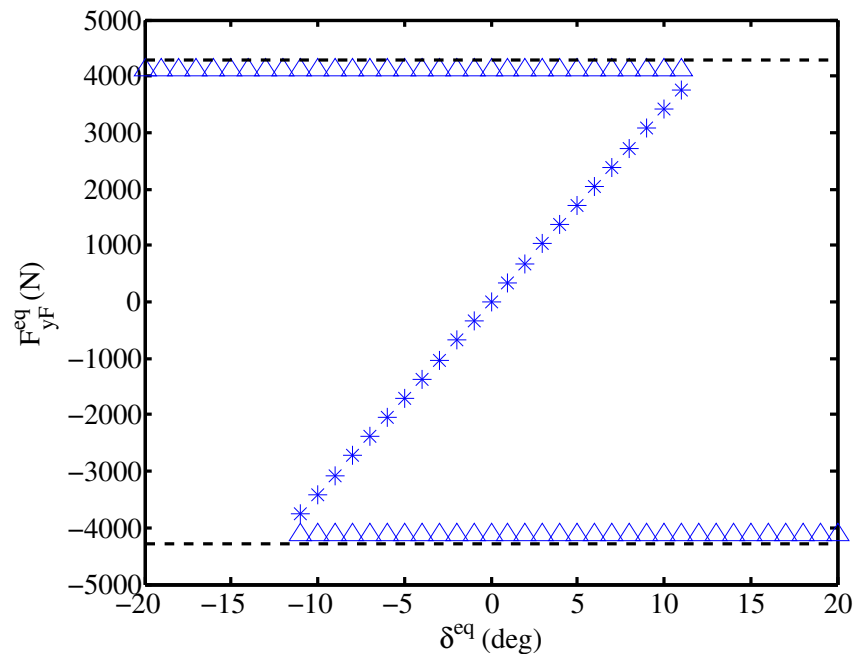


Figure 3.3: Equilibrium front lateral force versus steer angle with $U_x^{eq} = 8$ m/s for the two-state bicycle model.

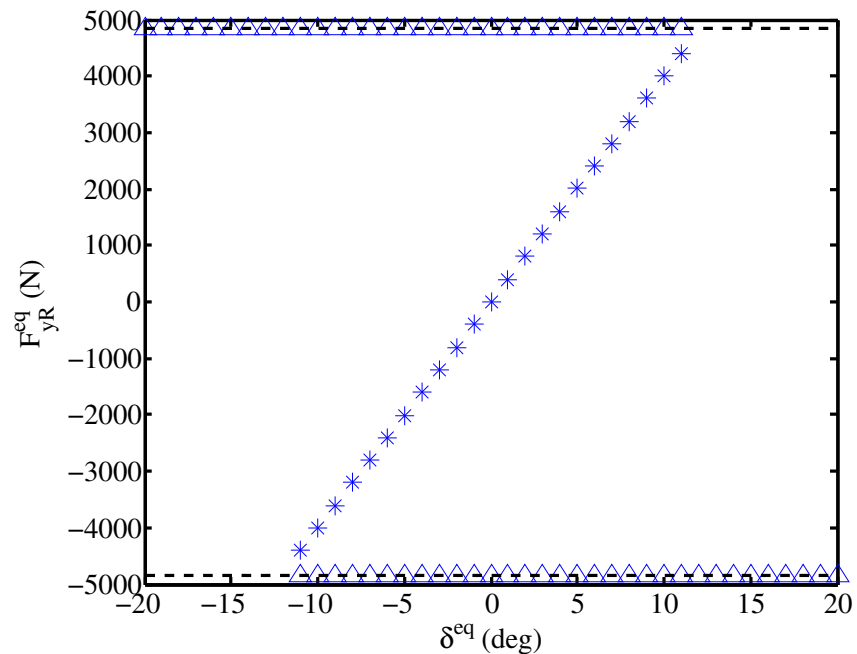


Figure 3.4: Equilibrium rear lateral force versus steer angle with $U_x^{eq} = 8$ m/s for the two-state bicycle model.

there is a nearly linear relationship between r^{eq} and δ^{eq} , with the vehicle yawing more in steady-state as δ^{eq} is increased. Finally, neither the front nor the rear lateral forces are saturated at these equilibria (Figures 3.3 and 3.4), as the equilibria all fall within the black dashed lines denoting the tire friction limits in both of these figures. Putting all of these observations together, it becomes clear that these are typical cornering equilibria.

The equilibria denoted by the triangles are drift equilibria because F_{yR}^{eq} is saturated. This is indicated in Figure 3.4 by the fact that F_{yR}^{eq} for all of these equilibria lies on the black dashed line representing the friction limit of the rear tire:

$$F_{yR}^{eq} = \mu_r F_{zR} \quad (3.5)$$

At larger steer angles, these drift equilibria have the characteristics often associated with drifting: a large equilibrium sideslip β^{eq} and countersteer, since the yaw rate r^{eq} and steer angle δ^{eq} have opposite sign at larger δ^{eq} .

The front lateral force F_{yF}^{eq} , while not completely saturated, is nearly saturated at all of the drift equilibria. In Figure 3.3, this is indicated by the fact that F_{yF}^{eq} for all the drift equilibria lies close to the black dashed line representing the front tire friction limit. Furthermore, F_{yF}^{eq} is constant at all of the drift equilibria.

These properties of F_{yF}^{eq} at drift equilibria are straightforward to verify analytically by computing an expression for F_{yF}^{eq} using Equation 3.5 and the fact that a yaw moment balance ($\dot{r} = 0$) must exist at the drift equilibria:

$$F_{yF}^{eq} = \frac{b}{a} F_{yR}^{eq} = \frac{b}{a} \mu_r F_{zR} \quad (3.6)$$

By inspection of Equation 3.6, it is clear that F_{yF}^{eq} must be constant because F_{yR}^{eq} is saturated (and therefore constant) at drift equilibria. Using the fact that $F_{zR} = amg/L$, where g is acceleration due to gravity and L is the wheelbase of the vehicle, Equation 3.6 becomes:

$$F_{yF}^{eq} = \frac{b}{L} \mu_r mg. \quad (3.7)$$

The front normal force $F_{zF} = bmg/L$, so the front tire friction limit is given by:

$$\mu_f F_{zF} = \frac{b}{L} \mu_f mg. \quad (3.8)$$

By comparing Equations 3.8 and 3.7, it should be clear that $F_{yF}^{eq} < \mu_f F_{zF}$ because $\mu_r < \mu_f$, confirming that the front tire is not saturated at drift equilibria. Since μ_r is only slightly less than μ_f , however, the front tire is still nearly saturated.

Because both the front and rear lateral forces are constant-valued at drift equilibria, the equilibrium yaw rate is constant-valued as well. This arises because of the relationship between r^{eq} , F_{yF}^{eq} , and F_{yR}^{eq} when the sideslip dynamics are in equilibrium (Equation 3.3a):

$$r^{eq} = \frac{F_{yF}^{eq} + F_{yR}^{eq}}{mU_x^{eq}} = \frac{\mu_r g}{U_x^{eq}} \quad (3.9)$$

This is consistent with the observed behavior of r^{eq} for the drift equilibria in Figure 3.2.

3.1.2 Phase portrait analysis

While the equilibrium analysis of the preceding section provides considerable insight into equilibria of the two-state model, it does not provide any information about the stability of these equilibria, or the dynamics of the model around them. Phase portrait analysis enables a straightforward examination of both.

Phase portraits are generated by simulating a model for a variety of initial conditions and plotting the resulting trajectories in the state space. For the two-state bicycle model, phase portraits are created by simulating the model for a fixed $\delta = \delta^{eq}$ and $U_x = U_x^{eq}$ and plotting the resulting sideslip and yaw rate trajectories in the $\beta - r$ plane. Figures 3.5, 3.6, and 3.7 show the phase portraits obtained using this technique with $U_x^{eq} = 8$ m/s and $\delta^{eq} = 0^\circ$, -5° , and -15° , respectively. The equilibrium locations in each plot are denoted by red dots.

Not surprisingly, the number of equilibria in each phase portrait matches the number of equilibria occurring at the corresponding δ^{eq} in Figures 3.1 through 3.4. For $\delta^{eq} = 0^\circ$ and $\delta^{eq} = -5^\circ$, there are three equilibria, with one stable and two

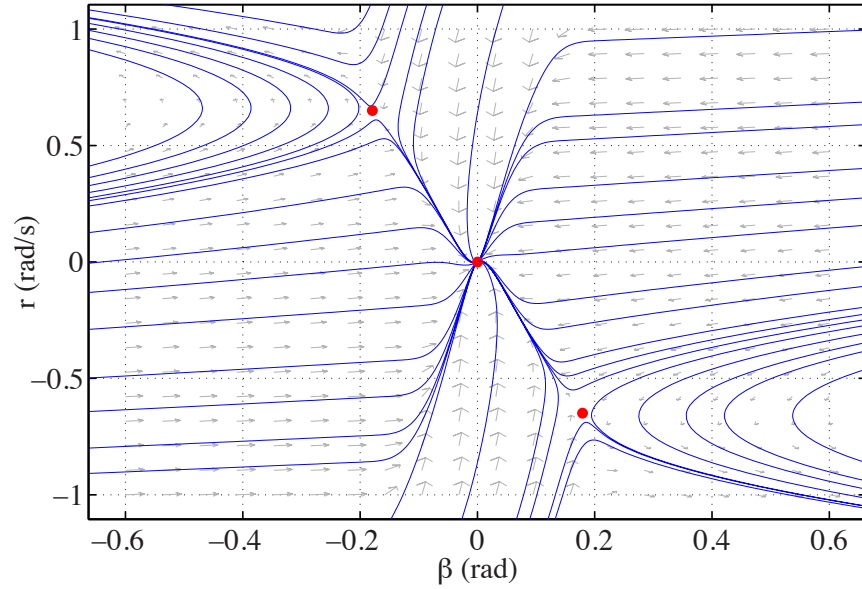


Figure 3.5: Phase portrait of state trajectories for the two-state bicycle model with $U_x^{eq} = 8$ m/s and $\delta^{eq} = 0^\circ$.

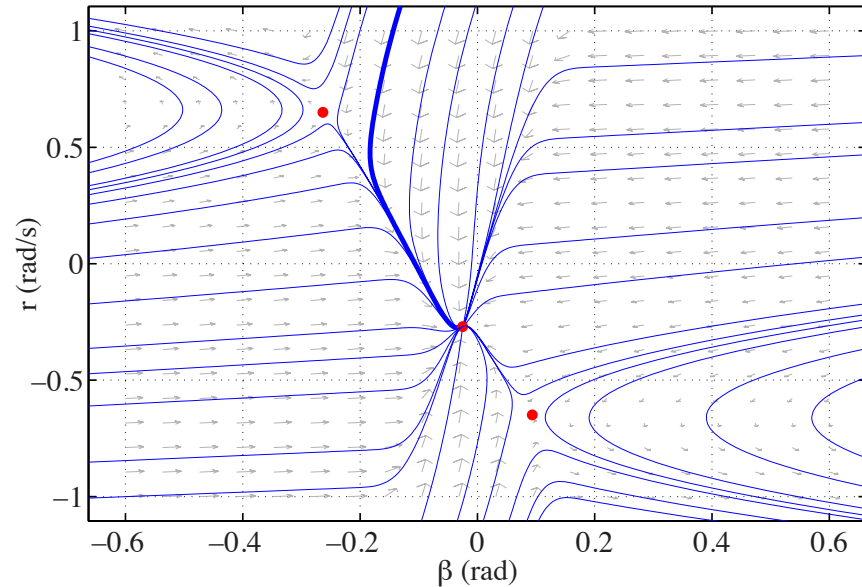


Figure 3.6: Phase portrait of state trajectories for the two-state bicycle model with $U_x^{eq} = 8$ m/s and $\delta^{eq} = -5^\circ$.

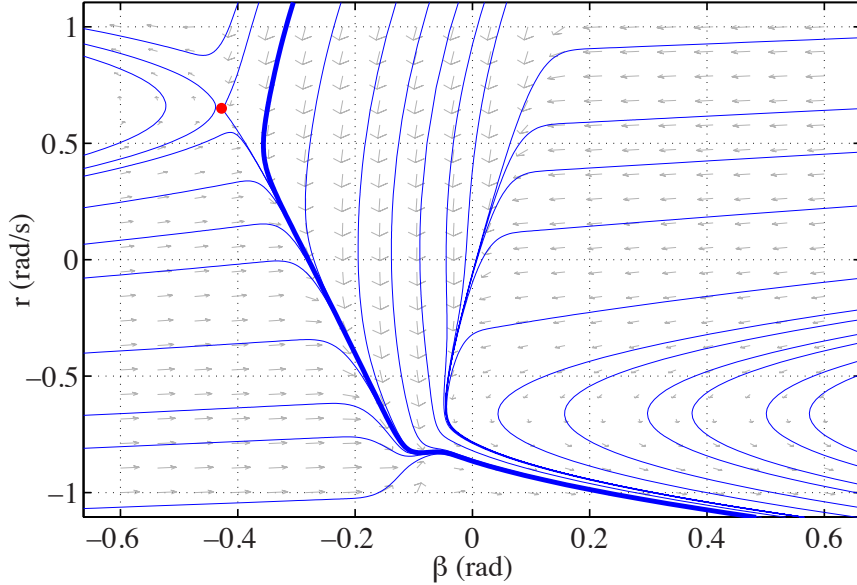


Figure 3.7: Phase portrait of state trajectories for the two-state bicycle model with $U_x^{eq} = 8 \text{ m/s}$ and $\delta^{eq} = -15^\circ$.

unstable. For $\delta^{eq} = -15^\circ$, there is only one equilibrium, and it is unstable. This is the result of a bifurcation in the dynamics of the system. For $\delta^{eq} = 0^\circ$, the equilibria are evenly spaced in the plane. For $\delta^{eq} = -5^\circ$, the central stable equilibrium and the unstable equilibrium in the lower right quadrant of the plane have moved closer to one another. These two equilibria continue to move closer to one another as δ^{eq} is increased, until a saddle-node bifurcation occurs and these equilibria “annihilate” one another, leaving the sole unstable equilibrium in the upper left quadrant.

The centrally-located stable equilibrium in the phase portrait for $\delta^{eq} = 0^\circ$ (Figure 3.5) corresponds to straight-ahead driving. In the case of the phase portrait for $\delta^{eq} = -5^\circ$ (Figure 3.5), the stable equilibrium corresponds to typical cornering at low lateral acceleration. It makes intuitive sense that both equilibria are stable since they represent everyday driving activities easily accomplished by an average (and comparatively unskilled) driver.

This means of course that the remaining equilibria in Figures 3.5 and 3.6 and the sole equilibrium in Figure 3.7 are drift equilibria. In the case of Figures 3.5 and 3.6,

there are left-hand and right-hand drift equilibria that correspond to drifting while turning left (positive yaw rate) and right (negative yaw rate), respectively. In Figure 3.7, there is only a left-hand drift equilibrium.

In all cases, the drift equilibria appear to be saddle points, meaning that a linearization of the dynamics around the equilibrium will have a real-valued positive eigenvalue and a real-valued negative eigenvalue. This means that a component of the dynamics around a drift equilibrium is stable and some trajectories (namely those near the eigenvector corresponding to the stable eigenvalue) are initially attracted towards the equilibrium. However, owing to the positive eigenvalue, the equilibria are still unstable overall and these trajectories are eventually repelled from the equilibrium. This instability arises from the rear tire saturation inherent to drift equilibria.

Another notable characteristic common to all the drift equilibria considered here are trajectories with dominant motion in the yaw rate direction of the state space. The trajectories shown in bold to the right of the left-hand drift equilibrium in Figures 3.5 through 3.7 typify this behavior. Along these trajectories, a precipitous drop in yaw rate occurs along with a more gradual decrease in sideslip magnitude. In the case of $\delta^{eq} = 0^\circ$ and $\delta^{eq} = -5^\circ$, these trajectories reflect a transition from the drift equilibrium to a typical cornering equilibrium, or an “exit” from the drift.

Thus, a close examination of the phase portraits indicates that the drift equilibria are saddle points and that yaw rate variations play a major role in the vehicle dynamics around these equilibria. These observations are rather qualitative in nature, but they can be corroborated quantitatively through analytical linearization of the vehicle dynamics around the drift equilibrium.

3.1.3 Linearized dynamics around the drift equilibria

Linearized dynamics around a drift equilibrium can be derived using a simple variational approach, where the dynamics of the two-state bicycle model are written in terms of perturbations in the states $\delta\beta$ and δr and the front lateral force δF_{yF} from

β^{eq} , r^{eq} , and F_{yF}^{eq} , respectively:

$$\frac{d}{dt}(\beta^{eq} + \delta\beta) = \frac{(F_{yF}^{eq} + \delta F_{yF}) + F_{yR}^{eq}}{mU_x^{eq}} - (r^{eq} + \delta r) \quad (3.10a)$$

$$\frac{d}{dt}(r^{eq} + \delta r) = \frac{a(F_{yF}^{eq} + \delta F_{yF}) - bF_{yR}^{eq}}{I_z} \quad (3.10b)$$

Note that perturbations δF_{yR} in the rear lateral force do not appear in Equation 3.10 because the rear tire lateral force is completely saturated at drift equilibria, meaning that $\delta F_{yR} = 0$ for any perturbations around a drift equilibrium of this model.

After some algebraic manipulations, the expressions in Equation 3.10 reduce to the following dynamics for perturbations $\delta\beta$ and δr in sideslip and yaw rate, respectively:

$$\dot{\delta\beta} = \frac{\delta F_{yF}}{mU_x^{eq}} - \delta r \quad (3.11a)$$

$$\dot{\delta r} = \frac{a\delta F_{yF}}{I_z} \quad (3.11b)$$

This representation of the lateral dynamics turns out to provide a lot of insight into the sideslip dynamics around a drift equilibrium. Differentiating Equation 3.11a and substituting Equation 3.11b for $\dot{\delta r}$ yields the following expression for $\ddot{\delta\beta}$, the second derivative of the sideslip perturbations with respect to time:

$$\ddot{\delta\beta} = \frac{1}{mU_x^{eq}}\delta\dot{F}_{yF} - \frac{a}{I_z}\delta F_{yF} \quad (3.12)$$

From Equation 3.12, $\ddot{\delta\beta}$ is comprised of two terms involving the front lateral force perturbation δF_{yF} . The first term is a function of the first derivative $\delta\dot{F}_{yF}$ with respect to time and reflects the direct effect of front lateral force perturbations upon $\delta\beta$ in Equation 3.11a. The second term is a function of δF_{yF} itself and reflects the effect of front lateral force perturbations acting through the yaw rate perturbation term $-\delta r$ in Equation 3.11a.

If δF_{yF} is increased to some value and held constant, the $\delta\dot{F}_{yF}$ term in Equation 3.12 is initially positive but eventually goes to zero, whereas the negative δF_{yF} term

persists and affects the sideslip dynamics indefinitely. This means the direct effect of δF_{yF} upon the sideslip perturbation dynamics is ultimately outweighed by the opposing effect of δF_{yF} acting through the $-\delta r$ term in these dynamics. In physical terms, the change in yaw rate resulting from a change in front lateral force eventually has a greater (and opposite) influence upon the sideslip dynamics than the change in front lateral force itself.

By computing a transfer function from front lateral force perturbations to sideslip perturbations using Equation 3.12, it becomes clear that the behavior above can be described in control theoretic terms by a RHP zero ($s = amU_x^{eq}/I_z$, where $amU_x^{eq}/I_z > 0$):

$$\frac{\Delta B(s)}{\Delta F_{yF}(s)} = \frac{1}{mU_x^{eq}} \frac{s - \frac{amU_x^{eq}}{I_z}}{s^2}. \quad (3.13)$$

Since the transfer function above is marginally stable, the strict definition for a non-minimum phase system (which requires stability) does not apply here. Nevertheless, the sideslip behavior resulting from the interaction of δF_{yF} and δr in the sideslip perturbation dynamics will have a non-minimum phase characteristic that is captured by the RHP zero in Equation 3.13.

While the above analysis provides considerable insight into the role of yaw rate in the sideslip dynamics, it does not provide a complete picture of the dynamics around a drift equilibrium. This is because front steering is the true input to the vehicle and front lateral force perturbations are actually a function of both steering and state perturbations. With this in mind, it makes sense to derive the linearized dynamics in terms of steering perturbations as well.

A front lateral force perturbation δF_{yF} can then be written in terms of steering and state perturbations using an effective front cornering stiffness \tilde{C}_{α_F} , which represents the local slope of the front tire force curve when operating at the equilibrium of

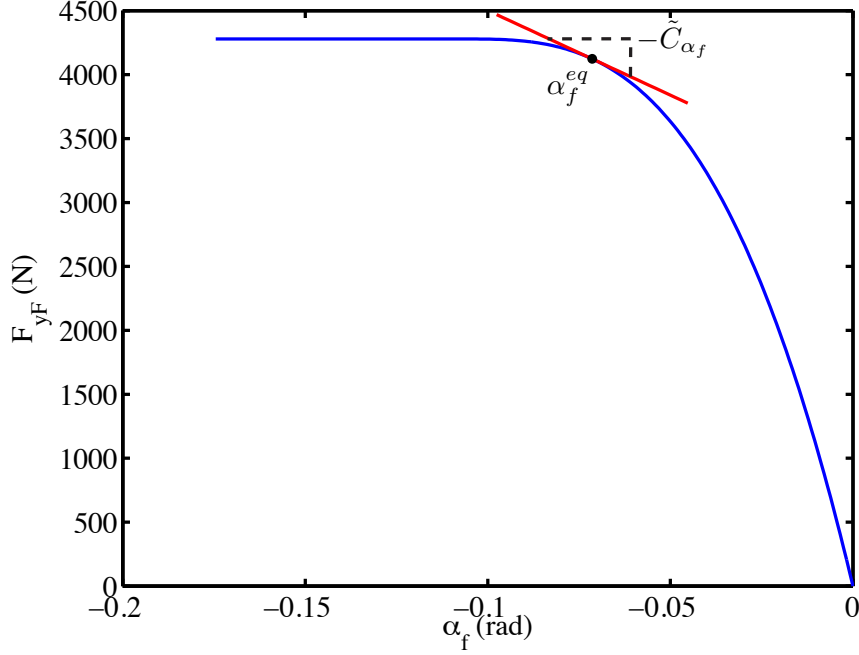


Figure 3.8: Graphical representation of the effective front cornering stiffness \tilde{C}_{α_F} at an equilibrium operating point on the front tire curve.

interest, as shown in Figure 3.8:

$$\delta F_{yF} = -\tilde{C}_{\alpha_F} \delta \alpha_F = -\tilde{C}_{\alpha_F} \left(\delta \beta + \frac{a}{U_x^{eq}} \delta r - \delta \delta \right) \quad (3.14a)$$

$$\tilde{C}_{\alpha_F} = - \left. \frac{\partial F_{yF}}{\partial \alpha_F} \right|_{\alpha_F^{eq}} \quad (3.14b)$$

Substituting Equation 3.14a into Equation 3.11 yields the following:

$$\dot{\delta \beta} = -\frac{\tilde{C}_{\alpha_F}}{m U_x^{eq}} \delta \beta - \left(\frac{a \tilde{C}_{\alpha_F}}{m U_x^{eq 2}} + 1 \right) \delta r + \frac{\tilde{C}_{\alpha_F}}{m U_x^{eq}} \delta \delta \quad (3.15a)$$

$$\dot{\delta r} = -\frac{a \tilde{C}_{\alpha_F}}{I_z} \delta \beta - \frac{a^2 \tilde{C}_{\alpha_F}}{I_z U_x} \delta r + \frac{a \tilde{C}_{\alpha_F}}{I_z} \delta \delta \quad (3.15b)$$

Defining $\Delta B(s)$, $\Delta R(s)$, and $\Delta \Delta(s)$ as the Laplace transforms of $\delta \beta$, δr , and $\delta \delta$ respectively, the following transfer functions from steer angle perturbations to state

perturbations can be derived by computing the Laplace transforms of the dynamics in Equation 3.15:

$$\frac{\Delta B(s)}{\Delta \Delta(s)} = \left(\frac{\tilde{C}_{\alpha_F}}{mU_x^{eq}} \right) \frac{s - \frac{amU_x^{eq}}{I_z}}{s^2 + \left(\frac{a^2\tilde{C}_{\alpha_F}}{I_z U_x^{eq}} + \frac{\tilde{C}_{\alpha_F}}{mU_x^{eq}} \right) s - \frac{a\tilde{C}_{\alpha_F}}{I_z}} \quad (3.16a)$$

$$\frac{\Delta R(s)}{\Delta \Delta(s)} = \left(\frac{a\tilde{C}_{\alpha_F}}{I_z} \right) \frac{s}{s^2 + \left(\frac{a^2\tilde{C}_{\alpha_F}}{I_z U_x^{eq}} + \frac{\tilde{C}_{\alpha_F}}{mU_x^{eq}} \right) s - \frac{a\tilde{C}_{\alpha_F}}{I_z}} \quad (3.16b)$$

Interestingly, these transfer functions for the perturbed dynamics apply to *all* of the drift equilibria for a given set of vehicle parameters and equilibrium longitudinal velocity. This is because the equilibrium front lateral force F_{yF}^{eq} (Equation 3.6) is constant across drift equilibria for a given set of vehicle parameters, meaning that \tilde{C}_{α_F} will be constant across drift equilibria as well.

By inspection, the coefficients of the first and second terms in the transfer function denominators are positive, while the third coefficient is negative since $a\tilde{C}_{\alpha_F}/I_z > 0$. For second order transfer functions, this is a necessary and sufficient condition to conclude that the transfer function has a right half-plane pole and therefore that the system is unstable around drift equilibria. The specific pole locations can be computed directly from the quadratic formula:

$$s_{1,2} = -\frac{1}{2} \left(c_1 \pm \sqrt{c_1^2 + 4c_0} \right) \quad (3.17a)$$

$$c_0 = \frac{a\tilde{C}_{\alpha_F}}{I_z} \quad (3.17b)$$

$$c_1 = \left(\frac{a^2\tilde{C}_{\alpha_F}}{I_z U_x^{eq}} + \frac{\tilde{C}_{\alpha_F}}{mU_x^{eq}} \right) \quad (3.17c)$$

Since $c_0 > 0$ and $c_1 > 0$, $\sqrt{c_1^2 + 4c_0} > c_1$. Therefore, one of the pole locations will be real-valued and positive while the other will be real-valued and negative, meaning that drift equilibria are indeed saddle points.

Like the transfer function derived in terms of front lateral force perturbations (Equation 3.13), the sideslip perturbation transfer function in Equation 3.16a has a

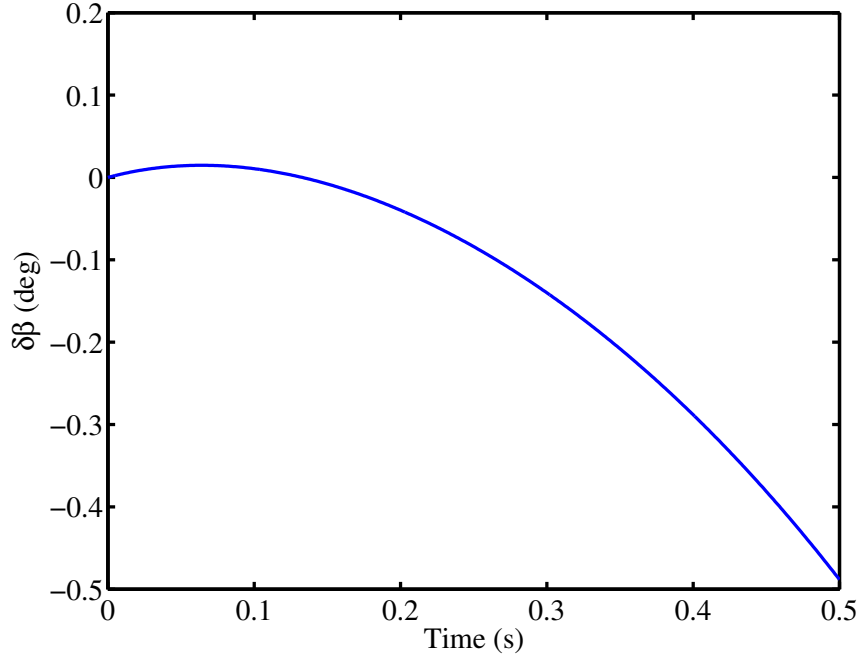


Figure 3.9: Step response of the linearized sideslip dynamics for the two-state model with $\tilde{C}_{\alpha_F} = 13,239$ N/rad and $\delta\delta = 0.5$ deg.

RHP zero located at $s = amU_x^{eq}/I_z$. This means that the physical intuition developed by analyzing the dynamics in terms of front lateral force perturbations also applies to steering perturbations as well. In particular, the direct effect of a steering perturbation upon the sideslip dynamics is also eventually overwhelmed by the effect of this perturbation upon the yaw rate term in the dynamics.

This can be observed in the response of the linearized sideslip dynamics in Equation 3.16a to a step $\delta\delta = 0.5$ deg as obtained with P1 vehicle parameters, $U_x^{eq} = 8$ m/s, and an effective cornering stiffness $\tilde{C}_{\alpha_F} = 13,239$ N/rad (Figure 3.9). This response has the non-minimum phase characteristic alluded to earlier, even though the linearized sideslip dynamics are not strictly non-minimum phase because they are unstable. The direct effect of the steering perturbation upon the sideslip dynamics initially increases $\delta\beta$, but the increase in δr also caused by the perturbation rapidly counteracts its direct effect and causes $\delta\beta$ to decrease in an unbounded fashion.

Analytical linearization has confirmed the properties of drift equilibria suggested

by phase portrait analysis. The drift equilibria are indeed saddle points, with pole locations that are actually independent of the equilibrium location for a given equilibrium longitudinal velocity and set of vehicle parameters. Furthermore, regardless of whether the linearization is derived in terms of front lateral force perturbations or steering perturbations, it has a RHP zero that reflects the considerable influence of changes in yaw rate upon the sideslip dynamics. This accounts for why a precipitous drop in yaw rate around drift equilibria, such as the one occurring along the bold trajectories in Figures 3.5 through 3.7, is associated with a decrease in sideslip magnitude and an exit from the drift.

3.2 Equilibria of the three-state model

The simplicity of the two-state model in the preceding section enables a straightforward, physically intuitive analysis of drift equilibria and the dynamics around them. However, this model omits longitudinal dynamics and the rear drive force input, which is a critical component of drifting based on findings in prior research.

With this in mind, much of the analysis in the preceding section is repeated here using the three-state bicycle introduced in Chapter 2. Recall that this model adds longitudinal dynamics and the rear drive force input, replacing the lateral force model and de-rated friction coefficient at the rear tire with a tire model that couples lateral and longitudinal tire forces via the friction circle relationship:

$$\dot{\beta} = \frac{F_{yF} + F_{yR}}{mU_x} - r \quad (3.18a)$$

$$\dot{r} = \frac{aF_{yF} - bF_{yR}}{I_z} \quad (3.18b)$$

$$\dot{U}_x = \frac{F_{xR} - F_{yF} \sin \delta}{m} + rU_x\beta, \quad (3.18c)$$

where F_{xR} is the rear drive force input and longitudinal velocity U_x is now a model state. As will become clear below, an equilibrium and phase portrait analysis of this model produces results quite similar to those obtained with the two-state model, but with added insight into the role of rear drive force at drift equilibria.

3.2.1 Calculating equilibrium locations

Determining the equilibrium locations of the three-state proceeds in the same fashion as for the two-state model. The equilibria occur where $\dot{\beta} = \dot{r} = \dot{U}_x = 0$, yielding the following algebraic system of equations:

$$\frac{F_{yF}^{eq} + F_{yR}^{eq}}{mU_x^{eq}} - r^{eq} = 0 \quad (3.19a)$$

$$\frac{aF_{yF}^{eq} - bF_{yR}^{eq}}{I_z} = 0 \quad (3.19b)$$

$$\frac{F_{xR}^{eq} - F_{yF}^{eq} \sin \delta^{eq}}{m} + r^{eq} U_x^{eq} \beta^{eq} = 0 \quad (3.19c)$$

Once again, the equilibrium lateral forces F_{yF}^{eq} and F_{yR}^{eq} are functions of the states and inputs, so this is a system of three equations in five unknown quantities: δ^{eq} , β^{eq} , r^{eq} , U_x^{eq} , and the equilibrium rear drive force F_{xR}^{eq} . Thus, it is necessary to constrain two of these quantities in order to solve the system of equations. Like before, δ^{eq} and U_x^{eq} are set to prescribed values and the system in Equation 3.19 is solved for β^{eq} , r^{eq} , and F_{xR}^{eq} .

Numerical solution of the system in Equation 3.19 with $U_x^{eq} = 8$ m/s and a range of δ^{eq} values yields the equilibrium solutions plotted in Figures 3.10 through 3.14. Several of these figures depict the same information considered in the equilibrium analysis of the preceding section, including equilibrium sideslip, yaw rate, and front lateral force as a function of equilibrium steer angle (Figures 3.10, 3.11, and 3.12, respectively). Figures 3.13 and 3.14 provide information specific to the three-state model, namely the equilibrium rear drive force and total rear tire force magnitude $F_R^{eq} = \sqrt{F_{xR}^{eq 2} + F_{yR}^{eq 2}}$ as a function of δ^{eq} , respectively. Note that F_R^{eq} is plotted rather than F_{yR}^{eq} , as the combined effect of the rear longitudinal and lateral tire forces must be considered in determining the extent of rear tire saturation.

For the parameter set under consideration, the three-state model exhibits the same two classes as the equilibria of the two-state model: typical cornering equilibria and drift equilibria. It is worth noting, however, that alternate tire and friction parameters can yield a third class of equilibria characterized by low-sideslip and complete front

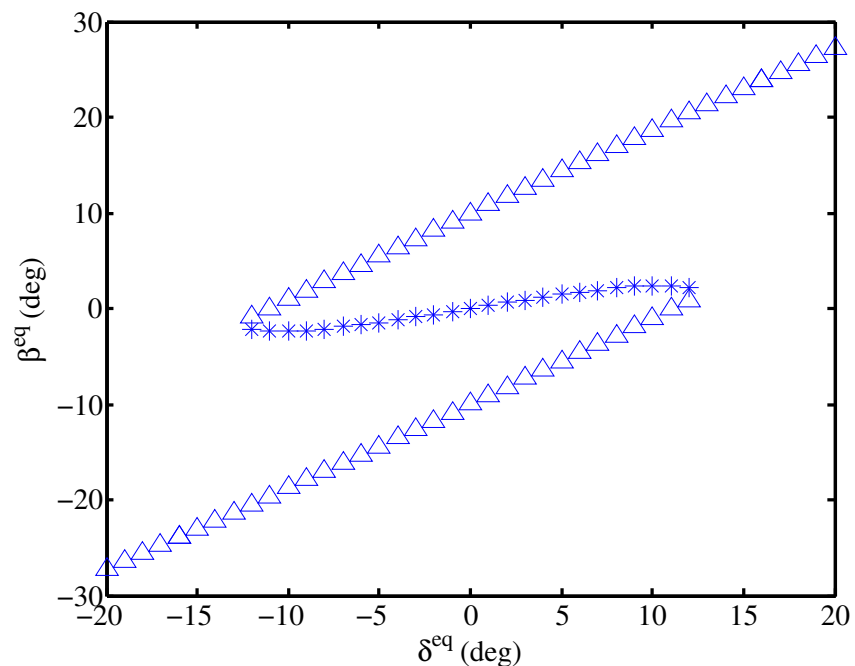


Figure 3.10: Equilibrium sideslip versus steer angle with $U_x^{eq} = 8$ m/s for the three-state bicycle model.

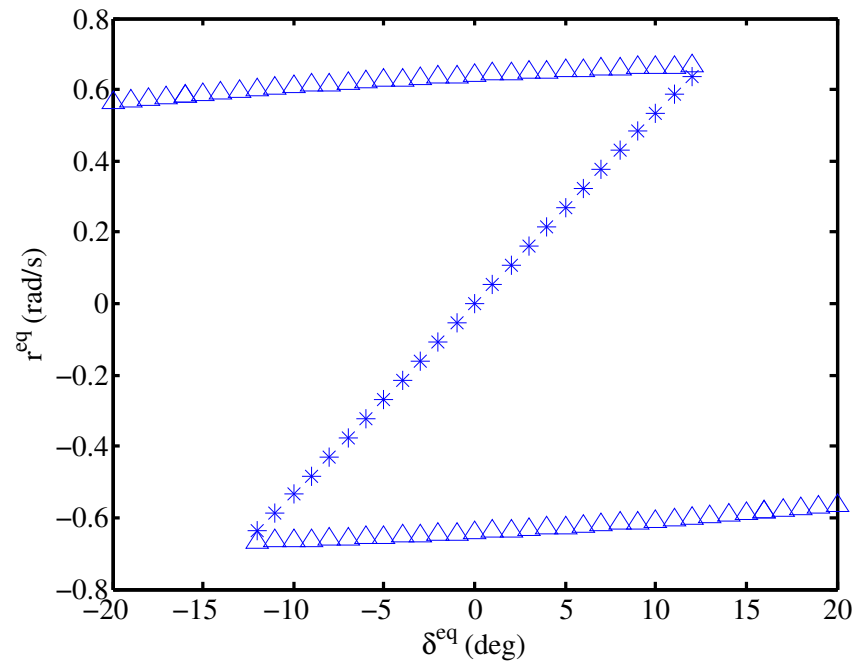


Figure 3.11: Equilibrium yaw rate versus steer angle with $U_x^{eq} = 8$ m/s for the three-state bicycle model.

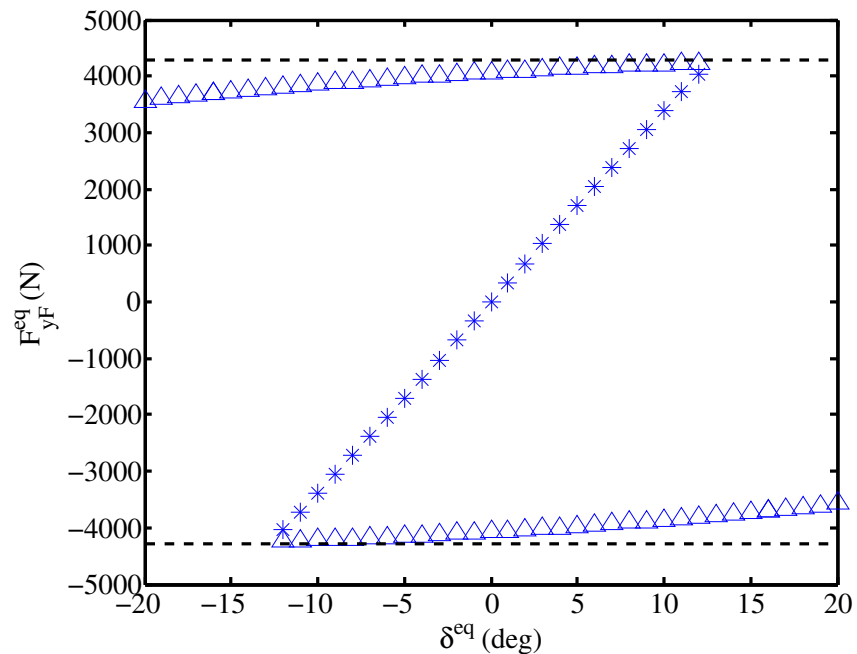


Figure 3.12: Equilibrium front lateral force versus steer angle with $U_x^{eq} = 8$ m/s for the three-state bicycle model.

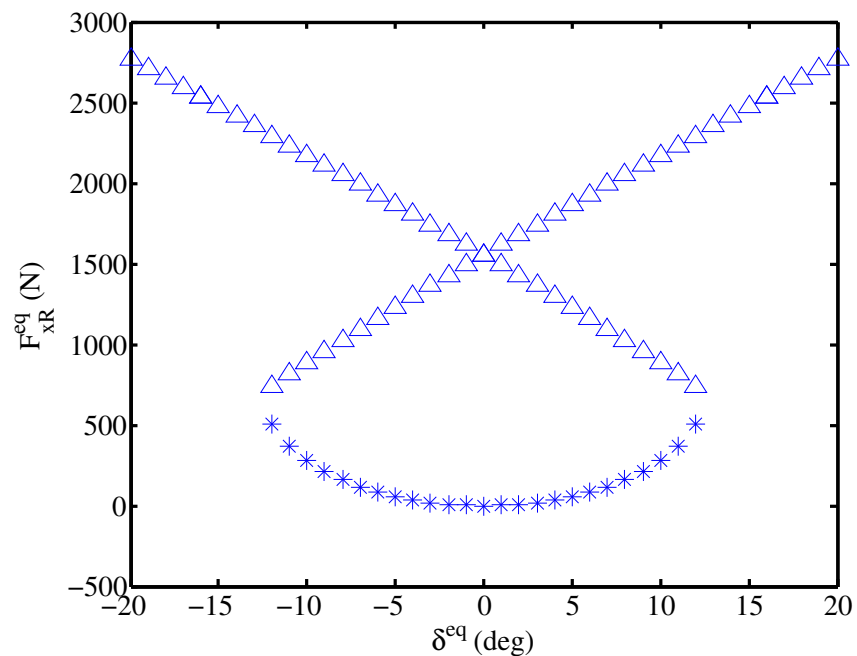


Figure 3.13: Equilibrium rear drive force versus steer angle with $U_x^{eq} = 8$ m/s for the three-state bicycle model.

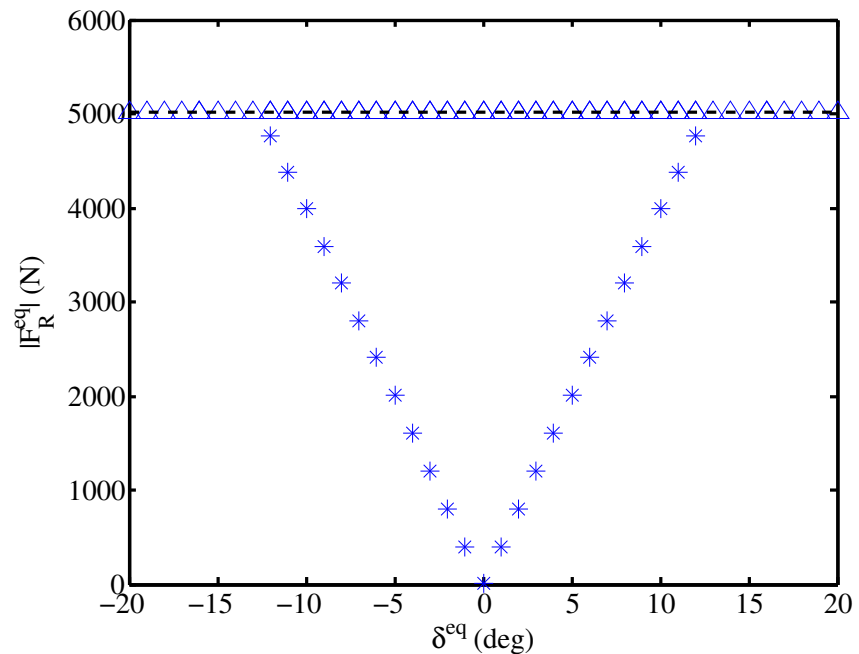


Figure 3.14: Rear tire force magnitude versus steer angle with $U_x^{eq} = 8$ m/s for the three-state bicycle model.

tire saturation, representing what is known as “limit understeer” cornering of the vehicle. This additional class of equilibria is discussed in greater detail in [22].

The equilibria denoted by asterisks (*) in Figures 3.10 through 3.14 are still typical cornering equilibria, and retain the same characteristics as earlier: the equilibrium sideslip β^{eq} is small, the vehicle turns in the same direction as it is steered, the vehicle’s yaw rate increases as it is steered more, and both tires are unsaturated. For the front tire, this is once again indicated in Figure 3.12 by the fact that that F_{yF}^{eq} for all of conventional cornering equilibria lies within the black dashed lines indicating the friction limits of the front tire. For the rear tire, this is indicated by the fact that the *total* rear tire force magnitude for these equilibria lies below the line indicating the rear tire friction limit.

The equilibria denoted by triangles (Δ) are once again drift equilibria at which the rear tire is saturated. In this case, complete rear tire saturation means that the total rear tire force is equivalent to the maximum force available from friction at the rear tire. This is clear in Figure 3.14 from the fact that all of the Δ -equilibria lie on the black dashed line representing the friction limit of the rear tire. There are definite similarities between these drift equilibria and those of the two-state model. As before, the front lateral force is nearly saturated, and the equilibria at large steer angles exhibit the high sideslip angle and countersteer commonly associated with drifting.

There are, however, some differences between these drift equilibria and those of the two-state model. Whereas r^{eq} is constant at drift equilibria of the two-state model, it decreases noticeably as the magnitude of δ^{eq} and β^{eq} increase for this model. Similarly, F_{yF}^{eq} is a constant, nearly-saturated value at drift equilibria of the two-state model. For this model, the equilibrium front lateral force at drift equilibria is closest to saturation at small δ^{eq} and β^{eq} but becomes less saturated as δ^{eq} and β^{eq} increase in magnitude.

Not surprisingly, these differences in the drift equilibria of the two models arise from the primary difference between the models: the incorporation of the rear drive force input, and the interesting effects of this ostensibly longitudinal input upon lateral behavior at the drift equilibria. While some amount of rear drive force is

required to maintain any equilibrium cornering condition, the rear drive force at all of the drift equilibria is quite large relative to the drive force at typical cornering equilibria. In fact, the drive force required for operation at any of calculated the drift equilibria is larger than the drive force at all of the calculated typical cornering equilibria.

This large rear drive force induces the complete rear tire saturation observed at drift equilibria. To be specific, the large F_{xR}^{eq} at drift equilibria drives the total rear tire force up to the friction limit for the tire:

$$\sqrt{F_{xR}^{eq 2} + F_{yR}^{eq 2}} = \mu F_{zR} \quad (3.20)$$

Geometrically speaking, this means that the tire operates on the friction circle at drift equilibria. Consequently, the rear lateral force at the equilibria is dictated directly by the amount of drive force applied at the equilibrium, and can be computed through simple re-arrangement of the expression in Equation 3.20:

$$F_{yR}^{eq} = \sqrt{\mu F_{zR}^2 - F_{xR}^{eq 2}} \quad (3.21)$$

Thus, it is the coupling of the rear tire lateral and longitudinal forces via the friction circle that makes the rear drive force influence the lateral equilibrium behavior of the vehicle. Note from Figure 3.13 that F_{xR}^{eq} at drift equilibria increases as δ^{eq} gets larger. From Equation 3.21, this means that F_{yR}^{eq} at drift equilibria decreases as δ^{eq} gets larger, rather than remaining constant; this produces the observed decreases in r^{eq} and F_{yF}^{eq} with δ^{eq} . More importantly, a comparison of Figures 3.10 and 3.13 reveals that F_{xR}^{eq} increases monotonically with the magnitude of β^{eq} at drift equilibria, suggesting that a deeper drift results from applying more drive force, at least in steady state.

3.2.2 Phase portraits around equilibria

Along the same lines as before, a phase portrait for the three-state bicycle model is generated by simulating the model's dynamics from a variety of initial conditions with the steering and rear drive force inputs held constant at values corresponding to

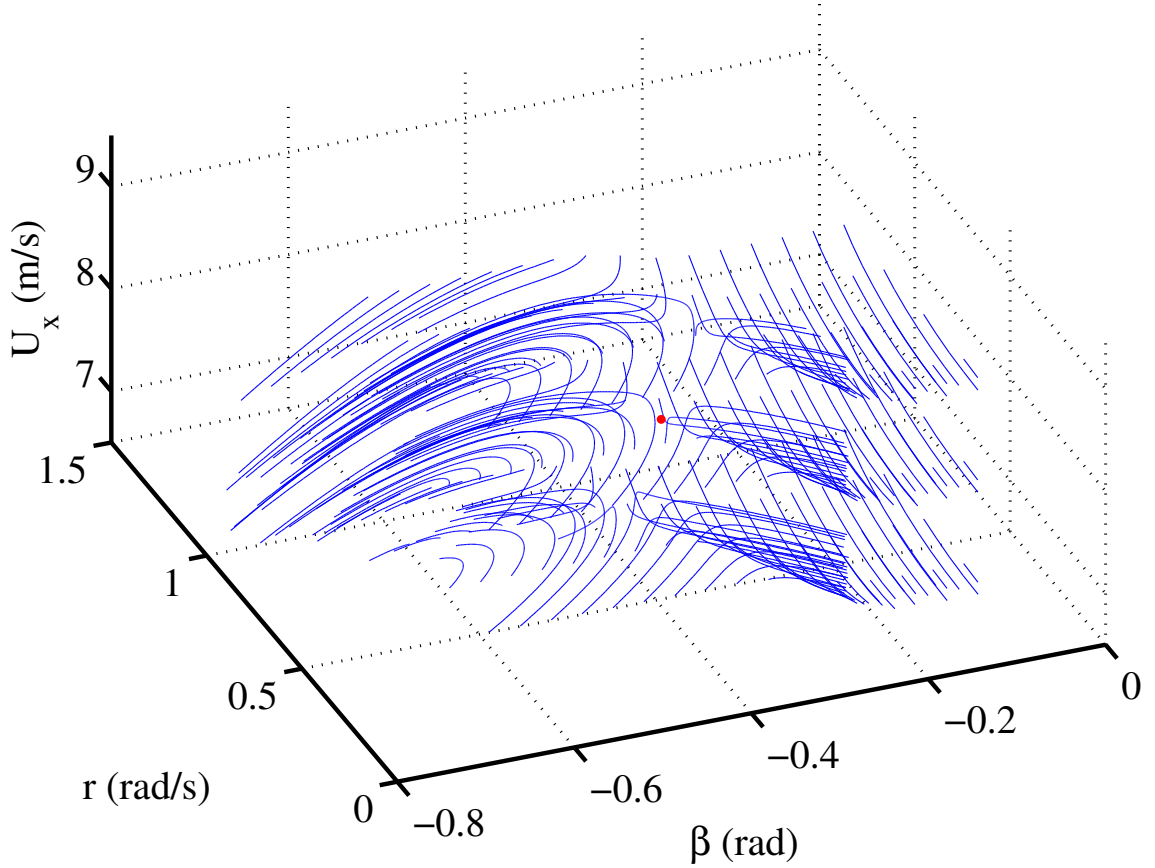


Figure 3.15: Phase portrait of state trajectories of the three-state bicycle model with $\delta^{eq} = -12^\circ$ and $F_{xR}^{eq} = 2293$ N.

an equilibrium of interest, e.g. $\delta = \delta^{eq}$ and $F_{xR} = F_{xR}^{eq}$.

In this case, however, the phase portrait requires visualization of the resulting state trajectories in three dimensions, since the model has three states. Figure 3.15 shows a phase portrait generated with $\delta^{eq} = -12^\circ$ and $F_{xR}^{eq} = 2293$ N, corresponding to the drift equilibrium located at $\beta^{eq} = -20.44^\circ$, $r^{eq} = 0.600$ rad/s, and $U_x^{eq} = 8$ m/s, indicated in the figure by a red dot.

This phase portrait is somewhat difficult to interpret, especially in the absence of the ability to view the state space from a variety of different perspectives. Fortunately, it is still possible to gain insights about the lateral dynamics of the

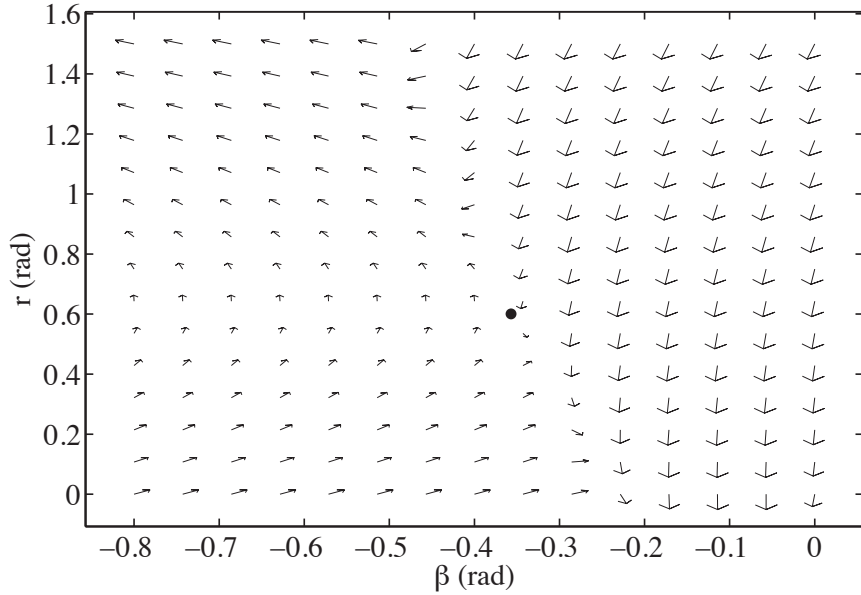


Figure 3.16: Two-dimensional section of the phase portrait for the three-state bicycle model: Vector field of sideslip and yaw rate derivatives when $U_x^{eq} = 8$ m/s with $\delta^{eq} = -12^\circ$ and $F_{xR}^{eq} = 2293$ N.

model around the drift equilibrium of interest by examining what is effectively a two-dimensional section of the phase portrait when $U_x = U_x^{eq} = 8$ m/s, shown in Figure 3.16. This section gives a flow field representing the sideslip and yaw rate state derivatives at the equilibrium longitudinal velocity, with the equilibrium location once again indicated by a dot.

The flow field indicates that the drift equilibria of the three-state model are saddle points, like the analogous equilibria of the two-state model. Furthermore, there still appears to be dominant motion in the yaw direction in the region to the right of the equilibrium, where a precipitous drop in yaw rate is associated with a decrease in sideslip magnitude and an exit from the drift.

These characteristics are corroborated by numerical computation of transfer functions from steer angle perturbations to sideslip and yaw rate perturbations for the equilibrium in the phase portrait (the analytical transfer functions are quite complex

in this case):

$$\frac{\Delta B(s)}{\Delta \Delta(s)} = \frac{2.007(s - 14.12)(s - 0.05167)}{(s + 9.742)(s - 2.774)(s - 0.1371)} \quad (3.22a)$$

$$\frac{\Delta R(s)}{\Delta \Delta(s)} = \frac{28.7456(s^2 + 0.1982s + 0.2382)}{(s + 9.742)(s - 2.774)(s - 0.1371)} \quad (3.22b)$$

While these transfer functions must differ from the ones for the two-state model (Equation 3.16) by virtue of being derived from a third-order model, there are multiple similarities between the transfer functions for both models.

The transfer functions in Equation 3.22 have one real-valued stable pole and two real-valued unstable poles. Relative to the two-state model, the three-state model has an additional unstable pole representing a mode that arises from incorporation of longitudinal dynamics. Nonetheless, the mixture of real-valued stable and real-valued unstable poles confirms that the drift equilibrium under consideration is still an unstable saddle point.

The sideslip perturbation transfer function at this drift equilibrium has two RHP zeros rather than one, but one of these zeros ($s = 14.12$) is at nearly the same location as the RHP zero in the linearization of the two state model ($s = amU_x^{eq}/I_z \approx 14.32$); this zero represents the same physical effect of yaw rate upon the sideslip dynamics. In order to see why, it is once again useful to study the linearized dynamics in terms of force perturbations. In particular, the linearized lateral dynamics of the three-state model take the following form when considering front lateral force perturbations alone (e.g., $\delta F_{xR} = \delta F_{yR} = 0$):

$$\dot{\delta\beta} = \frac{\delta F_{yF}}{mU_x^{eq}} - \frac{F_{yF}^{eq} + F_{yR}^{eq}}{mU_x^{eq2}} \delta U_x - \delta r \quad (3.23a)$$

$$\dot{\delta r} = \frac{a\delta F_{yF}}{I_z} \quad (3.23b)$$

While the sideslip perturbation dynamics in Equation 3.23a contain an extra term that is a function of longitudinal velocity perturbations, the coupling between the sideslip and yaw perturbation dynamics is the same as it is for the two-state model in Equation 3.11. This coupling results in an analogous RHP zero in the transfer function

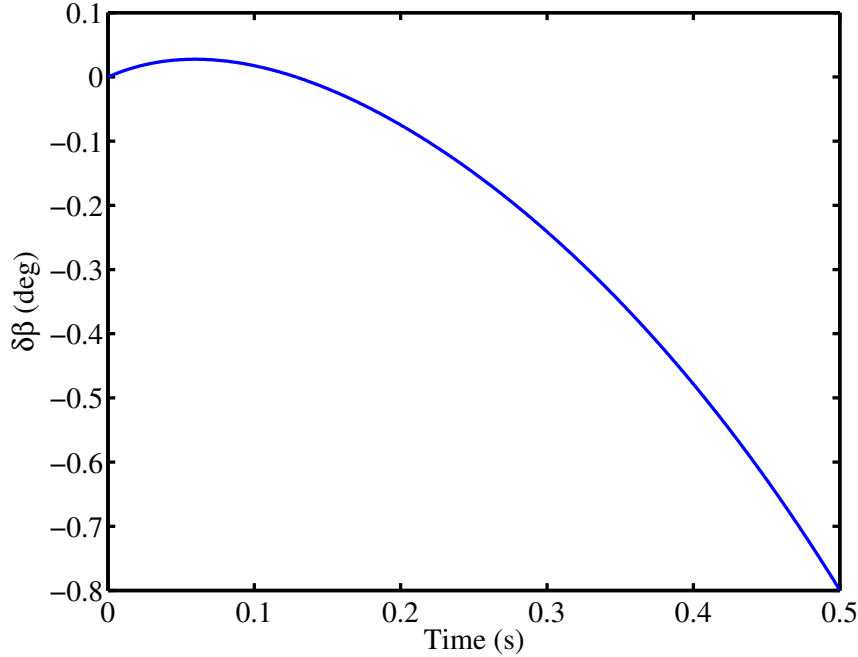


Figure 3.17: Step response of sideslip perturbation dynamics computed from the three-state model with $\delta\delta = 0.5$ deg

from steering perturbations to sideslip perturbations for the three-state model.

The response of the sideslip perturbation dynamics in Equation 3.22a to a step $\delta\delta = 0.5$ deg with $\delta F_{xR} = 0$ (Figure 3.17) demonstrates that this zero influences the sideslip dynamics in the same way that it does for the two-state model. Once again, the direct effect of the steering perturbation on sideslip is eventually (and quickly) outweighed by the effect of the steering perturbation acting through the yaw rate term in the sideslip dynamics.

Since the three-state model also has rear drive force as an input, it is also possible to numerically compute transfer functions from rear drive force perturbations to sideslip and yaw rate perturbations, along the same lines of Equation 3.22:

$$\frac{\Delta B(s)}{\Delta F_{xR}(s)} = \frac{-0.0000372(s + 20.91)(s + 0.6383)}{(s + 9.742)(s - 2.774)(s - 0.1371)} \quad (3.24a)$$

$$\frac{\Delta R(s)}{\Delta F_{xR}(s)} = \frac{0.000454(s + 4.371)(s + 0.8741)}{(s + 9.742)(s - 2.774)(s - 0.1371)} \quad (3.24b)$$

It has already been established that rear drive force influences the vehicle's lateral behavior at drift equilibria. The transfer functions in Equation 3.24 indicate that it is also possible to use this input to control the vehicle's lateral dynamics *around* drift equilibria as well. Moreover, it is worth noting that there are no RHP zeroes in either transfer function involving rear drive force perturbations. This indicates that rear drive force can actually be a more straightforward input for lateral control around a drift equilibrium than front steering.

3.3 Implications for control design

The analysis in this chapter demonstrates how the three-state model proposed in Chapter 2 achieves a balance between sufficient model fidelity and simplicity for control design. On one hand, the model incorporates rear drive force and provides considerable insight into the role of this input at drift equilibria. On the other, the model is simple enough that the physical intuition developed from the two-state lateral model applies to this three-state model as well.

Like higher fidelity models in prior research, the three-state model indicates that drift equilibria are associated with large rear drive forces. These large drive forces saturate the rear tire, and while this makes the drift equilibria unstable, it also couples the rear lateral and longitudinal forces via the friction circle. As a result, the rear drive force input influences the lateral behavior of the vehicle at drift equilibria and influences the lateral dynamics around drift equilibria as well. Since rear drive force is typically viewed as an input for controlling longitudinal dynamics, this could present new possibilities for control design.

Using the two-state model, it has been analytically demonstrated that the front lateral force is nearly saturated at drift equilibria, and that the linearized sideslip dynamics at drift equilibria have a RHP zero. Near-saturation of the front lateral force is significant because it means that control authority through the steering input will be asymmetric around drift equilibria; while it will be easy to reduce the front lateral force through steering, it will only be possible to increase the front lateral force a small amount before saturation occurs. The RHP zero in the linearized sideslip

dynamics is also important because it signifies that changes in yaw rate generated by steering ultimately have a greater effect upon the sideslip dynamics than the steering input itself. Considering that numerical analysis has also revealed these same two characteristics for a drift equilibrium of the three-state model, it is clear that the physical intuition gained from the two-state model must be taken into consideration when using the steering input for drift control.

Chapter 4

Control Design for Drifting

A fundamental challenge of vehicle control design using steering and rear drive force inputs, whether for drifting or less exotic ends, is the availability of only *two* inputs to control *three* states. As discussed at the beginning of Chapter 3, this constrains the achievable equilibrium conditions of the vehicle, but it has another implication as well: it is not possible to design a controller that moves the vehicle state along an arbitrary trajectory in the state space using these inputs. Any control design based on these inputs must respect constraints imposed by both their basic physical limitations and the nature of their influence upon the vehicle's dynamics.

The control design challenge explored in this chapter lies in understanding how the available steering and drive force inputs can be used to control the vehicle's state to a drift equilibrium while respecting these constraints. This is an essential part of developing a controller to drift a vehicle, as operation at an otherwise unstable drift equilibrium will require closed-loop stabilization.

The preceding chapter established that a combination of large drive force and countersteer is necessary to maintain operation at a drift equilibrium. Furthermore, it established that the rear drive force influences the lateral dynamics around drift equilibria because of rear tire saturation. However, the analysis in Chapter 3 did not provide a sense for how significant this influence is at drift equilibria relative to typical cornering conditions. Section 4.1 addresses this question by comparing the direct effect of the steering and rear drive force inputs upon the vehicle's dynamics

for different types of operating conditions. This analysis reveals that the rear drive force input has a greater direct influence upon the lateral dynamics at drift equilibria than at typical cornering equilibria. This is especially true at drift equilibria where the equilibrium sideslip β^{eq} is large; in fact, direct lateral control authority through the rear drive force input is comparable to that of the steering input when β^{eq} is large.

In light of the fact that steering and rear drive force can both be used to control the lateral dynamics of a vehicle around a drift equilibrium, Section 4.2 presents illustrative case studies of steering-based and drive force-based controllers to highlight the capabilities and limitations of each input in this capacity. From these case studies, it becomes clear that it makes physical sense to coordinate steer and rear drive force inputs because the front tire is nearly saturated at drift equilibria and effectively has unidirectional control authority as a result.

Section 4.3 uses the physical intuition developed preceding sections along with insights from Chapter 3 to design a controller that coordinates steering and rear drive force inputs to drift a vehicle. Experimental data from implementation of this controller on P1, given in Section 4.4, demonstrates that it achieves robust and sustained drifts under rather challenging test conditions involving significant friction variability.

4.1 The effects of vehicle inputs around equilibria

The effect of the rear drive force and steering inputs at different operating conditions can be interpreted in terms of their ability to influence the vehicle state derivatives around those operating conditions. Towards this end, this section examines the state space representation of the linearized vehicle dynamics around equilibria corresponding to different kinds of operating conditions. These dynamics take the form $\dot{\delta}x = A\delta x + B\delta u$, where $\delta x = [\delta\beta \ \delta r \ \delta U_x]^T$ is the vector of state perturbations and $\delta u = [\delta F_{yF} \ \delta F_{xR}]^T$ is the vector of input perturbations.

The focus of the analyses that follow is the input matrix B , which gives the partial derivatives of the three-state bicycle model dynamics with respect to each of

the inputs at the equilibrium condition of interest:

$$B = \left[\begin{array}{cc} \frac{\partial \dot{\beta}}{\partial F_{yF}} & \frac{\partial \dot{\beta}}{\partial F_{xR}} \\ \frac{\partial \dot{r}}{\partial F_{yF}} & \frac{\partial \dot{r}}{\partial F_{xR}} \\ \frac{\partial \dot{U}_x}{\partial F_{yF}} & \frac{\partial \dot{U}_x}{\partial F_{xR}} \end{array} \right] \Bigg|_{\beta^{eq}, r^{eq}, U_x^{eq}, F_{yF}^{eq}, F_{xR}^{eq}} = \begin{bmatrix} b_{11} & b_{12} \\ b_{21} & b_{22} \\ b_{31} & b_{32} \end{bmatrix} \quad (4.1)$$

Note here that the effect of the steering input on the linearized model is defined in terms of front lateral force perturbations δF_{yF} rather than steer angle perturbations $\delta\delta$. This is to facilitate easy comparison with rear drive force perturbations δF_{xR} , since δF_{yF} and δF_{xR} have the same units and are of similar magnitude.

The B matrix defines the direct influence of the inputs upon the vehicle states. Strictly speaking, both the input matrix B and coupling between states in the dynamics matrix A must be considered in order to fully understand the ability of a particular input to influence a given state. This is simply because an input may not have a direct influence upon a certain state but may still influence that state via cross-couplings between states in the system dynamics. Nevertheless, an examination of the input matrix still provides a physically intuitive way to demonstrate considerable variation in the capabilities of the inputs across different operating conditions.

The first column of B (b_{11} , b_{21} , and b_{31}) indicates the direct influence δF_{yF} upon the dynamics of sideslip, yaw rate, and longitudinal velocity perturbations, respectively. Along the same lines, the coefficients in the second column (b_{12} , b_{22} , and b_{32}) indicate the direct influence of δF_{xR} upon the state perturbation dynamics.

The b_{11} , b_{21} , and b_{32} entries of B are straightforward to derive directly from differentiation of the bicycle model equations and are constant across different equilibrium conditions:

$$b_{11} = \frac{1}{mU_x^{eq}} \quad (4.2a)$$

$$b_{21} = \frac{a}{I_z} \quad (4.2b)$$

$$b_{32} = \frac{1}{m}. \quad (4.2c)$$

The remaining three terms (b_{12} , b_{22} , and b_{31}), however, do vary with the equilibrium

condition under consideration.

Since F_{xR} does not appear explicitly in the sideslip or yaw rate dynamics of the three-state model, the entries b_{12} and b_{22} are dictated only by the extent of coupling between the rear tire lateral and longitudinal forces, and computed accordingly:

$$b_{12} = \left(\frac{1}{mU_x^{eq}} \right) \frac{\partial F_{yR}}{\partial F_{xR}} \Big|_{\alpha_R^{eq}, F_{xR}^{eq}} \quad (4.3a)$$

$$b_{22} = - \left(\frac{b}{I_z} \right) \frac{\partial F_{yR}}{\partial F_{xR}} \Big|_{\alpha_R^{eq}, F_{xR}^{eq}} \quad (4.3b)$$

The partial derivative $\partial F_{yR}/\partial F_{xR}$ of the rear lateral force with respect to the rear longitudinal force can be computed using the chain rule:

$$\frac{\partial F_{yR}}{\partial F_{xR}} = \frac{\partial F_{yR}}{\partial \xi_R} \frac{\partial \xi_R}{\partial F_{xR}}, \quad (4.4)$$

where ξ_R is the rear lateral force de-rating factor as defined in Chapter 2:

$$\xi_R = \frac{\sqrt{(\mu F_{zR})^2 - F_{xR}^2}}{\mu F_{zR}}. \quad (4.5)$$

The partial derivative $\partial F_{yR}/\partial \xi_R$ on the right-hand side Equation 4.4 is derived directly from differentiation of Equation 4.5, regardless of the equilibrium condition under consideration:

$$\frac{\partial \xi_R}{\partial F_{xR}} = - \frac{F_{xR}}{\mu F_{zR} \sqrt{(\mu F_{zR})^2 - F_{xR}^2}}. \quad (4.6)$$

The other partial derivative on the right-hand side, $\partial F_{yR}/\partial \xi_R$, is dependent upon the operating point $(\alpha_R^{eq}, F_{yR}^{eq})$ on the rear lateral force curve and therefore the extent of rear tire saturation. This plays a large role in dictating the expressions for (and magnitudes of) b_{12} and b_{22} at a given equilibrium condition.

Since the b_{31} entry of B describes the influence of front lateral force perturbations upon the longitudinal dynamics, it is derived from the partial derivative of the

$-\frac{1}{m}F_{yF}\sin\delta$ term in the longitudinal dynamics with respect to front lateral force:

$$b_{31} = \left. \frac{\partial}{\partial F_{yF}} \left(-\frac{1}{m}F_{yF}\sin\delta \right) \right|_{\alpha_F^{eq}, F_{yF}^{eq}} \quad (4.7)$$

Applying the product rule for differentiation, Equation 4.7 becomes:

$$b_{31} = -\frac{1}{m} \left(\sin\delta + F_{yF} \cos\delta \frac{\partial\delta}{\partial F_{yF}} \right) \Big|_{\alpha_F^{eq}, F_{yF}^{eq}} \quad (4.8)$$

The partial derivative $\partial\delta/\partial F_{yF}$ that appears in Equation 4.8 can be expressed as follows using the chain rule:

$$\frac{\partial\delta}{\partial F_{yF}} = \frac{\partial\delta}{\partial\alpha_F} \frac{\partial\alpha_F}{\partial F_{yF}} \quad (4.9)$$

From the definition of the front tire slip angle α_F (Equation 2.20a) solved for δ , $\partial\delta/\partial\alpha_F = -1$. From re-arrangement of the definition for the effective front cornering stiffness \tilde{C}_{α_F} given in Equation 3.14b, $(\partial\alpha_F/\partial F_{yF})|_{\alpha_F^{eq}, F_{yF}^{eq}} = -1/\tilde{C}_{\alpha_F}$. Substituting these expressions into Equation 4.9 and plugging the result into Equation 4.7 yields this expression for b_{31} :

$$b_{31} = -\frac{1}{m} \left(\sin\delta^{eq} + \frac{F_{yF}^{eq}}{\tilde{C}_{\alpha_F}} \cos\delta^{eq} \right) \quad (4.10)$$

Since b_{31} is a function of both the equilibrium front lateral force and steer angle, it will obviously vary with the equilibrium condition under consideration.

Putting all the matrix entries together yields the following expression for the input matrix B :

$$B = \begin{bmatrix} \frac{1}{mU_x^{eq}} & -\frac{1}{mU_x^{eq}} \left(\frac{\partial F_{yR}}{\partial \xi_R} \right) \Big|_{\alpha_R^{eq}, F_{xR}^{eq}} \left(\frac{F_{xR}}{\mu F_{zR} \sqrt{(\mu F_{zR})^2 - F_{xR}^2}} \right) \\ \frac{a}{I_z} & -\frac{b}{I_z} \left(\frac{\partial F_{yR}}{\partial \xi_R} \right) \Big|_{\alpha_R^{eq}, F_{xR}^{eq}} \left(\frac{F_{xR}}{\mu F_{zR} \sqrt{(\mu F_{zR})^2 - F_{xR}^2}} \right) \\ -\frac{1}{m} \left(\sin\delta^{eq} + \frac{F_{yF}^{eq}}{\tilde{C}_{\alpha_F}} \cos\delta^{eq} \right) & \frac{1}{m} \end{bmatrix} \quad (4.11)$$

The subsections that follow examine this input matrix for linearizations around three

types of equilibrium conditions: straight-ahead driving, typical cornering equilibria, and drift equilibria. In particular, they examine the evolution of the b_{12} , b_{22} , and b_{31} entries of Equation 4.11 across this range of equilibrium conditions.

4.1.1 Straight-ahead driving

When the vehicle is driving straight-ahead in steady-state, $\beta^{eq} = r^{eq} = 0$, $\delta^{eq} = 0$, and $F_{yF}^{eq} = F_{yR}^{eq} = F_{xR}^{eq} = 0$. Since the lateral states and steer angle are zero, it is also the case that $\alpha_F^{eq} = \alpha_R^{eq} = 0$.

Since the rear tire slip angle and the rear drive force are both zero for the straight-ahead equilibrium, the rear tire is obviously nowhere near saturation. Consequently, the partial derivative $\partial F_{yR}/\partial \xi_R$ is computed using the unsaturated region of the rear lateral force curve:

$$\frac{\partial F_{yR}}{\partial \xi_R} = -\frac{C_{\alpha R}^2}{3\xi_R^2 \mu F_{zR}} |\tan \alpha_R| \tan \alpha_R + \frac{2C_{\alpha R}^3}{27\xi_R^3 \mu^2 F_{zR}^2} \tan^3 \alpha_R \quad (4.12)$$

Using Equation 4.4, this leads to the following expression for $\partial F_{yR}/\partial F_{xR}$:

$$\frac{\partial F_{yR}}{\partial F_{xR}} = \left[\frac{2F_{xR}}{\mu F_{zR} \sqrt{(\mu F_{zR})^2 - F_{xR}^2}} \right] \left[\frac{C_{\alpha R}^2}{3\xi_R^2 \mu F_{zR}} |\tan \alpha_R| \tan \alpha_R - \frac{2C_{\alpha R}^3}{27\xi_R^3 \mu^2 F_{zR}^2} \tan^3 \alpha_R \right] \quad (4.13)$$

Since $\alpha_R^{eq} = 0$ and $F_{xR}^{eq} = 0$ in this case, $\partial F_{yR}/\partial F_{xR} = 0$ at the straight-ahead equilibrium condition. Therefore, from Equation 4.3, $b_{12} = b_{22} = 0$ and perturbations in the rear drive force have no direct influence upon the lateral dynamics in this case.

Along similar lines, Equation 4.10 simplifies to $b_{31} = 0$ for straight-ahead driving because $F_{yF}^{eq} = 0$ and $\delta^{eq} = 0$. Thus, the B matrix for the straight-ahead equilibrium condition is as follows, shown both in symbolic form and evaluated using P1 parameters and $U_x^{eq} = 8$ m/s:

$$B = \begin{bmatrix} \frac{1}{mU_x^{eq}} & 0 \\ \frac{a}{I_z} & 0 \\ 0 & \frac{1}{m} \end{bmatrix} = \begin{bmatrix} 7.3 * 10^{-5} & 0 \\ 1 * 10^{-3} & 0 \\ 0 & 5.8 * 10^{-4} \end{bmatrix} \quad (4.14)$$

Equation 4.14 indicates that the direct influence of the steering and rear drive force inputs upon the states are decoupled for perturbations around straight-ahead driving, in the sense that δF_{yF} only has a direct influence upon the lateral dynamics of the model and δF_{xR} only has a direct influence upon the longitudinal dynamics. This means that both the steering and drive force inputs are necessary to directly control the states of the vehicle around the equilibrium condition, and they are used in the manner that an average driver would expect: steering to control cornering of the vehicle (lateral dynamics) and rear drive force to control its speed (longitudinal dynamics).

4.1.2 Typical cornering

At typical cornering equilibria, where the vehicle operates in steady state with unsaturated tires, the input matrix B becomes more complicated because b_{12} , b_{22} , and b_{31} no longer evaluate to trivial expressions as they did in the preceding section. The matrix entries b_{12} and b_{22} , which are also expressed in terms of Equation 4.13 for this set of equilibria, are no longer zero because the equilibrium rear slip angle and drive force are non-zero. Along similar lines, $b_{31} \neq 0$ because the front lateral force and steer angle are also non-zero for this class of equilibria.

With this in mind, this section explores the evolution of these matrix entries with increasing equilibrium lateral acceleration a_y^{eq} for a representative set of typical cornering equilibria at which $U_x^{eq} = 8$ m/s. Figure 4.1 plots the values of b_{12} , b_{22} , and b_{31} for typical cornering equilibria from Chapter 3 (denoted by asterisks (*) in Figures 3.10 through 3.14) as a function of a_y^{eq} normalized by μg , the maximum achievable steady-state lateral acceleration.

Up to 40% of the steady-state acceleration limit, the input matrix for typical cornering does not change significantly from the input matrix for straight-ahead driving as given in Equation 4.14. Consider the input matrix when $a_y^{eq} = 0.4\mu g$, shown below:

$$B = \begin{bmatrix} 7.3 * 10^{-5} & -5.2 * 10^{-8} \\ 1 * 10^{-3} & 6.4 * 10^{-7} \\ -6.2 * 10^{-5} & 6 * 10^{-4} \end{bmatrix} \quad (4.15)$$

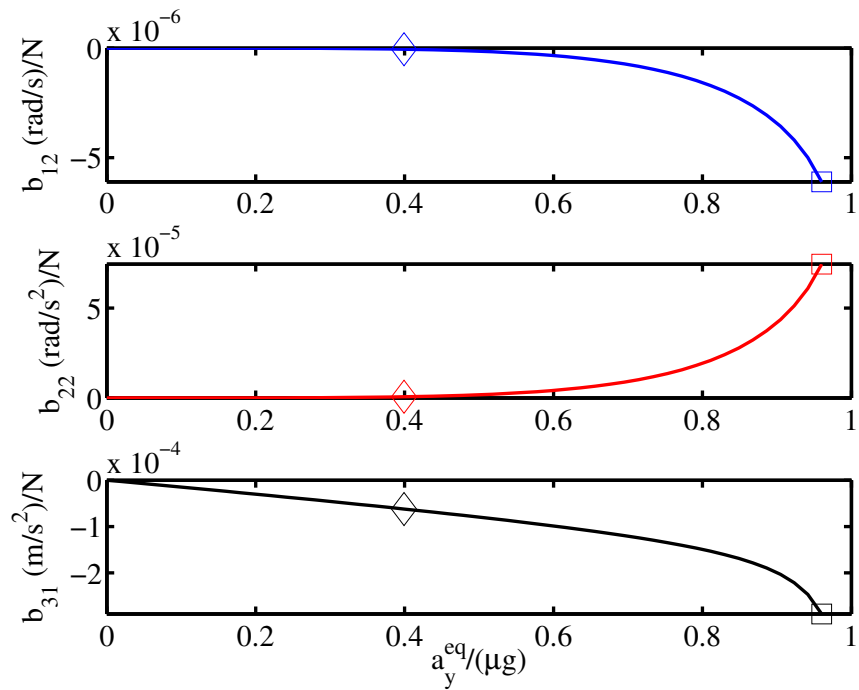


Figure 4.1: b_{12} (top), b_{22} (center), and b_{31} (bottom) versus $a_y^{eq}/(\mu g)$ for typical cornering at $U_x^{eq} = 8$ m/s, as computed using typical cornering equilibria from Chapter 3. The points marked by diamonds (\diamond) and squares (\square) denote the values of b_{12} , b_{22} , and b_{31} at 40% and 96% of the steady-state lateral acceleration limit, respectively.

In Equation 4.15, b_{12} and b_{22} are negligibly small relative to the analogous entries for front lateral force perturbations (b_{11} and b_{21} , respectively). This is consistent with the top two plots in Figure 4.1, which indicate that b_{12} and b_{22} are nearly zero when $a_y^{eq} \leq 0.4\mu g$, meaning that rear drive force perturbations essentially have no direct influence upon the lateral dynamics in this acceleration range. While $|b_{31}|$ (bottom panel of Figure 4.1) increases steadily in the 0-40% acceleration range, Equation 4.15 indicates that it is still an order of magnitude smaller than the corresponding matrix entry for drive force perturbations (b_{32}) when $a_y^{eq} = 0.4\mu g$. Physically, this means that front lateral force perturbations have a minimal direct effect upon the longitudinal dynamics when $a_y^{eq} \leq 0.4\mu g$. Practically speaking, the direct effect of the steering and drive force inputs is still effectively decoupled for typical cornering in the 0-40% acceleration range, with steering used to directly control the lateral dynamics and rear drive force used to directly control the longitudinal dynamics. Once again, this matches the intuition of the average driver, which makes sense, considering that average drivers usually corner at low to moderate lateral accelerations.

Physically speaking, b_{12} and b_{22} are nearly zero in the 0-40% range because F_{xR}^{eq} and F_{yR}^{eq} are small at these equilibria, meaning that the total tire force F_R^{eq} lies well within the boundary of the rear tire friction circle. Consequently, the rear lateral and longitudinal forces are only weakly coupled, which translates to a minimal ability to directly influence the lateral dynamics through rear drive force perturbations. Similarly, $|b_{31}|$ is relatively small because F_{yF}^{eq} and δ^{eq} are not especially large for steady cornering in this acceleration range.

For typical cornering at equilibrium accelerations above 40% of the steady-state limit, however, the input matrix begins to undergo a transformation. As $|b_{31}|$ continues to increase steadily, $|b_{12}|$ and $|b_{22}|$ increase precipitously, especially above $a_y^{eq} = 0.6\mu g$. The observed trend in b_{31} arises because F_{yF}^{eq} and δ^{eq} must both increase in order to sustain typical cornering at higher lateral acceleration. For the same reason, F_{yR}^{eq} must increase as well; this has the effect of bringing the total rear force F_R^{eq} closer to saturation and the boundary of the friction circle, which in turn considerably increases coupling of the rear longitudinal and lateral forces. This increase in coupling translates to an enhanced ability to directly influence the lateral

dynamics through rear drive force perturbations, as manifested by the increases in $|b_{12}|$ and $|b_{22}|$.

At $a_y^{eq} = 0.96\mu g$, the input matrix has changed considerably from the input matrix for $a_y^{eq} = 0.4\mu g$ (Equation 4.15):

$$B = \begin{bmatrix} 7.3 * 10^{-5} & -6.1 * 10^{-6} \\ 1 * 10^{-3} & 7.4 * 10^{-5} \\ -2.9 * 10^{-4} & 5.8 * 10^{-4} \end{bmatrix} \quad (4.16)$$

Equation 4.16 indicates that b_{12} and b_{22} are two orders of magnitude larger than they are for typical cornering at 40% of the steady-state acceleration limit, while b_{31} is one order of magnitude larger. Consequently, the direct effect of the steering and rear drive force inputs is no longer decoupled for typical cornering near the steady-state acceleration limit. At $a_y^{eq} = 0.96\mu g$, steering has a non-negligible direct influence upon the longitudinal dynamics and rear drive force has a non-negligible direct influence upon the lateral dynamics. Since racing routinely involves typical cornering at the limits of handling (especially on paved surfaces), the coupling evident in Equation 4.16 factors into vehicle control in competitive driving. When describing their technique, racecar drivers frequently make reference to “steering with the throttle,” reflecting their understanding of the altered capabilities of the inputs at the limits of handling.

The rear drive force input has a non-negligible direct influence upon the lateral dynamics during typical cornering at high-lateral acceleration because the rear tire approaches saturation under these conditions. This suggests that complete rear tire saturation could allow the rear drive force to have even more direct control authority over the lateral dynamics. This possibility is explored below by examining the input matrix for the linearized model around drift equilibria.

4.1.3 Drift equilibria

At drift equilibria, the entries b_{12} and b_{22} in the input matrix are given by considerably different expressions because the rear tire is saturated. From these expressions, it is easy to demonstrate that the rear drive force has significant direct control authority

over the lateral dynamics of the vehicle around drift equilibria, especially at higher sideslip drift equilibria.

When the rear tire is saturated, the partial derivative $\partial F_{yR}/\partial \xi_R$ is computed using the saturated portion of the rear lateral force curve:

$$\frac{\partial F_{yR}}{\partial \xi_R} = \mu F_{zR} \quad (4.17)$$

This results in the following expression for $\partial F_{yR}/\partial F_{xR}$ that is quite different (and simpler) than the one in Equation 4.13 for an unsaturated rear tire:

$$\frac{\partial F_{yR}}{\partial F_{xR}} = -\frac{F_{xR}}{\sqrt{(\mu F_{zR})^2 - F_{xR}^2}} \quad (4.18)$$

Equation 4.18 can be further simplified by taking advantage of the fact that the rear lateral and longitudinal forces are coupled via the friction circle when the rear tire is saturated:

$$\sqrt{F_{xR}^2 + F_{yR}^2} = \mu F_{zR}. \quad (4.19)$$

By inspection, the denominator of the right-hand side of Equation 4.18 is simply Equation 4.19 solved for $|F_{yR}|$:

$$\frac{\partial F_{yR}}{\partial F_{xR}} = -\frac{F_{xR}}{|F_{yR}|}. \quad (4.20)$$

Using Equation 4.20 to compute expressions for b_{12} and b_{22} from Equation 4.3, the input matrix around drift equilibria is as follows:

$$B = \begin{bmatrix} \frac{1}{mU_x^{eq}} & -\frac{1}{mU_x^{eq}} \left(\frac{F_{xR}^{eq}}{|F_{yR}^{eq}|} \right) \\ \frac{a}{I_z} & \frac{b}{I_z} \left(\frac{F_{xR}^{eq}}{|F_{yR}^{eq}|} \right) \\ -\frac{1}{m} \left(\sin \delta^{eq} + \frac{F_{yF}^{eq}}{C_{\alpha_F}} \cos \delta^{eq} \right) & \frac{1}{m} \end{bmatrix}. \quad (4.21)$$

When comparing equilibria at a given longitudinal velocity U_x^{eq} , Equation 4.21 indicates that the ratio $F_{xR}^{eq}/|F_{yR}^{eq}|$ dictates the magnitudes of b_{12} and b_{22} at drift equilibria. Since Chapter 3 established that F_{xR}^{eq} is large at drift equilibria, b_{12} and

b_{22} are of non-negligible magnitude at all drift equilibria. Amongst drift equilibria, however, the magnitude of the ratio $F_{xR}^{eq}/|F_{yR}^{eq}|$ increases with the magnitude of the equilibrium sideslip β^{eq} .

In order to see why, consider examples of drift equilibria from Chapter 3, denoted by a triangle (\triangle) in Figures 3.10 through 3.14. As $|\beta^{eq}|$ gets larger, F_{xR}^{eq} gets larger as well; in order for the rear tire to satisfy the friction circle constraint, this increase in F_{xR}^{eq} requires that F_{yR}^{eq} decreases as $|\beta^{eq}|$ increases. Consequently, the ratio $F_{xR}^{eq}/|F_{yR}^{eq}|$ increases monotonically with $|\beta^{eq}|$, reaching its largest values at drift equilibria where $|\beta^{eq}|$ is large.

As a result, the magnitudes of b_{12} and b_{22} are considerably larger for drift equilibria at high sideslip than they are for typical cornering equilibria at the same longitudinal velocity, even for typical cornering near the limits of handling. As an example, consider the input matrix for a drift equilibrium at which $U_x^{eq} = 8$ m/s and $\beta^{eq} \approx 20^\circ$:

$$B = \begin{bmatrix} 7.3 * 10^{-5} & -3.7 * 10^{-5} \\ 1 * 10^{-3} & 4.5 * 10^{-4} \\ -4.3 * 10^{-5} & 5.8 * 10^{-4} \end{bmatrix} \quad (4.22)$$

The values for b_{12} and b_{22} in the input matrix for this drift equilibrium are an order of magnitude larger than b_{12} and b_{22} in the input matrix for typical cornering at $U_x^{eq} = 8$ m/s and 96% of the steady-state lateral acceleration limit (Equation 4.16).

Furthermore, Equation 4.22 indicates that b_{12} and b_{22} for this drift equilibrium are comparable in magnitude to the analogous entries for front lateral force perturbations (b_{11} and b_{12} , respectively). In physical terms, this means that rear drive force perturbations have a comparable direct influence upon the lateral dynamics of the vehicle around this drift equilibrium. To put it simply, there are actually two effective inputs for lateral control in a neighborhood of the equilibrium.

Based on this result, drift equilibria can be characterized in terms of a tradeoff of stability for enhanced controllability: the rear tire saturation inherent to a drift makes drift equilibria open-loop unstable but also enables direct lateral control through the rear drive force, particularly at high sideslip drift equilibria. For a skilled driver capable of controlling a vehicle with saturated rear tires, this obviously incentivizes

operation around a drift equilibrium, especially on surfaces where friction is uncertain and added control flexibility can prove invaluable.

The ability to directly control the lateral dynamics through front steering as well as the rear drive force input expands the design space for a drift controller, as it opens up new possibilities for control strategy and structure. However, in order to design an effective drift controller, it is not sufficient to simply establish that these two inputs *can* directly control the lateral dynamics around a drift equilibrium. It is necessary to develop physical intuition for *how* these inputs should be used for this task, which is the subject of the next section.

4.2 Understanding the role of steering and rear drive force inputs in drifting

The control objective at the heart of this dissertation is ostensibly simple: design a controller to stabilize a desired drift equilibrium in order to enable sustained, robust operation of the vehicle at that equilibrium condition. Theoretically speaking, this should be achievable using a single input regulator design.

Such a regulator could use either the steering or rear drive force input, provided that each input can stabilize the unstable modes of the dynamics around the desired drift equilibrium on its own. In mathematical terms, a sufficient (but not necessary) condition for this to be true is that the controllability matrix for each input (as computed from the linearized dynamics around the desired equilibrium) is full rank:

$$\mathcal{C}_{F_{yF}} = \begin{bmatrix} B_{F_{yF}} & AB_{F_{yF}} & A^2B_{F_{yF}} \end{bmatrix} \quad (4.23a)$$

$$\mathcal{C}_{F_{xR}} = \begin{bmatrix} B_{F_{xR}} & AB_{F_{xR}} & A^2B_{F_{xR}} \end{bmatrix}, \quad (4.23b)$$

where $\mathcal{C}_{F_{yF}}$ is the controllability matrix for the front lateral force perturbations, $\mathcal{C}_{F_{xR}}$ is the controllability matrix for the rear drive force perturbations, and $B_{F_{yF}}$ and $B_{F_{xR}}$ are the columns of the input matrix corresponding to each input.

In the case of the drift equilibrium considered in Section 4.1.3, $\mathcal{C}_{F_{yF}}$ and $\mathcal{C}_{F_{xR}}$ are

as follows:

$$\mathcal{C}_{F_{yF}} = 10^{-3} * \begin{bmatrix} 0.072 & -1.04 & 0.24 \\ 1.04 & 0 & 0 \\ 0.042 & -3.16 & -2.16 \end{bmatrix} \quad (4.24a)$$

$$\mathcal{C}_{F_{xR}} = 10^{-3} * \begin{bmatrix} -0.037 & -0.50 & 0.13 \\ 0.45 & 0 & 0 \\ 0.58 & -1.67 & -1.00 \end{bmatrix} \quad (4.24b)$$

By inspection of Equation 4.24, the first column of both controllability matrices is linearly independent from the other two columns. Furthermore, the second and third columns of both matrices cannot be linearly dependent because their top ((1,2) and (1,3)) entries have opposite sign while their bottom ((3,2) and (3,3)) entries have the same sign. Therefore, both controllability matrices are full rank and it is possible to regulate the vehicle state in a neighborhood of this equilibrium using front lateral force or rear drive force perturbations alone.

Unfortunately, both of the inputs have characteristics that make a single-input regulator design using either input a poor choice from either a robustness or performance standpoint. This section presents two illustrative control designs that provide insight into why this is the case.

Section 4.2.1 examines a pure steering-based controller for the lateral dynamics around a drift equilibrium developed by the author in collaboration with Voser et al. in [40]. The experimental performance of this controller demonstrates that control authority via front lateral force is severely limited by front tire saturation, and that this saturation leads to major controller robustness issues.

Section 4.2.2 examines simulations of a simple drive-force based regulator. While these simulations establish that such a regulator is entirely plausible, it is not ideal as far as closed-loop performance is concerned. A fundamental conflict between lateral and longitudinal control objectives when using the rear drive force for regulation results in closed-loop trajectories that converge to the desired equilibrium in an indirect, circuitous fashion.

4.2.1 A steering-based controller for drifting

The steering-based controller in [40] is designed using a two-state bicycle model with lateral velocity U_y and yaw rate r as its states. The controller computes perturbations $\delta\delta$ from an equilibrium steer angle δ^{eq} based upon feedback of perturbations δU_y and δr in lateral velocity and yaw rate from their desired equilibrium values:

$$\delta\delta = -K_{U_y}\delta U_y - K_r\delta r \quad (4.25)$$

The controller gains K_{U_y} and K_r are chosen by linearizing the two-state model around a desired drift equilibrium and using pole placement to determine gains that locally stabilize the equilibrium.

Since this two-state model does not include longitudinal dynamics, the controller uses rear drive force input for a simple cruise control that operates in parallel with the steering-based drift controller. This cruise control uses proportional feedback of longitudinal velocity perturbations δU_x to compute a rear drive force input:

$$F_{xR} = -K_{U_x}\delta U_x \quad (4.26)$$

Figures 4.2 and 4.3 give experimental results obtained from implementation of this controller on the P1 testbed. The desired drift equilibrium and controller gains for the test are given in Table 4.1. Additional details on gain selection and experimental implementation can be found in [40].

The controller provides intermittent stabilization to the desired equilibrium condition, as indicated in the top two plots of Figure 4.2 by convergence of the vehicle sideslip angle and yaw rate to the desired equilibrium values indicated by black dashed lines. However, friction disturbances induce large deviations in the lateral states from their equilibrium values on multiple occasions, most notably at $t \approx 18$ s and $t \approx 32$ s. As indicated in the top plot of Figure 4.3, the controller responds to these disturbances by breaking out of countersteer and steering heavily into the turn in an attempt to increase the front tire lateral force. In both cases, this response is sufficient to eventually drive the states back to their equilibrium values.

Parameter	Value
δ^{eq}	-15°
U_y^{eq}	-4.2 m/s
β^{eq}	-27.7°
r^{eq}	0.613 rad/s
U_x^{eq}	8 m/s
K_{U_y}	-0.2 rad/(m/s)
K_r	0.5 s

Table 4.1: Target equilibrium and gains for implementation of the steering-based drift controller.

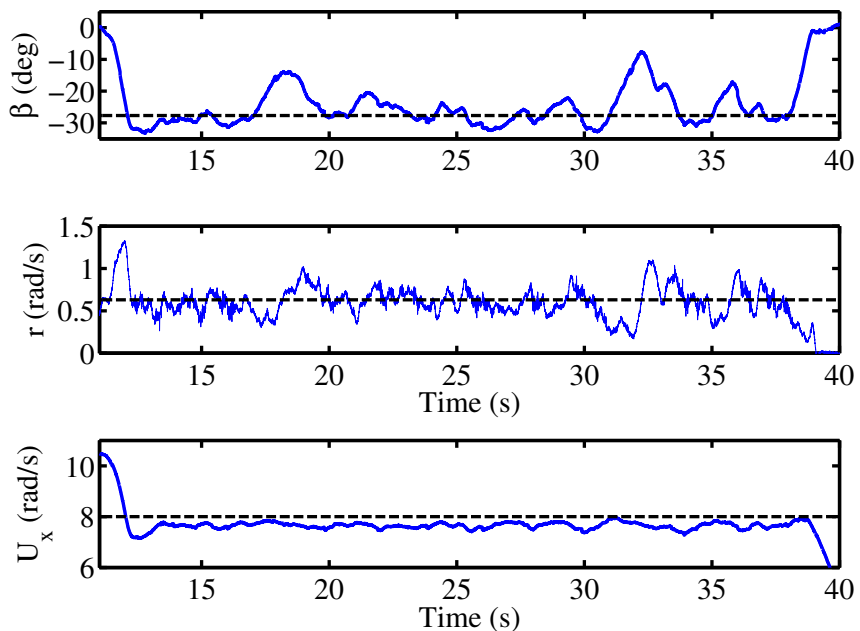


Figure 4.2: Sideslip angle (top), yaw rate (middle), and longitudinal velocity (bottom) for an experimental run with the steering-based drift controller.

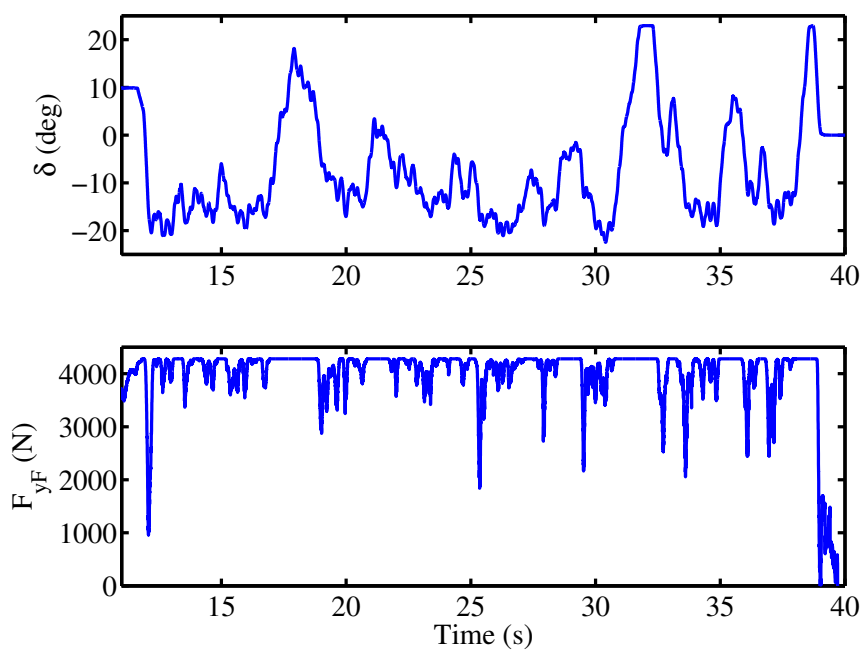


Figure 4.3: Steer angle (top) and front lateral force (bottom) for an experimental run of the steering-based drift controller.

When a large drop in yaw rate and sideslip magnitude occurs at $t \approx 39$ s, however, this is not the case. The controller once again breaks out of countersteer and steers heavily into the turn in an attempt to recover, but the vehicle exits from the drift and transitions to cornering in a conventional fashion.

The large state deviations at $t \approx 18$ s and $t \approx 32$ s and the uncontrolled exit from the drift at $t \approx 39$ s are all attributable to one cause: limited control authority through the front lateral force input. It was demonstrated in Chapter 3 with both the two-state and three-state bicycle models that the front lateral force at drift equilibria is nearly saturated. In practice, this means that control authority through the front lateral force input is essentially unidirectional. When operating around a drift equilibrium, a controller using steering or front lateral force as its input can easily decrease lateral force, but has a very limited ability to increase front lateral force. This is a hard constraint of the steering actuator when drifting, regardless of the particulars of the control design.

In practical terms, this means that a steering-based controller can effectively provide stabilization to the desired equilibrium from locations in the state space where the vehicle is in danger of spinning out because its yaw rate and sideslip magnitude are too large ($\delta r > 0$ and $\delta\beta < 0$ for a left-hand drift equilibrium). This is because the controller can respond in this scenario by increasing countersteer to decrease lateral force.

Conversely, the controller is relatively ineffective for providing stabilization to the desired equilibrium from regions of the state space where the vehicle is in danger of exiting the drift because its yaw rate has dropped and its sideslip magnitude is too shallow ($\delta r < 0$ and $\delta\beta > 0$ for a left-hand drift equilibrium). By steering into the turn in this scenario, the controller generates only a modest increase in the front lateral force before it rapidly saturates, indicated in the bottom plot of Figure 4.3 by several regions where F_{yF} flattens out at its friction limit. At best, this force limitation results in large state deviations before an eventual return to the equilibrium. In the worst case, it results in an unrecoverable exit from the drift.

Parameter	Value
δ^{eq}	-12°
F_{xR}^{eq}	2293 N
β^{eq}	-20.44°
r^{eq}	0.6 rad/s
U_x^{eq}	8 m/s
K_β	-3060 rad/(m/s)
K_r	6717.4 N/(rad/s)
K_{U_x}	-602.5 N/(m/s)

Table 4.2: Target equilibrium and gains for implementation of the drive force-based regulator

4.2.2 Regulation using rear drive force

The drive force-based regulator considered here computes a rear drive force perturbation δF_{xR} based upon full-state feedback of the state perturbations from their equilibrium values while the front lateral force is held at its equilibrium value:

$$\delta F_{xR} = -K_\beta \delta \beta - K_r \delta r - K_{U_x} \delta U_x \quad (4.27a)$$

$$\delta F_{yF} = 0 \quad (4.27b)$$

The controller gains K_β , K_r , and K_{U_x} are chosen using pole placement based upon a linearization of the model around a desired drift equilibrium. While the controller is designed using a linearized model, however, it is simulated using the full nonlinear dynamics of the three-state model in this analysis.

The results presented here have been generated using the desired drift equilibrium given in Table 4.2. Note that this is the same equilibrium for which the controllability matrix $\mathcal{C}_{F_{xR}}$ was computed at the beginning of this section (Equation 4.24b) and used to verify that the vehicle is locally controllable around this equilibrium using rear drive force perturbations alone. The controller gains used in simulation, given in Table 4.2, locally stabilize the desired drift equilibrium by placing the closed-loop poles of the equilibrium at -1 and $-1 \pm 0.5i$.

The simulation results are divided into two groups. The first group represents

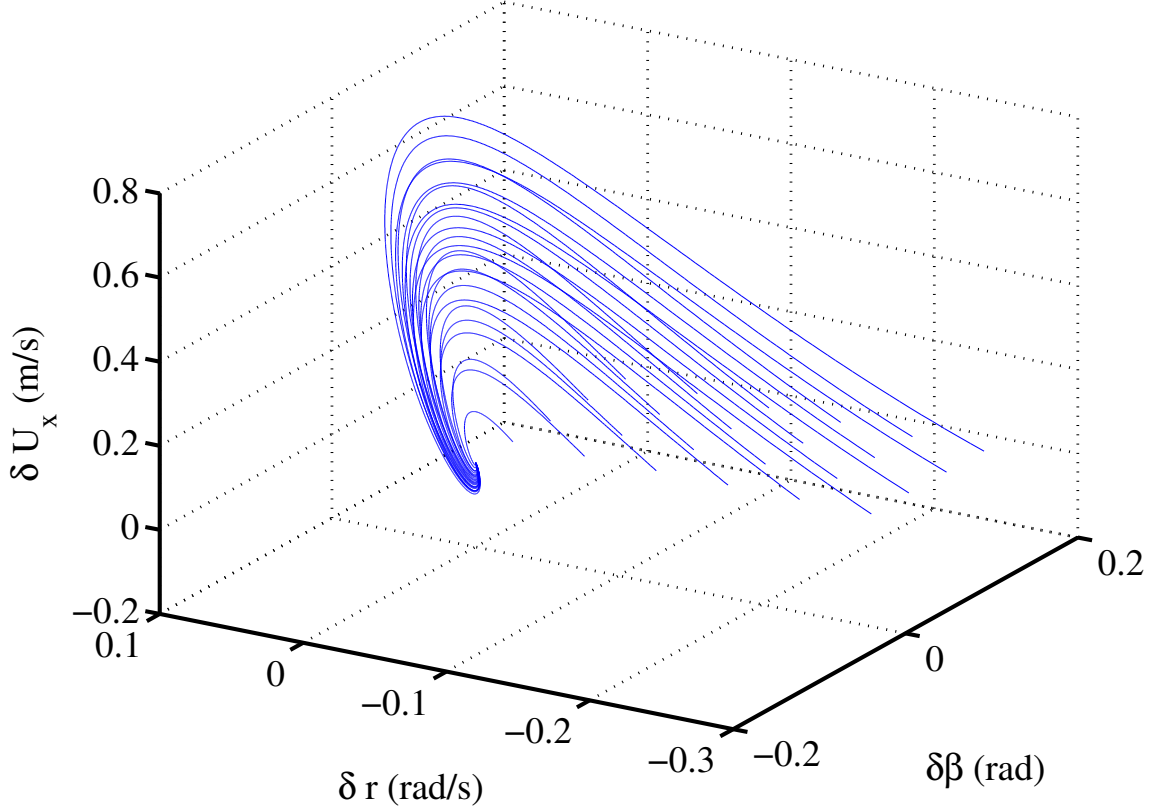


Figure 4.4: Phase portrait of state trajectories from initial conditions where $\delta\beta_0 > 0$, $\delta r_0 < 0$, and $\delta U_{x0} = 0$ for the drive force-based regulator.

simulation from initial conditions at which the vehicle is initially operating at the equilibrium longitudinal velocity but in danger of exiting from the drift. At these initial conditions, the vehicle sideslip angle is too shallow and the yaw rate is too low; for a left-hand drift equilibrium, this corresponds to $\delta\beta_0 > 0$, $\delta r_0 < 0$, and $\delta U_{x0} = 0$. Figure 4.4 gives a phase portrait of state trajectories originating from this region of the state space. Figures 4.5 and 4.6 plot δU_x , δF_{xR} , $\delta\beta$, and δr versus time for these trajectories.

The state trajectories in Figure 4.4 indicate that the controller successfully provides stabilization to the desired equilibrium (the origin in perturbation coordinates) when the vehicle is in danger of exiting from the drift. However, the path of these trajectories through the state space also highlights the fact that regulation of the

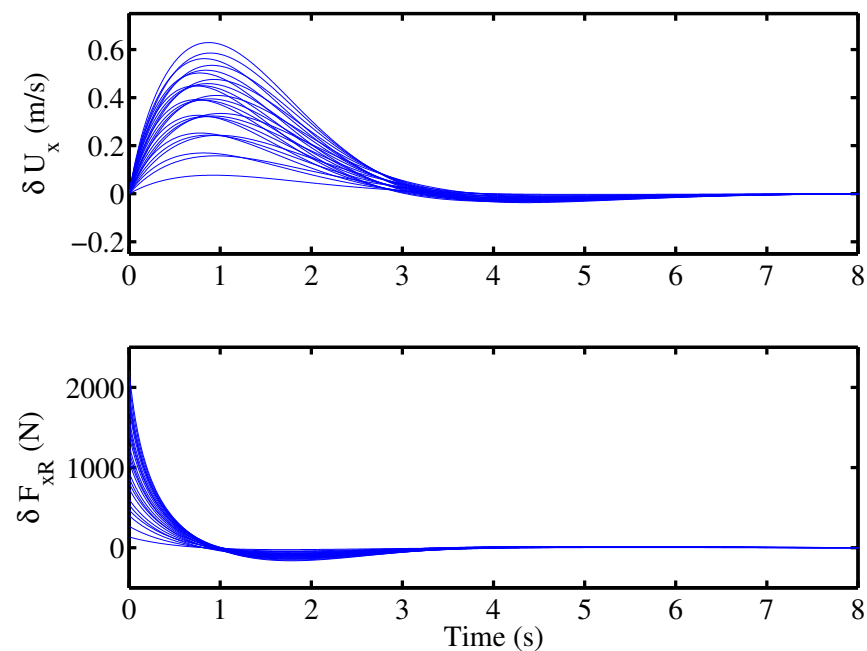


Figure 4.5: δU_x and δF_{xR} versus time for initial conditions where $\delta\beta_0 > 0$, $\delta r_0 < 0$, and $\delta U_{x0} = 0$ when using the drive force-based regulator.

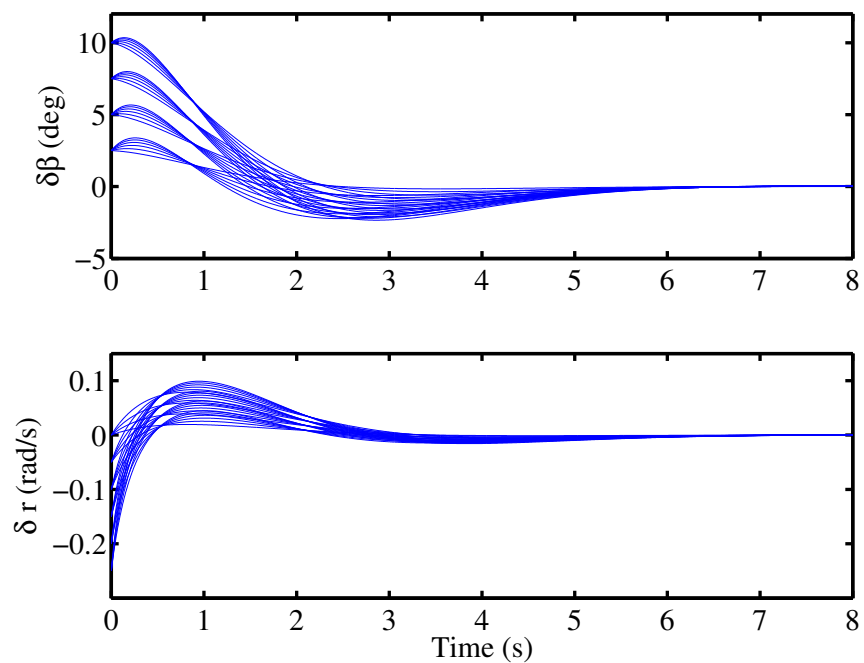


Figure 4.6: $\delta\beta$ and δr versus time for initial conditions where $\delta\beta_0 > 0$, $\delta r_0 < 0$, and $\delta U_{x0} = 0$ when using the drive force-based regulator.

lateral and longitudinal dynamics of the vehicle can be at odds with one another when using this input. Even though $\delta U_{x0} = 0$ for all the initial conditions considered, the longitudinal velocity error is driven upward along these trajectories before they eventually converge to the desired equilibrium.

Figure 4.5 indicates that this happens because the rear drive force commanded by the controller is initially rather large and positive. From a physical standpoint, this is because an increase in the rear drive force acts via the friction circle to decrease the rear lateral force, thereby increasing the yaw moment acting on the vehicle. This positive yaw moment causes the rapid increase in yaw rate evident in the bottom plot of Figure 4.6. The buildup of yaw rate subsequently acts through the sideslip dynamics to increase the sideslip magnitude, as indicated by the decrease in $\delta\beta$ towards zero in the bottom plot of Figure 4.6.

The second group of initial conditions considered in the simulation results represents the region of the state space where the vehicle is initially operating at the equilibrium longitudinal velocity but in danger of spinning out. In this region, both the vehicle's sideslip angle and yaw rate are too large; for a left-hand drift equilibrium, this corresponds to $\delta\beta_0 < 0$, $\delta r_0 < 0$, and $\delta U_{x0} = 0$. Figure 4.7 gives the phase portrait of state trajectories originating from this region, while Figures 4.8 and 4.9 plot δU_x , δF_{xR} , $\delta\beta$, and δr versus time for these trajectories.

Once again, the controller successfully provides stabilization to the desired equilibrium from all of the initial conditions considered, but there is still pronounced conflict between the lateral and longitudinal regulation objectives. All of the state trajectories in the phase portrait exhibit a fairly dramatic drop in δU_x from $\delta U_{x0} = 0$ as part of a rather circuitous path to the equilibrium through the state space.

Based on Figure 4.8, this behavior results from the controller initially commanding large reductions in the rear drive force ($\delta F_{xR} < 0$) in a region of the state space where the decelerative effect of $rU_x\beta$ term in the longitudinal dynamics is already significant. However, this drive force reduction is essential to regulation of the lateral dynamics; it acts through the friction circle to increase the rear lateral force, thereby reducing the yaw moment initially acting on the vehicle. The rapid drop in yaw rate that occurs as a result (top plot of Figure 4.9) then acts through the sideslip dynamics to

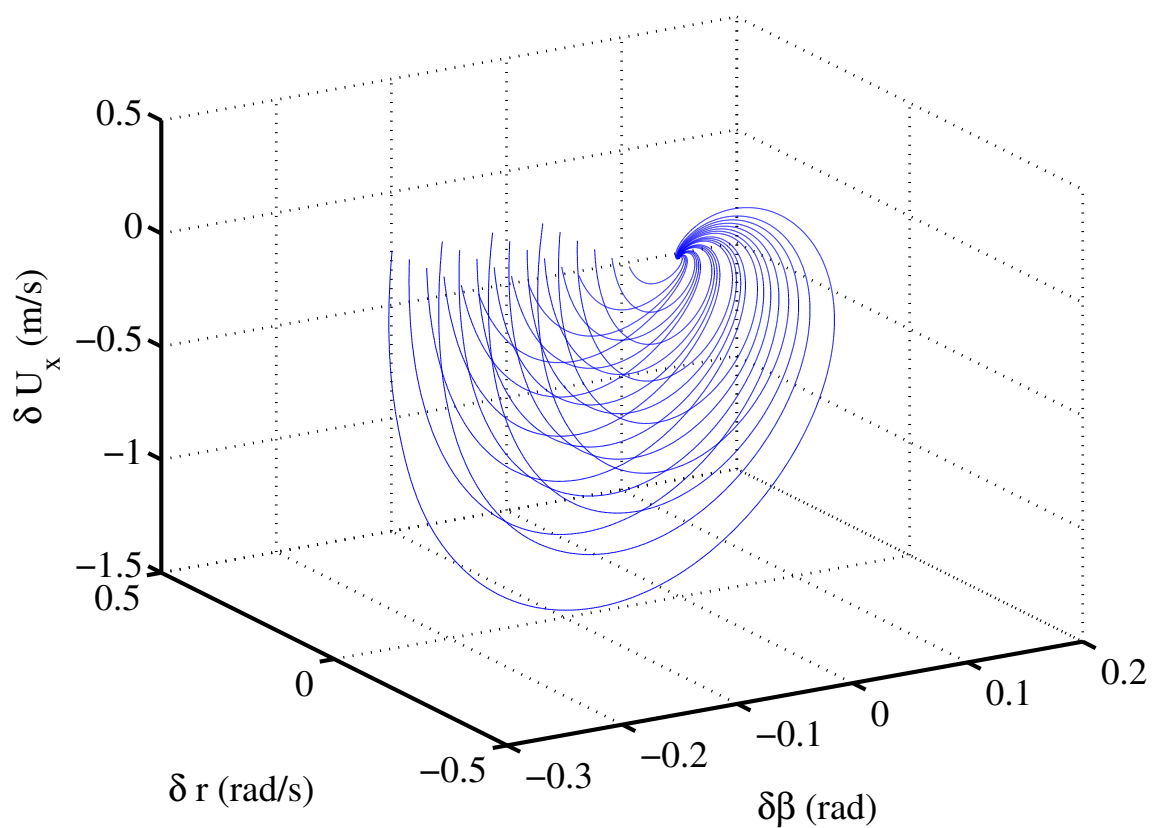


Figure 4.7: Phase portrait of state trajectories from initial conditions where $\delta\beta_0 < 0$, $\delta r_0 > 0$, and $\delta U_{x0} = 0$ for the drive force-based regulator.

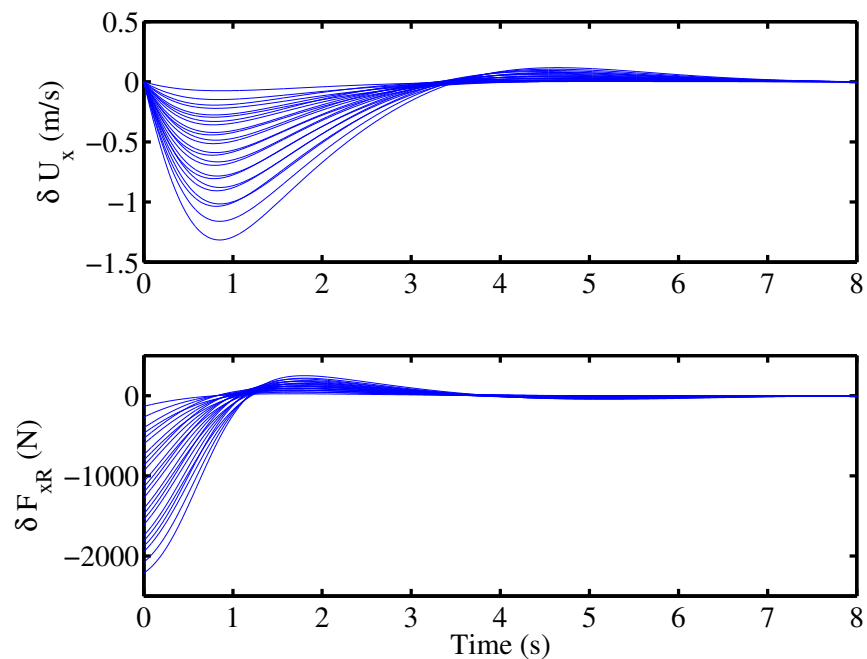


Figure 4.8: δU_x and δF_{xR} versus time for initial conditions where $\delta\beta_0 < 0$, $\delta r_0 > 0$, and $\delta U_{x0} = 0$ when using the drive force-based regulator.

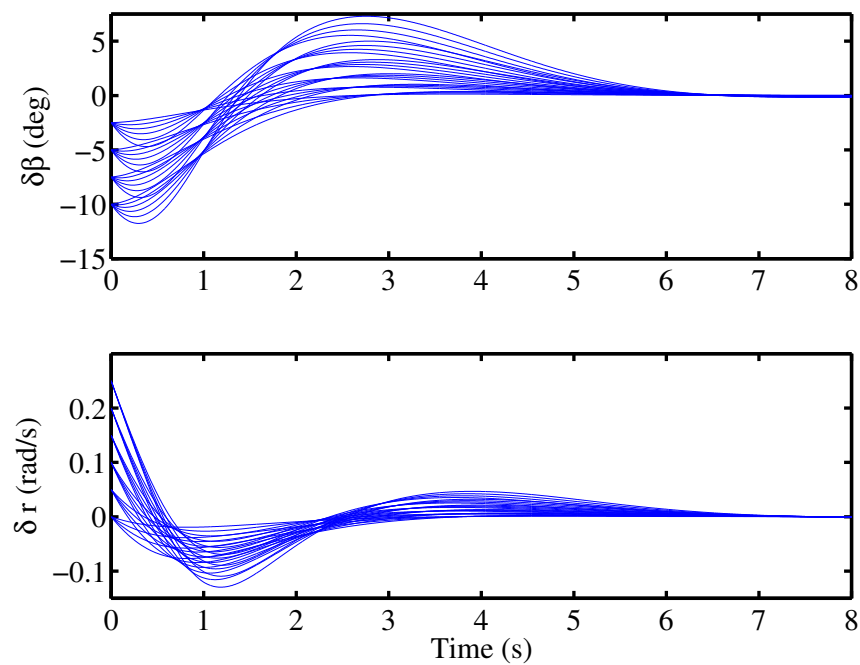


Figure 4.9: $\delta\beta$ and δr versus time for initial conditions where $\delta\beta_0 < 0$, $\delta r_0 > 0$, and $\delta U_{x0} = 0$ when using the drive force-based regulator.

decrease sideslip magnitude, as evidenced by the initial increase in $\delta\beta$ towards zero in the bottom plot of Figure 4.9.

The phase portraits for both sets of initial conditions indicate that a drive force-based regulator can successfully stabilize a drift equilibrium. But they also indicate that the closed-loop state trajectories take an indirect path to the equilibrium through the state space in which the magnitude of the longitudinal velocity error increases considerably at first before eventually converging back towards to zero. This behavior arises because of a fundamental incompatibility between lateral and longitudinal control objectives when using the rear drive force input. To put it simply, stabilization of the lateral dynamics requires rear drive force commands that will initially induce longitudinal velocity errors.

4.2.3 A roadmap for coordinating steering and rear drive force inputs

The case study in Section 4.2.1 established that control authority through front steering is essentially unidirectional because the front tire is already nearly saturated at drift equilibria. Section 4.2.2 demonstrated that modulation of the rear drive force can stabilize a vehicle to a drift equilibrium, but with performance tradeoffs that result from using this input for lateral control. Obviously, it makes sense to coordinate these two inputs in a fashion that addresses the limited control authority of the steering input while avoiding usage of the rear drive force input for lateral control where possible.

A simple, physically intuitive approach for coordinating the inputs that achieves these objectives is as follows:

1. **When control authority is available through steering ($|F_{yF}| < \mu F_{zF}$):**
Use the front lateral force input for lateral control and the rear drive force input for longitudinal control.
2. **When control authority through steering is friction-limited ($|F_{yF}| = \mu F_{zF}$):** Use the drive force input for lateral control in order to return to regions of state space where lateral control authority through front lateral force

is regained.

As it turns out, these two modes of operation correspond to the two scenarios considered in the controller case studies. The first mode reflects how the inputs should be used to control the yaw moment acting on the vehicle at initial conditions where the vehicle is in danger of spinning. The second mode reflects how the inputs should be used at initial conditions where the vehicle is in danger of exiting from the drift and into typical cornering.

When the vehicle is in danger of spinning, the control authority necessary to stabilize the vehicle is available through steering. The reduction in yaw moment needed to prevent the spin is easily achievable by a reduction in front lateral force (and away from saturation) through increased countersteer. This leaves the rear drive force input available to control the longitudinal dynamics of the vehicle, which includes counteracting the effect of front lateral force variations upon these dynamics.

When the vehicle is in danger of exiting the drift, however, a limited ability to increase front lateral force before the front tire saturates severely restricts lateral control authority through steering. This is because saturation of the front tire lateral force limits the ability to increase the yaw moment acting on the vehicle through steering. In this case, it is necessary to utilize the rear drive force input for lateral control, in spite of the effect this will have upon the longitudinal velocity of the vehicle. In particular, an increase in rear drive force can be used to decrease the rear lateral force, thereby increasing the yaw moment acting on the vehicle.

The coordination scheme described above directly reflects the stability-controllability tradeoff that is characteristic of drift equilibria. Rear tire saturation enables lateral control authority through the rear drive force, and that added control authority is used in this scheme whenever additional cornering force is no longer available at the front tire. This approach to using the inputs is central to the design of the drift controller described in the next section.

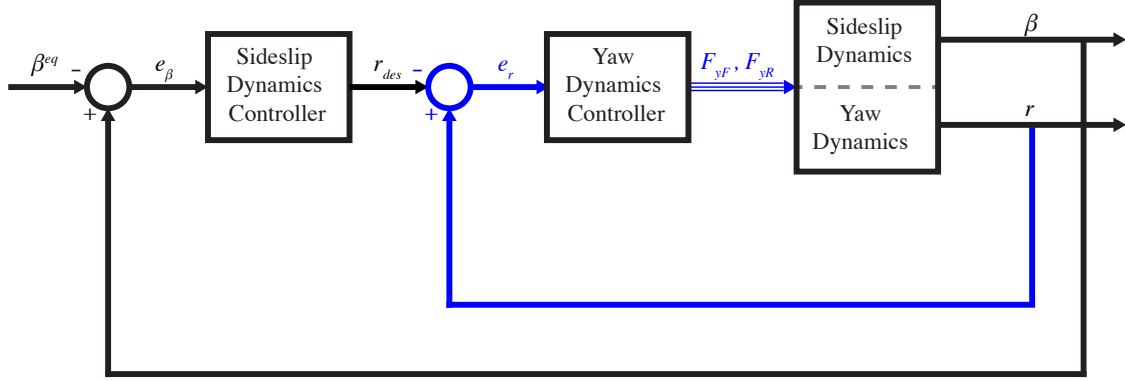


Figure 4.10: Nested loop structure of the drift controller. Blue signal paths denote the inner loop of the controller.

4.3 A controller for sustained drifting

This section draws upon the analysis of drift equilibria in Chapter 3 and the detailed analysis of the steering and rear drive force inputs in this chapter to develop a controller that coordinates steering and rear drive force inputs to enable sustained drifting. Unlike the controller case studies of the preceding section, this design is designed using the full nonlinear dynamics of the three-state bicycle model rather than a linearized model around a desired drift equilibrium, which only offers an accurate picture of the vehicle's dynamics in a neighborhood of the desired drift equilibrium. This nonlinear design approach is taken with the intent of being able to prescribe specific closed-loop lateral dynamics for the vehicle.

4.3.1 Overview of structure

The drift controller utilizes a variant of the dynamic surface control technique that is based on a nested-loop structure. Yaw rate is treated as a synthetic input to the sideslip dynamics in an outer loop, and tire forces are used to feedback linearize the yaw rate dynamics in an inner loop. This structure is depicted in Figure 4.10.

An intuitive rationale for this yaw rate-focused control structure comes from inspection of the lateral dynamics of the bicycle model:

$$\dot{\beta} = \frac{F_{yF} + F_{yR}}{mU_x} - r \quad (4.28a)$$

$$\dot{r} = \frac{aF_{yF} - bF_{yR}}{I_z} \quad (4.28b)$$

The most obvious argument for using yaw rate as a synthetic input to the sideslip dynamics is the appearance of yaw rate as a linear term in these dynamics, as is evident in Equation 4.28a. It is also important to consider that it is difficult to alter the sign or magnitude of the sum $F_{yF} + F_{yR}$ of the lateral forces in Equation 4.28a appreciably when both tires are at or near saturation, as is the case in performance driving. This is especially true relative to the weighted difference $\frac{a}{I_z}F_{yF} - \frac{b}{I_z}F_{yR}$ that gives the yaw moment acting on the vehicle in Equation 4.28b, where even comparably small changes in the lateral forces relative to one another can be used to affect considerable changes in the magnitude and sign of the yaw moment. Such changes in yaw moment generate large yaw variations that can in turn be used to control the sideslip dynamics.

Much of the analysis in this dissertation corroborates this intuitive justification. In Chapter 3, linearization around drift equilibria revealed the existence of a RHP zero in the transfer function from steering to sideslip that reflects the significant influence of changes in yaw rate over the sideslip dynamics. Furthermore, the drive force-based regulator in Section 4.2.2 demonstrates the effect of yaw rate variations in action. Simulations of this controller indicate that it regulates the lateral dynamics by generating large, rapid changes in yaw rate that in turn affect the sideslip dynamics.

Finally, phase portrait analysis of two- and three-state models in Chapter 3 revealed that trajectories corresponding to an exit from drifting into conventional cornering are associated with large drops in yaw rate. This is supported by the experimental yaw rate data in Figure 4.2 for the steering-based controller in Section 4.2.1. In this data, large decreases in sideslip magnitude at $t \approx 18$ s and $t \approx 32$ s as well as the complete exit from the drift at $t \approx 39$ s are all preceded by significant and rapid decreases in yaw rate.

With all this in mind, the outer loop of the controller is designed to compute a yaw command that varies in response to changes in sideslip magnitude. The inner loop, in turn, controls the vehicle's yaw rate to this outer loop command. A detailed derivation of the control law for each loop is presented below.

4.3.2 Outer loop design

As shown in Figure 4.10, the outer loop is designed to control the sideslip dynamics of the vehicle using a desired yaw rate r_{des} . The yaw command in this design utilizes a simple feedforward-feedback structure, with a feedforward yaw rate command and proportional feedback of sideslip error:

$$r_{des} = r^{eq} + K_\beta e_\beta = \frac{1}{mU_x^{eq}}(F_{yF}^{eq} + F_{yR}^{eq}) + K_\beta e_\beta, \quad (4.29)$$

where the equilibrium yaw rate r^{eq} serves as the feedforward command, $K_\beta > 0$ is the sideslip error feedback gain, and the sideslip error e_β is defined relative to the desired equilibrium sideslip β^{eq}

$$e_\beta = \beta - \beta^{eq} \quad (4.30)$$

This command is designed to vary the yaw command appropriately in response to sideslip variations from the equilibrium value. For a left handed drift equilibrium, $r^{eq} > 0$, $\beta^{eq} < 0$), a negative sideslip error ($e_\beta < 0$) signifies that the vehicle is operating at too deep of a sideslip angle and is in danger of spinning out. This results in $r_{des} < r^{eq}$, a reduction in the yaw rate command that will require a reduction in the yaw moment acting on the vehicle. Conversely, a positive sideslip error ($e_\beta > 0$) signifies that the sideslip angle is too shallow and that the vehicle is in danger of exiting from the drift into a more conventional cornering condition. This results in $r_{des} > r^{eq}$, a increase in the yaw command that will require an increase in the yaw moment acting on the vehicle. In either case, the change in the yaw command is consistent with prior analysis in this dissertation on the influence of yaw variations on the sideslip dynamics.

4.3.3 Inner loop design

In the inner control loop (shown in blue in Figure 4.10), the tire lateral forces are chosen in order to feedback linearize the yaw dynamics and enforce stable first order dynamics in the yaw rate error relative to the outer loop command r_{des} . This requirement can be expressed as follows:

$$\dot{e}_r = \dot{r} - \dot{r}_{des} = -K_r e_r, \quad (4.31)$$

where $e_r = r - r_{des}$ is the error in the yaw rate relative to the outer loop command, *not* relative to the equilibrium yaw rate r^{eq} . Substituting the yaw dynamics from Equation 4.28b for \dot{r} and $\dot{r}_{des} = K_\beta \dot{\epsilon}_\beta = K_\beta \dot{\beta}$ yields:

$$\dot{e}_r = \frac{aF_{yF} - bF_{yR}}{I_z} - K_\beta \left(\frac{F_{yF} + F_{yR}}{mU_x} - r \right) = -K_r e_r. \quad (4.32)$$

Re-writing the yaw rate as $r = e_r + r_{des}$, substituting for r_{des} from Eqn. (4.29) and collecting like terms yields the following control law:

$$k_1 F_{yF} - k_2 F_{yR} = -K_\beta^2 e_\beta - K_\beta r^{eq} - (K_\beta + K_r) e_r, \quad (4.33)$$

where $k_1 = \frac{a}{I_z} - \frac{K_\beta}{mU_x}$ and $k_2 = \frac{b}{I_z} + \frac{K_\beta}{mU_x}$. This control law does not dictate any individual control input but instead constrains a weighted difference of the front tire lateral force F_{yF} and rear tire lateral force F_{yR} . An increase in the controller command (the right hand side of Equation 4.33), for example, can be achieved by either an increase in F_{yF} , a decrease in F_{yR} , or some combination of the two commands. This is a mathematical reflection of the fact that the control law is based on the principle of controlling the yaw moment $\frac{a}{I_z} F_{yF} - \frac{b}{I_z} F_{yR}$ and is structurally similar as a result. Fortunately, this makes the control design quite amenable to application of the coordination scheme proposed in Section 4.2.3.

4.3.4 Input coordination scheme

As described in Section 4.2.3, the coordination scheme consists of two controller modes, where the mode of operation is dictated by the amount of cornering force available at the front tire. The first mode is based upon computing a front lateral force command for lateral control (realized through the steering input) and a drive force input for longitudinal control. The second mode is based upon computing a rear lateral force command for lateral control because the front lateral force is friction-limited. The rear lateral force command is then realized by the rear drive force via rear tire saturation and friction circle coupling.

For the sake of clarity, the derivation of the coordination scheme below focuses upon control of the vehicle about a left-handed drift equilibrium ($r > 0, F_{yF} > 0, F_{yR} > 0$). The derivation for a right-handed drift equilibrium is conceptually identical and follows in the same fashion.

Steering mode

When operating in steering mode, the controller attempts to satisfy the drift controller law using steering alone while a longitudinal controller operates in parallel to stabilize the vehicle to a desired longitudinal velocity. The longitudinal controller command F_{xR}^S in this mode (where the superscript “S” denotes the steering mode) simply consists of a feedforward term F_{xR}^{eq} and feedback of the longitudinal velocity error $e_{U_x} = U_x - U_x^{eq}$ with respect to the equilibrium longitudinal velocity:

$$F_{xR}^S = F_{xR}^{eq} - mK_{U_x}e_{U_x}. \quad (4.34)$$

The steering command for the drift controller comes from Equation 4.33 re-arranged to solve for a front lateral force command:

$$F_{yF}^S = \frac{1}{k_1}[k_2F_{yR}^S - K_\beta^2e_\beta - K_\beta r^{eq} - (K_\beta + K_r)e_r], \quad (4.35)$$

where F_{yR}^S is the computed rear lateral force when operating in steering mode. Note that in this mode, the rear lateral force is not treated as an input, but rather an

additional term in the controller command.

F_{yF}^S can be mapped to a desired front tire slip angle α_F^S through inversion of the brush tire model. A steer angle command δ^S can then be computed according to Equation 4.36, which is a rearrangement of the definition of the front tire slip angle:

$$\delta^S = \alpha_F^S - \arctan\left(\beta + \frac{a}{U_x}r\right) \quad (4.36)$$

If $F_{yF}^S < \mu F_{zF}$, then the drift controller command is satisfied in steering mode without needing to use the rear drive force for lateral control.

Drive force mode

In the event that the front lateral force command in steering mode exceeds the front tire force available from friction, ($F_{yF}^S > \mu F_{zF}$), the drift controller operates in drive force mode. In this mode, *both* the front and rear tire lateral forces are treated as lateral control inputs to the vehicle, and the rear lateral force command is mapped to a rear drive force input via the friction circle:

$$F_{yR}^D = \frac{1}{k_2} [k_1 \mu F_{zF} + K_\beta^2 e_\beta + K_\beta r^{eq} + (K_\beta + K_r) e_r] \quad (4.37a)$$

$$F_{xR}^D = \sqrt{(\mu F_{zR})^2 - (F_{yR}^D)^2} \quad (4.37b)$$

$$F_{yF}^D = \mu F_{zF}. \quad (4.37c)$$

F_{yF}^D , F_{yR}^D , and F_{xR}^D (where the superscript “D” denotes drive force mode) are the desired front lateral force, rear lateral force, and rear drive force when operating in drive force mode. As in the steering mode, the front lateral force command can be mapped to a steering command δ^D using the desired slip angle α_F^D and Equation 4.36.

In drive force mode, the front lateral force command Equation 4.37c is simply set to the maximum value allowed by friction. The desired rear lateral force Equation 4.37a is then computed by re-arranging Equation 4.33 to solve for rear lateral force assuming $F_{yF} = F_{yF}^D = \mu F_{zF}$. Since $F_{yF}^D < F_{yF}^S$, it follows that $F_{yR}^D < F_{yR}^S$.

Knowing that $F_{yR}^D < F_{yR}^S$, Equation 4.37b dictates that $F_{xR}^D > F_{xR}^S$. Thus, the

coordination scheme increases the rear drive force as the front tire force saturates. As this scenario is typically encountered when the vehicle's yaw rate and sideslip magnitude are too low, the coordination scheme is adding rear drive force to deepen the vehicle's drift, in much the same fashion as the drive force-based regulator of Section 4.2.2.

As with the drive force regulator, operation of this control design in drive force mode will induce positive errors in longitudinal velocity, especially since the controller is temporarily sacrificing control of e_{U_x} to use the rear drive force for control in the (e_β, e_r) plane. The potential stability issues associated with this behavior must be addressed in the analysis of the controller, and are explored in the next chapter. Unfortunately, this behavior reflects the challenges resulting from controlling three states using two inputs. In the absence of an additional input that would enable arbitrary trajectories through the state space, the vehicle's state trajectories are constrained by the nature of the available inputs' influence upon the three states.

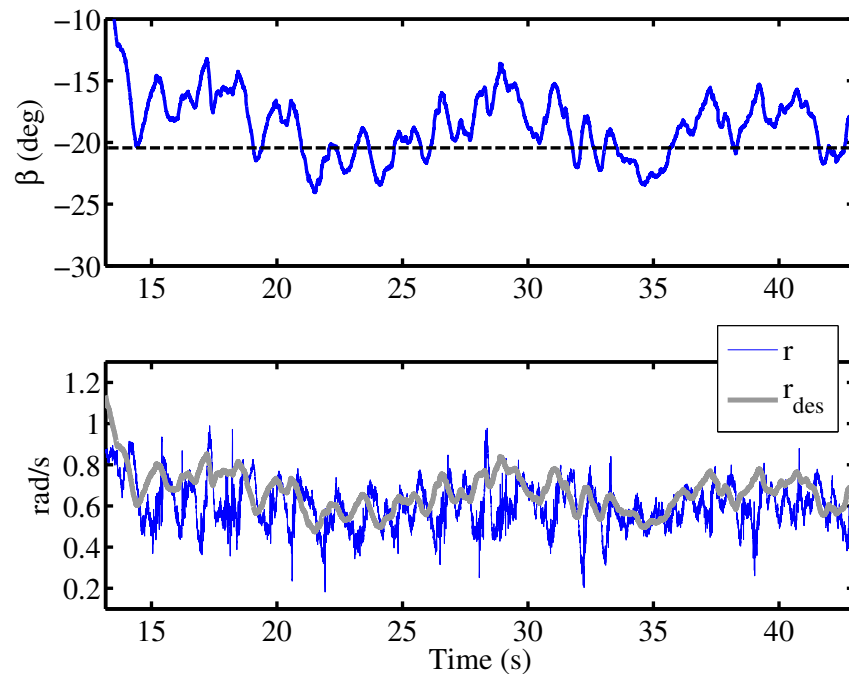
4.4 Experimental implementation

The controller described in the preceding section has been implemented on P1 using the target equilibrium and controller gains given in Table 4.3. The experimental run begins with an open-loop control sequence in which the vehicle is brought up to speed and then destabilized using regenerative braking at the rear wheels, at which point the controller is activated to stabilize the vehicle into a drift. The experimental data in Figures 4.11, 4.12, and 4.13 depicts the vehicle behavior following activation of the controller.

The data in Figures 4.11 through 4.13 indicate that the vehicle successfully drifts for more than 30 seconds before the experimental run is deliberately ended by a safety driver seated in P1 and monitoring the vehicle. From the top plot in Fig. 4.11, it is evident that the measured sideslip angle tracks the target sideslip (denoted by a dashed line) quite closely, with sideslip error rarely exceeding 3-5 degrees in magnitude. In fact, the sideslip angle remains within a range comparable to or better than that in measurements of drifts executed by a human driver [39].

Parameter	Value
δ^{eq}	-12°
F_{xR}^{eq}	2293 N
β^{eq}	-20.44°
r^{eq}	0.6 rad/s
U_x^{eq}	8 m/s
K_β	2 1/s ²
K_r	4 1/s
K_{U_x}	0.846 1/s

Table 4.3: Target equilibrium and gains for implementation of the drift controller.

Figure 4.11: Sideslip compared to β^{eq} (top) and yaw rate compared to r_{des} (bottom) during an experimental run.

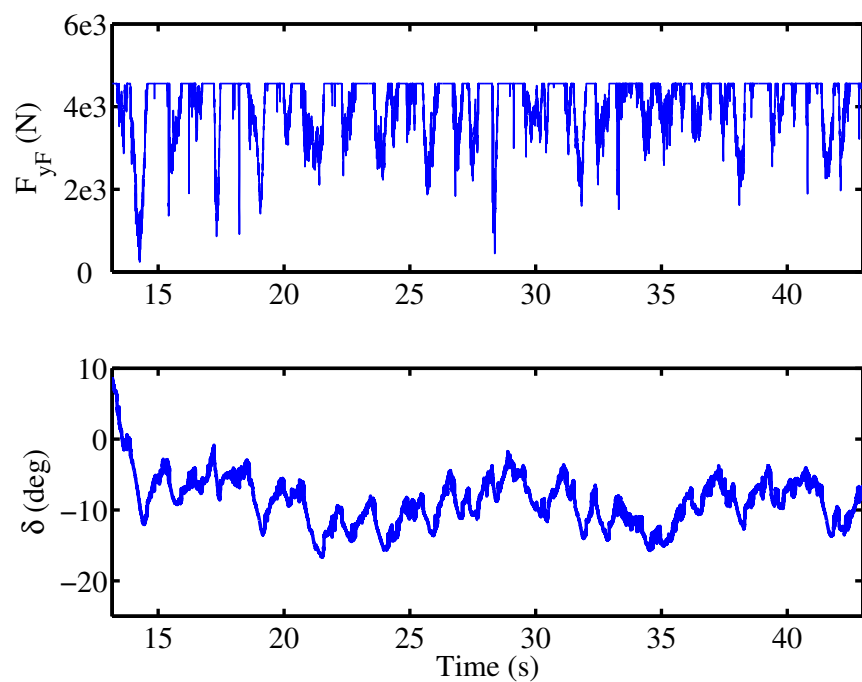


Figure 4.12: Front lateral force command (top) and steering command (bottom) during an experimental run.

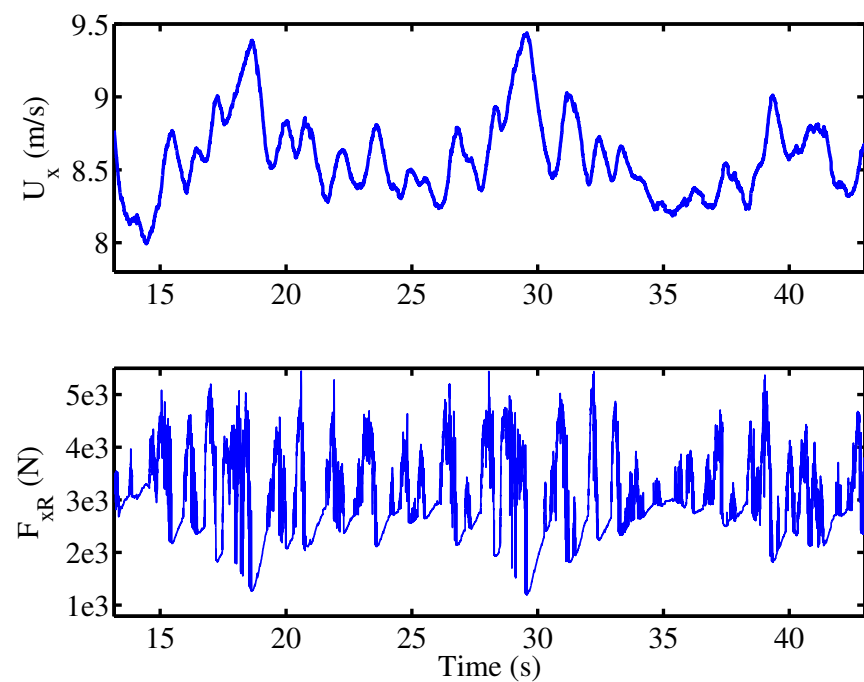


Figure 4.13: Longitudinal velocity (top) and rear drive force command (bottom) during an experimental run.

As observed in Chapter 2, friction on the test surface is highly variable, and the larger sideslip deviations are due primarily to friction disturbances acting through the yaw dynamics. The successive loop structure of the controller makes sideslip tracking performance contingent upon the ability of the inner yaw control loop to track the yaw command from the outer loop. Consequently, large yaw rate errors will eventually translate to large sideslip errors. It is no coincidence that increases in sideslip magnitude above the equilibrium value, such as at $t = 19$ s, are preceded by large increases in yaw rate (bottom plot of Fig. 4.11) caused by a drop in friction on the surface. Similarly, decreases in sideslip magnitude such as the one at $t = 31$ s are preceded by large drops in yaw rate caused by an increase in friction on the surface. In either case, the yaw errors are acting through the sideslip dynamics to induce sideslip errors.

The response of the controller to the two error scenarios described above demonstrates that the controller uses the steering and rear drive force inputs in a fashion consistent with the rationale developed in Section 4.2.3. When the vehicle's yaw rate increases significantly at $t \approx 19$ s, the desired yaw rate command r_{des} decreases. The resulting positive yaw rate error e_r requires the controller to command a decrease in the yaw moment acting on the vehicle. In this case, friction limitation at the front tire is not an issue, as the decrease in yaw moment can easily be achieved by a reduction in front lateral force.

Based on the reasoning in Section 4.2.3, it makes sense to use the front lateral force for lateral control and rear drive force for longitudinal control in this case, and this is precisely what the controller does. At $t \approx 19$ s, the controller is operating in steering mode and countersteers to reduce the front lateral force (Figure 4.12). The decrease in yaw moment reduces the yaw rate of the vehicle, which subsequently acts through the sideslip dynamics to decrease the sideslip magnitude. At the same time, the rear drive force is being used in parallel for longitudinal velocity control (bottom plot of Figure 4.13).

In the case where a precipitous drop in yaw rate occurs at $t \approx 31$ s, the controller commands a rapid increase in the yaw rate command r_{des} . The resulting negative yaw rate error e_r requires the controller to command an increase in yaw moment.

Initially, the controller attempts to achieve this increase while operating in steering mode, with an increase in front lateral force through reduced countersteer. However, the front tire quickly saturates (top plot of Fig. 4.12), and the yaw moment cannot be increased any further using steering.

From the rationale in Section 4.2.3, it makes sense at this point to use the rear drive force for lateral control, and this is reflected in the controller's operation. Upon saturation of the front tire, a transition from steering mode to drive force mode occurs. The rear drive force command (bottom plot of Fig. 4.13) becomes a lateral control input and rapidly climbs to reduce the rear lateral force magnitude. This increases the yaw moment acting on the vehicle, which drives the yaw rate up towards r_{des} . This yaw buildup then acts through the sideslip dynamics to increase sideslip magnitude. As expected, this controller response drives up the longitudinal velocity of the vehicle. However, the longitudinal velocity of the vehicle drops back towards the desired value as soon as the controller transitions from drive force mode back to steering mode, and the longitudinal velocity of the vehicle remains in a fairly tight range overall.

The experimental results indicate that a drift controller designed primarily from physical intuition can provide stabilization to a desired equilibrium across a large region of the state space, and in the presence of fairly significant friction variation. The next chapter demonstrates that there is a control theoretic interpretation for this controller that can be used to demonstrate stability characteristics that are consistent with the controller's successful performance in experiments.

Chapter 5

Stability Analysis

The drift controller presented in the preceding chapter was designed primarily using physical intuition. While the impressive performance and robustness of this controller is suggestive of a broad region of convergence around the desired drift equilibrium, there are no stability guarantees incorporated into the controller's design. In fact, there are certain aspects of the closed-loop dynamics that present challenges from a stability standpoint that must be addressed.

The usage of the rear drive force input for the dual purposes of lateral and longitudinal control represents a challenge as far as enforcing stability of the longitudinal dynamics of the vehicle. Recall that the controller's steering mode (in which steering is used for lateral control) incorporates longitudinal velocity error feedback into the rear drive force input, while the drive force mode uses the rear drive force exclusively for the purpose of lateral control. In the latter case, the controller temporarily sacrifices control of the longitudinal velocity error e_{U_x} for the sake of control in the (e_β, e_r) plane. Relative to the steering mode, operation in the drive force mode adds drive force to deepen the drift of the vehicle. This induces positive longitudinal velocity errors that did not prove problematic in experimental practice, but it remains to be shown how the added energy input to the system affects overall longitudinal stability in closed-loop.

This chapter examines the closed-loop dynamics of the vehicle around a desired drift equilibrium in order to develop a clearer picture (quite literally) of the controller's

stability characteristics. The chapter begins by deriving an alternate interpretation of the controller as a sliding surface controller. The closed-loop dynamics are then analyzed within the framework of this interpretation using multiple techniques in Section 5.2. Numerical linearization of the dynamics around the desired drift equilibrium used for implementation in Chapter 4 demonstrates local closed-loop stability of the equilibrium, while a numerically validated Lyapunov function is used to establish an invariant set around the equilibrium.

Phase portrait analysis of the closed-loop dynamics in Section 5.3 reveals that the controller has a rather broad region of convergence, much larger than the invariant set calculated using Lyapunov techniques. An examination of the phase portrait establishes that it is hard to make broader stability statements for the controller because the closed-loop longitudinal dynamics differs drastically depending upon which input is being used for lateral control. This difference arises because of the conflict between lateral and longitudinal control objectives when using the rear drive force for lateral control.

With this in mind, Section 5.4 examines a modified version of the controller that blends front lateral force and rear drive force for the purposes of lateral control (rather than just switching between them) while incorporating explicit stability guarantees for both the lateral and longitudinal dynamics. With this design, it is straightforward to demonstrate local stability of a drift equilibrium. Unfortunately, this controller proves to have an impractically small region of feasibility because there are large regions of the state space where control using the rear drive force is infeasible because of competition between lateral and longitudinal control objectives.

Thus, in an effort to design a controller that facilitates stability guarantees by using the front lateral force and rear drive force in a more coordinated fashion, an alternate manifestation of the conflict between lateral and longitudinal control objectives is encountered. In the end, this conflict is an unavoidable aspect of using rear drive force for drift control, and the simple coordination scheme used in the original design proves to be a more effective approach for controlling the vehicle in spite of this conflict.

5.1 Sliding surface interpretation

Even though the drift controller has been developed based on a successive loop structure, it is actually equivalent to a sliding surface controller that enforces first order, stable dynamics for a linear function of yaw rate and sideslip. This interpretation arises from examining the closed-loop behavior of the controller in slightly different coordinate system. As detailed in the preceding chapter, the inner loop of the controller is designed to control the yaw rate error e_r relative to the outer loop command r_{des} .

$$e_r = r - r_{des} \quad (5.1)$$

While this definition of yaw rate error makes sense within the context of the successive loop design, it is somewhat difficult to interpret the closed-loop dynamics in terms of e_r , since $r_{des} = r^{eq} + K_\beta e_\beta$ is both time-varying and coupled with the sideslip error $e_\beta = \beta - \beta^{eq}$. In studying the ability of the controller to stabilize to a desired equilibrium, it makes more sense to study the closed-loop dynamics in terms of the yaw rate error e'_r with respect to the (fixed) equilibrium yaw rate:

$$e'_r = r - r^{eq} \quad (5.2)$$

Fortunately, the two definitions of yaw rate error are related through a simple linear transformation. Substituting $r_{des} = r^{eq} + K_\beta e_\beta$ in Equation 5.1 yields the following:

$$e_r = r - (r^{eq} + K_\beta e_\beta). \quad (5.3)$$

Re-grouping the terms in Equation 5.3, the relationship between e_r and e'_r becomes evident:

$$e_r = (r - r^{eq}) - K_\beta e_\beta = e'_r - K_\beta e_\beta. \quad (5.4)$$

Thus, the yaw rate error e_r with respect to the outer loop command r_{des} can be written as a linear combination of the yaw rate error e'_r with respect to r^{eq} and sideslip error e_β with respect to β^{eq} .

From the preceding chapter, recall that the inner loop of the drift controller is

designed to impose stable first order dynamics on e_r , e.g. $\dot{e}_r = -K_r e_r$. In the (e_β, e'_r) space, this means that the controller imposes stable first order dynamics on the linear combination of e'_r and e_β defined by Equation 5.4:

$$\frac{d}{dt} (e'_r - K_\beta e_\beta) = -K_r (e'_r - K_\beta e_\beta) \quad (5.5)$$

These dynamics will eventually drive the linear combination $e'_r - K_\beta e_\beta$ to zero; thus, the drift controller acts as a sliding surface controller in terms of a sliding surface variable s that is equivalent to e_r transformed into the (e_β, e'_r) space:

$$\dot{s} = -K_r s \quad (5.6a)$$

$$s = e_r = e'_r - K_\beta e_\beta \quad (5.6b)$$

Level curves of s are shown as lines in the (e_β, e'_r) plane in Figure 5.1 when $K_\beta = 2$. In the (e_β, e'_r, e_{U_x}) space, the level curves of s are actually planes that are oriented vertically along these lines.

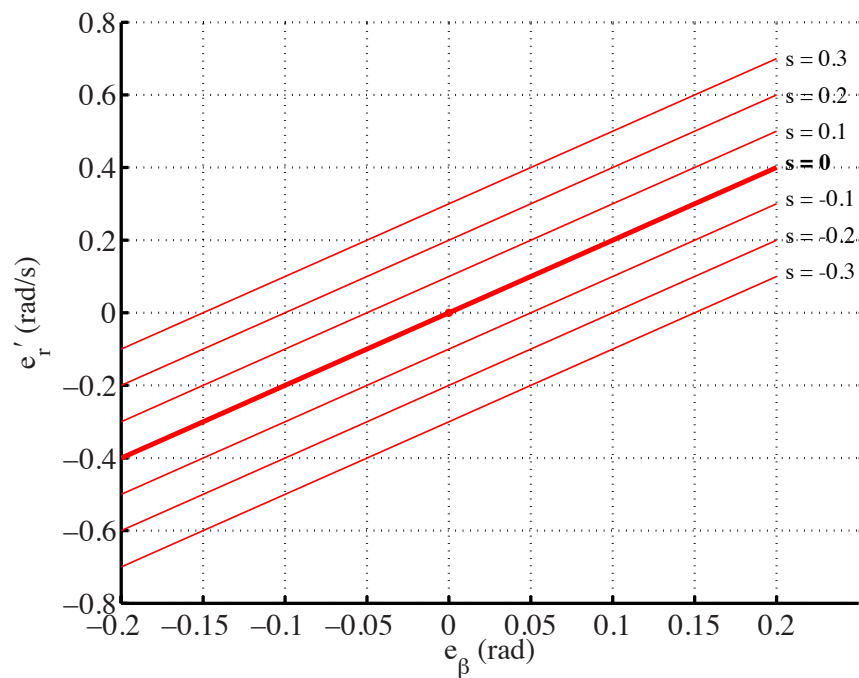


Figure 5.1: Level curves of the sliding surface variable s plotted in the (e_β, e'_r) plane.

5.2 Demonstration of closed-loop stability

5.2.1 Closed-loop dynamics

Throughout the remainder of this chapter, the closed-loop dynamics of the vehicle are considered in terms of sideslip error e_β , the sliding surface variable s introduced in the preceding section, and the longitudinal velocity error e_{U_x} . These dynamics are derived below, with an emphasis on expressing them in a form that separates out linear and nonlinear terms.

The closed-loop sideslip error dynamics are derived by starting with the open-loop sideslip dynamics and rewriting the yaw rate term as function of s and the outer loop command $r_{des} = r^{eq} + K_\beta e_\beta$:

$$\dot{e}_\beta = \frac{F_{yF} + F_{yR}}{mU_x} - (e_r + r_{des}) \quad (5.7a)$$

$$= \frac{F_{yF} + F_{yR}}{mU_x} - (s + r^{eq} + K_\beta e_\beta) \quad (5.7b)$$

$$= -K_\beta e_\beta - s + \frac{F_{yF} + F_{yR}}{mU_x} - \frac{F_{yF}^{eq} + F_{yR}^{eq}}{mU_x^{eq}}, \quad (5.7c)$$

where the tire lateral forces F_{yF} and F_{yR} are as computed in closed-loop. Note the substitution $r^{eq} = (F_{yF}^{eq} + F_{yR}^{eq}) / (mU_x^{eq})$ in Equation 5.7c, which arises from a simple rearrangement of the equation describing equilibrium of the sideslip state:

$$\dot{\beta} = \frac{F_{yF}^{eq} + F_{yR}^{eq}}{mU_x^{eq}} - r^{eq} = 0. \quad (5.8)$$

In order to derive the closed-loop longitudinal dynamics, the rear drive force command is written in the form shown below:

$$F_{xR} = F_{xR}^S + \Delta F_{xR} \quad (5.9a)$$

$$= F_{xR}^{eq} - mK_{U_x} e_{U_x} + \Delta F_{xR}, \quad (5.9b)$$

where F_{xR}^S is the rear drive force command in steering mode as defined in Chapter 4 and ΔF_{xR} is a force perturbation that accounts for changes in the rear drive force

command when the controller operates in drive force mode. Obviously, $\Delta F_{xR} = 0$ when the controller operates in steering mode and rear drive force is used for the purposes of longitudinal velocity control. When operating in drive force mode, $\Delta F_{xR} > 0$ since the controller increases the drive force relative to the steering mode command for the purposes of lateral control.

Using the expression for F_{xR} in Equation 5.9b, the closed-loop longitudinal dynamics for e_{U_x} take the following form:

$$\dot{e}_{U_x} = \frac{1}{m} (F_{xR}^{eq} - mK_{U_x}e_{U_x} + \Delta F_{xR} - F_{yF} \sin \delta) + rU_x\beta \quad (5.10a)$$

$$= -K_{U_x}e_{U_x} + \frac{1}{m}(F_{xR}^{eq} + \Delta F_{xR} - F_{yF} \sin \delta) + rU_x\beta, \quad (5.10b)$$

Combining Equations 5.7c and 5.10b with the dynamics $\dot{s} = -K_r s$ that are enforced for the sliding surface variable when operating within actuator limitations, the closed-loop dynamics of the vehicle can be expressed as follows:

$$\dot{e}_\beta = -K_\beta - s + \Delta_\beta \quad (5.11a)$$

$$\dot{s} = -K_r s \quad (5.11b)$$

$$\dot{e}_{U_x} = -K_{U_x}e_{U_x} + \Delta_{U_x}, \quad (5.11c)$$

where the Δ_β and Δ_{U_x} terms in Equations 5.23a and 5.23c are nonlinearities in the closed loop sideslip error and longitudinal velocity error dynamics, respectively:

$$\Delta_\beta = \frac{F_{yF} + F_{yR}}{mU_x} - \frac{F_{yF}^{eq} + F_{yR}^{eq}}{mU_x^{eq}} \quad (5.12a)$$

$$\Delta_{U_x} = \frac{1}{m}(F_{xR}^{eq} + \Delta F_{xR} - F_{yF} \sin \delta) + rU_x\beta. \quad (5.12b)$$

These non-linearities pose significant challenges from an analytical standpoint for multiple reasons. The bi-modal nature of the controller design means that Δ_β and Δ_{U_x} will be given by completely different expressions depending upon the controller's mode of operation. In both cases, this is because the closed-loop expressions for F_{yF} , F_{yR} , and ΔF_{xR} are entirely different in the steering and drive force modes. This

makes it difficult, for example, to bound these nonlinearities tightly because their mathematical properties vary significantly between modes.

The $-F_{yF} \sin \delta$ term in the longitudinal nonlinearity Δ_{U_x} also makes this nonlinearity difficult to manipulate analytically. This is because computation of the closed-loop steer angle δ requires determination of the front tire slip angle α_F^{des} associated with the corresponding front lateral force command:

$$\delta = \arctan \left(\beta + \frac{a}{U_x} r \right) - \alpha_F^{des} \quad (5.13)$$

In an experimental implementation of the controller, this is accomplished through a simple lookup table. In order to do this analytically, it would be necessary to invert the front tire lateral force model, which amounts to solving the equation below for α_F^{des} :

$$-C_{\alpha_F} \tan \alpha_F^{des} + \frac{C_{\alpha_F}^2}{3\mu F_{zF}} |\tan \alpha_F^{des}| \tan \alpha_F^{des} - \frac{C_{\alpha_F}^3}{27\mu^2 F_{zF}^2} \tan^3 \alpha_F^{des} = F_{yF}. \quad (5.14)$$

Needless to say, the analytical solution of this equation is quite involved, as it requires finding the zeros of a cubic polynomial in $\tan \alpha$. With this in mind, it should be clear that $-F_{yF} \sin \delta$ is a rather complex function of F_{yF} and the vehicle states.

In consideration of the above factors, Sections 5.2.2 and 5.2.3 employ numerical techniques to establish the stability of the desired drift equilibrium used for experiments in Chapter 4. The first of these sections establishes local stability of the equilibrium, while the second uses Lyapunov techniques to define an invariant set around the equilibrium. Unless otherwise stated, the numerical calculations performed in the remainder of this chapter are based on the desired drift equilibrium and controller parameters given in Table 5.1.

5.2.2 Local stability

Local stability of the desired drift equilibrium is demonstrated by examining the linearization of the closed-loop dynamics in Equation 5.11 at the equilibrium. In state space form, the linearized closed-loop dynamics take the form $\dot{x} = A_{CL}x$, where

Parameter	Value
δ^{eq}	-12°
F_{xR}^{eq}	2293 N
β^{eq}	-20.44°
r^{eq}	0.6 rad/s
U_x^{eq}	8 m/s
K_β	2 1/s
K_r	4 1/s
K_{U_x}	0.423 1/s

Table 5.1: Equilibrium data and controller gains used in stability analysis

$x = [e_\beta \ s \ e_{U_x}]^T$ and A_{CL} is the dynamics matrix for the linearization. This matrix is computed from the Jacobian of the closed-loop dynamics evaluated at the equilibrium. For the representation of the closed-loop dynamics in Equation 5.11, it is straightforward to derive the following expression for A_{CL} :

$$A^{CL} = \left[\begin{array}{ccc} -K_\beta + \frac{\partial \Delta_\beta}{\partial e_\beta} & -1 + \frac{\partial \Delta_\beta}{\partial s} & \frac{\partial \Delta_\beta}{\partial e_{U_x}} \\ 0 & -K_r & 0 \\ \frac{\partial \Delta_{U_x}}{\partial e_\beta} & \frac{\partial \Delta_{U_x}}{\partial s} & -K_{U_x} + \frac{\partial \Delta_{U_x}}{\partial e_{U_x}} \end{array} \right] \Bigg|_{x^{eq}}, \quad (5.15)$$

where Δ_β and Δ_{U_x} are the nonlinearities in the sideslip and longitudinal dynamics as defined in Equations 5.12a and 5.12b, respectively.

If one wanted to expand Equation 5.15 further, the partial derivatives of the sideslip nonlinearity Δ_β with respect to the states are straightforward to compute analytically. Owing to the complexity of the $-F_{yF} \sin \delta$ term in Δ_{U_x} , this is not the case for the partial derivatives of Δ_{U_x} with respect to the states.

Thus, A_{CL} is computed for the desired drift equilibrium in Table 5.1 by numerically solving for the partial derivatives of the nonlinearities:

$$A^{CL} = \begin{bmatrix} -2.324 & -1.487 & -0.0285 \\ 0 & 4 & 0 \\ -3.655 & -3.599 & -0.610 \end{bmatrix} \quad (5.16)$$

The eigenvalues of this matrix are -0.552, -2.390, and -4. Since all the eigenvalues have a negative real part, all the poles of the linearized system lie in the left half plane and the desired drift equilibrium is a stable node.

5.2.3 Computation of an invariant set

While the result in the preceding section shows that the controller must stabilize the desired equilibrium in some region around the equilibrium, it does not provide any information about the size or shape of this region. By using Lyapunov-based techniques to define an invariant set for the system, it is possible to develop an estimate for the region of convergence of the system.

A region of the state space around a desired drift equilibrium is said to be invariant if system trajectories that enter into the region never leave it. Barring the existence of a limit cycle within the invariant set, an invariant set around a stable equilibrium describes a region of convergence (though not necessarily the largest possible region of convergence) around that equilibrium. The existence of an invariant set around the equilibrium can be demonstrated by finding a Lyapunov function for the system of the form $V(x) = x^T P x$ ($P = P^T$, $P \succ 0$) for which there exists a level curve $V(x) = V_0$ (V_0 a constant) such that $\dot{V}(x) \leq 0$ whenever $V(x) \leq V_0$ (an invariant set). The challenge lies in finding a Lyapunov function for which this condition actually holds.

In this work, a candidate Lyapunov function is generated using the linearization of the system at the desired drift equilibrium. This corresponds to solving the continuous-time Lyapunov equation below for P :

$$A^{CL^T} P + P A^{CL} = -I, \quad (5.17)$$

where A_{CL} is the dynamics matrix for the linearized closed-loop dynamics at the desired drift equilibrium (defined in Equation 5.15 and given for the equilibrium of interest in Equation 5.16). Solution of the Lypaunov equation results in a matrix P that enforces $\dot{V}(x) = -x^T x \leq 0$ for the linear system $\dot{x} = A^{CL}x$. However, since the linearization is only a valid representation of the closed-loop dynamics in a neighborhood of the drift equilibrium, the matrix P computed in this manner only

represents a potential Lyapunov function for the actual closed-loop dynamics. The utility of this function in actually demonstrating an invariant set for the system must be tested numerically using the true closed-loop dynamics.

With the controller gains and drift equilibrium used for experimental implementation, solving Equation 5.17 gives the P below:

$$P = \begin{bmatrix} 4.695 & 1.080 & 0.534 \\ 1.080 & 8.340 & 0.286 \\ 0.534 & 0.286 & 0.355 \end{bmatrix}. \quad (5.18)$$

P can be tested numerically by computing $\dot{V}(x) = \dot{x}^T P x + e^T P \dot{x}$ for a range of state locations around $x = 0$. The derivative $\dot{x} = [\dot{\epsilon}_\beta \ \dot{s} \ \dot{e}_{U_x}]^T$ is computed using the closed-loop dynamics of bicycle model, accounting for all nonlinearities, tire force limitations, and steering angle limits:

$$\dot{\epsilon}_\beta = \dot{\beta} = \frac{1}{mU_x}(F_{yF}^{CL} + F_{yR}^{CL}) - r \quad (5.19a)$$

$$\dot{s} = \dot{r} - K_\beta \dot{\epsilon}_\beta = \left(\frac{a}{I_z} - \frac{K_\beta}{mU_x} \right) F_{yF}^{CL} - \left(\frac{b}{I_z} + \frac{K_\beta}{mU_x} \right) F_{yR}^{CL} - K_\beta r \quad (5.19b)$$

$$\dot{e}_{U_x} = \dot{U}_x = \frac{1}{m}(F_{xR}^{CL} - F_{yF}^{CL} \sin \delta^{CL}) + rU_x\beta, \quad (5.19c)$$

where F_{yF}^{CL} , F_{yR}^{CL} , F_{xR}^{CL} , and δ^{CL} are the values of the tire forces and steer angle as calculated when operating in closed-loop.

This numerical analysis reveals that the set $V(x) = x^T P x \leq 0.09$ defines an invariant set around $x = 0$. This particular level curve of $V(x)$ has been manually selected by finding as large an invariant set for the system as possible while ensuring that the conditions for an invariant set given earlier are satisfied. Figure 5.2 gives two-dimensional sections of the level curve corresponding to $V(x) = 0.09$ in the (e_β, e'_r) plane for a range of longitudinal velocities. The area contained within each of the sections gives the set of initial conditions within the invariant set at the corresponding longitudinal velocity.

The orientation of the invariant set is consistent with the means by which the

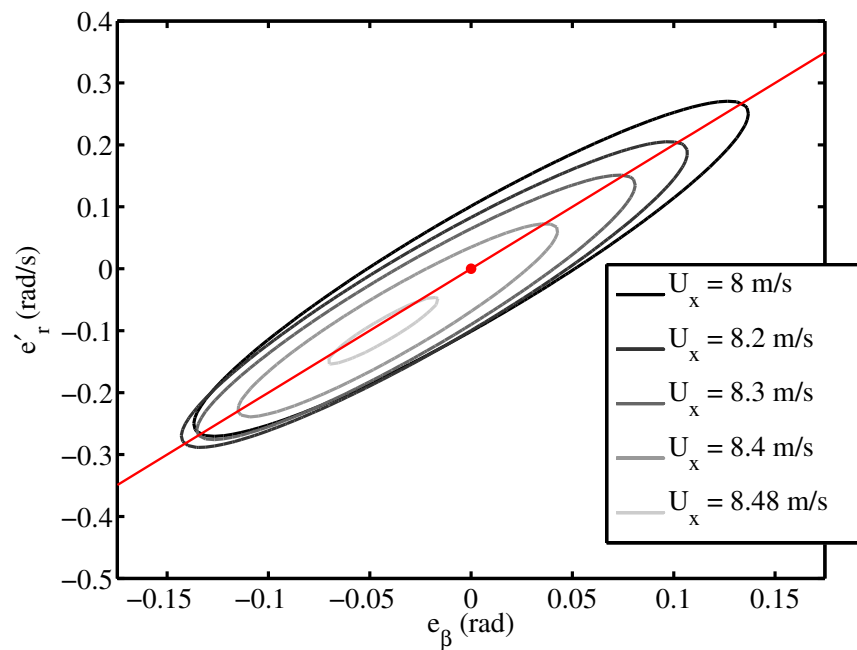


Figure 5.2: 2D sections of invariant set, $U_x = 8\text{--}8.48$ m/s. For reference, the $s = 0$ line is shown in red.

controller stabilizes the lateral dynamics of the vehicle. Since the controller is designed to stabilize s to zero, it makes sense that the invariant set is roughly aligned along the $s = 0$ level curve, shown with a red line in Figure 5.2.

By computing an invariant set around an equilibrium shown to be a stable node, a region of convergence has been established around this equilibrium. The size of the invariant set, however, is not consistent with the experimental performance of the controller, which is suggestive of a considerably larger region of convergence (while subject to significant friction variation, no less). A phase portrait of the closed-loop dynamics of the vehicle is very helpful in understanding why the Lyapunov function yields a rather conservative result.

5.3 Phase portrait analysis

The phase portrait analysis technique used in Chapter 3 to examine the open-loop dynamics of the vehicle is applied here to study the closed-loop dynamics around a desired drift equilibrium. In this case, the analysis is focused entirely upon three-dimensional visualizations of the vehicle's dynamics in the (e_β, e'_r, e_{U_x}) space, as opposed to analysis of the lateral dynamics alone in the sideslip-yaw rate plane. This is to facilitate a more complete understanding for the stability characteristics of both the lateral *and* longitudinal dynamics around the desired drift equilibrium.

The phase portraits are generated by simulating the closed-loop dynamics of the vehicle from initial conditions along level curves of the sliding surface variable s defined in Equation 5.6 for a broad range of sideslip errors e_β and longitudinal velocity errors e_{U_x} . Note that it is not necessary to define values for the steering and drive force inputs (as was the case for open-loop phase portraits), since the drift controller computes values for the inputs.

5.3.1 Region of convergence

Figures 5.3, 5.4, and 5.5 depict a phase portrait of the closed-loop dynamics of the system from multiple perspectives. The closed-loop dynamics have been simulated

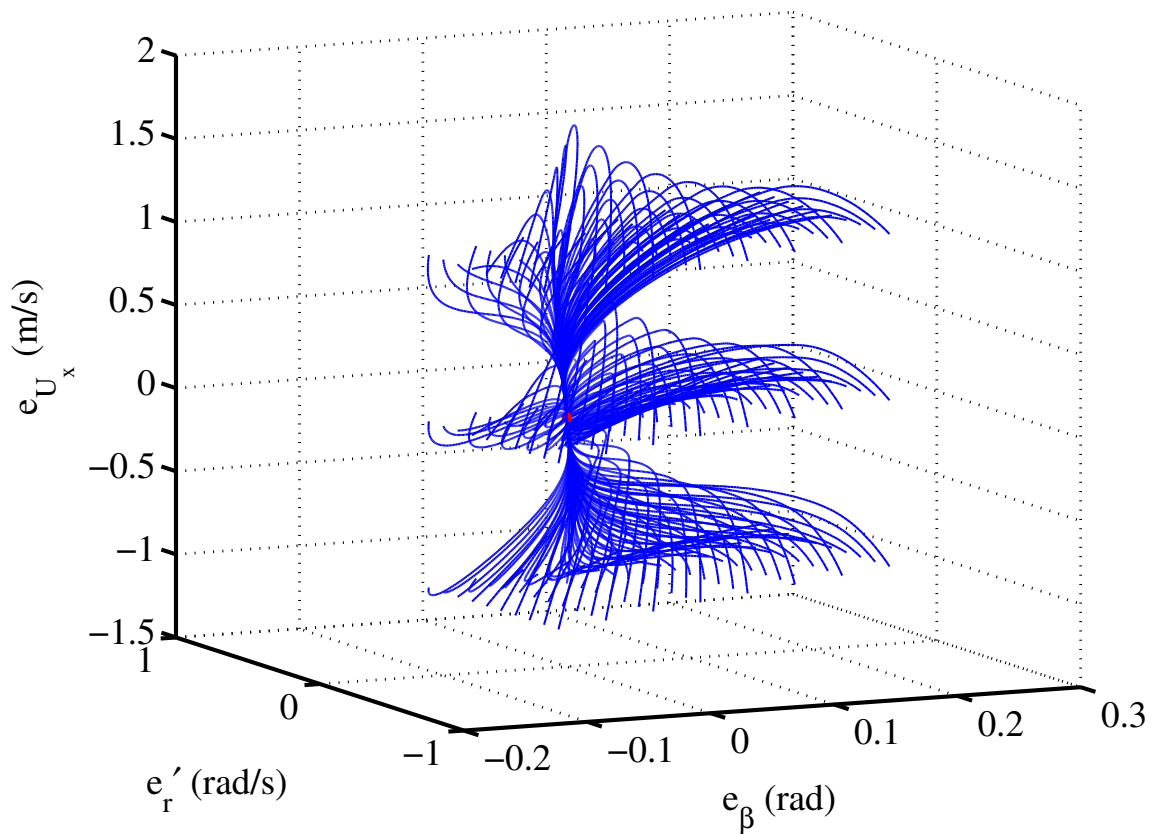


Figure 5.3: Phase portrait of closed-loop state trajectories, perspective view. The red dot denotes the desired drift equilibrium location.

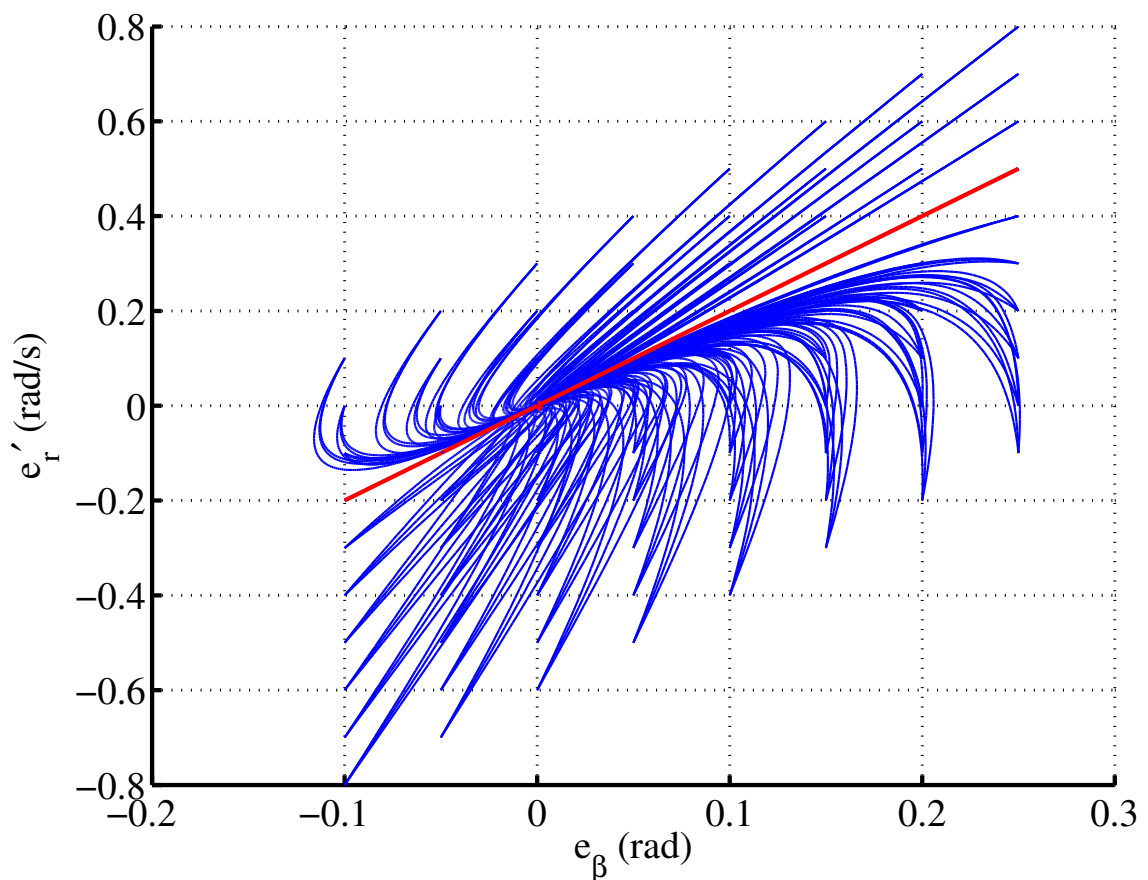


Figure 5.4: Phase portrait of closed-loop state trajectories, viewed from the $(e_\beta e'_r)$ plane. The red line denotes the $s = 0$ plane.

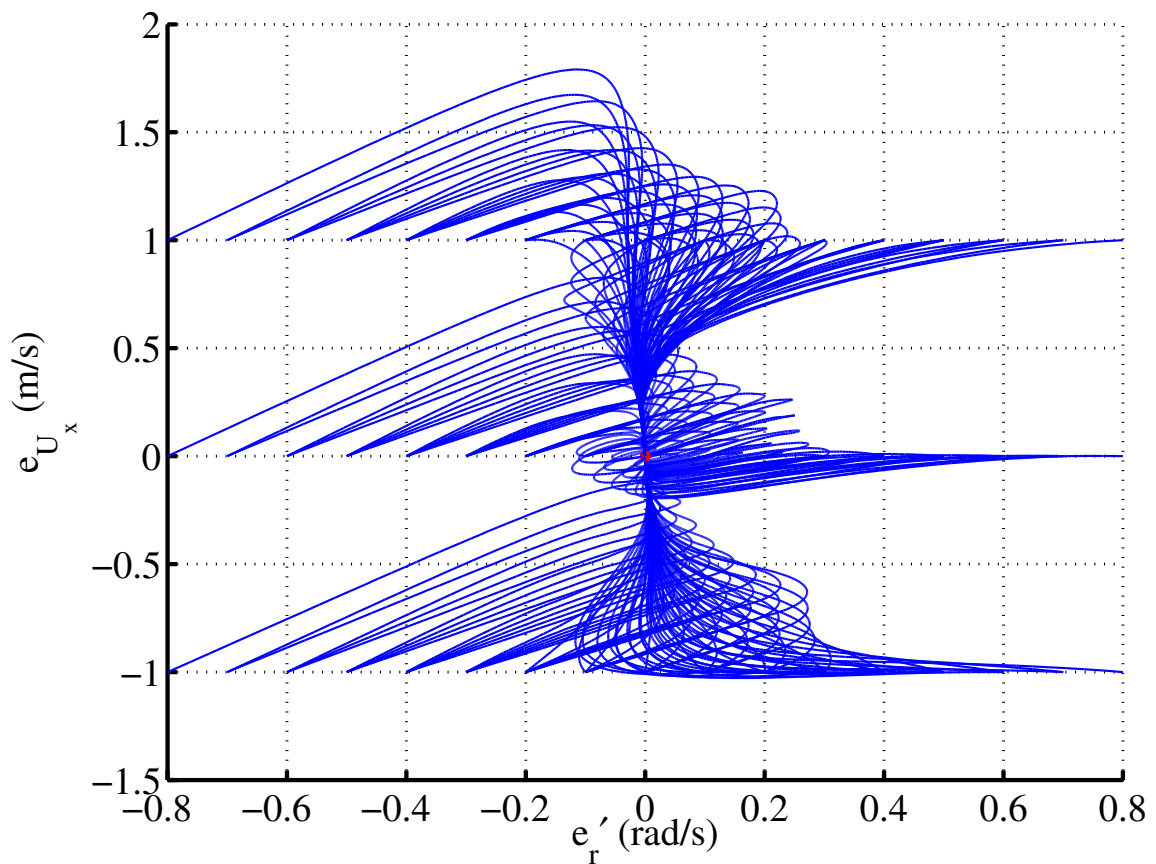


Figure 5.5: Phase portrait of closed-loop state trajectories, viewed from $e'_r - e_{Ux}$ plane. Red dot denotes desired drift equilibrium location.

for a range of initial conditions that roughly represents the region of the state space in which the controller operated in experiment. For state trajectories originating in this region, the controller operates within actuator constraints ($|\delta| \leq 23^\circ$, $0 \leq F_{xR} \leq \mu F_{zR}$) and the controller commands are therefore satisfied exactly.

Consistent with the results of Section 5.2.2, Figure 5.3 provides clear evidence that the controller stabilizes the desired drift equilibrium, given by the origin in the (e_β, e'_r, e_{U_x}) space. More importantly, all of the state trajectories over the broad range of initial conditions considered converge to the origin in Figures 5.3 through 5.5. This indicates that the region of convergence to the desired drift equilibrium is much larger than suggested by the invariant set in Figure 5.2, which is more consistent with the observed performance of the controller in experiments.

5.3.2 Graphical interpretation of sliding surface behavior

When viewed from the sliding surface perspective, the drift controller stabilizes trajectories to the drift equilibrium in two stages, each with a clear physical interpretation. During the first, “reaching phase” of controller operation, the controller drives state trajectories originating on non-zero level curves of s to the $s = 0$ plane. The reaching phase is evident in the phase portrait when it is viewed from the (e_β, e'_r) plane (Figure 5.4), where it is clear that state trajectories of the system are being driven towards the red line denoting the $s = 0$ plane from this perspective. Since $s = e_r$, the yaw rate error relative to the outer loop command r_{des} , this phase corresponds to the controller driving the tracking error between yaw rate and r_{des} to zero.

During the second, “sliding phase,” the state trajectories move along the $s = 0$ plane to the drift equilibrium, as depicted in Figures 5.6 and 5.7. Figure 5.6 demonstrates that motion of the state trajectories is restricted to the $s = 0$ plane during the sliding phase, while Figure 5.7 provides a closer look at the dynamics on this plane. Figure 5.6 reflects the fact that the vehicle state space collapses to two dimensions during the sliding phase. This occurs because operation on the $s = 0$ plane corresponds to the vehicle yaw rate tracking r_{des} perfectly. Consequently, $r = r_{des} = r^{eq} + K_\beta e_\beta$, meaning that yaw rate is a function of sideslip and no longer an

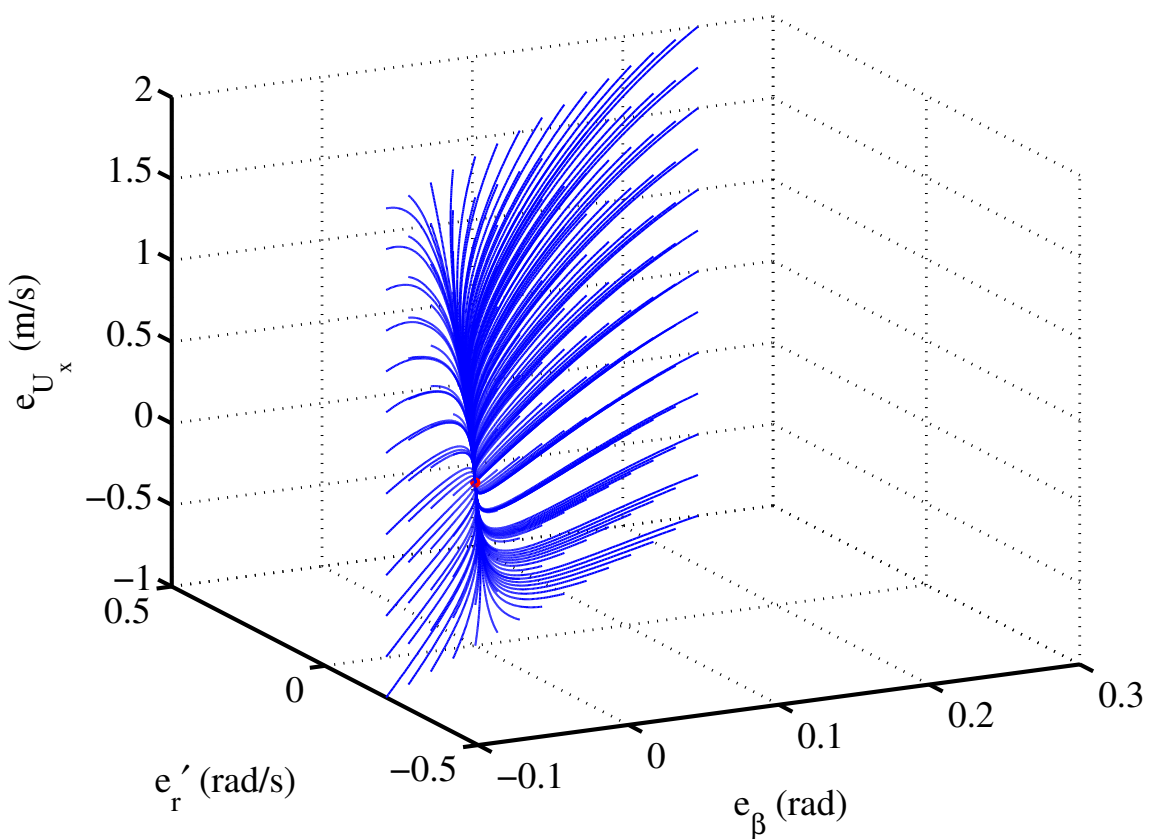


Figure 5.6: Sliding phase dynamics shown in the (e_β, e'_r, e_{U_x}) space. The red dot denotes desired the drift equilibrium location.

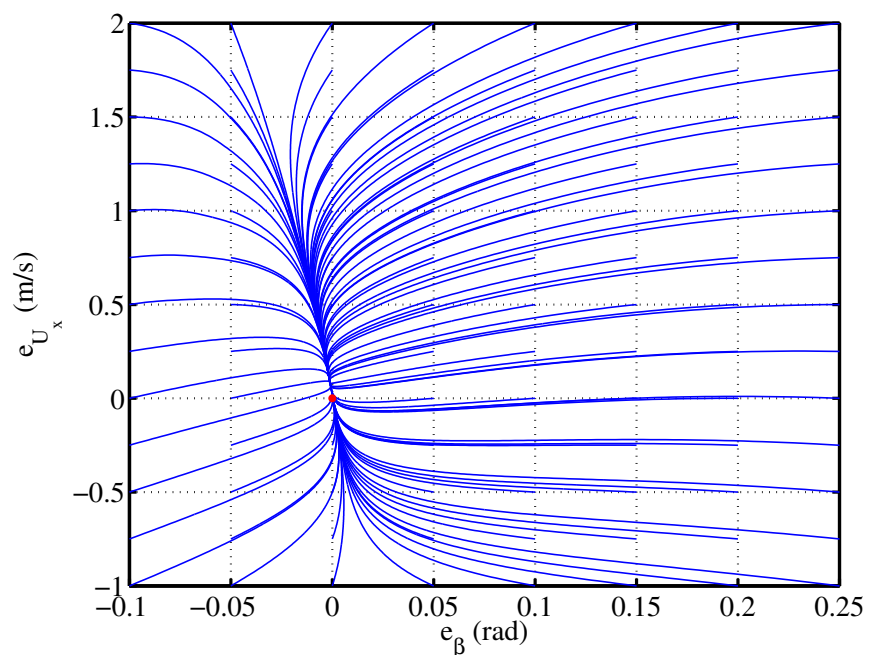


Figure 5.7: Two-dimensional view of the sliding phase dynamics (on the $s = 0$ plane). The red dot denotes desired drift equilibrium location.

independent vehicle state.

5.3.3 Analysis of the longitudinal dynamics

The phase portrait as viewed from the (e'_r, e_{U_x}) plane (Figure 5.5) provides considerable insight into the closed-loop longitudinal dynamics. In particular, Figure 5.5 highlights the stark differences in the longitudinal dynamics in some regions of the state space depending upon the mode of controller operation. As detailed below, these differences arise from the interaction (and competition) of lateral and longitudinal control objectives in these regions.

For state trajectories originating from initial conditions with $e_{U_{x0}} < 0$, there is no conflict between lateral and longitudinal control objectives. In the controller's steering mode, the rear drive force is used for longitudinal control and proportional feedback of e_{U_x} will yield an increase in the rear drive force input to bring up the longitudinal velocity of the vehicle. In the drive force mode, the added drive force that is needed for lateral control will also serve to increase the longitudinal velocity. Consequently, state trajectories in the phase portrait where $e_{U_{x0}} < 0$ all exhibit a monotonic increase in e_{U_x} towards $e_{U_x} = 0$.

For state trajectories originating from initial conditions with $e_{U_{x0}} > 0$, the picture is more complex. When operating in steering mode, proportional feedback of e_{U_x} in the rear drive force command produces a reduction in rear drive force. In drive force mode, however, usage of the rear drive force for lateral control produces an increase in drive force that directly conflicts with the longitudinal control objective. Thus, when $e_{U_{x0}} > 0$, an incompatibility between lateral and longitudinal control objectives emerges for operation in drive force mode that does not exist for operation in steering mode.

This conflict manifests itself as a significant difference in the behavior of state trajectories for which $e_{U_{x0}} > 0$ depending upon the initial mode of controller operation. State trajectories originating where the controller initially operates in steering mode, such as the bold black trajectory in Figure 5.5, exhibit a monotonic decrease in e_{U_x} towards $e_{U_x} = 0$. For state trajectories where the controller initially operates in drive

force mode, such as the bold red trajectory in Figure 5.5, e_{U_x} behaves in an entirely different fashion; it increases initially, but eventually converges back to $e_{U_x} = 0$ when the controller transitions back into steering mode and the rear drive force is once again used for longitudinal control.

The behavior in the latter case is completely consistent with the intuition and experiments presented in Chapter 4. The added drive force necessary to satisfy lateral control objectives (as in drive force mode) will come at the expense of an increase in longitudinal velocity, even if the vehicle is already operating above the desired equilibrium longitudinal velocity. The phase portrait is important because it verifies that operation in drive force mode does not destabilize the longitudinal dynamics at the initial conditions considered.

Qualitatively, this can be explained in terms of a natural coupling between the lateral and longitudinal dynamics of vehicle that is advantageous from a stability standpoint. The increase in rear drive force while in drive force mode initially acts through the longitudinal dynamics to drive up U_x . At the same time, it also increases the yaw moment acting on the vehicle to drive the vehicle's yaw rate r , which subsequently acts through the sideslip dynamics to increase $|\beta|$. In the case of operation around a left-handed drift equilibrium, $r > 0$ and $\beta < 0$, so yaw rate will become more positive and sideslip will become more negative as a result of operation in drive force mode.

Now, recall that the longitudinal dynamics of the bicycle model are as follows:

$$\dot{U}_x = \frac{1}{m} (F_{xR} - F_{yF} \sin \delta) + rU_x\beta. \quad (5.20)$$

The $rU_x\beta$ term in Equation 5.20 will become more negative as a result of the changes in r , U_x , and β described above. The deceleration due to this change in the $rU_x\beta$ term counteracts acceleration due to added drive force, which prevents U_x from increasing in an unbounded fashion while the controller operates in drive force mode.

Thus, the phase portrait establishes that temporarily sacrificing longitudinal control in the interest of lateral stabilization in drive force mode does not destabilize the longitudinal dynamics, at least over a fairly large range of initial conditions. But the

phase portrait also establishes that this technique results in a considerable difference in longitudinal behavior between the two controller modes; this is obvious from a cursory comparison of the black and red trajectories in Figure 5.5.

Intuitively, such a disparity in the longitudinal dynamics between the modes makes it difficult to find a single Lyapunov function that could be used to define an invariant set over a large range of initial conditions. While the method employed in Section 5.2.3 is by no means intended to generate the ideal Lyapunov function for the system, this disparity accounts at least in part for the conservatism of the invariant set generated using that method.

One approach for dealing with this issue is to blend the front lateral force and rear drive force inputs for lateral control in a more coordinated fashion, rather than switching between them. Intuitively, this can make it possible to enforce stable longitudinal dynamics that are more uniform in character across the state space.

5.4 An alternate drift controller design

Recall that the control law for the drift controller takes the following form:

$$k_1 F_{yF} - k_2 F_{yR} = f(e_\beta, s), \quad (5.21)$$

where $k_1 = \frac{a}{I_z} - \frac{K_\beta}{mU_x}$, $k_2 = \frac{b}{I_z} + \frac{K_\beta}{mU_x}$, and $f(e_\beta, s)$ is a function of the sideslip error e_β and the sliding surface variable $s = e_r$ defined in Section 5.1. As mentioned in Chapter 4, this control law only constrains a weighted difference of F_{yF} and F_{yR} ; nevertheless, the coordination scheme for the original controller solved for one input or the other depending upon its mode of operation. What is desired in this section is a design that solves for these inputs simultaneously.

This can be done by recognizing that it should be possible to achieve two different control objectives if a controller has two inputs. With this in mind, suppose that the drift controller is modified so that the front lateral force and rear drive force inputs must be chosen to impose stable first order dynamics on the sliding surface variable

s and the longitudinal velocity error e_{U_x} :

$$\dot{s} = \left(\frac{a}{I_z} - \frac{K_\beta}{mU_x} \right) F_{yF} - \left(\frac{b}{I_z} + \frac{K_\beta}{mU_x} \right) F_{yR} + K_\beta s + K_\beta^2 e_\beta + K_\beta r^{eq} = -K_r s \quad (5.22a)$$

$$\dot{e}_{U_x} = \frac{1}{m} (F_{xR} - F_{yF} \sin \delta) + rU_x \beta = -K_{U_x} e_{U_x}, \quad (5.22b)$$

where Equation 5.22a is an expanded version of Equation 5.21.

Equation 5.22 is a system of two equations in two unknowns F_{yF} and F_{xR} , since the rear tire lateral force $F_{yR} = \sqrt{(\mu F_{zR})^2 - F_{xR}^2}$ as a result of rear tire saturation. If it is possible to solve the system, the resulting control law has distinct advantages over the original design from a stability analysis standpoint. First, imposing explicit (stable) dynamics on e_{U_x} by design eliminates the complex non-linearities in the closed-loop longitudinal dynamics that made stability analysis difficult earlier. Second, there is no need to develop a specific coordination scheme for steering and rear drive force, as coordination of these inputs is implicit in solution of the system of equations.

The system in Equation 5.22 is quite difficult (if not impossible) to solve analytically for an explicit control law, and for a familiar reason: the $F_{yF} \sin \delta$ term appearing in the longitudinal control equation (Equation 5.22b). The inversion of the front tire model that is part of this term makes analytical solution of the system of equation impractical.

With this in mind, the controller is implemented here by solving the system of equations numerically. In particular, Equation 5.22 is solved numerically over a dense grid of state locations (e_β, s, e_{U_x}) in order to generate lookup tables that map a given state location to its corresponding front lateral force and rear drive force inputs.

5.4.1 Closed-loop dynamics and local stability

When operating within actuator limitations, the closed-loop dynamics when using the control strategy in Equation 5.22 are as follows:

$$\dot{e}_\beta = -K_\beta - s + \Delta_\beta \quad (5.23a)$$

$$\dot{s} = -K_r s \quad (5.23b)$$

$$\dot{e}_{U_x} = -K_{U_x} e_{U_x}. \quad (5.23c)$$

Note that the nonlinearity Δ_{U_x} in the longitudinal dynamics has been eliminated by design, but there is still a sideslip nonlinearity Δ_β . This nonlinearity takes the same form as for the original controller (Equation 5.12a), but the lateral forces in Δ_β do not have closed-form expressions in this case because the control equations are solved numerically.

The dynamics matrix A_{CL} for the linearization of the closed loop dynamics in Equation 5.23 is as follows:

$$A_{CL} = \begin{bmatrix} -K_\beta + \frac{\partial \Delta_\beta}{\partial e_\beta} & -1 + \frac{\partial \Delta_\beta}{\partial s} & \frac{\partial \Delta_\beta}{\partial e_{U_x}} \\ 0 & -K_r & 0 \\ 0 & 0 & -K_{U_x} \end{bmatrix} \Big|_{x^{eq}} \quad (5.24)$$

The fact that the alternate drift controller design imposes explicit dynamics on e_{U_x} results in a significant structural difference in A_{CL} for this alternate design relative to A_{CL} for the original drift controller (Equation 5.15). While the (3,1) and (3,2) entries of A_{CL} for the original controller were non-zero because of the nonlinearity Δ_{U_x} in the closed-loop longitudinal dynamics, they are zero for A_{CL} in Equation 5.24, meaning that it has an upper triangular structure.

Because A_{CL} is upper triangular, its eigenvalues are given by its diagonal entries. Relative to the original controller design, this makes it much easier to make statements about the local stability of the drift equilibrium. Since $K_r > 0$ and $K_{U_x} > 0$ by design, the eigenvalues corresponding to the (2,2) and (3,3) entries are both negative. In order for the equilibrium to be locally stable, the (1,1) entry must also be negative,

which leads to the following condition:

$$K_\beta - \frac{\partial \Delta_\beta}{\partial e_\beta} \Big|_{x^{eq}} > 0 \quad (5.25)$$

Because the lateral forces in Δ_β (Equation 5.12a) do not have closed-form expressions, the partial derivative $\frac{\partial \Delta_\beta}{\partial e_\beta}$ cannot be computed analytically. Thus, $\frac{\partial \Delta_\beta}{\partial e_\beta}$ must be approximated numerically in order to check that the inequality condition in Equation 5.25 holds for a given choice of K_β .

When using the gains and desired drift equilibrium under consideration here, $K_\beta = 2$ and $\frac{\partial \Delta_\beta}{\partial e_\beta} \Big|_{x^{eq}} \approx -0.846$. By inspection, the inequality condition in Equation 5.25 is satisfied and the desired drift equilibrium is therefore locally stable.

5.4.2 Phase portrait and feasibility analysis

Figures 5.8 through 5.10 give the phase portrait for the closed-loop dynamics with the alternate control design. For all the initial conditions considered, the controller operates within actuator limitations and enforces the control objectives in Equation 5.22.

The phase portrait clearly indicates that the controller stabilizes the desired drift equilibrium, consistent with the local stability analysis of the preceding section. Furthermore, it is clear from Figure 5.10 that all trajectories exhibit monotonic convergence of e_{U_x} to $e_{U_x} = 0$, in contrast with the complex, bi-modal behavior of e_{U_x} in phase portraits for the original controller (Figure 5.5). This is a direct consequence of prescribing stable, first order dynamics for e_{U_x} .

Unfortunately, this significant improvement in the behavior of the closed-loop longitudinal dynamics comes at a price. The phase portrait for this controller is plotted over a significantly smaller range of values for s than the phase portrait for the original controller (Figures 5.3 through 5.5) because this controller has a significantly smaller region of feasibility than the original design.

The region of feasibility around the equilibrium is restricted in two ways. There are large regions of the state space around the drift equilibrium where solutions to Equation 5.22 are not realizable within actuator constraints. There are also large

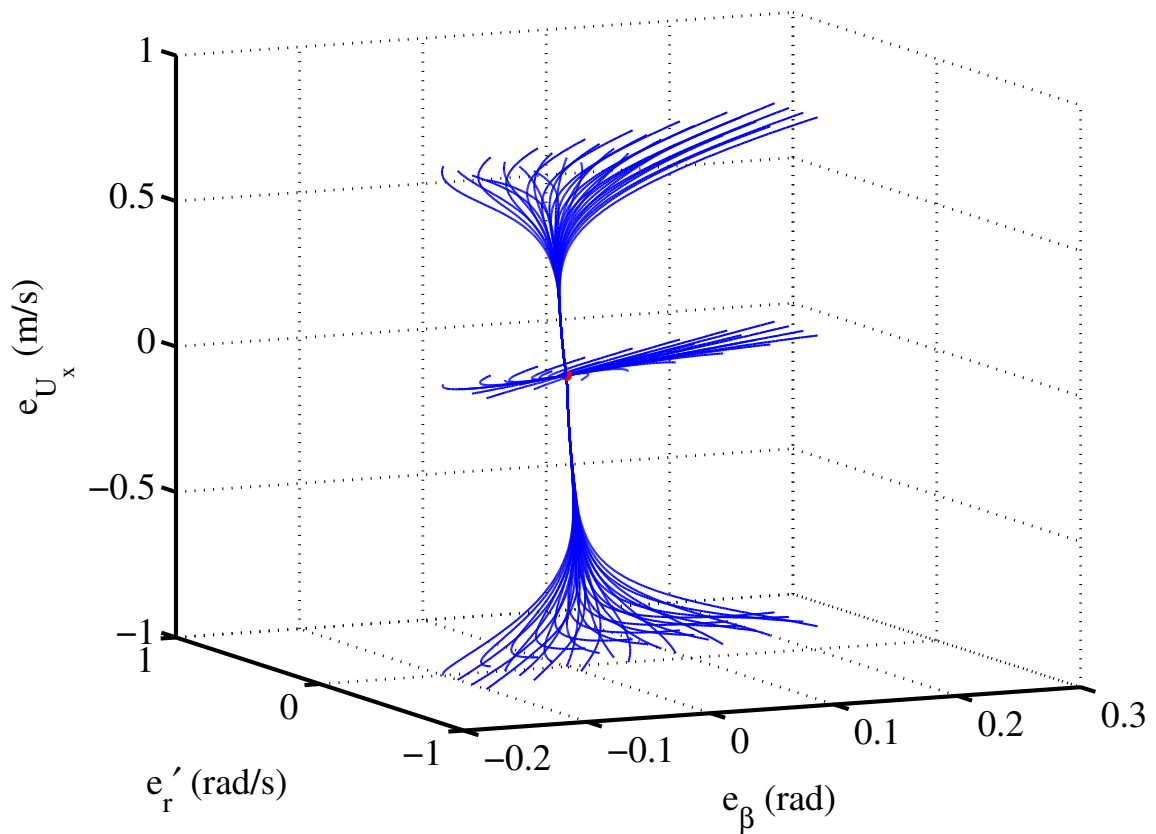


Figure 5.8: Phase portrait for the alternate drift controller, perspective view. The red dot denotes the desired drift equilibrium location.

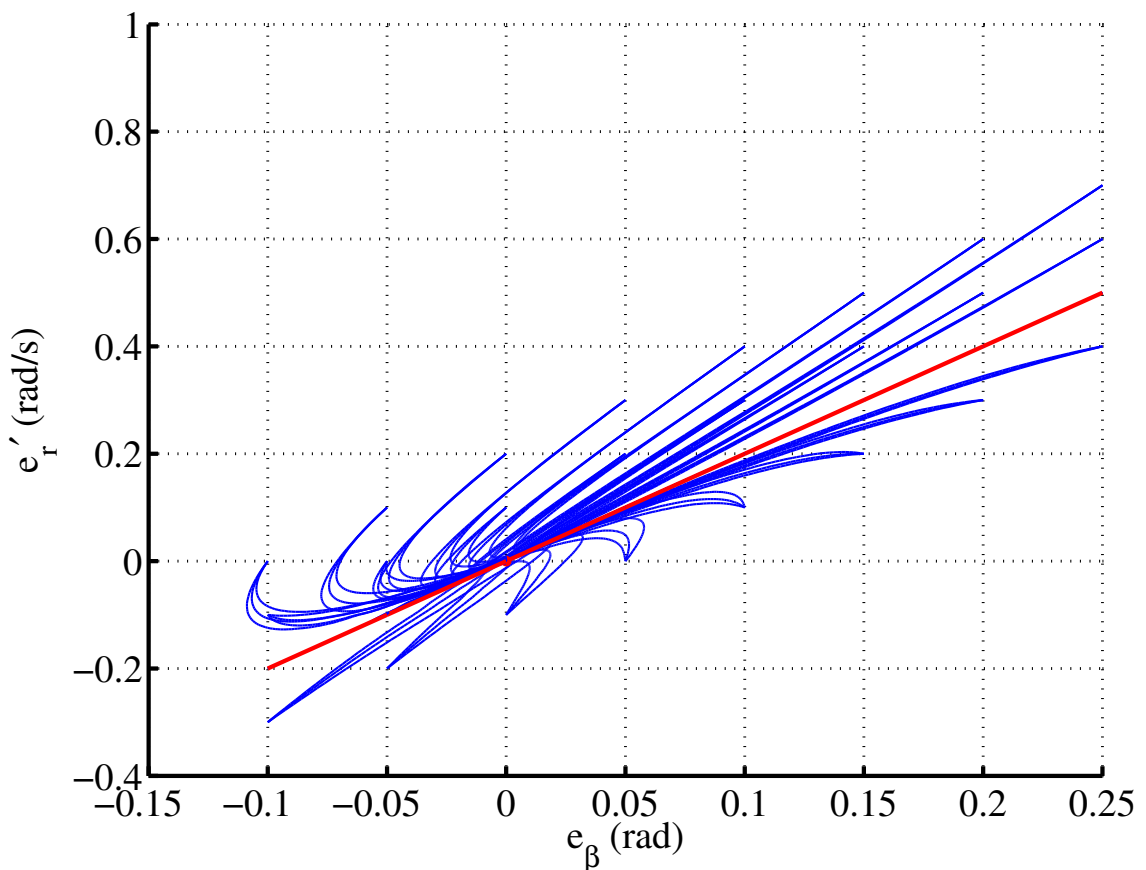


Figure 5.9: Phase portrait for the alternate drift controller, viewed from the (e_β, e'_r) plane. The red line denotes the $s = 0$ plane.

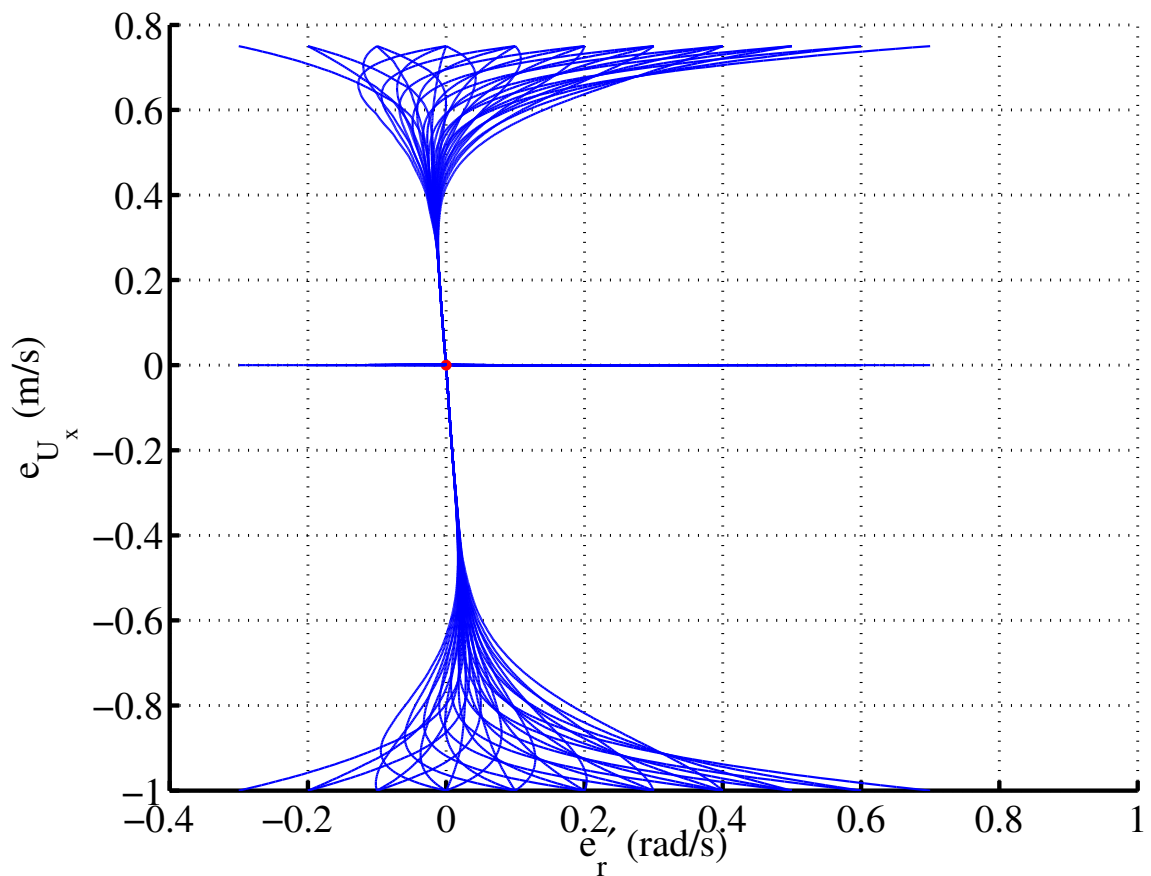


Figure 5.10: Phase portrait for the alternate drift controller, viewed from (e'_r, e_{U_x}) plane. The red dot denotes the desired drift equilibrium location.

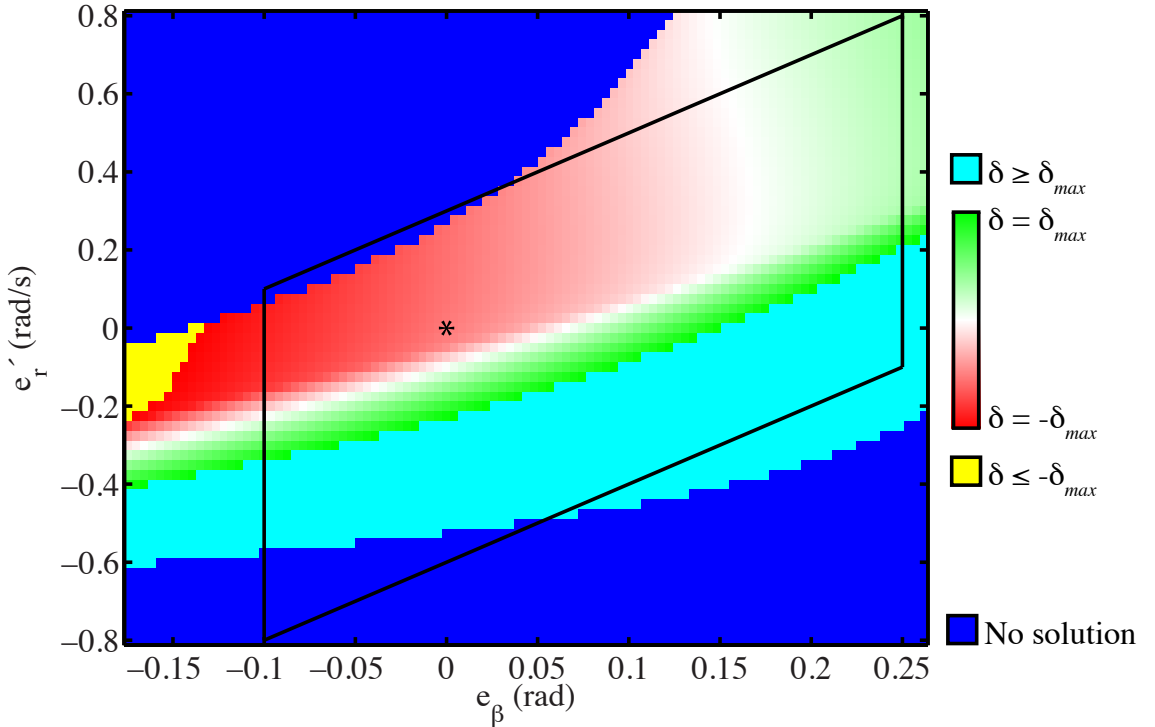


Figure 5.11: Steering solutions for the alternate drift controller when $\delta_{max} = 23^\circ$. Black lines denote the range in the (e_β, e'_r) plane over which the phase portrait for the original drift controller was plotted. The black asterisk denotes the desired drift equilibrium location.

regions of the state space where solutions simply do not exist.

In understanding the nature of these restrictions, it is very useful to visualize the solutions (or lack thereof) of the control equations in the state space. The solution maps in Figures 5.11, 5.12, and 5.13 use color gradients to depict solutions to the system in Equation 5.22 in the (e_β, e'_r) plane when $e_{U_x} = 0$ m/s.

In the solution maps, blue is used to denote regions of infeasibility where the numerical algorithm could not find a solution, even when using inputs from the nearest location with a valid solution as an initial guess. Teal and yellow areas in Figure 5.11 denote areas where the solution to the equations requires steering inputs outside P1's steering range. Thus, the combination of the blue, teal, and yellow areas in Figure 5.11 limits the region of feasibility for the controller when $e_{U_x} = 0$. For

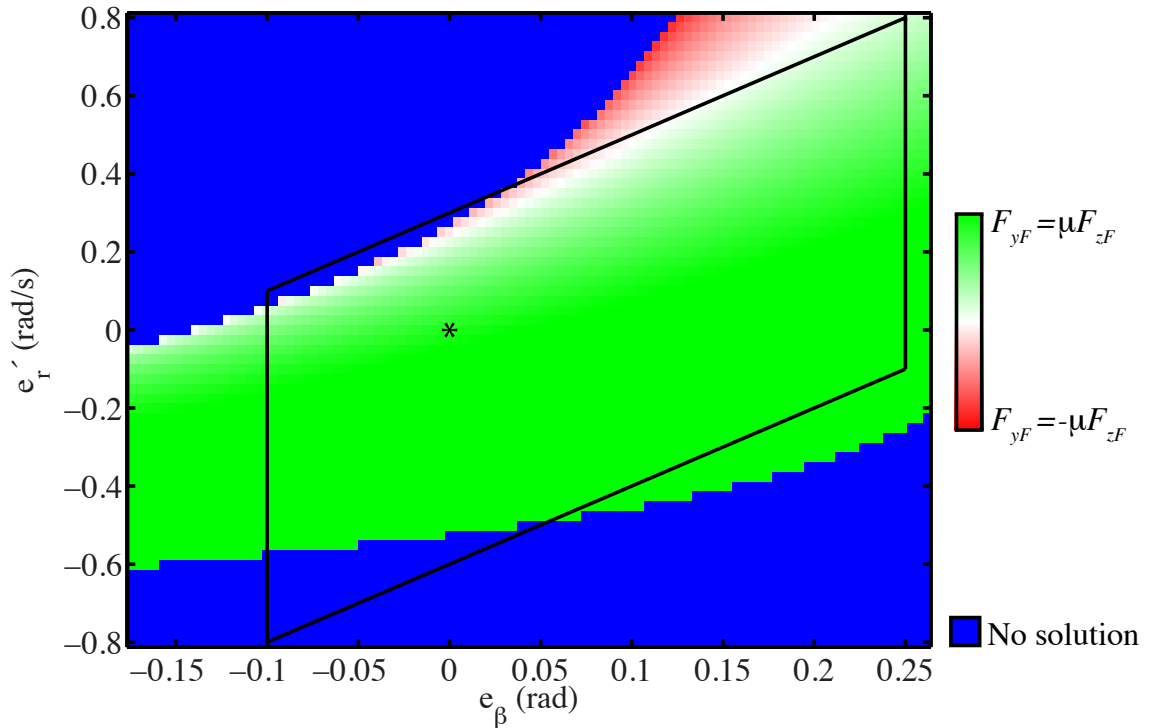


Figure 5.12: Front lateral force solutions for the alternate drift controller. Black lines denote the range in the (e_β, e'_r) plane over which the phase portrait for the original drift controller was plotted. The black asterisk denotes the desired drift equilibrium location.

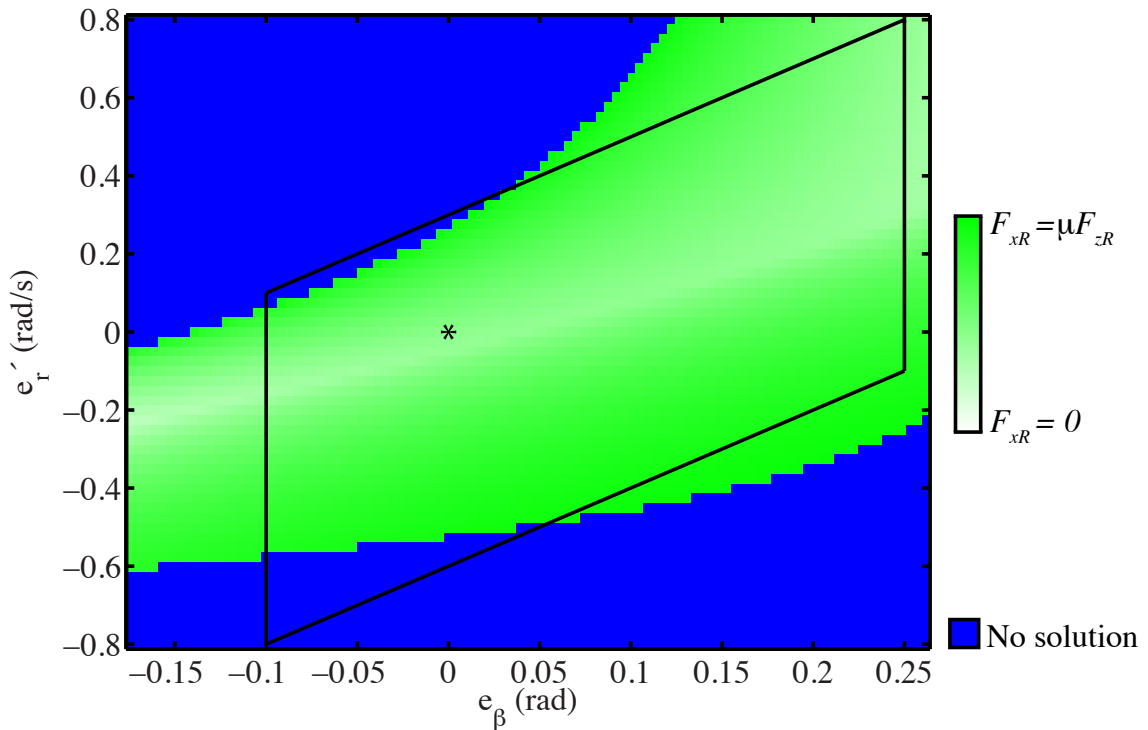


Figure 5.13: Rear drive force force solutions for the alternate drift controller. Black lines denote the range in the (e_β, e'_r) plane over which the phase portrait for the original drift controller was plotted. The black asterisk denotes the desired drift equilibrium location.

comparison, the black lines superimposed on the solution maps denote the region of convergence in the (e_β, e'_r) plane for the original controller as determined through phase portrait analysis (Figure 5.4).

Relative to the original control design, Figures 5.11 through 5.13 indicate that this control design is restricted by infeasibility in the upper left corner of the solution map (shown in blue in all three figures) and by steering limitations in the lower half of the map (the teal region in Figure 5.11). The former region arises as a result of the desired closed-loop longitudinal dynamics for the controller, while the latter region reflects the conflict between lateral and longitudinal control objectives when using the rear drive force input.

The infeasible region in the upper left corner arises because the controller increases the rear drive force up to the friction limit of the rear tire as the vehicle state approaches the boundary of this region (Figure 5.13). In order to understand why, consider Equation 5.22b solved for F_{xR} :

$$F_{xR} = F_{yF} \sin \delta - mrU_x\beta - mK_{U_x}e_{U_x} \quad (5.26)$$

The cross-coupling with the lateral states in this expression, which is necessary to feedback linearize the longitudinal dynamics, causes the observed controller response. Near the boundary of the infeasible region, yaw rate is large and positive while sideslip is large and negative. Consequently, the $-mrU_x\beta$ term in Equation 5.26 becomes large and positive as the vehicle state approaches the boundary of the upper left infeasible region, which translates to a significant increase in the rear drive force command. This increase in drive force counteracts the significant longitudinal deceleration that would otherwise result from the $rU_x\beta$ term in the longitudinal dynamics (Equation 5.20) in this region of the state space. Eventually, however, the rear drive force command necessary to balance out this term exceeds the friction capabilities of the rear tire, resulting in the observed infeasibility.

The large teal region in the lower half of Figure 5.11, where P1's steering range restricts the controller, reflects a conflict between the added drive force necessary for lateral control and the unwanted longitudinal acceleration from this force command.

As in the original design, Figure 5.13 indicates that this controller increases rear drive force when the yaw rate and sideslip magnitude are too low and the vehicle is in danger of exiting the drift. Since the vehicle is already operating at the equilibrium longitudinal velocity U_x^{eq} in these maps, this controller response inevitably requires more drive force than is necessary to enforce the desired closed-loop longitudinal dynamics and maintain U_x at its equilibrium value. Consequently, the drive force command will induce unwanted longitudinal acceleration.

In order to counteract this acceleration, the controller does something rather unusual; it attempts to use the $-F_{yF} \sin \delta$ term in the longitudinal dynamics (Equation 5.20) to control these dynamics. As the vehicle state approaches the boundary of the lower right infeasible region in the maps, Figure 5.11 indicates that the controller breaks out of countersteer and steers into the turn, which saturates the front lateral force, as indicated in Figure 5.12. Since both front lateral force and steer angle are becoming more positive, this controller response has the effect of making the $-F_{yF} \sin \delta$ term more negative, offsetting the longitudinal acceleration caused by added drive force. Even after the front lateral force is completely saturated and the $-F_{yF} \sin \delta$ term becomes $-\mu F_{zF} \sin \delta$, the controller continues to steer into the turn. This increases the component of the saturated front lateral force that counteracts the added drive force.

Even though this controller response makes mathematical sense, it is problematic on multiple levels. Qualitatively, it is not at all consistent with driver practice when drifting or the findings of this dissertation. When operating around a drift equilibrium, a driver (or controller) can only increase front lateral force a modest amount before encountering front lateral force saturation, so it makes little sense to steer significantly into the turn from a control authority standpoint. More fundamentally, the controller response described above requires a *much* larger steering range than is available on any vehicle. Within the teal region in Figure 5.11, the steer angle solutions approach 90° , which is well beyond P1's steering range ($\delta_{max} = 23^\circ$) or even the largest steering ranges found on production vehicles ($\delta_{max} \approx 35^\circ$). The steer angles required to make the $-F_{yF} \sin \delta$ term in Equation 5.20 an effective means for longitudinal control in this scenario are simply not realizable in practice.

5.5 The dilemma of rear drive force control

The original drift controller design uses one input at a time for lateral control, which results in significant variation of the longitudinal dynamics with the input in use. While experiments and phase portraits indicate excellent robustness and convergence characteristics in spite of this characteristic of the closed-loop dynamics, it does make an analytical demonstration of stability difficult.

It would seem that a natural solution to this problem is a modified design that blends inputs in a more coordinated fashion to satisfy lateral control objectives while also enforcing stable, uniform longitudinal dynamics. However, this is not the case, at least for the alternate control design considered here. The conflict between lateral and longitudinal control objectives that causes the variation in longitudinal dynamics in the original design results in a small region of feasibility for the alternate design. In terms of developing a controller with a broad enough region of feasibility to work in experiment, a simple, switching coordination scheme for the inputs proves to be more effective.

Regardless of the particulars of the controller design, a conflict of lateral and longitudinal objectives is an unavoidable physical reality of using the rear drive force input to drift. This conflict makes it difficult to develop a controller for which analytical stability guarantees are straightforward that also has a large region of feasibility. With this in mind, it makes sense to see if both these goals are achievable when using more flexible actuation schemes.

Chapter 6

Additional Actuation

When drifting, a limited ability to increase front lateral force before encountering saturation makes an additional lateral control input essential in order to increase the yaw moment acting on the vehicle. For a standard actuation scheme on a RWD vehicle, this means that the rear drive force must serve double duty as a longitudinal and lateral control input. While this approach enables skilled drivers and controllers alike to successfully drift a vehicle, the rear drive force input's dual role make it difficult to design a controller with a sufficiently large region of feasibility that also enforces closed-loop longitudinal dynamics for which stability guarantees are straightforward.

Suppose now that a vehicle has a third input that can generate a yaw moment. In theory, this additional input could be used to increase yaw moment when the front lateral force is saturated, leaving the rear drive force devoted solely to longitudinal control. Two such inputs that might enable this approach are considered this chapter: rear wheel steering (Section 6.1) and differential torque control at the rear axle (Section 6.2). However, in both cases, a disparity exists between what is conceptually possible with a third actuator and what is actually achievable with that additional actuator.

For the purposes of controlling around a drift equilibrium, Section 6.1 demonstrates that the rear wheel steering input does not actually provide additional flexibility in control design. In fact, it is subject to the same constraint as the rear drive force input when drifting, and cannot be used to generate a yaw moment without

significantly influencing the longitudinal dynamics as well.

Differential torque control at the rear axle, on the other hand, does allow considerable flexibility to specify yaw moment and longitudinal commands independently at the rear axle. However, by developing drift controllers that use this input in Sections 6.2.2 and 6.2.3, it becomes apparent that certain characteristics of the drift control problem are essentially independent of actuator configuration. Even with three inputs, a sliding surface design that enforces first order, stable dynamics for s and e_{U_x} is still better suited to the underlying physics of a drift equilibrium than a three objective design that explicitly decouples and stabilizes each state. Furthermore, like the two-input controller in Section 5.4 that has the same objectives, the three-input sliding surface controller still has a region of infeasibility that results from enforcing first order, stable dynamics for e_{U_x} .

Nevertheless, this controller demonstrates the utility of differential torques at the rear axle for circumventing the challenges that arise from using the rear drive force input for combined lateral and longitudinal control. In particular, this controller has a region of convergence nearly as large that of the original drift controller while also enabling an analytical demonstration of local exponential stability of the desired drift equilibrium.

6.1 Rear wheel steering

6.1.1 Modeling

In the same fashion as front wheel steering, rear wheel steering enables control of the rear tire slip angle and therefore the rear lateral force. There are examples of production systems enabling a few degrees of rear wheel steering capability [15] as well as research testbeds with full range rear wheel steering [3].

Only minor modifications to the bicycle model used thus far are necessary to incorporate a rear wheel steering input. As shown in Figure 6.1, the vehicle now has a front steer angle δ_F and rear steer angle δ_R . With this modification, the governing

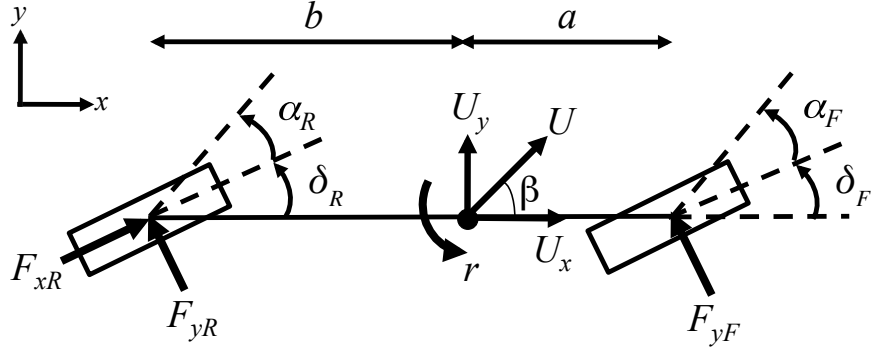


Figure 6.1: Bicycle model of a RWD vehicle with rear wheel steering capability.

equations for sideslip, yaw rate, and longitudinal velocity become:

$$\dot{\beta} = \frac{F_{yF} + F_{yR} \cos \delta_R + F_{xR} \sin \delta_R}{mU_x} - r \quad (6.1a)$$

$$\dot{r} = \frac{aF_{yF} - b(F_{yR} \cos \delta_R + F_{xR} \sin \delta_R)}{I_z} \quad (6.1b)$$

$$\dot{U}_x = \frac{F_{xR} \cos \delta_R - F_{yR} \sin \delta_R - F_{yF} \sin \delta_F}{m} + rU_x\beta. \quad (6.1c)$$

The rear lateral force F_{yR} can be modeled in essentially the same fashion as earlier, by using the rear drive force F_{xR} as a de-rating input. But the rear tire slip angle must be modified to incorporate the effect of the rear steer angle:

$$\alpha_R = \arctan \left(\beta - b \frac{r}{U_x} \right) - \delta_R \quad (6.2)$$

Within the context of drift control design, the rear wheel steering input is of interest because it makes it possible to treat rear lateral force as a direct input, rather than controlling the rear lateral force through rear tire saturation and the rear drive force. This opens up the possibility of controlling F_{yR} independently of F_{xR} , and therefore generating yaw moments using rear wheel steering while the rear drive force is used for longitudinal control.

However, this possibility only exists when the rear tire is not saturated and the rear tire forces are not coupled via the friction circle. When this is the case, rear

wheel steering enables open-loop stable “pseudodrift” equilibria at which the tire slip angles are quite small but the vehicle sideslip is large because the rear wheel is steered out of the turn; these equilibria are considered in Section 6.1.2. As defined in this dissertation, though, drifting inherently involves rear tire saturation. Consequently, rear wheel steering does not actually provide a distinct input from rear drive force for generating yaw moments around a true drift equilibrium, as is demonstrated in Section 6.1.3.

6.1.2 Pseudodrift equilibria

With the addition of rear wheel steering, a vehicle can operate at an arbitrarily defined equilibrium condition, so long as that condition is achievable within actuator and friction limitations. This is simply because three inputs can be used to make any location in a three-dimensional state space (in this case the (β, r, U_x) space) an equilibrium point, subject to the aforementioned constraints. Thus, it should not be surprising that rear wheel steering enables steady-state operation at conditions not achievable with standard inputs.

Suppose that the equilibrium conditions of the model in Equation 6.1 are computed by specifying values for equilibrium sideslip (β^{eq}), longitudinal velocity (U_x^{eq}), and front steer angle δ_F^{eq} while solving for equilibrium yaw rate r^{eq} , rear steer angle (δ_R^{eq}), and rear drive force F_{xR}^{eq} . When β^{eq} is fixed at a large value, some of the corresponding equilibrium conditions involve complete saturation of the rear tire, much like the drift equilibria that exist for standard inputs. But there are also pseudodrift equilibria at which vehicle sideslip angle is large while the tire slip angles and rear drive force are quite small; Figure 6.2 depicts such an equilibrium graphically, showing front and rear steer angles, the velocity vector at the CG, and the velocity vector at the front and rear tire contact patches. In the absence of rear wheel steering, kinematic coupling dictates the rear slip angle must be large if the vehicle sideslip is large, so this is obviously an equilibrium that is not achievable with front wheel steering alone.

Table 6.1 provides data for a pseudodrift equilibrium, as computed using $\delta_F =$

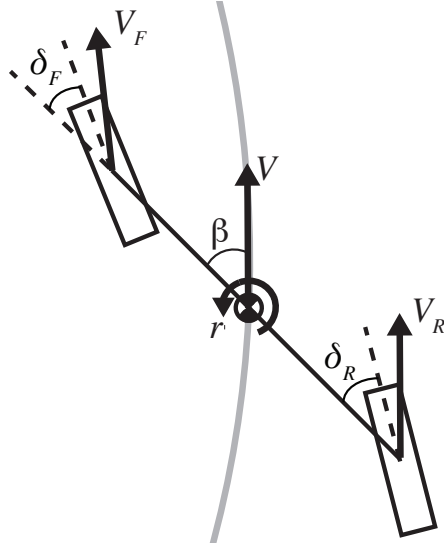


Figure 6.2: Graphical representation of a pseudodrift equilibrium.

-15° , $\beta^{eq} = -20.44^\circ$, and $U_x^{eq} = 8$ m/s (note that the values chosen for β^{eq} and U_x^{eq} are the same as for the drift equilibrium used for control design in the preceding chapters). From this table, the disparity between the vehicle sideslip angle and the tire slip angles is quite obvious. While the vehicle sideslip angle is on the order of 20 degrees in magnitude, both the front and rear tire slip angles are less than 2 degrees in magnitude. This is possible because of significant countersteer at *both* the front and rear tires, which serves to reduce the magnitude of the slip angles at both tires.

Because both tire slip angles are small and the equilibrium rear drive force is quite small, neither the front nor the rear tire is saturated at the pseudodrift equilibrium. As a result, the equilibrium is locally stable; this should be evident from the open-loop phase portrait in Figure 6.3 that has been generated by simulating the model in Equation 6.1 using the equilibrium values for the inputs in Table 6.1.

The observations above suggest that pseudodrift equilibria have far more in common with the typical cornering equilibria than drift equilibria, since typical cornering equilibria are also stable and associated with small tire slip angles and a small rear drive force. Roughly speaking, pseudodrift equilibria can be viewed as offset versions of typical cornering equilibria. At pseudodrift equilibria, large front and rear steer

Parameter	Value
δ_F^{eq}	-15°
δ_R^{eq}	-21.8°
F_{xR}^{eq}	203 N
β^{eq}	-20.44°
r^{eq}	0.43 rad/s
U_x^{eq}	8 m/s
α_F^{eq}	-1.74°
α_R^{eq}	-1.62°

Table 6.1: Pseudodrift equilibrium data

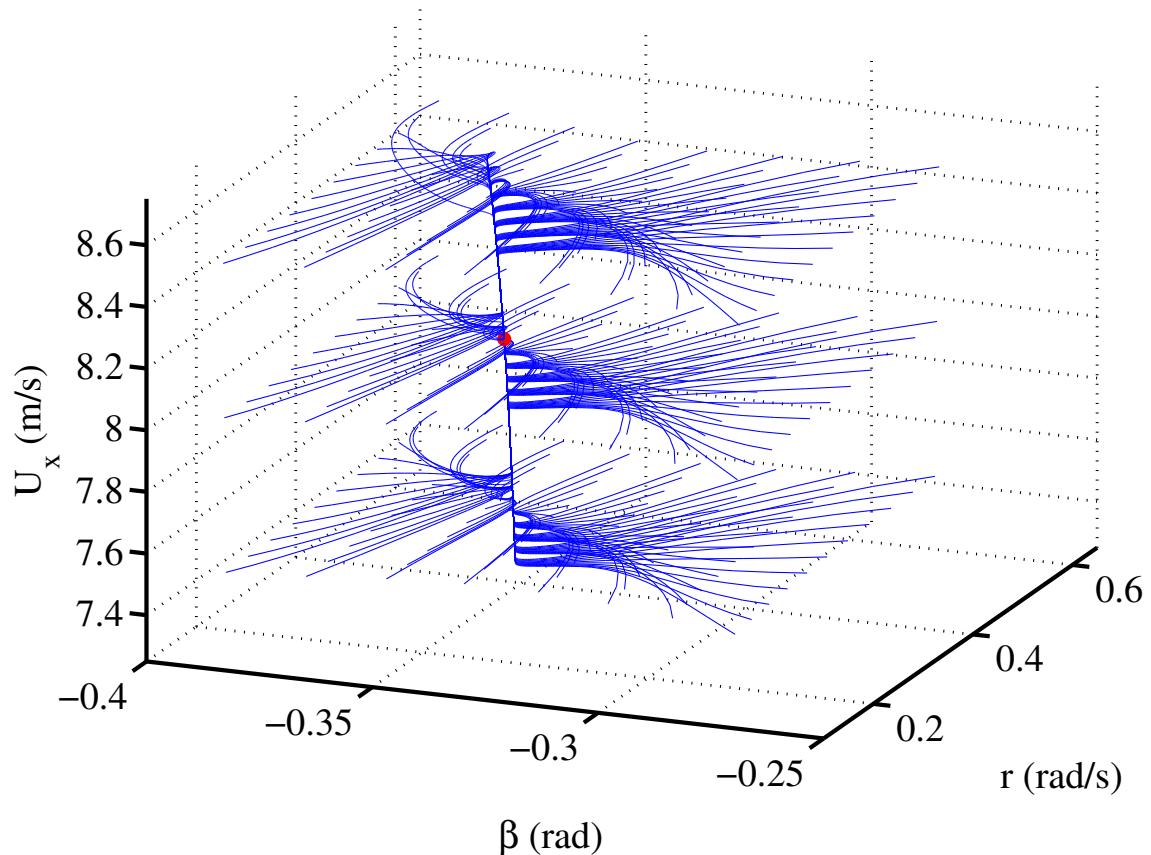


Figure 6.3: Phase portrait of open-loop state trajectories around a pseudodrift equilibrium, perspective view. The red dot denotes the pseudodrift equilibrium location.

angles of the same sign are necessary to make the tire slip angles small. But this combination of steer angles creates a significant angular offset between the heading of the vehicle and the direction of the velocity vectors at the tire contact patches, resulting in a large vehicle sideslip angle. Viewed from this perspective, pseudodrifting equilibria are not particularly interesting within the context of this dissertation, as they do not reflect high-sideslip cornering as it is undertaken by skilled drivers, in the presence of large rear slip angles and rear tire saturation.

6.1.3 Rear wheel steering around a true drift equilibrium

In order to understand the effect of rear wheel steering around a true drift equilibrium, it is helpful to examine control of a saturated rear tire from a slightly different perspective. Thus far, a cartesian representation of the friction circle has been used to model the coupling of lateral and longitudinal forces at the rear tire when it is saturated:

$$\sqrt{F_{xR}^2 + F_{yR}^2} = \mu F_{zR} \quad (6.3)$$

An alternate but physically equivalent representation for friction circle coupling is in terms of the thrust angle ϕ , which describes the angle of the resultant force $F_R = \sqrt{F_{xR}^2 + F_{yR}^2}$ at the rear tire relative to the longitudinal axis of the tire:

$$\phi = \arctan \frac{F_{yR}}{F_{xR}} \quad (6.4)$$

The thrust angle can be used to express rear tire forces in what amounts to a polar coordinate system:

$$F_{xR} = F_R \cos \phi \quad (6.5a)$$

$$F_{yR} = F_R \sin \phi \quad (6.5b)$$

When the rear tire is saturated, friction circle coupling dictates that the rear resultant force $F_R = \mu F_{zR}$. In this case, the expressions for the rear tire forces are only a

function of the thrust angle ϕ :

$$F_{xR} = \mu F_{zR} \cos \phi \quad (6.6a)$$

$$F_{yR} = \mu F_{zR} \sin \phi \quad (6.6b)$$

Using Equation 6.6, the governing equations for the three state bicycle model with standard inputs (front steering and rear drive force) when the rear tire is saturated become:

$$\dot{\beta} = \frac{F_{yF} + \mu F_{zR} \sin \phi}{m U_x} - r \quad (6.7a)$$

$$\dot{r} = \frac{a F_{yF} - b \mu F_{zR} \sin \phi}{I_z} \quad (6.7b)$$

$$\dot{U}_x = \frac{\mu F_{zR} \cos \phi - F_{yF} \sin \delta_F}{m} + r U_x \beta. \quad (6.7c)$$

From this alternate representation, the role of the rear drive force in controlling drifting becomes clear. Modulation of the rear drive force alters the rear thrust angle, and therefore the direction that the saturated resultant force $F_R = \mu F_{zR}$ is pointing. Within the context of this interpretation, a conflict between lateral and longitudinal control objectives can emerge when using the rear drive force input to drift because it is not necessarily possible to point the resultant force in a direction that will satisfy both objectives.

Along the same lines, the governing equations with rear wheel steering and rear tire saturation are as follows:

$$\dot{\beta} = \frac{F_{yF} + \mu F_{zR} (\sin \phi \cos \delta_R + \cos \phi \sin \delta_R)}{m U_x} - r \quad (6.8a)$$

$$\dot{r} = \frac{a F_{yF} - b \mu F_{zR} (\sin \phi \cos \delta_R + \cos \phi \sin \delta_R)}{I_z} \quad (6.8b)$$

$$\dot{U}_x = \frac{\mu F_{zR} (\cos \phi \cos \delta_R - \sin \phi \sin \delta_R) - F_{yF} \sin \delta_F}{m} + r U_x \beta. \quad (6.8c)$$

Applying trigonometric identities for angle addition, the governing equations simplify

to the following expressions:

$$\dot{\beta} = \frac{F_{yF} + \mu F_{zR} \sin(\phi + \delta_R)}{mU_x} - r \quad (6.9a)$$

$$\dot{r} = \frac{aF_{yF} - b\mu F_{zR} \sin(\phi + \delta_R)}{I_z} \quad (6.9b)$$

$$\dot{U}_x = \frac{\mu F_{zR} \cos(\phi + \delta_R) - F_{yF} \sin \delta_F}{m} + rU_x\beta. \quad (6.9c)$$

Equation 6.9 has the same structure as the governing equations for the bicycle model with standard inputs when the rear tire is saturated (Equation 6.7). The only difference is that the thrust angle ϕ is replaced by the sum $\phi + \delta_R$ of the thrust angle and rear steer angle. This means that there is still effectively only one input at the rear tire, in the form of the angle $\phi + \delta_R$ between the saturated resultant force and the longitudinal axis of the vehicle. The ability to control this angle in two different ways does not eliminate the fact that it will not always be possible to point the resultant force in a direction that satisfies both lateral and longitudinal control objectives. Thus, for the purposes of eliminating competition between these objectives when drifting, rear wheel steering does not actually provide any benefits over the rear drive force input alone.

Based on the analysis in Sections 6.1.2 and 6.1.3, rear wheel steering is not a particularly useful form of additional actuation when it comes to drift control. While it can be used to enable high-sideslip cornering with unsaturated tires at pseudodrift equilibria, it does not provide any additional actuation capability around a true drift equilibrium where the rear tire is saturated. In this case, it is not really a distinct input from the rear drive force input. While it can be a useful for drifting vehicles that cannot generate large enough rear drive torques to saturate the rear tires, it is subject to the same conflict of lateral and longitudinal control objectives as the rear drive force input.

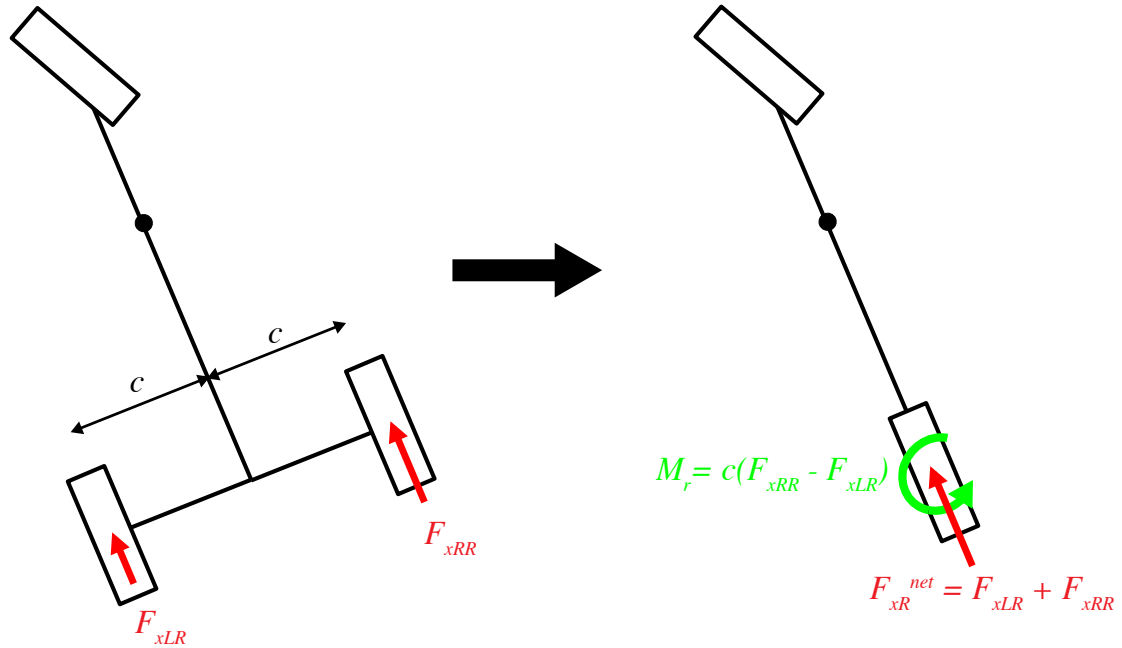


Figure 6.4: Left: Bicycle model with the rear lumped tire expanded to show independent longitudinal force inputs at left rear and right rear tires. Right: Bicycle model with an equivalent rear axle yaw moment and net longitudinal force.

6.2 Differential torque control at the rear axle

6.2.1 Modeling

Within this work, differential torque control at the rear axle refers to the capability to independently control the drive and braking torques at each of the rear wheels, and therefore the longitudinal force generated at each rear wheel. In practice, independent control of rear drive torques could be achieved through the use of torque vectoring systems already available on production vehicles or the use of independent drive motors for each rear wheel. Independent braking capability is already available as part of the ESC systems that are standard on US vehicles as of 2012.

Differential torque control is intriguing from a vehicle control standpoint because it enables an additional way to generate a yaw moment, through differentials in longitudinal force between the left rear and right rear wheels. In order to see this,

consider the left side of Figure 6.4, where the rear lumped tire of the bicycle model has been separated into left rear and right rear tires that are a distance $2c$ apart, where c is the half the track width of the vehicle. The longitudinal force inputs F_{xLR} and F_{xRR} at each rear tire are independent and can be positive (drive) or negative (braking) within the friction limits of the tire. Each of the rear tire forces generates a yaw moment about the CG of the car by acting through a moment arm of length c . By summing the yaw moment contributions from each tire, the total yaw moment M_r generated by the rear axle is given by the following expression:

$$M_r = c(F_{xRR} - F_{xLR}). \quad (6.10)$$

Thus, the rear axle yaw moment is linearly proportional to the longitudinal force differential between the rear tires.

The net longitudinal force F_{xR}^{net} input at the rear axle is simply given by the sum of the longitudinal force contributions from each rear tire:

$$F_{xR}^{net} = F_{xLR} + F_{xRR}. \quad (6.11)$$

Equations 6.10 and 6.11 can be used to modify the three-state bicycle model to incorporate the effect of differential torque control at the rear axle. As shown on the right side of Figure 6.4, the rear lumped tire in the modified model has a net longitudinal force input defined by Equation 6.11 and a yaw moment input defined by Equation 6.10. Taking into account this modification, the dynamics of the bicycle model are now as follows:

$$\dot{\beta} = \frac{F_{yF} + F_{yR}}{mU_x} - r \quad (6.12a)$$

$$\dot{r} = \frac{aF_{yF} - bF_{yR} + M_r}{I_z} = \frac{aF_{yF} - bF_{yR} + c(F_{xRR} - F_{xLR})}{I_z} \quad (6.12b)$$

$$\dot{U}_x = \frac{F_{xR}^{net} - F_{yF} \sin \delta}{m} + rU_x\beta = \frac{(F_{xLR} + F_{xRR}) - F_{yF} \sin \delta}{m} + rU_x\beta. \quad (6.12c)$$

The lateral force F_{yR} for the rear lumped tire must be modeled slightly differently when using differential torque control at the rear axle. In particular, the lateral

forces for each rear tire must be treated independently. In general, this could be accomplished with the coupled brush tire model in Section 2.1.2 applied to each rear tire individually rather than a lumped rear tire. For a drift equilibrium where the equilibrium sideslip β^{eq} is large, though, a simpler approach is possible by recognizing that the slip angles for both rear tires will be very large in the state space around such an equilibrium. In this case, one can safely assume both tires are saturated and the lateral force at each rear tire can be calculated using the friction circle and longitudinal force input for that tire:

$$F_{yRR} = \sqrt{(0.5\mu F_{zR})^2 - F_{xRR}^2} \quad (6.13a)$$

$$F_{yLR} = \sqrt{(0.5\mu F_{zR})^2 - F_{xLR}^2}. \quad (6.13b)$$

Note that Equation 6.13 assumes operation around a left-hand drift equilibrium, meaning that $F_{yRR} > 0$ and $F_{yLR} > 0$. Also note that the friction circles for the individual rear tires both have a radius of $0.5\mu F_{zR}$ because lateral weight transfer effects are neglected in this conceptual study. Equipped with expressions for F_{yLR} and F_{yRR} , the total rear lateral force is simply given by the lateral force contribution from each rear tire:

$$F_{yR} = F_{yLR} + F_{yRR} = \sqrt{(0.5\mu F_{zR})^2 - F_{xRR}^2} + \sqrt{(0.5\mu F_{zR})^2 - F_{xLR}^2}. \quad (6.14)$$

Within the context of this work, differential torque control is potentially useful because of the ability to simultaneously satisfy lateral and longitudinal control objectives by choosing a left-to-right differential in rear longitudinal force (Equation 6.10) *and* a net rear longitudinal force (Equation 6.11). For example, if the vehicle is in danger of exiting the drift while operating at or above the equilibrium longitudinal velocity, it would be ideal to generate a positive yaw moment on the vehicle without disturbing the longitudinal dynamics. When using steering and rear drive force actuation, this is not really possible, as added drive force is the only effective way to generate a positive yaw moment in this scenario. If controlling the rear longitudinal forces independently, however, a large drive force on the right rear wheel and a large

braking force on the left rear wheel can be used to generate a significant positive yaw moment while keeping the net rear longitudinal force relatively small, as might be required to satisfy a longitudinal control objective.

The subsequent sections explore two control designs that take advantage of this new input capability. The first design attempts to enforce stable, decoupled dynamics for all three vehicle states. The second design is a three-input extension of the successive loop structure that has been the basis of drift control design thus far.

6.2.2 Stable decoupled dynamics using differential torque control

Control design

If enough inputs are available, a standard approach in nonlinear control design is to feedback linearize all of a system's states so that they have stable, first order dynamics. With the incorporation of differential torque control at the rear axle, the vehicle has three inputs which theoretically may be used to implement this strategy. Enforcing stable, first order dynamics for the vehicle states relative to their desired equilibrium values amounts to solving the following system of three equations in three unknowns F_{yF} , F_{xLR} , and F_{xRR} :

$$\dot{e}_\beta = \frac{F_{yF} + F_{yR}}{mU_x} - r = -K_\beta e_\beta \quad (6.15a)$$

$$\dot{e}'_r = \frac{aF_{yF} - bF_{yR} + c(F_{xRR} - F_{xLR})}{I_z} = -K_r e'_r \quad (6.15b)$$

$$\dot{e}_{U_x} = \frac{(F_{xLR} + F_{xRR}) - F_{yF} \sin \delta}{m} + rU_x \beta = -K_{U_x} e_{U_x}, \quad (6.15c)$$

where e_β , e'_r , and e_{U_x} are the errors in sideslip, yaw rate, and longitudinal velocity with respect to their equilibrium values, as defined previously. Note that this controller is designed to stabilize e_β and e'_r individually, rather than a linear combination of these states, as is accomplished by the successive loop structure developed in Chapter 4. Such a design is appealing because no additional analysis necessary to establish stability of the closed loop dynamics; the closed-loop dynamics enforced by design

Parameter	Value
δ^{eq}	-12°
F_{xR}^{eq}	2293 N
β^{eq}	-20.44°
r^{eq}	0.6 rad/s
U_x^{eq}	8 m/s
K_β	1 1/s
K_r	1 1/s
K_{U_x}	0.423 1/s

Table 6.2: Parameters used for implementation of the control equation in Equation 6.15.

are stable by inspection.

Controller implementation and analysis

Since the system in Equation 6.15 is very difficult to solve analytically, this control strategy is implemented by solving Equation 6.15 numerically over a dense grid in the (e_β, e'_r, e_{U_x}) space to create a map from state locations to input solutions. A set of solutions has been generated here using the desired drift equilibrium and controller parameters given in Table 6.2 (note that the desired drift equilibrium is also the equilibrium used for analysis in Chapter 5). Since this is a conceptual study of a controller design, the solutions are computed assuming a steering range comparable to that found on production vehicles ($\delta_{max} = 35^\circ$) rather than P1's steering range ($\delta_{max} = 23^\circ$), which can prove quite restrictive when operating at high values of yaw rate and sideslip.

The solution maps in Figures 6.5 through 6.7 provide a visualization of the input solutions when $e_{U_x} = 0$ m/s. Just like the solution maps used for analysis of the control design in Section 5.4, the blue areas of these Figures denote infeasible regions of the state space where the numerical solver did not find an input solution. On the positive side, the solutions computed for the right rear and left rear longitudinal forces (Figures 6.6 and 6.7, respectively) indicate that these inputs are being used in the fashion expected, especially when the vehicle is in danger of exiting the drift. As the

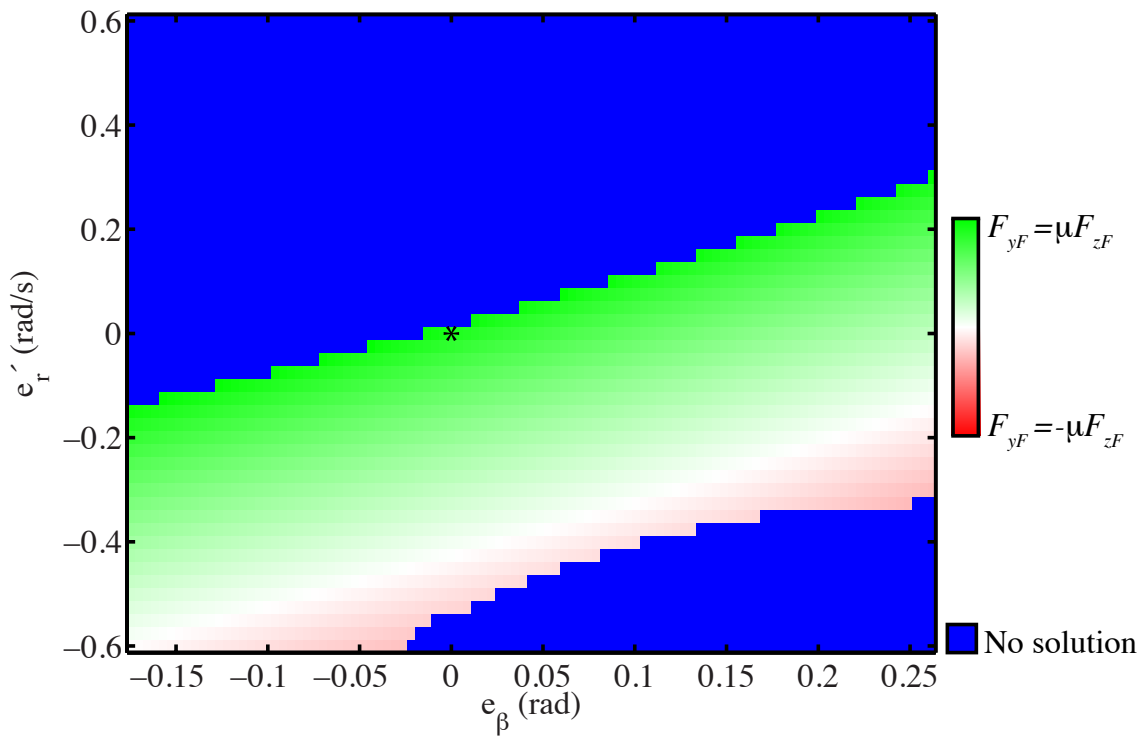


Figure 6.5: Front lateral force solutions for the three-objective drift controller. An asterisk denotes the desired drift equilibrium location.

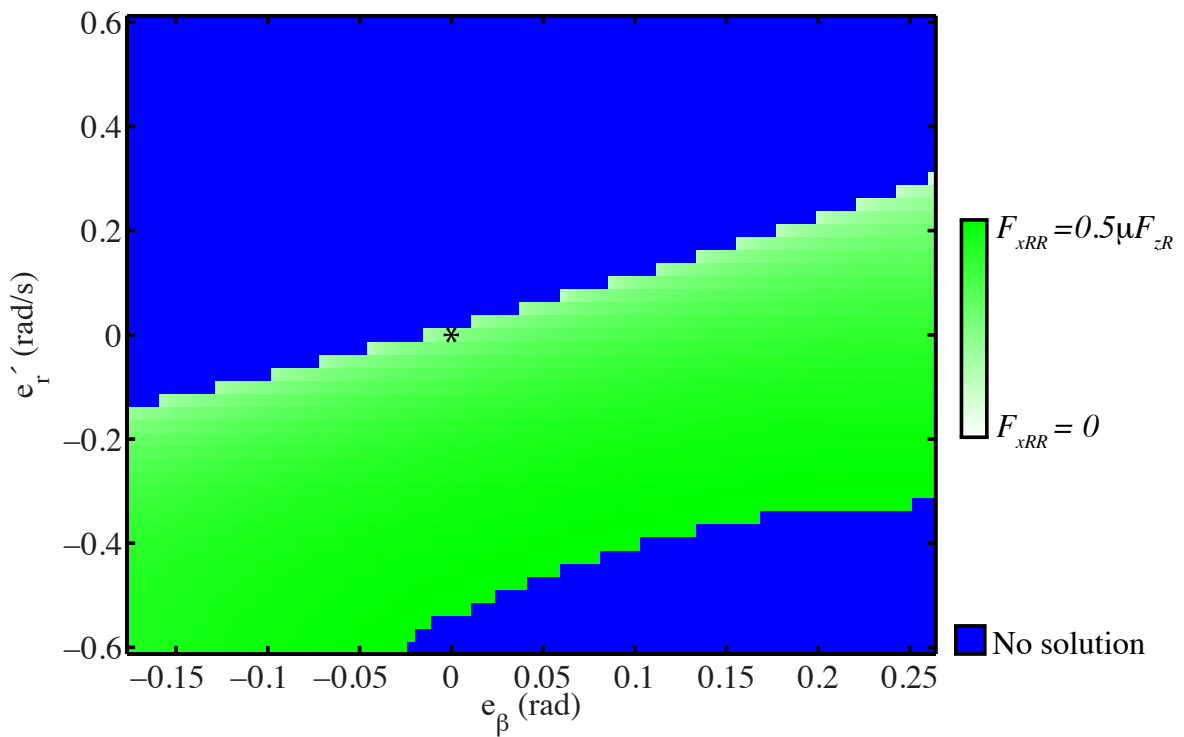


Figure 6.6: Right rear longitudinal force solutions for the three-objective drift controller. An asterisk denotes the desired drift equilibrium location.

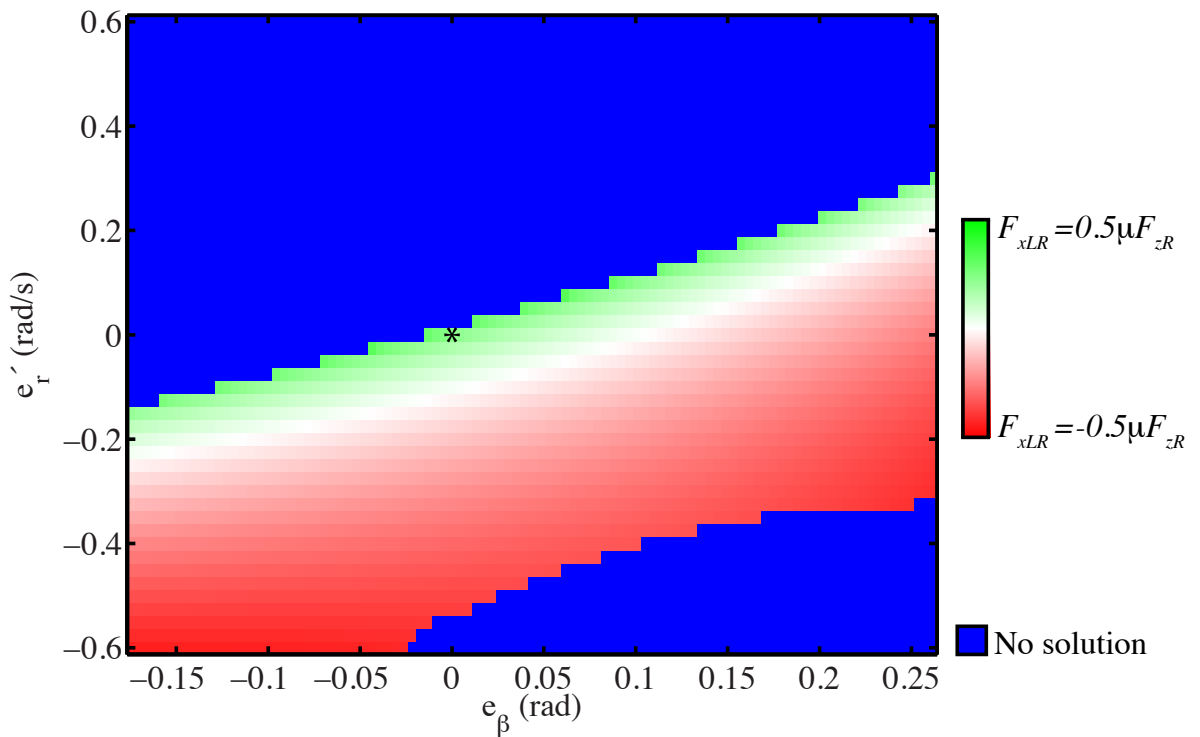


Figure 6.7: Left rear longitudinal force solution for the three-objective drift controller. An asterisk denotes the desired drift equilibrium location.

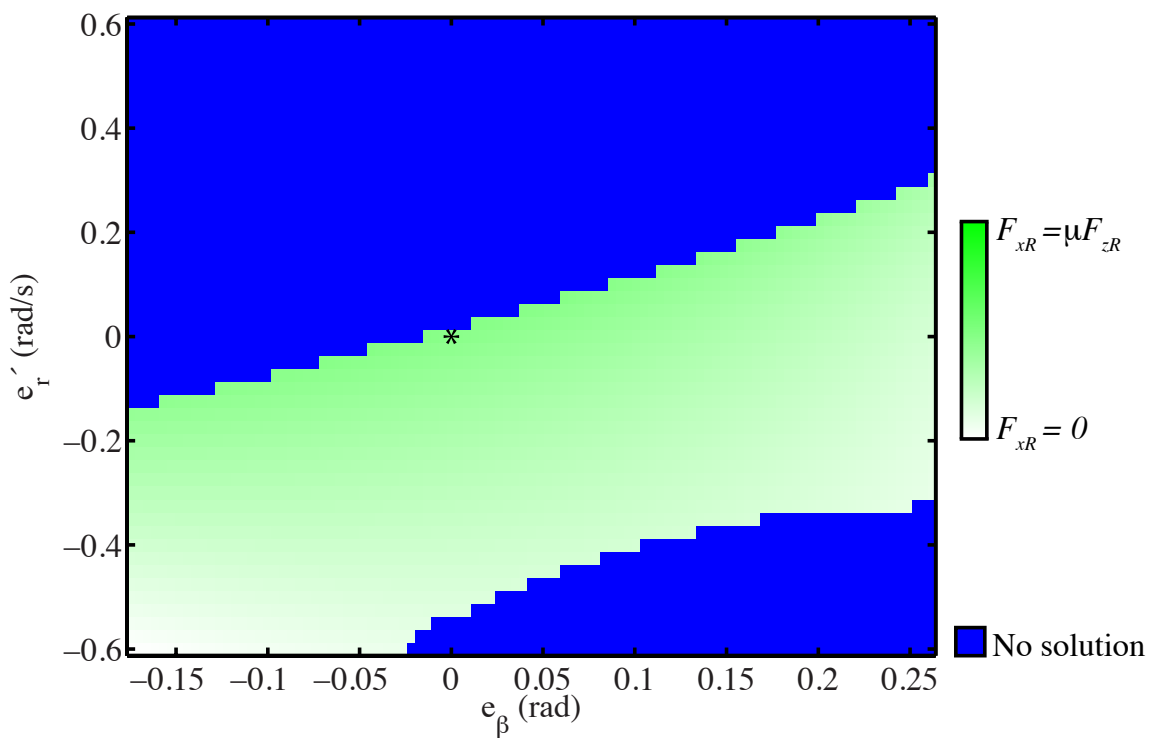


Figure 6.8: Net rear longitudinal force solutions for the three-objective drift controller. An asterisk denotes the desired drift equilibrium location.

vehicle's yaw rate drops below its equilibrium value ($e'_r < 0$), the controller brakes the left rear wheel while driving the right rear wheel, which creates a significant positive yaw moment. At the same time, the net rear longitudinal force (Figure 6.8) is comparatively small, consistent with the fact that less drive force is required for longitudinal control as the magnitude of deceleration due to the $rU_x\beta$ term in Equation 6.15c decreases. Thus, differential torque inputs at the rear axle successfully enable to the controller to satisfy both the lateral and longitudinal control objectives in this scenario.

Unfortunately, the solution maps also indicate that the region of feasibility for this controller is impractically small. Even when $e_{U_x} = 0$ m/s, the desired equilibrium location (denoted by a black asterisk) lies right along the boundary of the large infeasible region occupying the upper portion of Figures 6.5 through 6.8. This means that there will sometimes be no solution to the control equations for small perturbations from the desired drift equilibrium, which severely limits the usefulness of the controller.

This control approach becomes infeasible so close to the desired equilibrium condition because of the way the controller uses the front lateral force input, represented by the solution map in Figure 6.5. As the vehicle state approaches the boundary of the upper infeasible region, the front lateral force command increases until the front tire saturates at the boundary. Because the front lateral force is already nearly saturated at a drift equilibrium, it makes sense that it lies near the boundary of the infeasible region; this is simply a manifestation of a limited ability to increase front lateral force before saturation occurs when operating around a drift equilibrium.

The observed behavior of the front lateral force input is perplexing because it directly conflicts with the intuition developed in this dissertation on the role of yaw moment control in drifting. This intuition dictates that the yaw moment acting on the vehicle should be decreased as the vehicle's yaw rate increases, and vice versa. For yaw moment control through the front steering input, this corresponds to a decrease in front lateral force with increasing yaw rate. The front lateral force commands associated with this controller reflect the exact opposite trend; Figure 6.8 indicates that F_{yF} increases as e'_r increases.

This behavior arises because the controller in this section is predicated upon the idea of controlling the sideslip dynamics directly through tire forces. This is simply not an effective approach because of the RHP zero in the sideslip dynamics when using the front lateral force input. This RHP zero dictates that the direct effect of front lateral force upon the sideslip dynamics is ultimately overwhelmed by the yaw rate term in the sideslip dynamics as a result of the front lateral force acting through the yaw dynamics.

Therefore, when the controller tries control the sideslip dynamics by using F_{yF} to balance the force term $(F_{yF} + F_{yR})/(mU_x)$ and yaw rate term $-r$ in Equation 6.15a, it is fighting the natural dynamics at the drift equilibrium. As r increases for a given sideslip e_β and the controller attempts to increase F_{yF} in response, this effect is further exacerbated by a limited ability to increase front lateral force before the front tire saturates and the controller becomes infeasible.

While feedback linearization in the fashion employed by this design may obscure the underlying dynamics at a drift equilibrium, it does not eliminate these dynamics. Even with the added flexibility of a third input, the drift controller must still take these dynamics into account. The next section uses insights from previous chapters to develop a controller using differential torques that respects the constraints imposed by these dynamics.

6.2.3 Sliding surface control using differential torques

Control design

The successive loop structure used for the preceding designs in this dissertation was chosen in recognition of the RHP zero in the sideslip dynamics when using the front lateral force input. By thinking of yaw rate as a synthetic input to the sideslip dynamics and using tire forces to control yaw rate, this design acknowledged that the yaw rate term in the sideslip dynamics ultimately has a greater effect upon the sideslip dynamics than front lateral force directly. With this in mind, it makes sense to revisit this controller framework here. While the preceding designs used the successive loop structure with two inputs (steering and rear drive force), it is easily adapted to include

differential torques at the rear axle.

Section 5.1 established that the successive loop structure developed in Chapter 4 is equivalent to a sliding surface controller that imposes first order, stable dynamics on a sliding surface variable $s = e'_r + K_\beta e_\beta$. Suppose now that the same approach proposed in Section 5.4 is applied here, where this structure for lateral control is combined with feedback linearization of the longitudinal dynamics to enforce stable, first order dynamics for e_{U_x} . This amounts to the controller simultaneously satisfying the two equations below as its control objectives:

$$\dot{s} = -K_r s \quad (6.16a)$$

$$\dot{e}_{U_x} = -K_{U_x} e_{U_x} \quad (6.16b)$$

Substituting the dynamics of the bicycle model with differential torque inputs at the rear axle (Equation 6.12) into Equation 6.16 leads to the following system of equations:

$$(I) \quad \begin{aligned} \dot{s} &= \left(\frac{a}{I_z} - \frac{K_\beta}{m U_x} \right) F_{yF} - \left(\frac{b}{I_z} + \frac{K_\beta}{m U_x} \right) F_{yR} + \frac{c}{I_z} (F_{xRR} - F_{xLR}) \\ &\quad + K_\beta s + K_\beta^2 e_\beta + K_\beta r^{eq} = -K_r s \end{aligned} \quad (6.17a)$$

$$(II) \quad \dot{e}_{U_x} = \frac{1}{m} (F_{xLR} + F_{xRR} - F_{yF} \sin \delta) + r U_x \beta = -K_{U_x} e_{U_x} \quad (6.17b)$$

These control equations are quite similar to the ones for the design considered in Section 5.4, but with modifications to reflect differential torque control capability at the rear axle. These modifications are intriguing from a control design standpoint because there are now three inputs (F_{yF} , F_{xLR} , F_{xRR}) available to satisfy two control objectives. This allows for increased flexibility in control design that will be leveraged to make stronger stability statements for this drift controller than the prior designs in this dissertation.

Considering that the dynamics enforced by the controller for s and e_{U_x} in Equation 6.16 are stable by inspection, the main challenge in making stability statements is the closed-loop sideslip dynamics, which are not explicitly stabilized by the controller.

For any combination of three inputs satisfying the control law in Equation 6.16, the closed-loop sideslip dynamics will take the same form that they do for the two-input sliding surface controllers in Chapter 5:

$$\dot{e}_\beta = -K_\beta e_\beta - s + \Delta_\beta, \quad (6.18)$$

where Δ_β is a nonlinearity reflecting the deviation of the force terms in the sideslip dynamics from their equilibrium values:

$$\Delta_\beta = \frac{F_{yF} + F_{yR}}{mU_x} - \frac{F_{yF}^{eq} + F_{yR}^{eq}}{mU_x^{eq}}. \quad (6.19)$$

This nonlinearity is the primary source of difficulty in a stability analysis, since the other two terms in Equation 6.18 are linear.

Any attempt to analytically demonstrate local stability of the desired drift equilibrium in some bounded region \mathcal{S} around the equilibrium must account for the nonlinearity in Equation 6.19 in some fashion. One approach for doing this is to locally bound the nonlinearity in Equation 6.18 over \mathcal{S} . Obviously, this requires that Δ_β is actually a boundable quantity in \mathcal{S} . The lateral force terms F_{yF} and F_{yR} appearing in the Equation 6.18 are not problematic in this respect because their values are restricted by the friction limits of the tires, regardless of state location. The U_x term in the denominator of Equation 6.19 requires that \mathcal{S} only includes state locations where $U_x > 0$ in order for Δ_β to be boundable in \mathcal{S} ; this is a simple consequence of the fact that Δ_β is unbounded when $U_x = 0$.

Therefore, for a set of state locations \mathcal{S} satisfying the conditions enumerated in the preceding paragraph, it should be possible to bound Δ_β . The flexibility of three inputs when satisfying only two control objectives proves quite useful for establishing such a bound. Suppose that the control inputs F_{yF} , F_{xRR} , and F_{xLR} are chosen in \mathcal{S} such that they not only satisfy the control laws in Equation 6.17 but also enforce a bound on Δ_β^2 using a quadratic function of the vehicle state $x = [e_\beta \ s \ e_{U_x}]^T$:

$$\Delta_\beta^2 \leq x^T Q x \quad \text{for } x \in \mathcal{S}, \quad (6.20)$$

where Q is a diagonal matrix that contains the bound weighting factors $q_\beta > 0$, $q_s > 0$, and $q_{U_x} > 0$:

$$Q = \begin{bmatrix} q_\beta & 0 & 0 \\ 0 & q_s & 0 \\ 0 & 0 & q_{U_x} \end{bmatrix}. \quad (6.21)$$

Equipped with this bound, the closed-loop dynamics within \mathcal{S} can be described as follows:

when $x \in \mathcal{S}$:

$$\dot{x} = A^{CL}x + B^{NL}\Delta_\beta \quad (6.22a)$$

$$\Delta_\beta^2 \leq x^T Q x, \quad (6.22b)$$

where the closed-loop dynamics matrix A^{CL} and input nonlinearity matrix B^{NL} are defined in Equations 6.23 and 6.24, respectively:

$$A^{CL} = \begin{bmatrix} -K_\beta & -1 & 0 \\ 0 & -K_r & 0 \\ 0 & 0 & -K_{U_x} \end{bmatrix} \quad (6.23)$$

$$B^{NL} = \begin{bmatrix} 1 \\ 0 \\ 0 \end{bmatrix} \quad (6.24)$$

The closed-loop dynamics and bound on Δ_β as expressed in Equation 6.22 are quite convenient from a stability analysis standpoint. As demonstrated in a subsequent section, the representation in Equation 6.22 makes it straightforward to derive a linear matrix inequality (LMI) that can be used to produce a Lyapunov function certifying exponential stability of the system within \mathcal{S} .

Of course, this representation is predicated on having a technique for determining control inputs at a given state location that enforce the desired dynamics for s and e_{U_x} while also satisfying the sideslip nonlinearity bound. An optimization-based approach is employed here for this purpose. With this approach, the problem of computing

control inputs at a given state location amounts to finding inputs that minimize a cost function subject to six constraints, summarized below and labeled using the Roman numerals (I) through (VI).

(I) and (II) are nonlinear equality constraints representing the control laws to enforce the desired dynamics for s and e_{U_x} and are labeled accordingly in Equation 6.17. (III) is an inequality constraint representing the bound on the sideslip nonlinearity in Equation 6.20 written out in terms of tire forces and expressed in a slightly different form:

$$(III) \quad \left| \frac{F_{yF} + F_{yR}}{mU_x} - \frac{F_{yF}^{eq} + F_{yR}^{eq}}{mU_x^{eq}} \right| \leq \sqrt{q_\beta e_\beta^2 + q_r s^2 + q_{U_x} \cdot e_{U_x}^2} \quad (6.25)$$

Finally, (IV) through (VI) are inequality constraints that reflect input limitations due to friction:

$$(IV) \quad -\mu F_{zF} \leq F_{yF} \leq \mu F_{zF} \quad (6.26a)$$

$$(V) \quad -0.5\mu F_{zR} \leq F_{xRR} \leq 0.5\mu F_{zR} \quad (6.26b)$$

$$(VI) \quad -0.5\mu F_{zR} \leq F_{xLR} \leq 0.5\mu F_{zR}. \quad (6.26c)$$

Combining constraints (I) through (VI) with a quadratic cost on actuator effort that is based upon deviations of the inputs from their equilibrium values leads to this optimization problem:

for variables F_{yF}, F_{xRR}, F_{xLR}

$$\text{minimize} \quad (F_{yF} - F_{yF}^{eq})^2 + (F_{xRR} - F_{xRR}^{eq})^2 + (F_{xLR} - F_{xLR}^{eq})^2 \quad (6.27a)$$

$$\text{subject to} \quad (I)-(VI) \quad (6.27b)$$

Since (I) and (II) are nonlinear equality constraints, the optimization problem in Equation 6.27 is not convex. As a result, the solutions to Equation 6.27 around a desired drift equilibrium may represent local (rather than global) minima. In this analysis, however, global optimality of the input solutions with respect to the objective in Equation 6.27a is not of particularly great concern. Optimization is being

used here primarily as a way to coordinate three inputs to drift a vehicle and gain physical insight from the solutions computed.

However, non-convexity of Equation 6.27 also implies that multiple solutions (corresponding to different local minima) may be possible at a given state location. As described later on, this means that special care must be taken when numerically solving Equation 6.27 to ensure smoothness of the solutions around a desired drift equilibrium.

Computation of a stability guarantee using LMIs

In theory, solution of the optimization problem in Equation 6.27 will yield a region \mathcal{S} around the drift equilibrium in which the closed-loop dynamics and sideslip non-linearity are described by Equation 6.22. In concrete terms, \mathcal{S} will correspond to the region of feasibility for the optimization problem (e.g., the region around the desired drift equilibrium where the optimization problem in Equation 6.27 has solutions).

Local exponential stability within \mathcal{S} can be demonstrated by finding a Lyapunov function of the form $V(x) = x^T Px$ ($P \succ 0$, $P = P^T$) such that the following condition on the time derivative $\dot{V}(x)$ of the Lyapunov function holds for some $\rho > 0$ when $x \in \mathcal{S}$:

$$\dot{V}(x) \leq -\rho V(x) \quad (6.28)$$

For the dynamics in Equation 6.22, Equation 6.28 translates to this pair of conditions for all $x \in \mathcal{S}$:

$$x^T(A^{CL}P + PA^{CL})x + x^T PB^{NL}\Delta_\beta + \Delta_\beta B^{NL^T}Px \leq -\rho x^T Px \quad (6.29a)$$

$$\text{when } \Delta_\beta^2 \leq x^T Q x. \quad (6.29b)$$

Using an augmented state vector $\begin{bmatrix} x & \Delta_\beta \end{bmatrix}^T$, Equation 6.29 can be re-written in matrix

form :

$$\begin{bmatrix} x \\ \Delta_\beta \end{bmatrix}^T \begin{bmatrix} A^{CL}P + PA^{CL} + \rho P & PB^{NL} \\ B^{NL^T}P & 0 \end{bmatrix} \begin{bmatrix} x \\ \Delta_\beta \end{bmatrix} \leq 0 \quad (6.30a)$$

$$\text{when } \begin{bmatrix} x \\ \Delta_\beta \end{bmatrix}^T \begin{bmatrix} -Q & 0 \\ 0 & 1 \end{bmatrix} \begin{bmatrix} x \\ \Delta_\beta \end{bmatrix} \leq 0 \quad (6.30b)$$

By inspection of Equation 6.30, the conditions for stability can be expressed in terms of a pair of linear matrix inequalities (LMIs):

$$\begin{bmatrix} A^{CL}P + PA^{CL} + \rho P & PB^{NL} \\ B^{NL^T}P & 0 \end{bmatrix} \preceq 0 \quad (6.31a)$$

$$\text{when } \begin{bmatrix} -Q & 0 \\ 0 & 1 \end{bmatrix} \preceq 0 \quad (6.31b)$$

By applying the s-procedure for LMIs [7], the pair of LMIs in Equation 6.31 can be reduced to a single LMI if there exists a scalar $\tau \geq 0$ such that the following is true:

$$\begin{bmatrix} A^{CL}P + PA^{CL} + \rho P & PB^{NL} \\ B^{NL^T}P & 0 \end{bmatrix} \preceq \tau \begin{bmatrix} -Q & 0 \\ 0 & 1 \end{bmatrix} \quad (6.32)$$

Along with the conditions $\tau > 0$, $P = P^T$, and $P \succ 0$, the LMI in Equation 6.32 can be used to formulate a semidefinite program (SDP) to find a Lyapunov function demonstrating exponential stability of the system in \mathcal{S} . This SDP would be a feasibility problem intended to find *some* P satisfying all the required conditions, but not necessarily an ideal solution for P in terms of demonstrating a large region of convergence for the system.

This is because the resulting P would not necessarily account for the natural energy characteristics of a vehicle. Generally speaking, most of a vehicle's kinetic energy is associated with the vehicle's longitudinal velocity U_x . This is relevant in formulating Lyapunov functions for vehicle dynamics because these functions have energy-like characteristics. If a Lyapunov function $V(x)$ places a similar weighting on

all three states (that is to say, P_{11} , P_{22} , and P_{33} have comparable magnitude), most of the “energy” associated with $V(x)$ will come from the $P_{33}e_{U_x}^2$ term. In this case, a region of convergence defined using a level curve of $V(x)$ will be quite conservative in the e_{U_x} direction because of all the “energy” that is associated with e_{U_x} . With this in mind, it makes sense to formulate $V(x)$ so that it is de-sensitized to the energy stored in the vehicle’s longitudinal mode.

This can be done by augmenting the feasibility SDP proposed above to include a linear objective function that minimizes P_{33} :

$$\text{for variables } P, \tau$$

$$\text{minimize } P_{33} \quad (6.33a)$$

$$\text{subject to } P = P^T \quad (6.33b)$$

$$P \succeq \epsilon I \quad (6.33c)$$

$$\tau \geq 0 \quad (6.33d)$$

$$\begin{bmatrix} A^{CL}P + PA^{CL} + \rho P + \tau Q & PB^{NL} \\ B^{NLT}P & -1 \end{bmatrix} \preceq 0 \quad (6.33e)$$

The matrix inequality in Equation 6.33c is a non-strict approximation to the strict inequality $P \succ 0$ that enforces positive definiteness of P . This approximation requires that the eigenvalues of P are greater than some value ϵ , where ϵ is a small positive number. $\epsilon = 0.01$ has been used for the results generated here.

It is important to note that the SDP in Equation 6.33 imposes a stricter stability condition than is required for the drift controller under consideration. This SDP seeks to find a Lyapunov function certifying *global* exponential stability of a system whose dynamics are given by Equation 6.22 everywhere in the state space. Thus, if the SDP should prove infeasible, it is not necessarily impossible to demonstrate local exponential stability within the region \mathcal{S} where these dynamics actually apply. If the SDP does yield a solution, however, it obviously applies for all $x \in \mathcal{S}$. Fortunately, the latter case proves to be true for the controller implementation presented in the next section.

Parameter	Value
K_β	2 1/s
K_r	4 1/s
K_{U_x}	0.423 1/s
q_β	3.9
q_s	3.9
q_{U_x}	0.01

Table 6.3: Parameters used for solution of the optimization problem in Equation 6.27

Implementation and analysis

The results presented below have been generated using the drift equilibrium in Table 6.2 and the parameter set given in Table 6.3. Note that the controller gains (K_β , K_r , K_{U_x}) in Table 6.3 are the same as the ones used for analysis in Chapter 5. As in the preceding section, it is assumed that $\delta_{max} = 35^\circ$ when evaluating the controller to reflect the steering range available on a production vehicle, rather than the more restrictive steering range available on P1.

The weighting factors (q_β , q_s , and q_{U_x}) for the sideslip nonlinearity bound in Equation 6.25 are also provided in Table 6.3. Note that q_{U_x} is significantly smaller than q_β or q_s because e_{U_x} can be an order of magnitude larger than e_β and s under normal conditions. In light of this disparity in magnitude, a similar weighting on e_{U_x} as e_β and e'_r would lead to an overly conservative bound on the sideslip nonlinearity.

Controller inputs have been computed by solving the optimization problem in Equation 6.27 over a dense grid of state locations using a MATLAB implementation of the interior point algorithm in [8]. In order to help ensure smoothness of the controller inputs, solutions to Equation 6.27 have been generated by starting at the equilibrium (where the input solutions are already known) and working outward, using the nearest computed solution (from an adjacent location in the grid) as an initial guess at each state location. As with the numerical controller implementations presented earlier, the inputs computed in this fashion have been used to assemble lookup tables from state locations to their corresponding input solutions.

Figures 6.9 through 6.11 show a phase portrait of the closed-loop dynamics of the

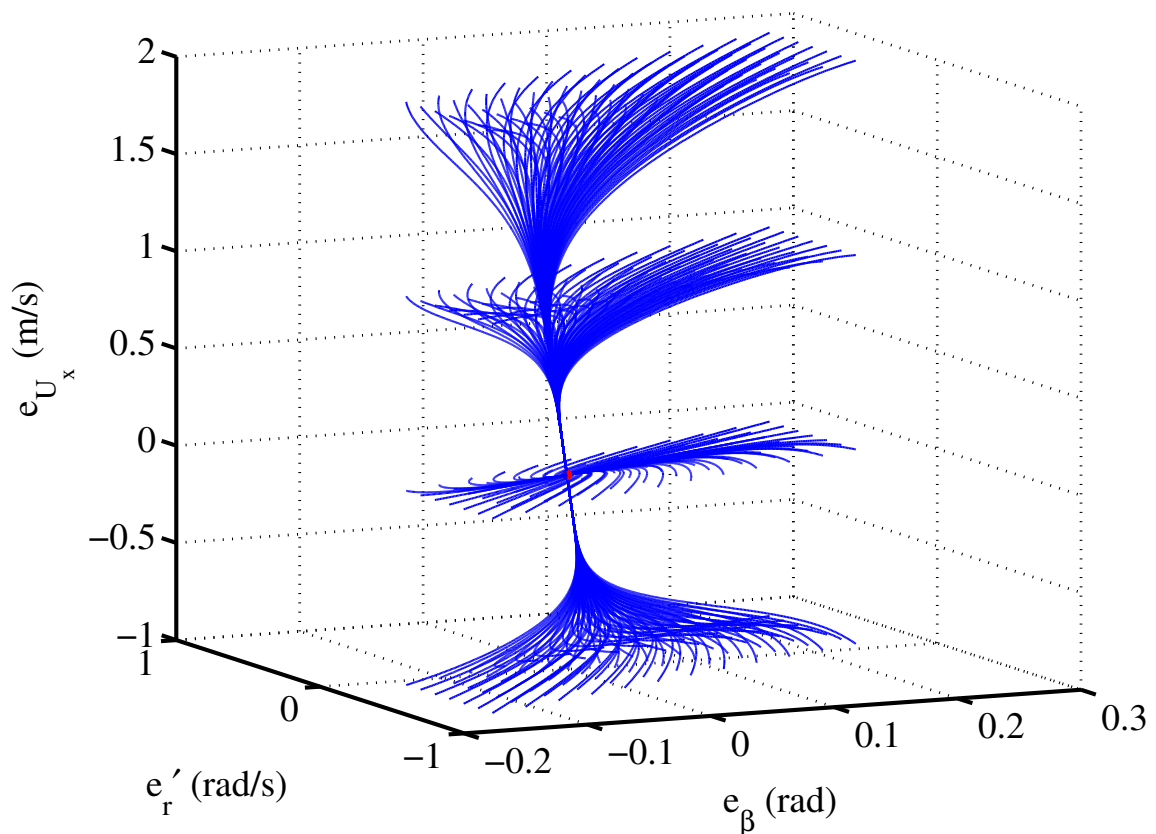


Figure 6.9: Phase portrait of closed-loop state trajectories for the three-input sliding surface controller, perspective view. The red dot denotes the desired drift equilibrium location.

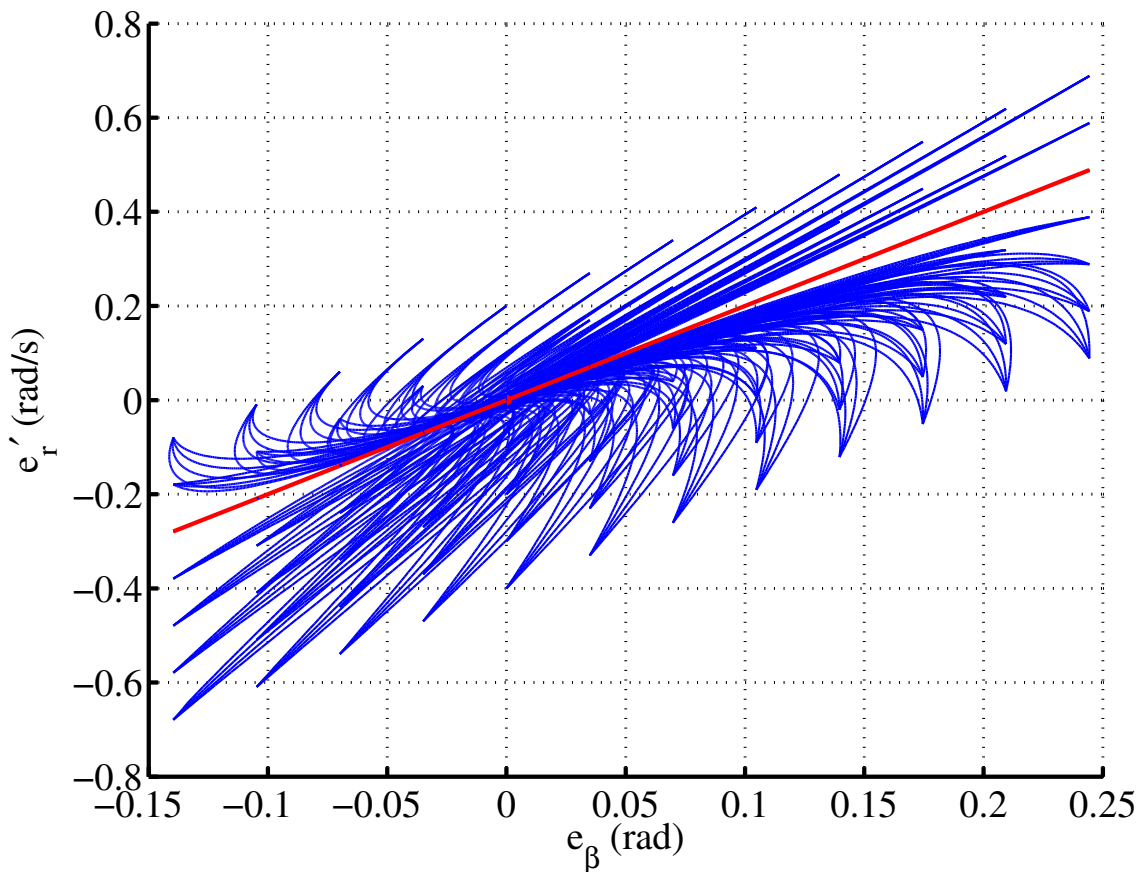


Figure 6.10: Phase portrait of closed-loop state trajectories for the three-input sliding surface controller, viewed from the (e_β, e'_r) plane. The red line denotes the $s = 0$ plane.

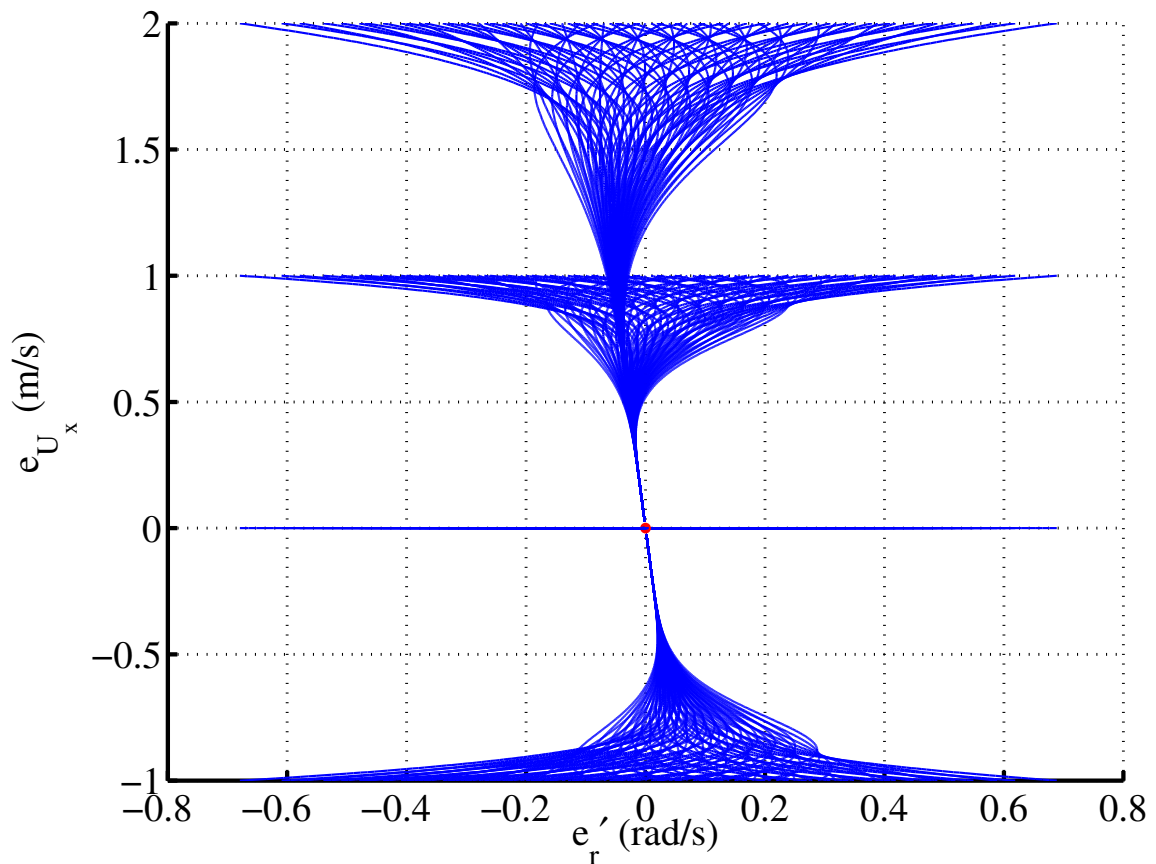


Figure 6.11: Phase portrait of closed-loop state trajectories for the three-input sliding surface controller, viewed from the (e'_r, e_{U_x}) plane. The red dot denotes the desired drift equilibrium location.

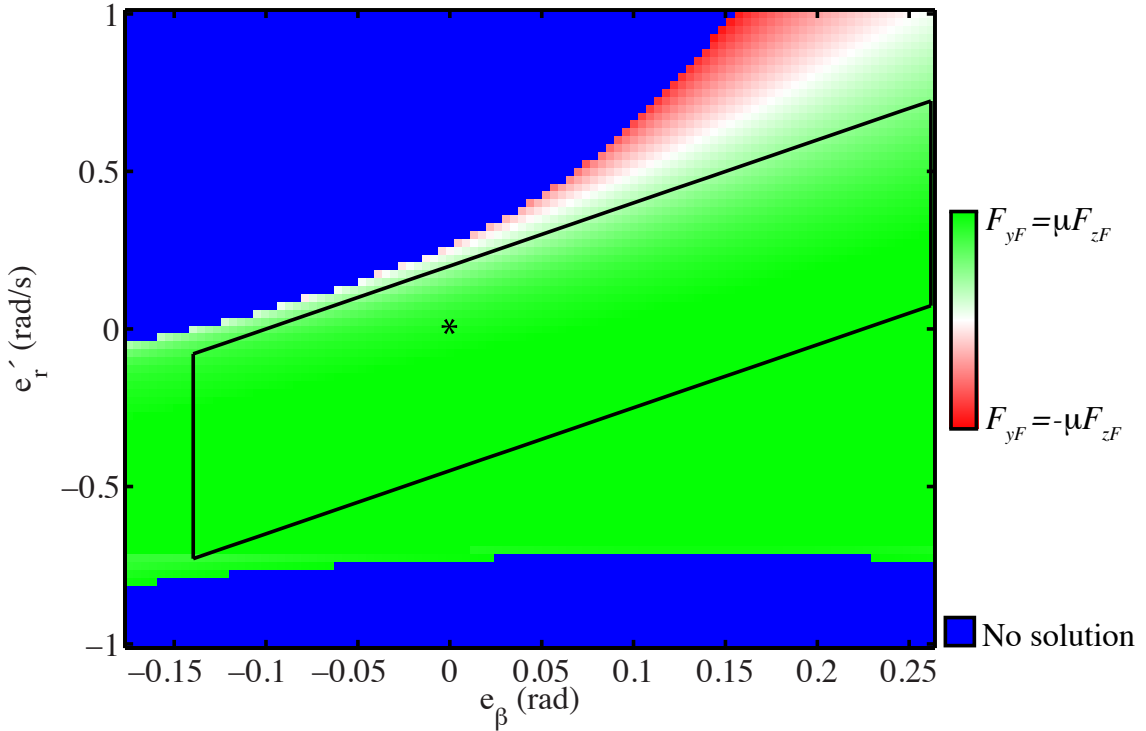


Figure 6.12: Front lateral force solutions for the three-input sliding surface design. The black boundary denotes the range of initial conditions in e_β and e'_r used in the phase portrait for this controller. The asterisk denotes the desired drift equilibrium location.

vehicle when using the controller derived from solutions of Equation 6.27. The phase portrait clearly indicates that the controller stabilizes the desired drift equilibrium and creates a large region of convergence around the equilibrium. Nonetheless, the region of convergence is still somewhat smaller than the one established for the original drift controller design through phase portrait analysis (Figures 5.3 through 5.5) because the region of feasibility is smaller for this design.

In order to see this, consider the solution maps for this controller when $e_{U_x} = 0$ in Figures 6.12 through 6.15, where the blue areas once again denote infeasible regions of the state space. Relative to the similar two-input design in Section 5.4 (Figures 5.11 through 5.13), this controller allows operation over a considerably broader range of states in the lower half of the map, where conflict between lateral and longitudinal

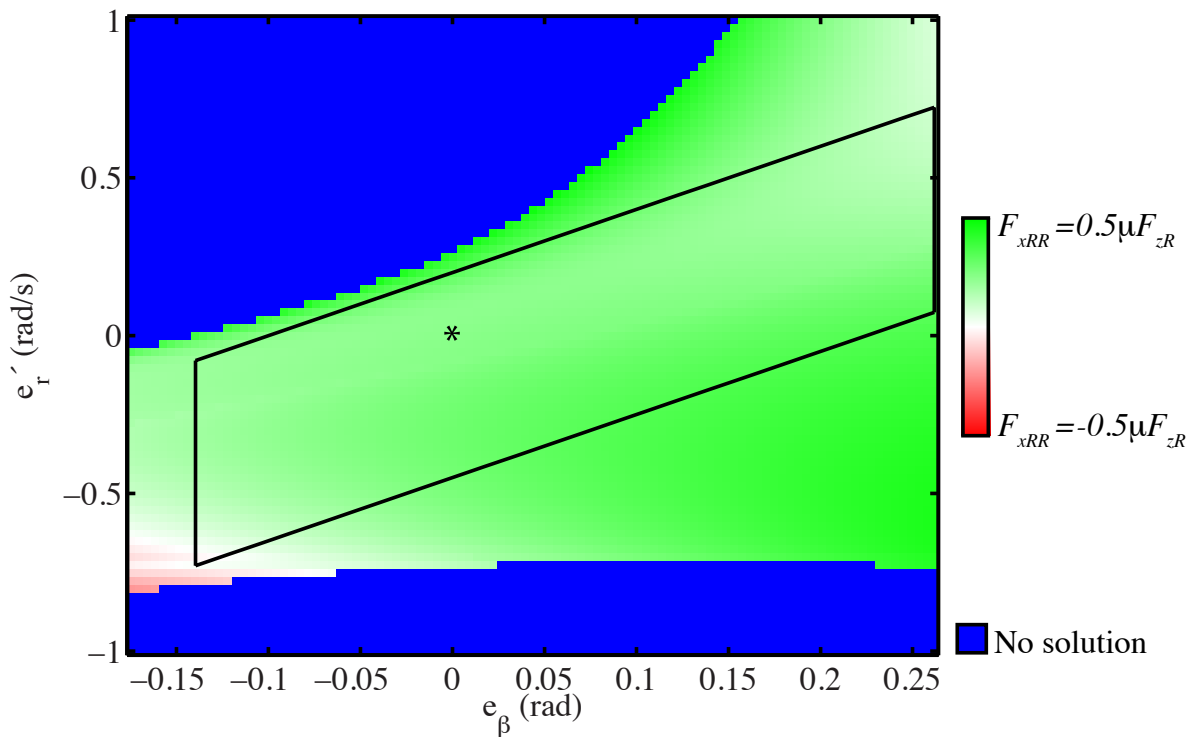


Figure 6.13: Right rear longitudinal force solutions for the three-input sliding surface design. The black boundary denotes the range of initial conditions in e_β and e'_r used in the phase portrait for this controller. The asterisk denotes the desired drift equilibrium location.

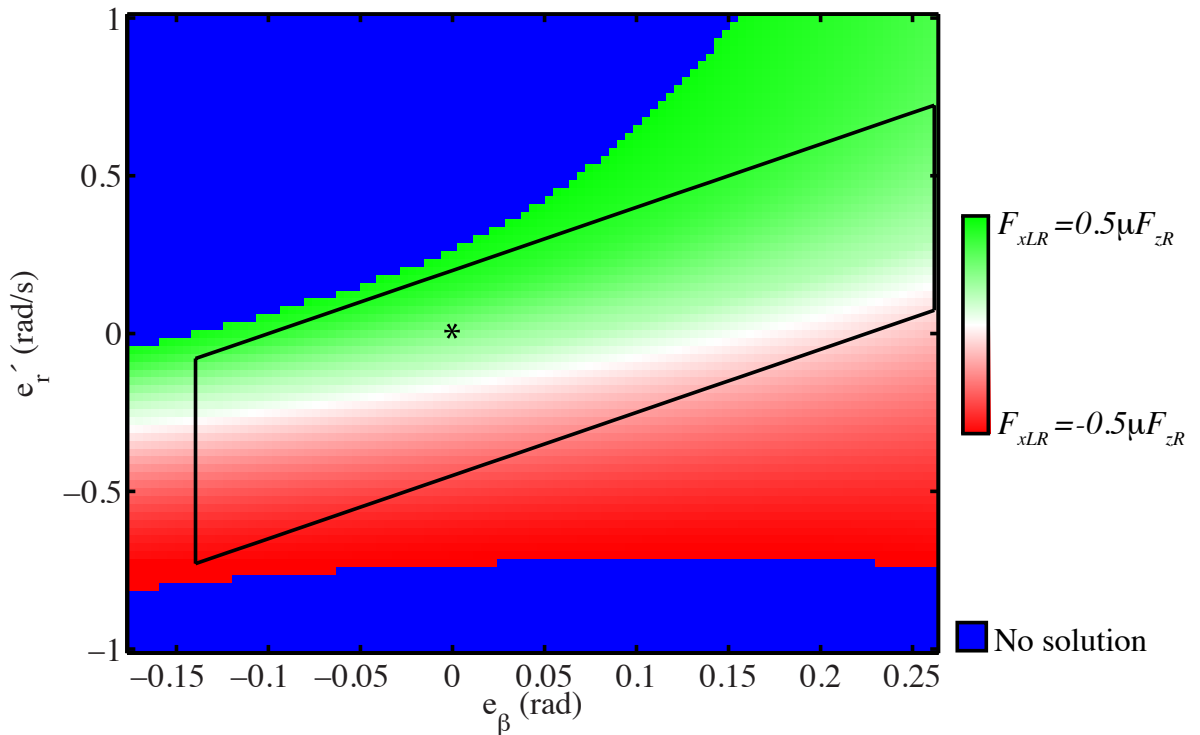


Figure 6.14: Left rear longitudinal force solution for the three-input sliding surface design. The black boundary denotes the range of initial conditions in e_β and e'_r used in the phase portrait for this controller. The asterisk denotes the desired drift equilibrium location.

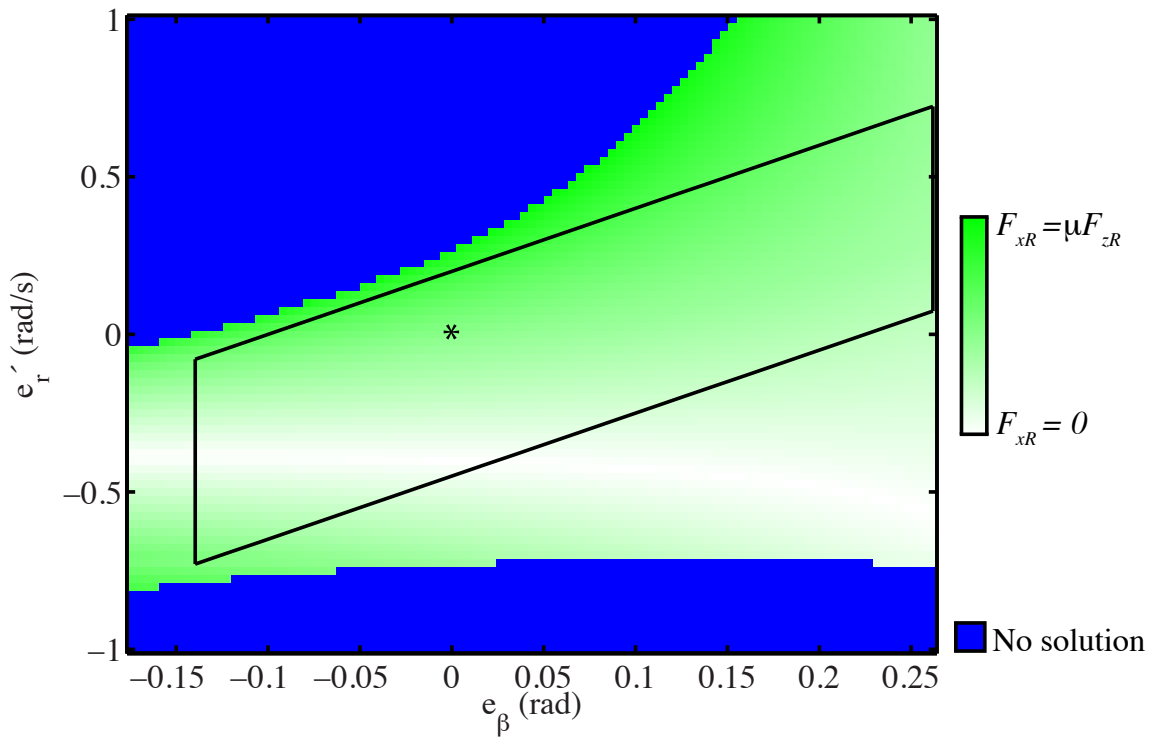


Figure 6.15: Net rear longitudinal force solutions for the three-input sliding surface design. The black boundary denotes the range of initial conditions in e_β and e'_r used in the phase portrait for this controller. The asterisk denotes the desired drift equilibrium location.

control objectives made the two-input controller infeasible. This improvement reflects the benefit of using differential torque control to generate a positive yaw moment through braking at the left rear wheel (Figure 6.14) and drive force at the right rear wheel (Figure 6.13).

The infeasible region occurring along the bottom edge of the solution maps arises because the controller is braking the left rear wheel at its friction limit in order to generate a positive yaw moment of sufficient magnitude. Relative to the initial conditions considered in the phase portrait (indicated by the black boundary in the solution maps), this infeasible region only becomes an issue when both e_β and e'_r are large and negative, meaning that the vehicle simultaneously has a large sideslip angle and low yaw rate, and this state condition is not commonly encountered in practice.

The other infeasible region that appears in the maps, however, is considerably more restrictive. This region, situated in the upper left corner of the solution maps, arises where both the right rear and left rear wheels are being driven at their friction limits, as shown in Figures 6.13 and 6.14.

This region is very similar in shape, size, and location to an infeasible region encountered for the two-input sliding surface design in Section 5.4, as should be evident from the solution maps for this controller in Figures 5.11 through 5.13. This is because the physics that are responsible for this infeasible region are unaffected by the addition of differential torque control. Enforcing stable, first order dynamics for e_{U_x} still requires cancellation of the $rU_x\beta$ term in the longitudinal dynamics using the net rear drive force $F_{xR}^{net} = F_{xLR} + F_{xRR}$, as shown in Equation 6.17b. Along the boundary of the infeasible region in question, the net rear drive force that is necessary to counter deceleration due to the $rU_x\beta$ term approaches the friction limit of the rear axle, as shown in Figure 6.15. Since the infeasible region arises from a constraint on the net rear drive force, the ability to control the rear longitudinal forces independently does little to influence the shape or size of this region.

In addition to restricting the range of operation for the the controller, this infeasible region also limits the stability statements that can be made using the Lyapunov function found by solving the SDP in Equation 6.33. For the controller parameters considered here and exponential decay parameter $\rho = 0.05$, solution of this SDP using

the convex optimization software CVX [32, 18] yields the matrix P below:

$$P = \begin{bmatrix} 0.4966 & -0.1265 & 0 \\ -0.1265 & 0.2417 & 0 \\ 0 & 0 & 0.01 \end{bmatrix}. \quad (6.34)$$

The Lyapunov function $V(x) = x^T P x$ with P as defined in Equation 6.34 demonstrates local exponential stability of the desired drift equilibrium and is valid anywhere within the feasible region of the controller . This represents the strongest stability statement made for any of the drift controllers considered in this dissertation.

In spite of this, the region of convergence computed using $V(x)$ ends up being rather conservative because of the restrictive infeasible region described earlier. The best possible estimate for the region of convergence using $V(x)$ is given by the largest level curve $V(x) = V_0^{\max}$ that fits within the feasible region for the controller. Figure 6.16 depicts an approximation to $V(x) = V_0^{\max}$ computed by finding the largest level curve that is contained within the range of initial conditions used for the phase portrait in Figures 6.9 through 6.11. When compared to the infeasible regions for the controller when $e_{U_x} = 0$, it is clear that the upper left infeasible region constrains the maximum size of the level curve and is responsible for the conservatism of the estimate. Because the feasible region for the controller is so asymmetric about the equilibrium, any region of convergence calculated using a function that is symmetric about the equilibrium (such as an ellipsoid) will inevitably be a conservative estimate of the true region of convergence.

In terms of addressing the conflict between lateral and longitudinal control objectives that arises with the rear drive force input, the controller presented above is successful. When using the rear drive force input for control design, it proved difficult to develop a controller that facilitates analytical stability guarantees that also has a large region of feasibility. By incorporating differential torques at the rear axle into the sliding surface structure, it becomes straightforward to analytically demonstrate local exponential stability of the drift equilibrium while also having a relatively large region of feasibility.

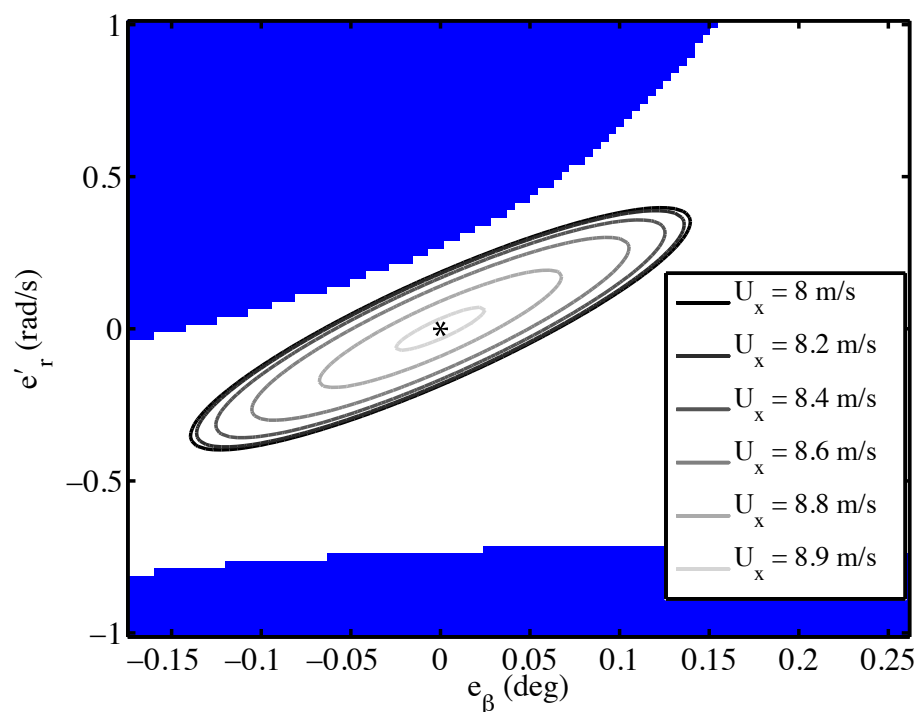


Figure 6.16: Approximate region of convergence calculated using the Lyapunov function defined by Equation 6.34 as compared to the infeasible region when $e_{U_x} = 0$ for the three-input sliding surface controller.

Nevertheless, the region of feasibility for this controller is still somewhat smaller than that for the original drift controller design because of the excessive rear drive force needed to enforce first-order, stable longitudinal dynamics. This result represents a challenge of the drift control problem that is essentially independent of additional actuation. Fortunately, this challenge is not insurmountable; it simply indicates that the desired longitudinal dynamics must be designed in a more nuanced fashion that accounts for the natural longitudinal dynamics of the vehicle.

Chapter 7

Conclusions

Through analysis and control design to enable sustained operation of a rear wheel drive (RWD) vehicle at drift equilibria, this dissertation has developed a more thorough characterization of these operating conditions. While the rear tire saturation inherent to these equilibria is responsible for their open-loop instability, it has other implications as well. As the rear tires approach saturation, their lateral and longitudinal forces become increasingly coupled, to the point that rear drive force can be used to control the rear lateral forces once the tires are completely saturated. Consequently, rear tire saturation enables the rear drive force to act as a second input to the vehicle's lateral dynamics. With this in mind, drift equilibria are not characterized merely by a loss of open-loop vehicle stability, but rather a *tradeoff* of open-loop stability for enhanced vehicle controllability.

For skilled drivers capable of stabilizing a vehicle around a drift equilibrium, the associated increase in lateral control authority provides an incentive to drift when racing on surfaces with uncertain friction, where additional flexibility to alter the vehicle's trajectory is obviously valuable. But enhanced controllability also has applications in a vehicle safety context, especially for the development of collision avoidance and mitigation systems for agile autonomous vehicles. Such systems are predicated on the ability to alter a vehicle's orientation and trajectory while satisfying rather restrictive environmental constraints; this is a task that is facilitated by the availability of an extra lateral control input.

In order to access this added control authority, these systems must be able to deliberately induce rear tire saturation and provide closed-loop stabilization around drift equilibria, much like the skilled drivers mentioned above. However, development of a controller for this purpose is rendered challenging by certain physical properties of drift equilibria that must be taken into account.

In particular, two characteristics of the front steering input around drift equilibria are central to the design of a drift controller. The first of these characteristics is the existence of a right half plane (RHP) zero in the transfer function from steering perturbations to sideslip perturbations that is derived from the linearized vehicle dynamics around the drift equilibrium. Physically, this RHP zero indicates that the direct influence of front lateral force upon the sideslip dynamics is ultimately outweighed by the influence of front lateral force upon the yaw rate term in the sideslip dynamics. This property of the sideslip dynamics motivates a successive loop structure for a drift controller, in which yaw rate is used to control sideslip in an outer loop and tire forces are used to control yaw rate to the outer loop command in an inner loop.

The second characteristic of the steering input that figures prominently in drift controller design is near-saturation of the front lateral force at drift equilibria. Because of this property, the steering input essentially has unidirectional control authority around drift equilibria. Steering can easily reduce the yaw moment acting on the vehicle through a reduction in front lateral force, but can only increase the yaw moment a modest amount before the front tire saturates. As a consequence, coordination of the front steering and rear drive force to circumvent this limitation is essential, with the rear drive force input used for lateral control wherever control authority through steering is limited by front tire saturation.

The drift controller in this dissertation incorporates the above insights into its design. More importantly, it validates these insights by enabling sustained, robust operation of a by-wire test vehicle around a desired drift equilibrium. Furthermore, it achieves this result on a test surface reminiscent of the surfaces encountered in rally racing, where friction is uncertain and varies considerably.

The experimental performance of this controller and phase portraits of the closed-loop dynamics are both suggestive of a broad region of convergence around a desired drift equilibrium. However, this is challenging to demonstrate analytically because of a fundamental constraint of the rear drive force input. When rear drive force is used for the dual purposes of lateral and longitudinal control, a conflict arises between the lateral and longitudinal control objectives. Specifically, the rear drive force input needed to stabilize the lateral dynamics in some scenarios directly opposes the longitudinal control objective by initially inducing additional longitudinal velocity error. This conflict makes it difficult to design a drift controller with prescribed longitudinal dynamics that also has a sufficiently large region of feasibility (and by extension, region of convergence) around the desired drift equilibrium.

One way of addressing this issue is additional actuation to generate a yaw moment on the vehicle while leaving the rear drive force for longitudinal control. An example of such actuation is differential torque control at the rear axle, which makes it possible to generate a yaw moment by applying different longitudinal forces at each rear wheel while also satisfying a net longitudinal force command. Nevertheless, an effective control design using this actuation must still account for the physical properties of drift equilibria, especially the RHP zero and front lateral force limitation described above. With this in mind, this dissertation incorporates differential torque control into the same successive loop structure used in the original drift controller while leveraging the flexibility of a third input to make analytical stability statements more straightforward.

With this controller, it is possible to analytically demonstrate local exponential stability of the desired drift equilibrium, and phase portraits indicate a fairly large region of convergence. Therefore, differential torque control can be used to effectively address the issues stemming from a conflict of lateral and longitudinal control objectives when using the rear drive force input to drift. Nevertheless, the region of convergence and scope of the analytical stability guarantee for this design are still restricted by an infeasible region of the state space. This infeasible region is a reflection of the desired closed-loop dynamics chosen for the controller rather than the

properties of a particular actuator. Fortunately, this means that the controller's region of feasibility could conceivably be expanded by altering the desired closed-loop longitudinal dynamics for the vehicle.

7.1 Future Work

The drift controller designed and successfully implemented in this dissertation provides a fundamental understanding of control strategies that enable a vehicle to operate with saturated rear tires while taking advantage of the associated controllability benefits. From this foundation, there are multiple directions for future research. Some of these directions continue to focus upon particular aspects of the drift control problem, while other involve extension of these control strategies to more practical vehicle control problems.

7.1.1 Refinement of drifting using differential torque control

The control design that uses differential torque control at the rear axle shows promise as a viable approach for developing a drift controller with an analytical stability guarantee that also has a large enough region of feasibility to enable experimental implementation. However, certain refinements to the design are necessary before it makes sense to proceed with experimental implementation.

Incorporation of weight transfer effects

While the lumped tire model used throughout this dissertation reflects the effect of lateral weight transfer upon the net force capability at an axle, it does not capture the effect of weight transfer upon the individual wheels at an axle. In the study of differential torque control at the rear axle conducted in Section 6.2.3, it was assumed that the normal load on both wheels at the rear axle is equivalent for the sake of simplicity. In reality, weight transfer occurs from the inside wheels in a corner to the outside wheels, meaning that the normal loads on the rear wheels will not be equivalent at non-zero lateral accelerations. Considering that this effect is not insignificant

when cornering at the limits of lateral acceleration, it makes sense to incorporate it into a drift controller that relies upon the rear wheels being modeled individually. The primary effect of this modification would be upon the force capability of each rear wheel, and therefore the control authority available through the longitudinal force at each wheel. Consequently, this modification is relevant for implementation of the controller, but is not really a conceptual change in its design. The overall functionality and behavior of the controller would not be changed appreciably by incorporating weight transfer.

Design of desired closed-loop longitudinal dynamics

The drift controllers considered in this dissertation indicate that longitudinal control design plays a large role in dictating the region of feasibility for a controller. When using a longitudinal control law based on physical intuition that is not designed to impose a certain set of dynamics, feasibility is not an issue, but the resulting closed-loop dynamics are not particularly amenable to stability analysis. Conversely, when attempting to enforce a straightforward, stable structure for the closed-loop longitudinal dynamics, the controller's region of feasibility is restricted but stability guarantees are easier. For the drift controller using differential torques at the rear axle, the latter scenario is responsible for an infeasible region of the state space that is the primary roadblock to expanding the region of convergence and scope of analytical stability statements for this controller.

In order to address this issue, the desired closed-loop longitudinal dynamics for the controller should be redesigned to achieve a balance between feasibility over a sufficiently large region of the state space and structure for the sake of stability analysis. One approach to doing this might be desired longitudinal dynamics that include stabilizing linear terms but do not omit nonlinearities that can require significant control effort to cancel out and are easy to bound locally; a good example is the $rU_x\beta$ term in the longitudinal dynamics of the bicycle model. Using this approach, it may be possible to produce closed-loop longitudinal dynamics that are still fairly easy to manipulate in stability analysis while ensuring that the drift controller is feasible over a sufficiently large region of the state space.

7.1.2 Extension to agile autonomous vehicle research

The primary control objective of the controllers in this dissertation, namely to stabilize a vehicle to a particular drift equilibrium, is somewhat abstract when compared to objectives of collision mitigation and avoidance systems that are presently a focus of agile autonomous vehicle research. Even so, the controllers and underlying control strategies presented here can be adapted to these more practical ends in future development.

Incorporation of environmental variables

Since the controllers in this dissertation are intended to stabilize a drift equilibrium defined in terms of vehicle-fixed velocity states, they do not incorporate any information about the environment that is pertinent to collision avoidance and mitigation, such as obstacles or a desired path. In order to encode such information, it is necessary to incorporate positional states into the control design.

For applications where position control objectives are realizable using quasi-steady-state cornering, this may be possible using a hierarchical approach that builds on the drift controllers developed here. In such an approach, position control objectives are mapped to variation of the desired drift equilibrium in time, and the desired drift equilibrium is tracked using control techniques from this dissertation modified to accommodate a time-varying control objective.

Transient maneuvers with rear tire saturation

In some scenarios, collision avoidance and mitigation objectives may require sudden changes in vehicle orientation and trajectory for which an assumption of quasi-steady-state operation is not reasonable. These scenarios require transient operation with rear tire saturation, while the drift controllers in this dissertation are designed for steady-state operation. Nevertheless, the strategy used by these controllers to coordinate steering and rear drive force inputs is also valid for transient cornering with rear tire saturation, and could be applied to the design of controllers for this purpose.

7.2 Outlook

Through a comprehensive study of drifting, it has become clear that there exists a broader perspective from which to view the role of rear tire saturation in vehicle dynamics. While it is true that rear tire saturation contributes to vehicle instability, it also offers the opportunity to control a vehicle's trajectory in a considerably more flexible way. This is because rear tire saturation essentially decouples the direction that the vehicle is moving from the direction it is pointed and allows direct lateral control of the vehicle through two inputs instead of one. Both these attributes have applications in a safety context by making it easier to avoid collisions with obstacles and other vehicles.

Taking advantage of the opportunity presented by rear tire saturation requires algorithms that can stabilize the vehicle while the rear tires are saturated, and this dissertation establishes that it is possible to design controllers capable of this objective. Furthermore, the fundamental understanding of vehicle dynamics with rear tire saturation developed in this work provides a foundation on which to develop collision avoidance and mitigation techniques leveraging these dynamics. In light of this, it is not difficult to imagine an exciting future in which autonomous vehicles take advantage of rear tire saturation instead of avoiding it, using the car control skills of a racecar driver to enable new possibilities for vehicle control.

Bibliography

- [1] Federal Motor Vehicle Safety Standards: Electronic Stability Control Systems, Controls and Displays. Docket number NHTSA-2007-27662.
- [2] M. Abdulrahim. On the dynamics of automobile drifting. In *Proceedings of SAE World Congress 2006*, April 2006. SAE Technical Paper 2006-01-1019.
- [3] Craig E. Beal. *Applications of Model Predictive Control to Vehicle Dynamics for Active Safety and Stability*. Ph.D. thesis, Stanford University, 2011.
- [4] Craig E. Beal and J. Christian Gerdes. Controlling Vehicle Instability through Stable Handling Envelopes. In *Proceedings of the 2011 ASME Dynamic Systems and Control Conference, Arlington, Virginia, USA*. ASME Dynamic Systems and Control Division, November 2011.
- [5] J. E. Bernard, L. Segel, and R. E. Wild. Tire shear force generation during combined steering and braking manueuvres. *SAE World Congress*, 1977. Paper number 770852.
- [6] Carrie G. Bobier and J. Christian Gerdes. Staying within the nullcline boundary for vehicle envelope control using a sliding surface. *Vehicle System Dynamics*, 2012. Accepted for publication.
- [7] S. Boyd, L. El Ghaoui, E. Feron, and V. Balakrishnan. *Linear Matrix Inequalities in System and Control Theory*, volume 15 of *Studies in Applied Mathematics*. SIAM, Philadelphia, PA, June 1994.

- [8] R.H. Byrd, J.C. Gilbert, and J. Nocedal. A trust region method based on interior point techniques for nonlinear programming. *Mathematical Programming*, 89(1):149–185, 2000.
- [9] I. Chakraborty, P. Tsiotras, and J. Lu. Vehicle posture control through aggressive maneuvering for mitigation of T-bone collisions. In *Decision and Control and European Control Conference (CDC-ECC), 2011 50th IEEE Conference on*, pages 3264 –3269, Dec. 2011.
- [10] Jennifer N. Dang. Statistical Analysis of the Effectiveness of Electronic Stability Control Systems. Technical report, National Highway Traffic Safety Administration (NHTSA), July 2007. DOT HS 810 794.
- [11] Howard Dugoff, P.S. Fancher, and Leonard Segel. An analysis of tire traction properties and their influence on vehicle dynamic performance. In *Proceedings of the SAE World Congress, Paper 700377*. 1970.
- [12] J. Edelmann and M. Plochl. Handling characteristics and stability of the steady-state powerslide motion of an automobile. *Regular and Chaotic Dynamics*, 14:682–692, 2009. 10.1134/S1560354709060069.
- [13] J. Edelmann, M. Plochl, P. Lugner, W. Mack, and A. Falkner. Investigations on the powerslide of automobiles. In *Proceedings of AVEC 2008*, 2008.
- [14] J. Edelmann, M. Plochl, and P. Pfeffer. Analysis of steady-state vehicle handling and driver behaviour at extreme driving conditions. In *Proceedings of IAVSD 2011*, 2011.
- [15] T. Eguchi, Y. Sakita, K. Kawagoe, S. Kaneko, K. Mori, and T. Matsumoto. Development of “Super Hicas”, a new rear wheel steering system with phasereversal control. 1989. SAE Technical Paper 891978.
- [16] E Fiala. Lateral forces on rolling pneumatic tires. In *Zeitschrift V.D.I.* 96. 1954.

- [17] Michael Gipser. Ftire : a physically based application-oriented tyre model for use with detailed mbs and finite-element suspension models. *Vehicle System Dynamics*, 43(Supplement):76–91, 2005.
- [18] M. Grant and S. Boyd. Graph implementations for nonsmooth convex programs. In V. Blondel, S. Boyd, and H. Kimura, editors, *Recent Advances in Learning and Control*, Lecture Notes in Control and Information Sciences, pages 95–110. Springer-Verlag Limited, 2008. http://stanford.edu/~boyd/graph_dcp.html.
- [19] A. Gray, Y. Gao, T. Lin, J.K. Hedrick, H.E. Tseng, and F. Borrelli. Predictive control for agile semi-autonomous ground vehicles using motion primitives. In *American Control Conference (ACC), 2012*, pages 4239 –4244, June 2012.
- [20] R. Hadekel. The mechanical characteristics of pneumatic tyres. In *S and T Memo TPA3/TIB*. 1952.
- [21] P. Helnwein, C. J. Lie, G. Meschke, and H. A. Mang. A new 3-D finite element model for cord-reinforced rubber composite: application to analysis of automobile tires. *Finite elements in analysis and design*, 14(1):1–16, 1993.
- [22] R. Hindiyeh and J.C. Gerdes. Equilibrium analysis of drifting vehicles for control design. In *Proceedings of DSCC 2009*, October 2009.
- [23] Robert C Hoffman, Jeffrey L Stein, Lucas S Louca, and Kunsoo Huh. Using the milliken moment method and dynamic simulation to evaluate vehicle stability and controllability. *ASME Conference Proceedings*, (47063):173–180, 2004.
- [24] S. Inagaki, I. Kushiro, and M. Yamamoto. Analysis on vehicle stability in critical cornering using phase-plane method. *JSME Review*, 16(2):287 – 292, 1994.
- [25] Matthijs Klomp. *Longitudinal Force Distribution and Road Vehicle Handling*. Ph.D. thesis, Chalmers University of Technology, 2010.
- [26] M. Koishi, K. Kabe, and M. Shiratori. Tire cornering simulation using an explicit finite element analysis code. *Tire Science and Technology*, 26(2):109–119, April 1998.

- [27] Shad Laws, Christopher Gadda, Scott Kohn, Paul Yih, J. Christian Gerdes, and J. Craig Milroy. Steer-By-Wire Suspension and Steering Design for Controllability and Observability. In *IFAC World Congress, Prague, Czech Republic*, 2005.
- [28] Linhbergh Nguyen, June 2010. Photo of Nobuhiro Tajima's Suzuki SX4 at the 2010 Pikes Peak International Hillclimb.
- [29] E. Ono, S. Hosoe, and H.D. Tuan. Bifurcation in vehicle dynamics and robust front wheel steering control. *IEEE Transactions on Control System Technology*, 6(3):412–420, 1998.
- [30] Hans B. Pacejka. *Tire and Vehicle Dynamics*. Society of Automotive Engineers, Warrendale, PA USA, 2nd edition, 2005.
- [31] Hans B. Pacejka and Egbert Bakker. The magic formula tyre model. *Vehicle System Dynamics*, 21(S1):1–18, 1992.
- [32] CVX Research. CVX: Matlab software for disciplined convex programming, version 2.0 beta. <http://cvxr.com/cvx>, September 2012.
- [33] E. J. Rossetter, J. P. Switkes, and J. C. Gerdes. Experimental Validation of the Potential Field Lanekeeping System. *International Journal of Automotive Technology*, 5(2):95–108, 2004.
- [34] J. Ryu and J.C. Gerdes. Integrating inertial sensors with GPS for vehicle dynamics control. *Journal of Dynamic Systems, Measurement, and Control*, 126(2):243–254, 2004.
- [35] P. S. Shoemaker. Tire engineering by finite element modeling. *SAE World Congress*, 1984. Paper number 840065.
- [36] J. T. Tielking. A finite element tire model. *Tire Science and Technology*, 1(1):50–63, January 1983.

- [37] Anton T. van Zanten, Rainer Erhardt, Georg Pfaff, Friedrich Kost, Uwe Hartmann, and Thomas Ehret. Control Aspects of the Bosch-VDC. In *Proceedings of the International Symposium on Advanced Vehicle Control*, June 1996.
- [38] E. Velenis, E. Frazzoli, and P. Tsotras. Steady-state cornering equilibria and stabilization for a vehicle during extreme operating conditions. *International Journal of Vehicle Autonomous Systems*, 8(2–4):217–241, 2010.
- [39] E. Velenis, D. Katzourakis, E. Frazzoli, P. Tsotras, and R. Happee. Stabilization of steady-state drifting for a RWD vehicle. In *Proceedings of AVEC 2010*, 2010.
- [40] C. Voser, R. Hindiyeh, and J.C. Gerdes. Analysis and control of high sideslip manoeuvres. *Vehicle System Dynamics*, 48(Supplement 1):317–336, 2010.